Charmed Particle Production and Decay in a High Energy Photoproduction Experiment

Roger Forty

Imperial College
London

A thesis submitted to the University of London
for the degree of Doctor of Philosophy

May 1988

ABSTRACT

An investigation into the properties and production characteristics of charmed mesons is presented. The data are taken from a high energy photoproduction experiment, NA14, which collected 17 million triggers in the period 1985–86, at a mean energy of 100 GeV.

The theoretical context of the work is described, including the models of photoproduction and weak decay. The production of the photon beam and the detectors that make up the apparatus are discussed, with particular emphasis on the construction, operation and performance of a high resolution silicon microstrip detector—important for the isolation of charm signals.

Data reduction, track reconstruction and particle identification are discussed, and details are given of the vertex finding algorithms that have been developed, which are crucial for the enrichment of charm. Signals are presented in the decay channels $D^0 \to K\pi$ and D_s , $D^+ \to \phi\pi$.

The properties of the D_s and D^+ signals are investigated, including their lifetimes, with a value measured for the D_s of:

$$\tau\,(D_s) = 0{\cdot}33\,^{+0{\cdot}12}_{-0{\cdot}08} \pm 0{\cdot}03 \ \text{ps}$$

The mass of the D_s is measured as $1969{\cdot}8 \pm 1{\cdot}9 \pm 2{\cdot}4$ MeV/c^2, and the angular distributions of the D_s and D^+ decays are found to be consistent with their pseudoscalar spin-parity assignment.

The production characteristics of the D_s and D^+ signals are investigated, including the energy, x_F, and p_T distributions, and are found to be consistent with the predictions of a Monte Carlo simulation based on the first order QCD process, γg-fusion. The particle-antiparticle asymmetries are found to be $0{\cdot}29 \pm 0{\cdot}19$ for the D_s and $-0{\cdot}31 \pm 0{\cdot}30$ for the D^+. The production ratio is measured:

$$\frac{\sigma\,(D_s)}{\sigma\,(D^+)} = 0{\cdot}54 \pm 0{\cdot}17 \pm 0{\cdot}23$$

These values agree with those predicted by the Monte Carlo, which uses the Lund scheme for hadronisation, indicating that the parameters of this scheme—taken largely from e^+e^- results—are suitable for charm photoproduction.

CONTENTS

List of Figures

List of Tables

Notation

Symbols

Ordinary (scalar) physical variables are represented using *plain italic* type. Vector quantities are represented with ***bold italic*** type. Matrices are represented with **bold roman** type, and their elements with plain roman type.

Particle notation

The use of a symbol for a particle is generally taken to include the corresponding antiparticle, except in situations where this is clearly not the case (such as the discussion of particle-antiparticle asymmetries). For example, 'D^0' includes D^0 and $\overline{D}^0$.

The recently rationalised Particle Data Group [1] system of notation is used throughout for particle names (with one exception: their J/ψ is denoted simply ψ). In particular, the particle formerly known as the F-meson is denoted D_s.

Chapter 1

INTRODUCTION

This thesis concerns a high energy physics experiment named NA14. In this introduction, an overview of the aims and techniques of high energy physics is given, along with a general description of the experiment. Finally the structure of the thesis is outlined.

1.1 High energy physics

Overview

High energy physics is the study of the fundamental structure of matter. It is, as a consequence, the study of the very small, since to understand the behaviour of a large system it is instructive to investigate its component parts and their interactions.

In the study of the structure of matter it is found that macroscopic objects are composed of molecules, collections of chemically bonded atoms. Atoms are the smallest unit of an element that maintains its chemical properties, but they are not elementary as they may be readily ionised. Ionisation involves the removal from the atom of one of its component particles, the electron, the first example of a particle for which there is no evidence of substructure.

As well as electrons, the atom has a nucleus, made up in turn of neutrons and protons, the *nucleons*. Other, short-lived, particles of a similar nature to nucleons may be created when sufficient energy is available, as in the collision of cosmic rays with the atmosphere, or similar phenomena created in the laboratory. These particles are themselves composite, but their components, the *quarks*, represent the current limit to this quest for deeper substructure, as they appear to be truly elementary.

Quarks come in various types, or *flavours*: the *up* and *down* quarks that make up the nucleons, and other more exotic flavours including the *strange*, *charmed* and *beauty* (otherwise known as *bottom*) quarks. The work in this thesis is concerned with particles containing the charmed quark.

High energy physics thus involves the study of the properties of the elementary particles such as the quarks and the electron, and the forces that determine their interactions. A brief summary of the theory will be given in the next chapter, along with an account of the phenomenology relevant to this thesis.

Experimental features

The size of the smallest feature of an object that may be resolved is limited by the wavelength of the probe used, which for energy E is given by the de Broglie relationship:

$$\lambda = \frac{hc}{E}$$

For $\lambda \sim 10^{-15}$ m, the size of the nucleon, the equivalent energy is about 1 GeV. High energy physics experiments therefore involve the transfer of energies of at least this order of magnitude into volumes small compared with the nucleon size.

The high energies are achieved by supplying particles with kinetic energy in an accelerator to form a *beam*. The acceleration is provided by the electromagnetic force, so the accelerated beam particles must be charged. In a linear accelerator they travel a single time down a straight beam pipe, receiving energy from radio-frequency cavities; this has the disadvantage of requiring a great length to achieve high energies. Alternatively, in a cyclic accelerator, a magnetic field is used to constrain the beam to a circular path, of radius R given by:

$$R = \frac{p}{qB}$$

where p is the beam particle momentum, q is its charge, and B is the magnetic field strength. As the particles circulate, radio-frequency cavities at one or more points on the ring boost the energy. Typically 10^5 circuits are required before the full energy is achieved, so beam stability is very important. During the acceleration the magnetic field must be correspondingly increased to confine the beam to a constant radius, so that it may be enclosed in a small diameter beam pipe.

The accelerated particles are then directed onto a target. In *fixed target* experiments, a significant fraction of the beam energy is not available in the centre-of-mass frame, since momentum conservation requires that the kinetic energy after the collision is high. The energy in the centre-of-mass frame is given by:

$$E^* = (M^2 + m^2 + 2ME)^{1/2}$$

where m is the mass of the beam particle, E is its energy and M is the mass of the target particle (in units where $c = 1$). For a typical beam energy of 100 GeV, taking the effective target mass to be that of the proton, about 1 GeV/c^2, and neglecting the beam particle rest-mass, this gives a centre-of-mass energy of only ~ 14 GeV.

Collider experiments, on the other hand, utilise all the beam energy by making the target a second, counter-rotating beam. Then the particles of both colliding beams have momentum of the same magnitude but opposite direction, and the centre of mass is stationary in the laboratory frame. One pays the price of lower interaction rate, however, and the colliding particles must be both stable and charged, limiting the range of interactions that may be studied (compared to fixed target experiments, for which secondary beams may be produced using the primary, accelerated, particles).

The centre-of-mass energy available in the interaction of the beam and target particles may be used in the creation of new particles, provided their quantum numbers obey certain conservation laws (such as the conservation of charge). Some of these interaction products will be unstable, and decay to generate further particles. The process of the interaction of beam and target leading to product particles constitutes an *event*.

The interaction products emerge from the interaction point, typically at relativistic speeds, and the experimental detectors record their passage so that the event may be later reconstructed and analysed. In general the passage of a particle through a detector produces an analogue signal (for example the amount of ionisation produced in a silicon detector). Storage of the signal may be achieved in a variety of ways—for example the photographic record of a bubble chamber—but if it is required to study a large number of interactions then electronic storage is most suitable. This involves both the electronic read-out of the signal, with amplification and signal shaping if necessary, and *digitisation,* the translation from analogue to digital form. The digitised outputs from all the detectors are multiplexed by the data acquisition system and then read by a computer and finally written to magnetic tape for subsequent analysis.

It is necessary for the data acquisition system to know when to read out the apparatus. This requires a *trigger*, a signal created from the rapid inspection of a subset of the apparatus that indicates whether an event of interest has occurred. By triggering selectively on a particular property of the event (such as the presence of an electron) the volume of data that must be written to tape may be substantially reduced.

Whilst data are being taken, the apparatus must be monitored to check the performance of the detectors and to detect any faults. Due to the high cost of running an experiment and fierce competition for 'beam time', data taking and its attendant on-line monitoring take place day and night, run in shifts by the participants in an experiment. The tapes of data are then available for off-line processing, with event reconstruction and finally the physics analysis.

1.2 The NA14 experiment

NA14 is an experiment at CERN, a European centre for high energy physics in Switzerland. It takes its name from the North Area, a site dedicated to fixed target experiments, of which it was the fourteenth to be approved—see Figure 1.1. The experiment utilises a beam of high energy photons, created indirectly using 450 GeV protons from the Super Proton Synchrotron (SPS) accelerator (the position of which is illustrated in Figure 1.1).

The apparatus of the experiment is shown in Figure 1.2. It is large, with dimensions of approximately 26 m along the beam direction, and 6 m transverse to the beam. This elongated shape is a consequence of the fixed target kinematics, since the angle θ in the laboratory frame of a particle that travels at angle θ' in the centre-of-mass frame is given by:

$$\tan\theta = \frac{1}{\gamma^*}\frac{\sin\theta'}{\cos\theta' + \beta^*/\beta'}$$

where β' is the particle velocity in the centre-of-mass frame, β^* is the relative velocity of the frames, and $\gamma^* = (1-\beta^{*2})^{-1/2}$.

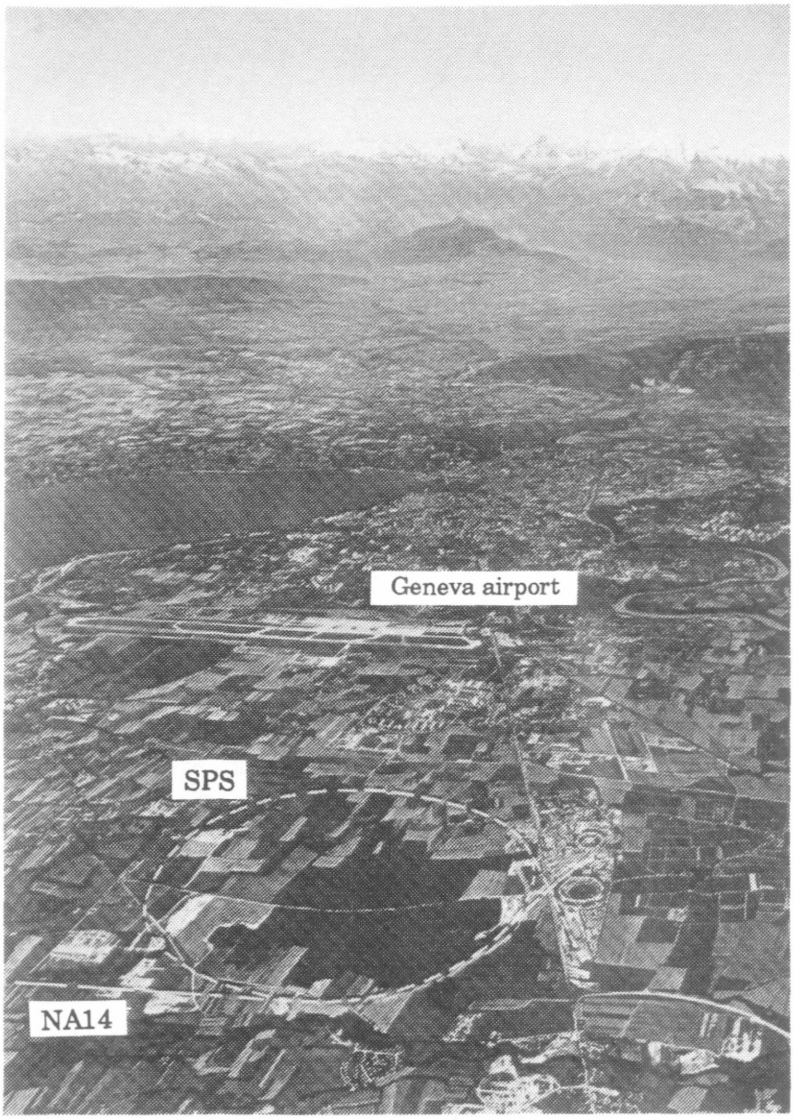

Figure 1.1 *Aerial view of CERN*

For NA14, β^* may be found using the fact that the momentum sum is zero in the centre-of-mass frame:

$$p - E\beta^* = M\beta^*$$

where p is the photon momentum, E is the photon energy and M is the target mass. But

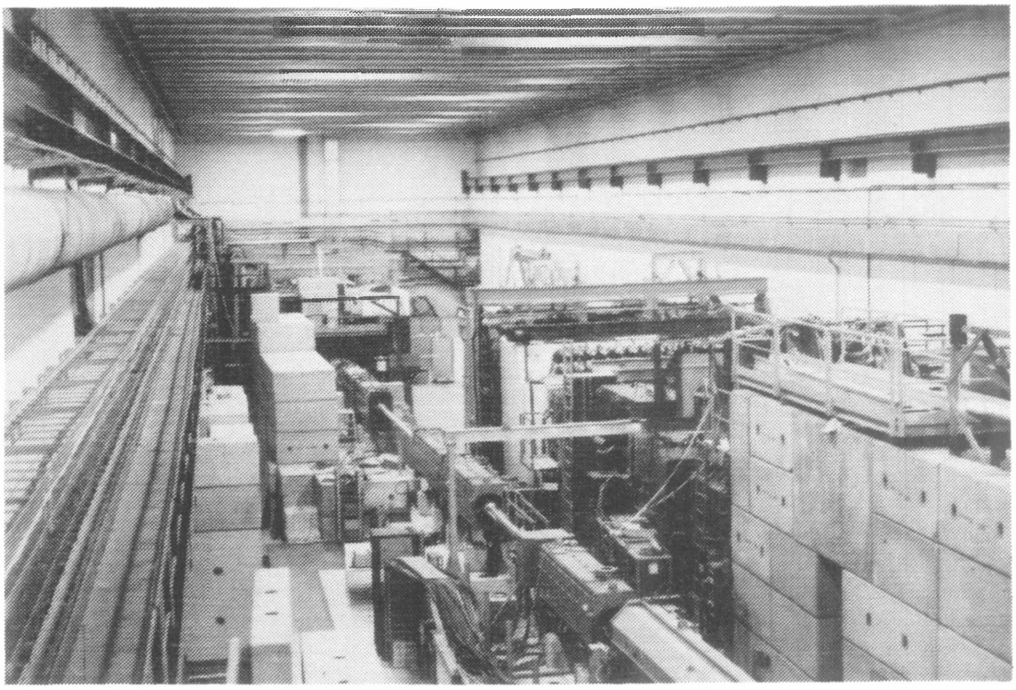

Figure 1.2 *View of the NA14 apparatus*

$p = E$ for a photon, so:

$$\beta^* = \frac{E}{(E+M)}$$

Now $E \sim 100$ GeV, $M \sim 1$ GeV/c^2, so $\beta^* \sim 0.99$ and $\gamma^* \sim 7$. Hence for a relativistic particle emitted perpendicular to the beam direction in the centre-of-mass frame ($\beta' \sim 1, \theta' = 90°$):

$$\tan\theta \approx \frac{1}{\gamma^*\beta^*}$$

giving $\theta \approx 4°$, with the result that in the laboratory frame the interaction products emerge in a narrow forward cone, along the beam direction.

The large dimensions of the apparatus are a consequence of the detection methods employed. An insight can be gained by considering one technique, the measurement of momentum from the deflection of a charged particle in a magnetic field: in traversing a distance L through a region of constant magnetic field B, a particle of charge q and momentum p will be deflected a distance d given by:

$$d \sim \frac{L^2 q B}{p}$$

so the deflection is inversely proportional to the momentum of the particle, and to obtain a

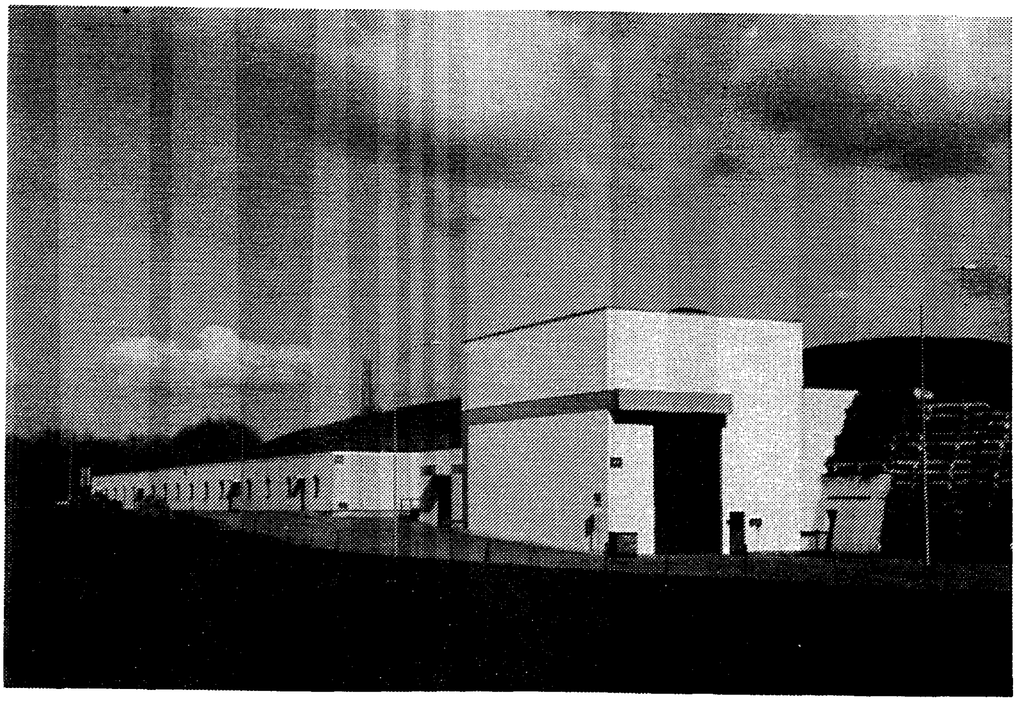

Figure 1.3 The NA14 counting room

given deflection as the beam energy is increased, the dimensions of the region of magnetic field must increase.

The apparatus stands in an underground hall, the 'zone', to which there is no access whilst data taking is in progress due to the dangerously high level of radiation. The parts of the apparatus used in the trigger are read by the electronics which decides whether the event is of interest, and this process must be done quickly (in less than $\sim 1\ \mu s$) to prevent the loss of the signals from the rest of the apparatus. At these time-scales the time taken for signals to travel down cables becomes significant, so the trigger logic is kept as close to the apparatus as is feasible; the components that may require human intervention are situated in a screened area next to the zone. All other remote controls and monitoring equipment are kept, along with the data-acquisition computer, in the counting room above ground. This may be seen in Figure 1.3.

The work described in this thesis concerns the study of short-lived charmed particles. One way to recognise events that contain such particles is to search for the decay vertex formed by the tracks of the decay products (see Figure 1.4). These tracks do not in general point to the primary vertex, but are offset by a distance δ, and for a particle

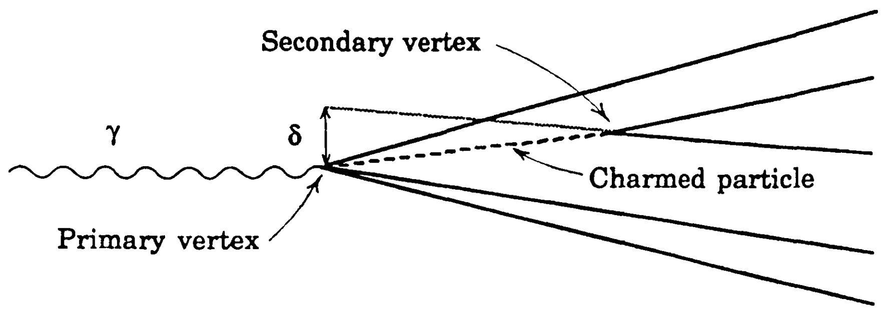

Figure 1.4 *Charmed particle decay*

of lifetime τ:

$$\delta \sim c\tau$$

independent of the energy of the decaying particle (see Section 8.2). Thus for a typical charmed particle of lifetime $\sim 5 \times 10^{-13}$ s, the offset is of the order of 150 μm, and a high resolution detector is necessary to see it. Such a vertex detector is used in NA14, composed of two parts: an active target (*active* because the material serving as a target itself acts as a detector for ionising particles) and a microstrip tracking detector.

The scale of high energy physics experiments is such that they are usually run by large international collaborations of physicists, and NA14 is no exception, with a population of around fifty participants from the following institutes:

	CERN
France:	*Collège de France Paris, LAL Orsay, Saclay, Strasbourg*
Greece:	*National Technical University Athens*
Poland:	*Warsaw University*
Spain:	*Universidad Autónoma Barcelona*
U.K:	*Imperial College London, Southampton University*

The different institutes generally took responsibility for separate parts of the apparatus. Imperial College was responsible for the microstrip detector and I had a specific responsibility for its monitoring and data acquisition. For this reason, and because of its importance in the identification of events containing charmed particles, prominence is given to the device in this thesis.

1.3 Outline of the thesis

In the next chapter, the theoretical background to the experimental work of the thesis is described. After a brief overview of the theoretical structure of the subject, details are given about charm spectroscopy, photoproduction, and weak decays.

In Chapter 3, the apparatus of the experiment is described, with discussion of the requirements of particle detection, the principles of operation of the detectors that make up the apparatus, and their configuration. Further details are given in Chapter 4 concerning the silicon vertex detector, including the techniques of detector fabrication and operation.

The data taking is discussed in Chapter 5, with details of the detector monitoring and of the trigger used by the experiment. Included in this chapter are tests that were made of the microstrip detector prior to the data taking runs, and the performance of the device during the runs.

The first step in the analysis of the data that were recorded, data processing, involves the use of filters to reduce the data-sample, and the running of production to reconstruct the tracks of each event. This is described in Chapter 6.

The analysis of the events for charm then follows. This relies heavily on the reconstruction of vertices formed by the tracks of each event, so Chapter 7 is devoted to the vertex finding techniques that were developed. They are then applied in Chapter 8, where the charm analysis is described, leading to the isolation of various charm signals. In Chapter 9 the physics results that have been extracted from these signals are presented, followed by a discussion of the conclusions drawn from the analysis.

Chapter 2

THEORETICAL BACKGROUND

In this chapter the theoretical background to the experimental work of the thesis is described. A brief overview of the theoretical structure of the subject is given first, to put the work into context. Then the particular topics of photoproduction and the decay of charmed mesons are addressed.

I The Standard Model

2.1 Introduction

The *Standard Model* [2] is the name given loosely to the set of theories that describe the experimental results of high energy physics. As yet there is no evidence of behaviour that violates this scheme, although there are theoretical and æsthetic arguments which suggest that it is not a complete picture. In this part of the chapter, the Standard Model will be outlined.

Particles

The physical world is composed of elementary particles, which may be classified according to their *quantum numbers*, that designate intrinsic properties of the particles such as their charge and spin. There are various types of particle, and for each particle type there is a corresponding antiparticle with the same mass but opposite quantum numbers (e.g. charge). The statistical properties of particles are intimately related to

Generation	Quarks			Leptons		
	Type	Q	I^3	Type	Q	I^3
1	u (up) d (down)	+2/3 -1/3	+1/2 -1/2	ν_e e^-	0 -1	+1/2 -1/2
2	c (charm) s (strange)	+2/3 -1/3	+1/2 -1/2	ν_μ μ^-	0 -1	+1/2 -1/2
3	t (top)? b (bottom)	+2/3 -1/3	+1/2 -1/2	ν_τ τ^-	0 -1	+1/2 -1/2

Table 2.1 *The fundamental constituents of matter*

their spin: those with half-integral spin (in units of $\hbar$) are *fermions* (i.e. they obey Fermi-Dirac statistics—requiring for example that no two fermions may occupy the same state), whilst those with integral spin are *bosons* (i.e. obey Bose-Einstein statistics).

Matter is built out of two types of fundamental fermion, for which there is no experimental evidence for structure at a scale of 10^{-17} m:

(i) *Quarks* have fractional electric charge, are massive, and come in various types, known as 'flavours';

(ii) *Leptons* have integral charge, and for each massive charged lepton there is a corresponding neutral, massless neutrino.

These particles are listed in Table 2.1, separated into *generations*—successive higher mass groups of particles whose properties closely match those of the previous generations. The *top* quark has not yet been discovered experimentally, but its existence is postulated to complete the third generation. Also given in the table for the particles are their charge, Q, and third component of weak isospin, I^3 (discussed below). The quarks and leptons are distinguished according to the interactions they are affected by.

Interactions

Classically, interactions were described according to a 'field' picture; this is replaced in

Force	Gauge boson	Dimensionless coupling	
Gravitational	graviton	$GM^2/\hbar c$	$\sim 10^{-37}$
Weak	$W^{\pm}, Z^0$	$M^2 c G_F/\hbar^3$	$\sim 10^{-5}$
Electromagnetic	γ (photon)	$e^2/4\pi\hbar c$	$\sim 10^{-2}$
Strong	g (gluon)	α_s	~ 1 ($r > 1$ fm)
			< 1 ($r < 1$ fm)

***Table 2.2** The fundamental forces*

quantum theory by the exchange of quanta—bosons that mediate the force. The strengths of the forces may be compared by constructing a dimensionless measure from relevant parameters: see Table 2.2. Traditionally the forces are classified as four types:

(i) *Gravitational.* Gravity affects all particles, but is negligible compared to the other forces at the mass scales relevant to experimental high energy physics. It has also been found difficult to quantize (although its mediating boson, the graviton, has been postulated), and the theory of gravitation remains of a very different character to those of the other forces. Because of this theoretical difficulty it does not form a part of the standard model.

(ii) *Electromagnetic*; the interaction that couples to charge, mediated by the photon. The theory that describes it, Quantum Electrodynamics (QED) has been successfully tested to great precision. Due to its success, it is expected that theories of the other interactions are of a similar character.

(iii) *Strong.* A force that affects quarks, but not leptons. The quark flavours are conserved in strong decays. The mediating boson is the *gluon*, which is neutral, massless and flavourless, but couples to *colour*, the strong force analogue of electrical charge. The corresponding theory is known as Quantum Chromodynamics (QCD). The effective coupling constant of the strong interaction depends on the momentum transfer (Q^2) of the process investigated (or equivalently the corresponding distance scale—see Table 2.2); the coupling strength decreases as the Q^2 increases (unlike in QED, where the strength *increases* as the Q^2 increases). This leads to 'asymptotic freedom': for very high momentum transfer the quarks are essentially free, and as a result perturbation theory can be used for QCD calculations at large Q^2.

(iv) *Weak*. This interaction was discovered first in β-decay, and is felt by all known particles. It can change quark flavour in particle decays, but is readily observable only when the strong and electromagnetic decays are forbidden by conservation laws. It has been unified with the electromagnetic force, in the *electroweak* theory, and its mediating bosons are the massive W and Z particles, whose mass is responsible for the apparent weakness of the coupling compared to that of electromagnetism—due to the short range associated with a massive propagator.

Free quarks are never found. Instead they are bound by the strong force into *hadrons*, which may be of two types: *baryons* formed from three quarks (such as the proton, with quark content uud), or *mesons* formed from a quark and an antiquark (such as the pion, $u\bar{d}$). These combinations arise from the 3 available colours (and corresponding anticolours) of quarks; the observed particles are colour singlets, which may be formed using a quark of each colour (baryons) or a colour-anticolour combination (mesons). Since quarks have spin 1/2, baryons are fermions, whilst mesons are bosons. The numerous quark flavours permit a wealth of different particles to be constructed in this fashion.

In QCD the simple constituent 'valence' quark picture of hadrons is complicated by the 'sea', formed by the radiation of gluons and the creation of quark-antiquark pairs. The hadron constituents—quarks and gluons—are generally referred to as *partons*.

2.2 QED

The theories of the various interactions are formulated in terms of Lagrangian field theory, using (from classical mechanics) the Euler-Lagrange equation for a field $\phi(\boldsymbol{x},t)$:

$$\frac{\partial}{\partial x_\mu}\left(\frac{\partial L}{\partial(\partial\phi/\partial x_\mu)}\right) - \frac{\partial L}{\partial \phi} = 0$$

where the *Lagrangian density* L is defined by:

$$\int L \,\mathrm{d}^3x = T - V$$

(the difference of the kinetic and potential energy of the system). The equation of motion follows from minimising:

$$\int L \,\mathrm{d}^4x$$

The *Hamiltonian H* is also used, defined by:

$$\int H \, \mathrm{d}^3x = T + V$$

In QED, the appropriate Lagrangian for a free fermion field ψ is (from Dirac's equation):

$$L = \overline{\psi}\,(i\gamma^{\mu}\partial_{\mu} - m)\,\psi$$

where γ^{μ} are the standard Dirac γ-matrices, and m is the mass of the fermion. The requirement of *local gauge invariance* is then applied, i.e. the Lagrangian should be invariant with respect to an arbitrary local phase change $\alpha(x)$:

$$\psi \rightarrow \psi' = \mathrm{e}^{i\alpha}\,\psi$$

This entails the introduction of a generalised 'covariant' derivative:

$$\partial_{\mu} \rightarrow \mathrm{D}_{\mu} = \partial_{\mu} - ie\,A_{\mu}$$

where e is the electronic charge, and A_{μ}, the *gauge field*, satisfies:

$$A_{\mu} \rightarrow A_{\mu} + \frac{1}{e}\,\partial_{\mu}\,\alpha$$

This gauge field is identified with the photon field, i.e. the gauge postulate identifies the form of the interaction. The concept of gauge invariance appears to be crucial for the *renormalisation* of the theory: divergences arising from self-energy may be absorbed into the definition of the constants (such as mass and charge), to ensure that calculations remain finite. The QED Lagrangian for a fermion field thus becomes:

$$L = \overline{\psi}\,(i\gamma^{\mu}\partial_{\mu} - m)\,\psi + e\overline{\psi}\,\gamma^{\mu}A_{\mu}\,\psi + \frac{1}{4}F_{\mu\nu}F^{\mu\nu} \tag{2.1}$$

where the gauge-invariant field strength tensor has been introduced:

$$F_{\mu\nu} = \partial_{\mu}\,A_{\nu} - \partial_{\nu}\,A_{\mu}$$

Note that a mass term for the photon of the form $m^2A_{\mu}A^{\mu}$ is prohibited by gauge invariance.

The electromagnetic interaction of two charged particles may be considered as the exchange of a photon (to lowest order), as illustrated in Figure 2.1. The invariant amplitude for the process is given by the product of electromagnetic 'currents' and a propagator term for the exchanged photon, with a coupling constant e from each vertex of the diagram:

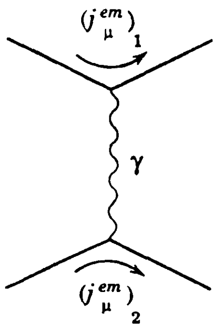

Figure 2.1 *Electromagnetic interaction*

$$\mathcal{M} = -\frac{e^2}{q^2}(j^{em}_\mu)_1 (j^{em\,\mu})_2$$

where q is the momentum of the photon. The current is given by:

$$j^{em}_\mu = -\bar{\psi}\gamma_\mu Q\psi$$

where the charge operator Q has been introduced, with eigenvalues ± 1 according to the charge of the particle.

2.3 Electroweak theory

Early theory

By analogy with electromagnetism, Fermi [3] suggested that the invariant amplitude for β-decay should be of the form:

$$\mathcal{M} = G_F J^{-\mu} J^+_\mu = G_F(\bar{u}_n \gamma^\mu u_p)(\bar{u}_\nu \gamma_\mu u_e)$$

where G_F is a weak coupling constant, $J_\mu^\pm$ are the charged currents, raising or lowering the charge, and u_i are the Dirac spinors for the particles i. The lack of a propagator term is due to the 4-particle vertex nature of the proposed interaction, see Figure 2.2. This was quite successful, but had to be modified when parity violation was discovered [4], by the incorporation of a parity violating term in the currents [5]:

$$\gamma_\mu \to \gamma_\mu \frac{1}{2}(1-\gamma_5)$$

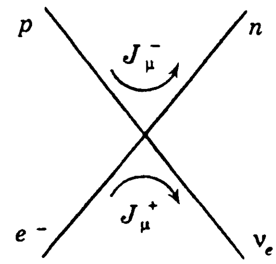

Figure 2.2 *Fermi β-decay*

giving:

$$J_\mu = J_\mu^+ = \bar{u}_\nu \gamma_\mu \frac{1}{2}(1-\gamma_5)\, u_e \equiv \bar{\nu}_L \gamma_\mu e_L$$

$$J_\mu^\dagger = J_\mu^- = \bar{u}_n \gamma_\mu \frac{1}{2}(1-\gamma_5)\, u_p \equiv \bar{n}_L \gamma_\mu p_L$$

where the short-hand notation e has been introduced for u_e, (etc.), and the subscript L indicates that it is the left-handed component that is taken. The theory therefore has a (V – A) structure, since $\bar{u}\gamma_\mu u$ transforms like a vector, and $\bar{u}\gamma_\mu\gamma_5 u$ transforms like an axial vector under Lorentz transformations. Then:

$$\mathcal{M} = \frac{4\,G_F}{\sqrt{2}} J^{\mu\dagger} J_\mu \tag{2.2}$$

where the numerical factor preserves the old definition of G_F. This formulation of the theory suffers from 'unitarity' problems, i.e. the non-conservation of probability, but it survived until superseded by the Weinberg-Salam theory [6] that unified the weak and electromagnetic forces.

Weinberg-Salam theory

The charged weak currents may be rewritten using a 2-dimensional form for the left-handed spinors:

$$\chi_L = \begin{bmatrix} \nu \\ e \end{bmatrix}_L$$

and using the 'step up/down' operators:

$$\tau_\pm = \frac{1}{2}(\tau_1 \pm i\tau_2)$$

where τ_i are the Pauli spin matrices. Then:

$$J_\mu^\pm = \bar{\chi}_L \gamma_\mu \tau_\pm \chi_L$$

$$J_\mu^3 = \overline{\chi}_L \gamma_\mu \frac{1}{2} \tau_3 \chi_L \tag{2.3}$$

to complete an isospin triplet of weak currents:

$$J_\mu^i = \overline{\chi}_L \gamma_\mu \frac{1}{2} \tau_i \chi_L \qquad (i = 1, 2, 3)$$

The corresponding charges, the components of weak isospin:

$$I^i = \int J_0^i(x)\, \mathrm{d}^3 x$$

obey the commutation relation:

$$[I_i, I_j] = i\, \varepsilon_{ijk}\, I_k$$

where ε_{ijk} is the standard antisymmetric tensor, and they therefore generate an SU(2) algebra.

The electromagnetic interaction is incorporated through a further current, the 'weak hypercharge' current:

$$j_\mu^Y = \overline{\psi} \gamma_\mu Y \psi$$

where weak hypercharge Y is defined by:

$$Q = I^3 + \frac{Y}{2}$$

i.e:

$$j_\mu^{em} = J_\mu^3 + \frac{1}{2} j_\mu^Y \tag{2.4}$$

The hypercharge operator generates a symmetry group U(1), so the symmetry group of the theory is enlarged to SU(2) × U(1).

The electromagnetic current couples to the photon via a term in the Lagrangian:

$$e\, j^{em\,\mu} A_\mu \tag{2.5}$$

It is postulated that the electroweak currents couple to vector bosons: $W_\mu{}^i$ (a triplet) couple to $J_\mu{}^i$ with strength g, and B_μ (a singlet) couples to $j_\mu{}^Y$ with strength $g'/2$, giving the electroweak interaction:

$$g J^{i\mu} W_\mu^i + \frac{g'}{2} j^{Y\mu} B_\mu$$

The combinations:

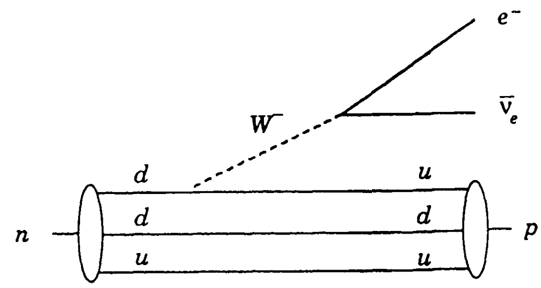

***Figure 2.3** Weinberg-Salam β-decay*

$$W_\mu^{\mp} = \sqrt{\frac{1}{2}}\,(W_\mu^1 \pm i\,W_\mu^2)$$

give the charged bosons, and $W_\mu{}^3$ and B_μ are neutral.

The masses of the bosons are generated by symmetry breaking. As for QED, adding a simple mass term for the boson fields to the Lagrangian would violate gauge invariance, and make the theory unrenormalisable. Instead, the Higgs mechanism [7] is used, adding a complex doublet of scalar fields, and then allowing spontaneous symmetry breaking to absorb three of the scalar degrees of freedom as longitudinal polarisations of the vector bosons, leaving three massive gauge fields and a massive scalar Higgs particle. The neutral fields mix to produce mass eigenstates:

$$A_\mu = B_\mu \cos\theta_W + W_\mu{}^3 \sin\theta_W \quad \text{(massless)}$$
$$Z_\mu = -B_\mu \sin\theta_W + W_\mu{}^3 \cos\theta_W \quad \text{(massive)}$$

where the mixing parameter, θ_W known as the 'weak mixing angle', is determined by experiment to give $\sin^2\theta_W \sim 0{\cdot}23$. The charged gauge bosons have mass:

$$M_W = \frac{1}{2} g\,v$$

where v is the vacuum expectation value of the scalar field, and the mass of the neutral gauge boson is related to M_W by:

$$\frac{M_W}{M_Z} = \cos\theta_W$$

The weak interaction is now seen as an exchange of $W^{\pm}$ and Z^0 particles. For example, the β-decay shown in Figure 2.2 is interpreted as the transition of a d-quark to a u-quark via the emission of a virtual W-boson. See Figure 2.3.

The electroweak neutral current interaction is thus given by:

$$g\, J^3_\mu W^{3\,\mu} + \frac{g'}{2} j^Y_\mu B^\mu = \left(g \sin\theta_W J^3_\mu + g' \cos\theta_W \frac{j^Y_\mu}{2} \right) A^\mu + \left(g \cos\theta_W J^3_\mu - g' \sin\theta_W \frac{j^Y_\mu}{2} \right) Z^\mu$$

The first term is the electromagnetic interaction, so by comparison with Equations 2.4 and 2.5, we have:

$$g \sin\theta_W = g' \cos\theta_W = e$$

The charged current interaction is given by:

$$\frac{g}{\sqrt{2}} \left(J^\mu W^+_\mu + J^{\mu\,\dagger} W^-_\mu \right)$$

where we have used:

$$\frac{1}{2}(\tau_1 W^1 + \tau_2 W^2) = \sqrt{\frac{1}{2}}\,(\tau_+ W^+ + \tau_- W^-)$$

The invariant amplitude may then be calculated, following the QED procedure:

$$\mathcal{M} = \left(\frac{g}{\sqrt{2}} J_\mu \right) \frac{1}{M_W^2} \left(\frac{g}{\sqrt{2}} J^{\mu\,\dagger} \right)$$

where the factor $(1/M_W^{\,2})$ comes from the approximation to the W propagator at low Q^2. Hence, by comparison with Equation 2.2, we have:

$$\frac{G_F}{\sqrt{2}} = \frac{g^2}{8 M_W^2}$$

Quark mixing

As noted above, the fundamental fermions are grouped in left-handed pairs for their weak interactions. The partner of the u-quark is the d-quark, and so on. However, the eigenstates of the weak interaction need not in general be the same as the mass eigenstates, so we introduce weak mixing of the states [8]: the partner of the u-quark becomes:

$$d' = d \cos\theta_C + s \sin\theta_C$$

i.e. mixed with the s-quark state, where the mixing angle θ_C is known as the Cabibbo angle—to be determined by experiment. The decay $K^+ \rightarrow \mu^+ \nu_\mu$ is expected (from phase space) to occur at about 18 times the rate of the decay $\pi^+ \rightarrow \mu^+ \nu_\mu$. However, from Figure 2.4, it can be seen that the kaon decay amplitude will involve a factor $\sin\theta_C$, whilst the pion decay will involve a factor $\cos\theta_C$, so the ratio of decay rates will be modified by $\tan^2\theta_C$.

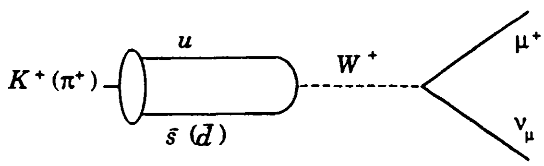

Figure 2.4 *K^+ (π^+) decay to $\mu^+\nu_\mu$*

Experimentally it is found that:

$$\frac{\Gamma(K^+ \to \mu^+\nu_\mu)}{\Gamma(\pi^+ \to \mu^+\nu_\mu)} \sim 1{\cdot}34$$

Hence $\tan^2\theta_C \sim 0{\cdot}05$.

The hadronic neutral current from the (u, d') pair of states will have the form (from Equation 2.3):

$$u\bar{u} + d\bar{d}\cos^2\theta_C + s\bar{s}\sin^2\theta_C + (s\bar{d} + \bar{s}d)\sin\theta_C\cos\theta_C \tag{2.6}$$

where the γ-matrices and overall factors have been suppressed. However, it can be seen from this that strangeness-changing neutral currents exist, given by the last term in the expression. See Figure 2.5. Experimentally:

$$\frac{\Gamma(K_L^0 \to \mu^+\mu^-)}{\Gamma(K_L^0 \to all)} \sim 10^{-8}$$

i.e. these reactions are strongly suppressed. This was explained by the GIM mechanism [9]—involving the prediction of an additional quark, the charmed quark c. The c-quark and s-quark then form a doublet, with the weak partner of the c-quark given by:

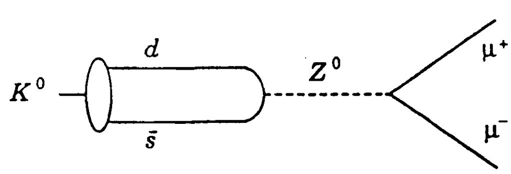

Figure 2.5 *K^0 decay to $\mu^+\mu^-$*

$$s' = -d \sin\theta_C + s\cos\theta_C$$

in a corresponding manner to the (u, d') doublet. This introduces further terms into the neutral current:

$$c\bar{c} + s\bar{s}\cos^2\theta_C + d\bar{d}\sin^2\theta_C - (s\bar{d} + \bar{s}d)\sin\theta_C\cos\theta_C$$

and (comparing Equation 2.6) results in the cancellation of the strangeness-changing component.

The mixing of quark states may be straightforwardly extended to 6 quark flavours, requiring a (3×3) mixing matrix (known as the Kobayashi-Maskawa matrix [10]). The hadronic charged current becomes:

$$J_\mu = u_i^\dagger \gamma_\mu \frac{(1-\gamma_5)}{2} \mathrm{V}_{ij} d_j$$

where:

$$\boldsymbol{u} = \begin{bmatrix} u \\ c \\ t \end{bmatrix} \qquad \boldsymbol{d} = \begin{bmatrix} d \\ s \\ b \end{bmatrix}$$

and:

$$\mathbf{V} = \begin{bmatrix} \mathrm{V}_{ud} & \mathrm{V}_{us} & \mathrm{V}_{ub} \\ \mathrm{V}_{cd} & \mathrm{V}_{cs} & \mathrm{V}_{cb} \\ \mathrm{V}_{td} & \mathrm{V}_{ts} & \mathrm{V}_{tb} \end{bmatrix}$$

Instead of the single Cabibbo angle, the mixing matrix now has 4 parameters—out of the 18 real parameters required (allowing each element to be complex), 5 are unobservable (and therefore unimportant) phases, and the requirement of unitarity provides 9 constraints, leaving 3 angles and one overall phase (that permits CP-violation [11]) to be determined by experiment. Ignoring CP-violation, the matrix may be approximately parameterised [12] as:

$$\mathbf{V} \sim \begin{bmatrix} 1 & \lambda & \lambda^3 \\ -\lambda & 1 & \lambda^2 \\ -\lambda^3 & -\lambda^2 & 1 \end{bmatrix}$$

where $\lambda \sim \sin\theta_C$. (This is an experimental observation—there is no justification for it in the Standard Model). Interactions involving a KM-matrix element of $O(\lambda)$ (or higher powers) are thus referred to as Cabibbo-suppressed (or *very* Cabibbo-suppressed).

2.4 QCD

The theory of the strong interaction, QCD, follows the structure of QED, and is a locally gauge invariant theory. The U(1) gauge group is replaced by the SU(3) group of colour. As for QED, the free Lagrangian is:

$$L_0 = \bar{q}_j (i\gamma^\mu \partial_\mu - m) q_j$$

where only one quark flavour has been shown, and the index j runs over the 3 colour fields. We require L_0 to be invariant under an arbitrary gauge transformation:

$$q(x) \rightarrow e^{i\alpha_a(x)\lambda_a/2} q(x)$$

where λ_a ($a = 1, ..., 8$) are the Gell-Mann matrices—linearly independent, traceless (3×3) matrices. They form a non-abelian group, since they do not all commute:

$$[\lambda_a/2, \lambda_b/2] = i f_{abc} \lambda_c/2$$

where f_{abc} are the *structure constants* of the group. As in QED, we introduce gauge fields, although 8 are now required, $G_\mu{}^a$. The corresponding covariant derivative becomes:

$$\partial_\mu \rightarrow D_\mu = \partial_\mu + ig\frac{\lambda_a}{2} G_\mu^a$$

where g is the coupling constant, and for gauge invariance we require:

$$G_\mu^a \rightarrow G_\mu^a - \frac{1}{g}\partial_\mu \alpha^a - f^{abc}\alpha_b G_{\mu c} \tag{2.7}$$

Thus the QCD Lagrangian becomes:

$$L = \bar{q}(i\gamma^\mu \partial_\mu - m) q - g(\bar{q}\gamma^\mu \frac{\lambda_a}{2} q) G_\mu^a - \frac{1}{4} G_{\mu\nu}^a G_a^{\mu\nu}$$

where the final term represents the kinetic energy of the $G_\mu{}^a$ fields, in a similar fashion to that of A_μ in Equation 2.1, but with a more complicated form due to the additional term in Equation 2.7:

$$G_{\mu\nu}^a = \partial_\mu G_\nu^a - \partial_\nu G_\mu^a - g f^{abc} G_{\mu b} G_{\nu c} \tag{2.8}$$

The $G_\mu{}^a$ fields represent the gluons, and the last term of Equation 2.8 indicates that they have self-coupling. This is a result of the non-abelian structure of the theory, and follows from the fact that the gluons themselves carry colour.

The symmetry of the complete Standard Model, involving the Salam-Weinberg electroweak theory and QCD, is thus $SU(3) \times SU(2) \times U(1)$. This model has been successful in describing the experimental results of high energy physics to date, but serious questions remain unanswered: why is there more than one generation of fundamental fermions? What is the source of the various mass scales and (relevant to this thesis) the KM-matrix parameters? How may gravity be included? Questions such as these provide motivation for the future development of the theory.

2.5 Charm physics

The charmed quark was postulated in 1970, as noted above, to account for the experimentally observed lack of strangeness-changing weak neutral currents, by invoking the GIM mechanism. It was discovered in 1974 [13], in the guise of the ψ-meson, the bound state of the charmed quark and its antiquark. The characteristic which indicated the presence of a new quantum number was the narrow width of the excitation observed, indicating that the particle was long-lived. Particles with *naked* charm (i.e. formed from a charmed quark with other lighter quarks, and thus with a non-zero value for the charm quantum number) are of too high mass to be produced in ψ decay, so the constituent charmed quark and antiquark of the ψ must lose their charm quantum number by mutual annihilation, a suppressed process. Particles with naked charm were first observed in 1975 [14].

Charm spectroscopy

With the charmed quark there were now four quark flavours, and the hadrons predicted by the quark model are displayed in Figure 2.6. There are 6 low-lying charmed meson states formed from combinations of light quarks with the charmed quark: three pseudoscalars, D^0 ($c\bar{u}$), D^+ ($c\bar{d}$), $D_s{}^+$ ($c\bar{s}$); and three vector partners of these states, which decay electromagnetically or via single pion emission to the pseudoscalars. The D^+ was first discovered, followed by the D^0. The D_s was searched for, and early indications gave it a mass of about 2030 MeV/c^2 [15]. The first unambiguous evidence for the particle was found in 1983 [16], with a mass of about 1970 MeV/c^2, and subsequent experiments have confirmed this, although the total world statistics for the D_s remain low. The three vector

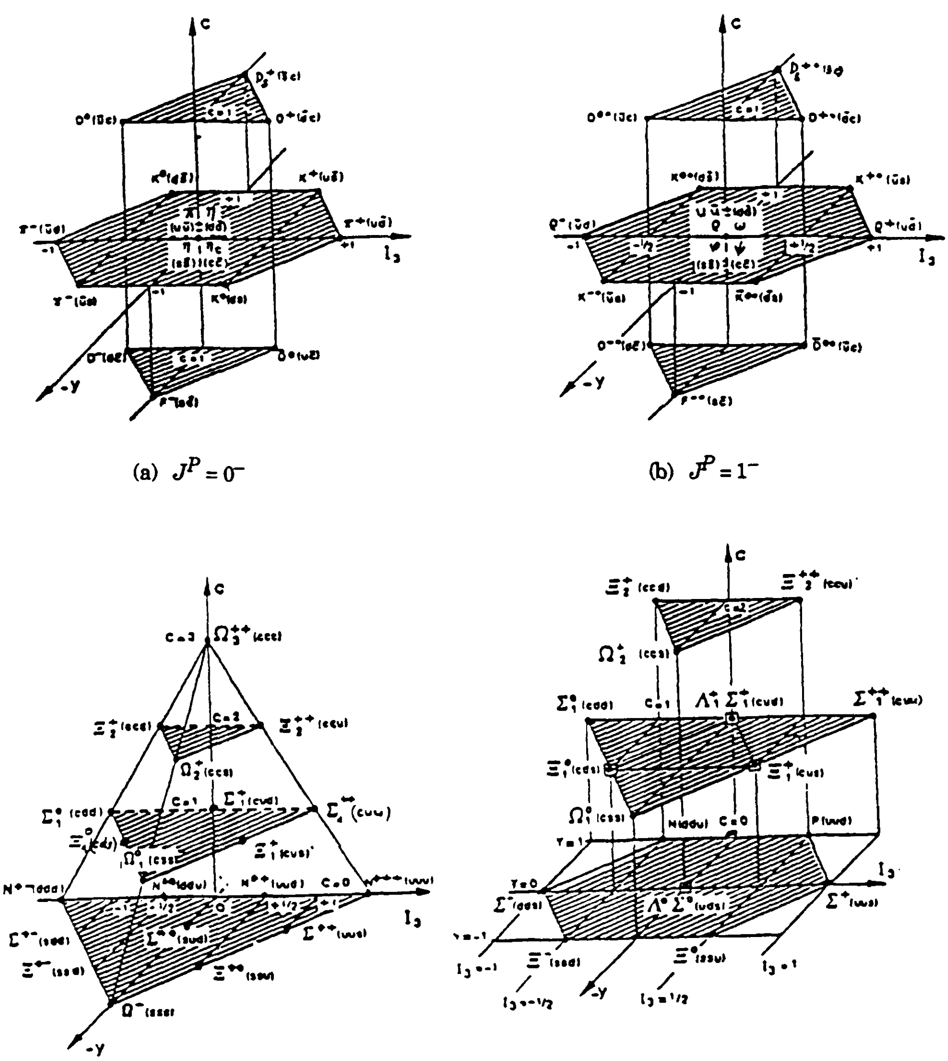

(a) $J^P = 0^-$ (b) $J^P = 1^-$

(c) $J^P = 1/2^+$ (d) $J^P = 3/2^+$

Figure 2.6 *Hadron classification for four quark flavours*

partners have also been seen.

Among the charmed baryons, four decay weakly: the Λ_c^+, Ξ_c^+, Ξ_c^0, and Ω_c^0. Of these, the Λ_c (cud) is well established experimentally, and the Ξ_c^+ (cus) has been recently discovered [17]. One experiment has seen indications of the Ω_c (css), and the field of heavy quark spectroscopy remains an active area of experimental study [18].

Charm experiments

Over the past few years, charm physics has been explored by almost every variety of high energy physics experiment. The original investigation of neutral currents was made with neutrino fixed target experiments, and the ψ was discovered by both an e^+e^- collider experiment, and a proton fixed target experiment. In the past, e^+e^- collider experiments have dominated the field, through their ability to tune the beam energy to that of a resonance such as the ψ'', which decays almost exclusively to charmed final states. They thus achieved high statistics for charmed particle decays, but generally with low spatial precision for vertex reconstruction. Their lifetime measurements had therefore to be obtained from small offsets of broad impact parameter distributions. Prominent experiments of this type were ARGUS [19] and MarkIII [20].

Recently the emphasis has shifted towards fixed target experiments, utilising high precision vertex detectors. NA14 is of this type, as is NA32 [21], another CERN experiment (using a hadronic beam). A further experiment currently producing results is E691 [22] at Fermilab, which took an impressive 100 million triggers using a very similar set-up to NA14, with photon beam and microstrip detectors.

Aims of NA14

The NA14 experiment was proposed in 1978 [23], to investigate hard scattering in photoproduction. The large momentum transfer involved in hard scattering is seen as a large transverse component of the momentum of the interaction products. The interactions of photons and quarks were studied through the measurement of Compton scattering: the QED Compton process is simply the scattering of a photon off a parton of the target nucleon (Figure 2.7 (a)), and in a similar process, QCD Compton scattering, the

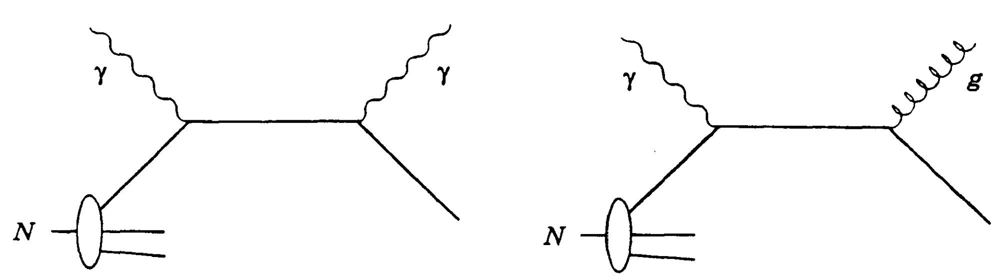

(a) QED Compton (b) QCD Compton

Figure 2.7 *Compton scattering*

out-going photon is replaced by a gluon (Figure 2.7(b)). The cross-sections for these processes have been calculated within the Standard Model, and the experimental results [24] were consistent with expectations. The standard fractionally charged quark model was supported, whilst certain integer charged quark models were discounted.

In 1982 an upgrade of the apparatus was proposed [25] to study the photoproduction of heavy flavours. This involved the addition of a vertex detector to be sensitive to the short-lived particle decays.

Whilst the vertex detector was developed, a beam-dump experiment was performed in 1984, to investigate beauty production through the search for events containing like-sign muon pairs. This work provided an upper limit for the beauty photoproduction cross-section of 3·0 nb at a 90 % confidence level.

Finally the upgraded experiment (renamed NA14') was operational, and after a test run in 1984, data were collected during the Summer of 1985. Further runs took place in the Summer and Autumn of 1986. The experiment was intended to investigate the photoproduction of charmed particles, so in the next part of this chapter the theory of photoproduction will be discussed.

II Photoproduction

2.6 Introduction

The high energy interaction of photons with matter may occur by various mechanisms [26]:

(i) *Point-like*: the photon interacts directly with one of the partons from the target nucleon, as in the QED and QCD Compton effects that were shown in Figure 2.7;

(ii) *Hadron-like*: the photon dissociates into quarks and gluons which then interact with the target. This type of interaction may be further classified:

(a) The photon may couple to one of the vector meson (such as the ρ, ω, ϕ, ψ, etc.) which have the same quantum numbers as the photon. The meson then interacts with the target, as shown in Figure 2.8.

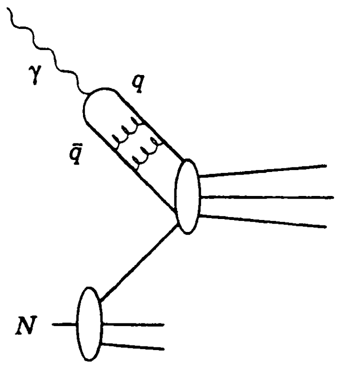

Figure 2.8 Photon interaction as a vector meson

(b) The photon dissociates into a quark pair, one of which then interacts with the target, as illustrated in Figure 2.9; this is the so-called *anomalous component* of the photon's interaction. It has similar characteristics to hadroproduction, but with different structure functions. This process involves large p_T, and therefore may be calculated using perturbative QCD.

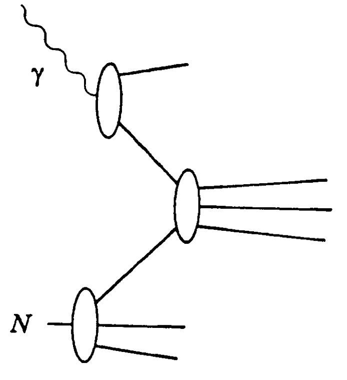

Figure 2.9 Anomalous component of the photon interaction

Vector Meson Dominance

An early model [27] proposed that the coupling of the photon to the target via a vector meson state dominates the photon's interaction, hence 'Vector Meson Dominance' (VMD). This assumption permits calculations to be made of the production characteristics, which are found to agree reasonably well with the data. The photon is treated as a superposition of the 1^- vector meson states, as shown in Figure 2.10, and the invariant amplitude then becomes:

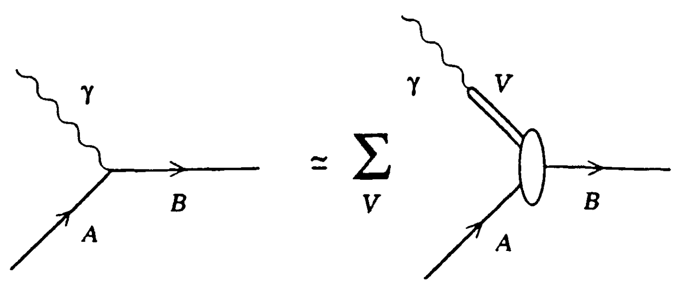

Figure 2.10 *Vector meson dominance*

$$\mathcal{M}(\gamma A \to B) = e \sum_V \frac{1}{g_V} \frac{m_V^2}{m_V^2 - q^2 - i\,\Gamma_V m_V} \mathcal{M}(VA \to B)$$

where V is a vector meson of mass m_V and total width Γ_V, g_V is the coupling of the vector meson determined from its leptonic decay, and:

$$q^2 = (p_A - p_B)^2$$

The momentum transfer involved in this process is low, so QCD calculations cannot be performed in this non-perturbative regime. VMD is expected to be important for low p_T production.

Charm photoproduction

The momentum transfer of a process leading to the production of a quark with mass m_q and transverse momentum p_T is given by:

$$Q^2 \sim {m_q}^2 + {p_T}^2$$

Therefore for the photoproduction of charm, $Q^2 > {m_c}^2 \sim 2\ \mathrm{GeV}^2/c^4$, substantially greater than the hadronisation scale of QCD. Hence, due to the large mass of the charm quark, perturbative QCD is valid even for low p_T, and charm photoproduction is therefore a good place to test it.

2.7 γg-fusion

The lowest order diagram for the QCD calculation of charm photoproduction is shown in Figure 2.11. The photon interacts with a gluon from the target nucleon, so this is known

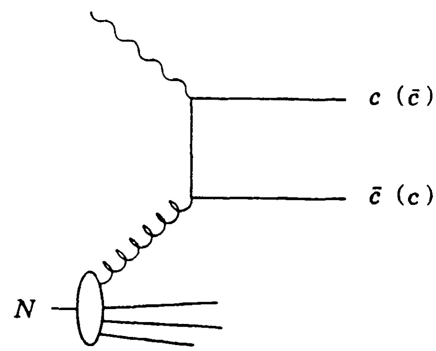

Figure 2.11 *Photon-gluon fusion*

as *photon-gluon fusion* (γg-fusion). It has been calculated using QCD [28,29,30], where (in this case) the higher order contributions are not expected to be substantial. The cross-section is given by:

$$\sigma(s) = \int_{x_{min}}^{1} \sigma_{\gamma g}(xs)\, G(x)\, \mathrm{d}x$$

where x is the fraction of the momentum of the target nucleon carried by the gluon, $G(x)$ is the structure function of the gluon in the nucleon, $\sigma_{\gamma g}$ is the cross-section of the subprocess $\gamma g \rightarrow c\bar{c}$, and x_{min} is the lower limit of x. The Mandelstam s-variable of the γN system is given by:

$$s = m_N (m_N + 2\, E_\gamma)$$

For charm production:

$$x_{min} = \frac{4\, m_c^2}{s}$$

giving $x_{min} \sim 0{\cdot}05$ for a photon energy of 100 GeV.

The cross-section $\sigma_{\gamma g}$ has been calculated [28]:

$$\sigma_{\gamma g} = \frac{\pi\, \alpha\, \alpha_s\, e_c^2}{\hat{s}} \left[(3 - \beta^4) \ln \left(\frac{1+\beta}{1-\beta} \right) - 2\, \beta\, (2 - \beta^2) \right]$$

where:

$$\beta = \left(\frac{p_c}{E_c} \right)_{CM} = \sqrt{1 - \frac{4\, m_c^2}{\hat{s}}}$$

and $\hat{s} = xs$ is the s-variable of the γg subprocess.

The calculation of the charm photoproduction cross-section therefore depends on the gluon structure function, the mass of the charmed quark, and the value taken for Q^2 (which affects the coupling constant, $\alpha_s(Q^2)$, and the gluon structure function).

Choice of Q^2

From inspection of the γg-fusion diagram, the following choice of Q^2 might be considered suitable:

$$Q^2 = -m_c^2$$

where m_c is the mass of the virtual (charmed) quark that is exchanged. Then:

$$Q^2 = -\hat{t} = \hat{s}\frac{(1-\beta\cos\theta)}{2} - m_c^2$$

where θ is the angle between the gluon and charmed quark in the centre of mass frame. However, this choice differs for the two charge-conjugate diagrams, due to the sign of the $\cos\theta$ term. A more symmetric choice is:

$$Q^2 = \hat{s}_{threshold} = 4\,m_c^2$$

and this is usually adopted.

Mass of the charmed quark

Since the charmed quark is not found as a free particle, its mass is not well known. It is determined from the masses of bound states of the charmed quark with other quarks, so the binding energy confuses the calculation. Furthermore the mass is renormalised by self-energy terms, and hence depends on Q^2. It is usually taken as:

$$m_c = \frac{M(\psi)}{2} \sim 1{\cdot}5\ \mathrm{GeV}/c^2$$

Since the theoretical calculations depend strongly on m_c, its uncertainty leads to substantial errors on the predictions.

Gluon structure function

From deep inelastic scattering experiments [31], it has been determined that the gluons carry about half of the momentum of the nucleon, so we must have:

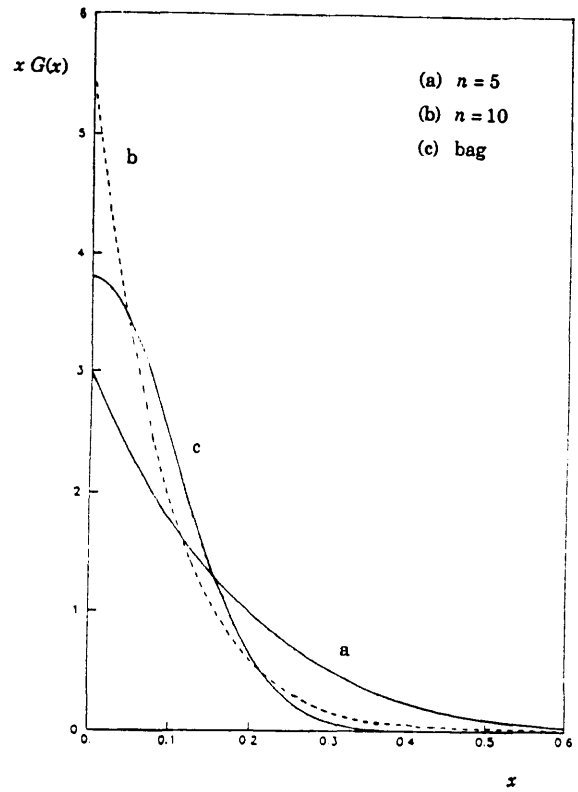

Figure 2.12 The gluon structure function

$$\int_0^1 x\, G(x)\, \mathrm{d}\, x \sim \frac{1}{2}$$

In the limit $x \to 1$, we would have a single parton (the gluon) carrying all the momentum of the nucleon, which is clearly impossible. The structure function must therefore vanish in this limit. As the limit is approached, the other partons have vanishing momentum, and hard gluon exchanges are necessary to transfer their momentum to the fast parton. These considerations lead to the 'dimensional counting rule' result [32] that:

$$x\, G(x) \sim (1-x)^{2n_s - 1}$$

where n_s is the minimum number of other partons involved (apart from the one under investigation). For the gluon structure function, $n_s = 3$ (the three valence quarks of the nucleon) and hence:

$$x\, G(x) \sim (1-x)^5$$

The evolution of the structure function with Q^2 leads to an increase in the value of the exponent, which has been calculated to give values of $n \sim 7$–10 at $Q^2 \sim 10\ \mathrm{GeV}^2/c^2$ [33].

Various other models have been used to predict the shape of the structure function, such as for example the 'bag' model [29], in which the gluon is considered as confined in a bag of the dimensions of the nucleon; the various results are shown in Figure 2.12. As can be seen, the models all predict a strong peaking of the structure function at low x.

2.8 Other processes

In this section the other possible mechanisms for the photoproduction of charm, apart from γg-fusion, are discussed. Their contributions are not expected to be substantial.

Radiative corrections

Radiative corrections to the γg-fusion diagram, such as that in Figure 2.13, might be expected to contribute to the cross-section. They have not been calculated, but estimations made [34] using VMD indicate that they add only $\sim 10\,\%$ to the bare diagram's contribution.

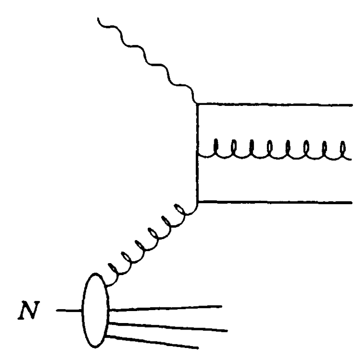

Figure 2.13 *Radiative correction to γg-fusion*

Anomalous component

Other higher order diagrams involving the dissociation of the photon into quarks and gluons contribute to the anomalous component of the photon. The diagram shown in Figure 2.14 (a) involves the subprocess $q\bar{q} \to c\bar{c}$; the photon dissociates into a quark-antiquark pair, and either the antiquark from the photon couples to a nucleon valence quark, or the quark from the photon couples to an antiquark from the nucleon

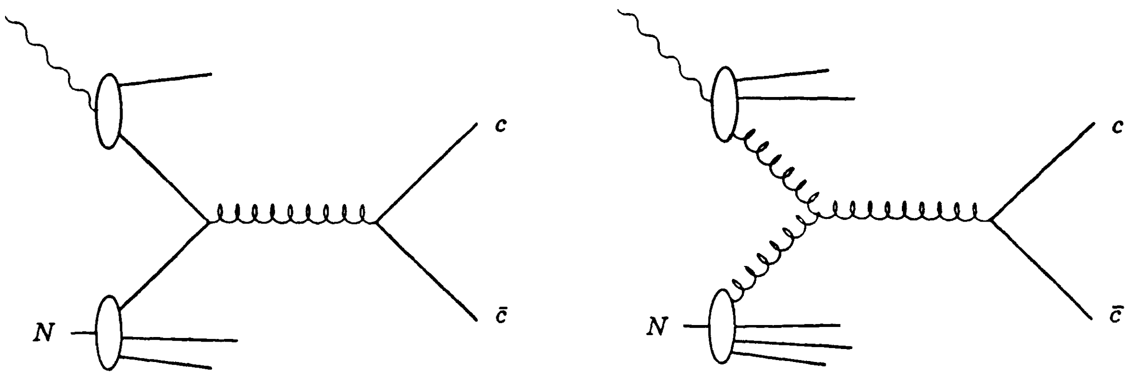

(a) $q\bar{q} \to c\bar{c}$ (b) $gg \to c\bar{c}$

Figure 2.14 *Anomalous component contributions*

'sea'. The quark structure functions of the photon and the nucleon are therefore involved [35].

This process is of order $\alpha\alpha_s^2$, and should therefore be suppressed relative to γg-fusion (of order $\alpha\alpha_s$). However, the x_{min} lower limit to the cross-section integration enhances this process, since the quark structure functions are not peaked at low x, unlike that of the gluon. This process will therefore dominate at large Q^2, but at photon energies in the range that is of interest here, the contribution is small (a few percent).

For the diagram shown in Figure 2.14 (b), the subprocess is $gg \to c\bar{c}$. Similar arguments to those for the previous diagram apply, but now the gluon structure functions are involved, peaked at low x, so the x_{min} limit will lead to further suppression of contributions of this form.

Intrinsic charm

Charm is expected to be present (at a low level) in the sea of the nucleon, and may therefore lead to a contribution to charm photoproduction of the QCD Compton type, as shown in Figure 2.15. This contribution is calculated taking a structure function for charm in the nucleon normalised to about 1 % of the total. It is found [34] to be small, and decreases with Q^2.

Charm cross-section

The calculated contributions of these various effects to the total charm cross-section is

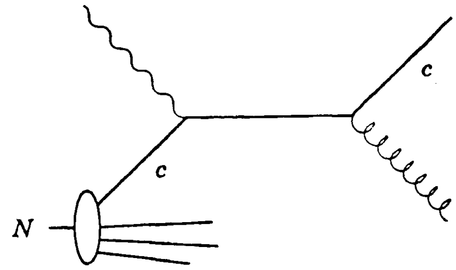

Figure 2.15 *Intrinsic charm*

shown in Figure 2.16, as a function of energy. The predicted total charm cross-sections (from QCD for various charmed quark masses [36], and from VMD [37]) are compared with data from various experiments in Figure 2.17. Note the rise in cross-section towards an asymptotic limit. The agreement with the data is good.

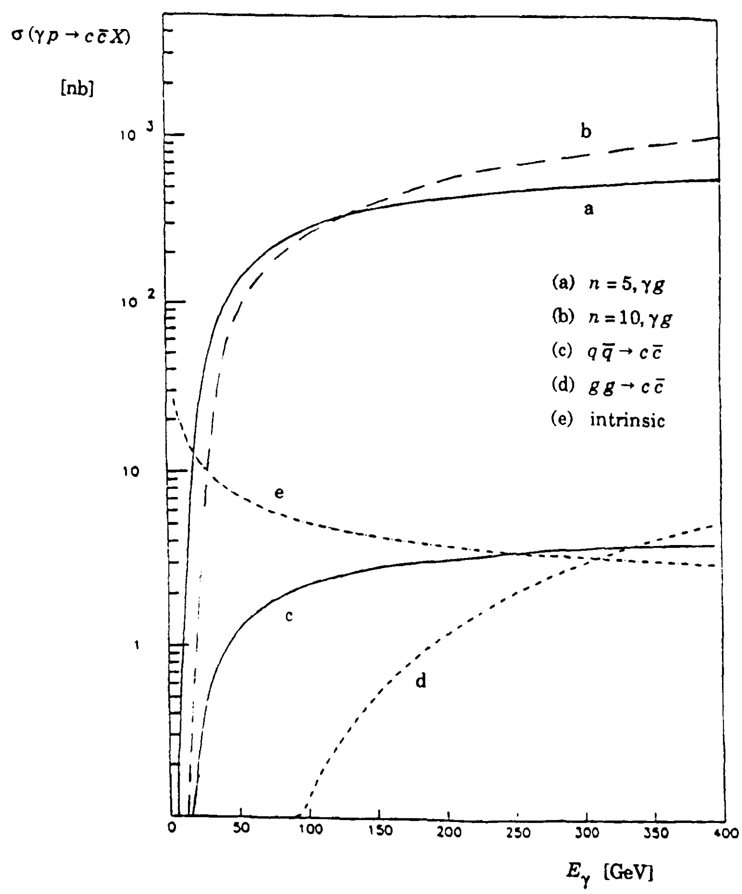

Figure 2.16 *Contributions to the total charm cross-section*

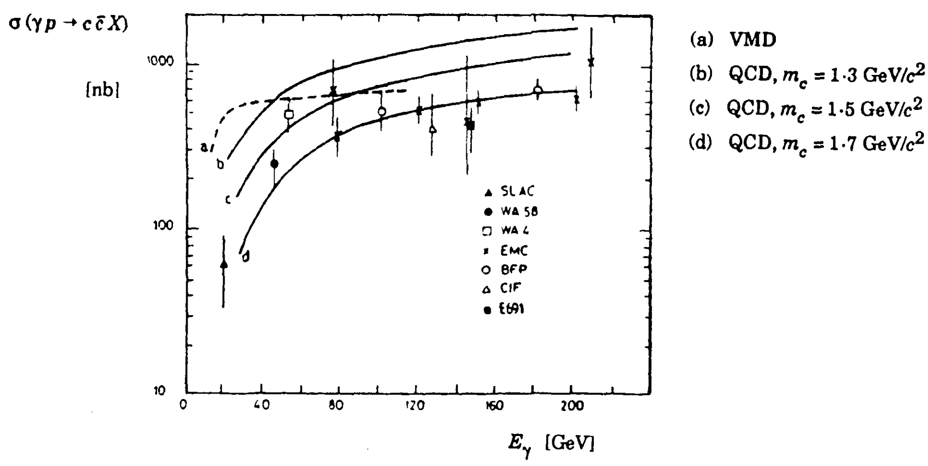

Figure 2.17 *Comparison of charm cross-section predictions with data*

At the energy of NA14 ($<E> \sim 100$ GeV), the photoproduction charm cross-section is about 500 nb/nucleon. This may be compared with the total photoproduction hadronic cross-section of about 100 μb/nucleon. Thus $\sigma_{c\bar{c}}/\sigma_{TOT} \sim 0{\cdot}5 \times 10^{-2}$ for photoproduction. By comparison, for hadroproduction $\sigma_{c\bar{c}}/\sigma_{TOT} \sim (0{\cdot}5\text{–}1) \times 10^{-3}$, making the recognition of charm decays correspondingly more difficult. Furthermore, the lowest order QCD diagrams for hadroproduction are $O(\alpha_s^2)$, (compared with $O(\alpha_s)$ for photoproduction), and involve two structure functions (instead of one). The higher order corrections are also expected to be more significant. Photoproduction therefore has various advantages for the study of charm production mechanisms.

2.9 Hadronisation

The mechanism of charm photoproduction at the parton level appears to be well understood: as described above, the situation is simple, with the dominant contribution coming from γg-fusion. The observed final state, however, consists of hadrons rather than free quarks, so the charmed quarks that are produced must be *hadronised*, i.e. they must in some way combine with other quarks to form hadrons. The simplicity of the QCD description of the charmed quark production makes this a good field for testing models of hadronisation, in the non-perturbative regime. This is achieved by the use of *Monte Carlo* techniques—the computer simulation of the processes involved.

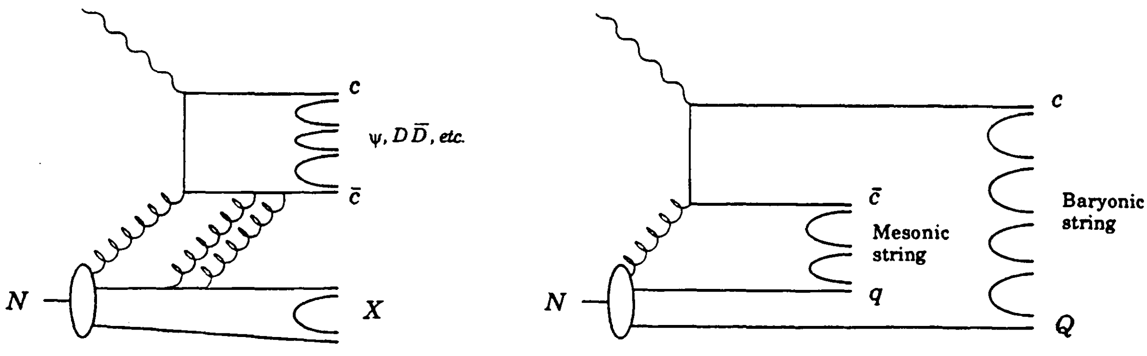

(a) Diffractive (b) Non-diffractive

Figure 2.18 *Hadronisation schemes*

Diffractive scattering

Considering the interaction of the beam photon and the target nucleon, the particles may combine to produce new particles essentially at rest in the centre-of-mass frame. This is *central* production, characterised by the isotropic distribution of interaction products. Alternatively, one of the interacting particles may simply be excited into a more massive state, with the same quantum numbers, which then decays. This is loosely termed *diffractive* scattering, and results in the forward production of particles, with a relatively low multiplicity. For charm photoproduction, the diffractive process may be visualised as shown in Figure 2.18 (a).

The relative importance of diffractive and non-diffractive processes has been calculated using VMD, and it is predicted [34] that the diffractive charm cross-section is only a few percent of the total.

Nuclear effects

Photoproduction events may be further classified according to the behaviour of the nucleus. In an *incoherent* event, the photon interacts with an individual nucleon, and nuclear break-up results. This is seen through the existence of 'black tracks'—highly ionising nuclear fragments—that are isotropically distributed in the nuclear rest-frame, and therefore are typically at large transverse angles to the beam direction in the laboratory, and 'grey tracks'—evaporation protons from the nuclear disintegration.

In *coherent* events, on the other hand, the nucleus interacts as a whole, and simply recoils, without disintegrating. These events are diffractive, and for charm production on a silicon target their contribution is calculated [25] as:

$$\sigma_{c\bar{c}}(coherent) \sim 0.3\ \sigma_{c\bar{c}}(diffractive)$$

The effect of the nucleus on the measured cross-sections is usually parameterised as:

$$\sigma\,(\gamma A \rightarrow c\bar{c} + X) = A^{\alpha}\,\sigma\,(\gamma N \rightarrow c\bar{c} + X)$$

where A is the mass number of the nucleus. If there were no *shadowing* (the obscuring effect of nucleons, on other nucleons in the nucleus) then a value $\alpha = 1$ would be expected for incoherent interactions, and $\alpha = 2$ for coherent interactions (since the effect is on the interaction *amplitude*, which appears squared in the cross-section); if shadowing is present, these values will be reduced. The high mass of the charmed quark makes charm photoproduction a hard process, and furthermore the total hadronic cross-section of the photon is relatively low (compared with that of hadrons), so little shadowing is expected. Experimentally [38] a value $\alpha \sim 0{\cdot}94$ has been measured for incoherent ψ-meson photoproduction, and $\alpha \sim 1{\cdot}4$ for coherent (indicating that in this case shadowing is more significant).

Monte Carlo simulation

The technical details of the Monte Carlo simulation used by the experiment will be given in Chapter 6; here the physics input for the simulation of charm photoproduction is described [39].

The first order QCD calculation is used for the production of charm, via the γg-fusion mechanism. The gluon structure function $xG(x) \sim (1-x)^5$ is assumed, no Q^2 evolution is introduced, and the mass of the charmed quark is taken as $1{\cdot}5$ GeV/c^2.

The hadronisation is non-diffractive, using the 'dual parton' model [40], in which the hadrons are generated along two 'strings'—regions of gluon flux of the type used in the Lund fragmentation scheme [41]—as shown in Figure 2.18 (b). The *mesonic string* stretches between the charmed antiquark and a quark from the target nucleon, whilst the *baryonic string* stretches between the charmed quark and the remaining diquark of the nucleon. The structure functions of the nucleon fragments are taken from low p_T physics [42]; the structure function of the quark is taken as:

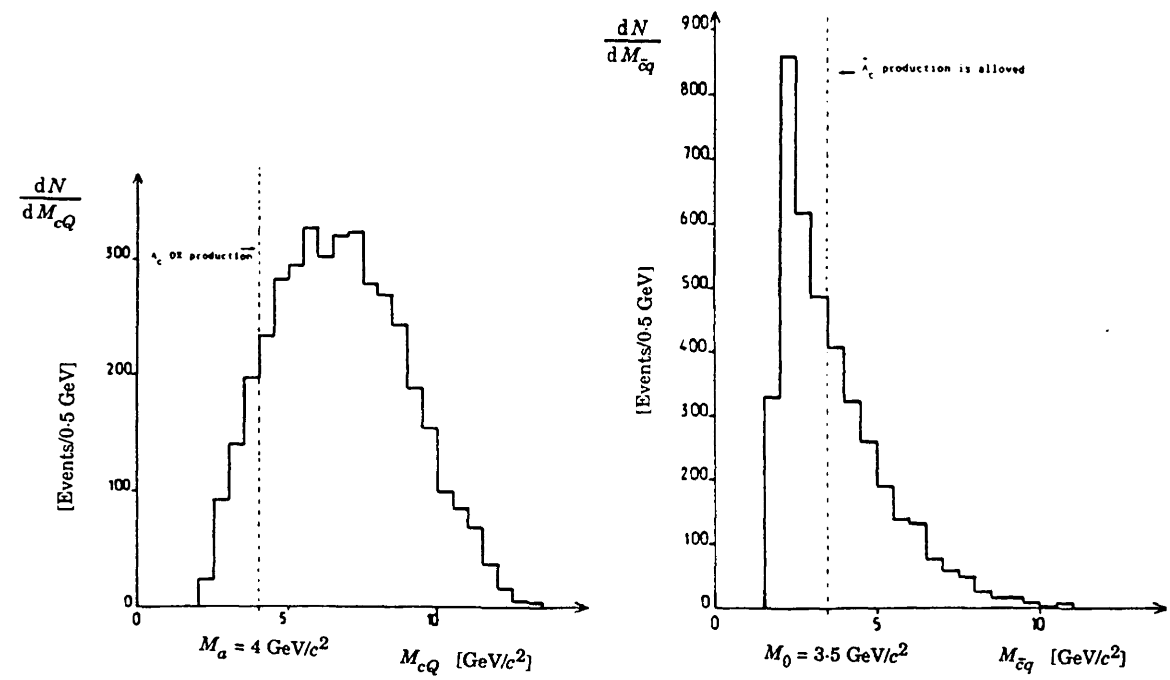

(a) Baryonic (b) Mesonic

***Figure 2.19** Dual parton model string masses*

$$f(x) \sim \frac{1}{\sqrt{x}}(1-x)^{3/2}$$

giving an $x^{-1/2}$ behaviour for the quark and an $x^{3/2}$ behaviour for the diquark at low x. Hence most of the target energy is taken by the diquark, as shown in Figure 2.19, where the masses of the two strings generated by the Monte Carlo are shown. This inequality in the string masses can lead to particle-antiparticle asymmetry for the charmed particles produced. Hadrons are created along the two independent strings using the Lund scheme [41], in which quark-antiquark pairs and diquark-antidiquark pairs are created along the length of the string until the available energy has been exhausted.

Particle-antiparticle asymmetry

In the perturbative QCD calculation of charm photoproduction, the charmed quark and antiquark are produced in an equivalent fashion. The source of any particle-antiparticle asymmetry must therefore be in the hadronisation.

For the Λ_c-baryon, the Λ_c^+ contains a c-quark, and is therefore formed in the baryonic

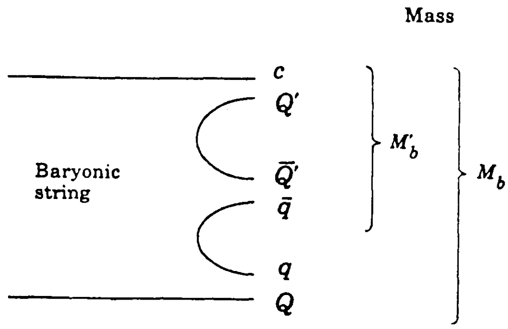

Figure 2.20 *Baryonic string mass*

string, whilst the Λ_c^- contains a $\bar{c}$-quark, and is formed in the mesonic string. The Lund scheme generates diquark-antidiquark pairs with constant probability, but if the string mass is too small then such a pair cannot be produced. The low mass of the mesonic string would therefore be expected to result in a suppression of Λ_c^- relative to Λ_c^+ production. However, not all of the mass of the baryonic string is available for forward Λ_c^+ production, since the initial diquark from the target forms an uncharmed baryon as shown in Figure 2.20, and only the fraction $M_b' < M_b$ of the mass is available. Thus the forward production of charmed baryons and antibaryons is similar.

The remaining source of asymmetry between Λ_c^+ and Λ_c^- production is the formation at low mass of an excited baryonic state by the charmed quark and the diquark of the baryonic string. This may then decay to form a Λ_c^+ with other hadrons, resulting in 'associated production' of the charmed baryon with a charmed meson from the mesonic string:

$$\gamma N \to \Lambda_c \bar{D} X$$

This effect is expected to be strongly energy dependent, and in the simulation a threshold value M_a is chosen, such that if $M_b < M_a$ the cQ system decays into $\Lambda_c X$. Experimentally it is found [43] that there is about 70 % associated production at 20 GeV, and a value of M_a = 4 GeV is chosen to reproduce this result. For the mesonic string, there is a threshold for production of Λ_c^- at $M(\Lambda_c) + M(N)$ = 3·2 GeV, due to the requirement of baryon number conservation. This inhibits the production of Λ_c^- at low energy, but is insignificant for higher energies; below the threshold only charmed mesons are produced.

The D-$\bar{D}$ asymmetry reflects the Λ_c -$\bar{\Lambda}_c$ asymmetry, with the additional feature that for associated $\Lambda_c\bar{D}$ production the $\bar{D}$-mesons are produced forward, and therefore are usually detected with high efficiency in the apparatus. This is only a small effect at high energies, since Λ_c production is only about 10 % of D production.

The D_s is generally produced along with a $\bar{D}$, rather than as $D_s\bar{D}_s$. At low energy an excess of D_s^- might be expected due to associated production with the Λ_c^+, but the D_s^- production (in the mesonic string) is suppressed by phase space considerations: a K must also be produced for strangeness conservation, and the mass of the mesonic string is already low. This latter effect dominates the former, and more D_s^+ are expected than D_s^-.

Production ratios

The ratio of D^+ to D^0 production depends on the rate of production of D^*-mesons, since the D^{*0} cannot decay to the D^+ (due to kinematics). The D^{*+}, on the other hand, decays to D^+ or D^0 with approximately equal probability. Experimentally [44] a value for the ratio of D^+ to

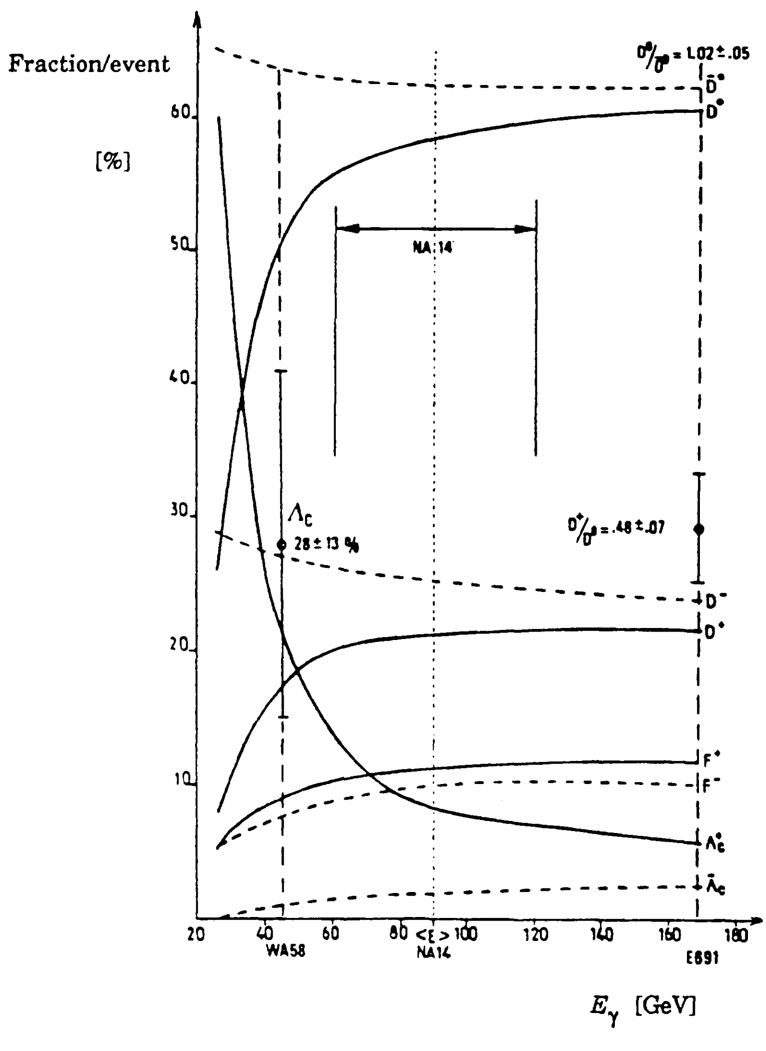

Figure 2.21 *Production rate predictions*

D^0 production of 0·48 ± 0·07 is found, indicating that 3 times more D^* are produced than D, which agrees with the value from the simulation.

The production of the D_s requires the contribution of a strange quark from the sea, and is therefore expected to occur with a lower probability than the production of the D^+. The production ratio may be estimated by comparison with experimental results for uncharmed production: the ratio of K- to π-meson production in continuum e^+e^- annihilations indicates that the ratio $s\bar{s}$/total ~ 15 % [16]. Assuming that this fraction is also correct for charmed production, and allowing for the ratio of D^+ to D^0 discussed above, this leads to a prediction of the ratio of D_s to D^+ production of ~ 0·5.

The results of the Monte Carlo simulation are presented in Figure 2.21, where the expected production rates for the various charmed particles are given as a function of their energy. These will be of interest for discussion of experimental results presented in this thesis. Other Monte Carlo predictions, for the energy and $p_T{}^2$ distributions, will be described along with the results in Chapter 9.

III Charm Decay

2.10 Introduction

The weak decay of charmed particles [45] may proceed via three categories of decay:

(i) *Purely leptonic.* For a pseudoscalar meson D, the decay is of the form $D \to l\bar{\nu}_l$. This may only occur through the annihilation of the quarks of the meson, as shown in Figure 2.22, and therefore provides a measure of the coupling of the hadronic

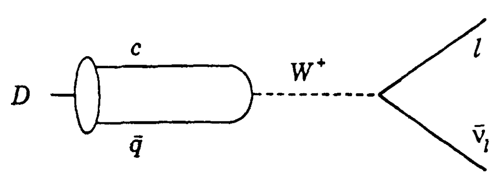

Figure 2.22 *Leptonic decay*

current to the vacuum, i.e. the matrix element:

$$< 0|J_\mu|D> = -i f_D q_\mu$$

where q is the 4-momentum of the meson, and f_D is the overlap of the quarks in the D wavefunction, introduced by analogy to pion decay [46]. Theoretical predictions give $f_D \sim 100$–250 MeV [47]. The decay rate is calculated using [46]:

$$\mathrm{d}\Gamma = \frac{1}{2E} \overline{|\mathcal{M}|^2}\, \mathrm{d}Q \tag{2.9}$$

where $\mathrm{d}Q$ is the invariant phase space, and E is the energy of the meson. This gives:

$$\Gamma(D(c\bar{q}) \to l\bar{\nu}_l) = \frac{G_F^2}{8\pi} |V_{cq}|^2 f_D^2 m_D\, m_l^2\, \mathcal{F} \tag{2.10}$$

where $\mathcal{F}$ is a phase space factor, given here by:

$$\mathcal{F} = \left(1 - \frac{m_l^2}{m_D^2}\right)^2$$

These decays are strongly *helicity suppressed*: due to the (V – A) structure of the weak charged current, and the conservation of angular momentum, a spin zero state cannot decay to a massless fermion-antifermion pair via the weak charged current; when the fermion masses are small compared to their energy the process is still strongly suppressed. For example [48]:

$$B(D^+ \to \mu^+\nu_\mu) < 8{\cdot}4 \times 10^{-4} \quad (90\ \%\ \mathrm{CL})$$

(ii) *Semileptonic*, i.e. $D \to Xl\bar{\nu}_l$. This occurs primarily through the β-decay of the charmed quark. See Figure 2.23. Decays of this form are known as *spectator* decays, as the light quark in the charmed meson is assumed not to play any part in the decay.

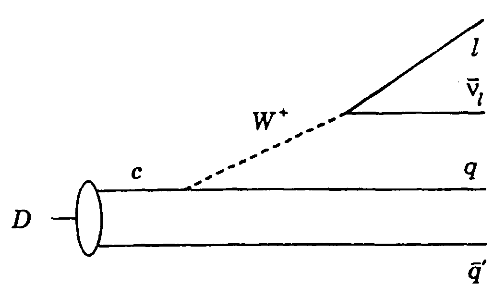

Figure 2.23 *Semileptonic decay*

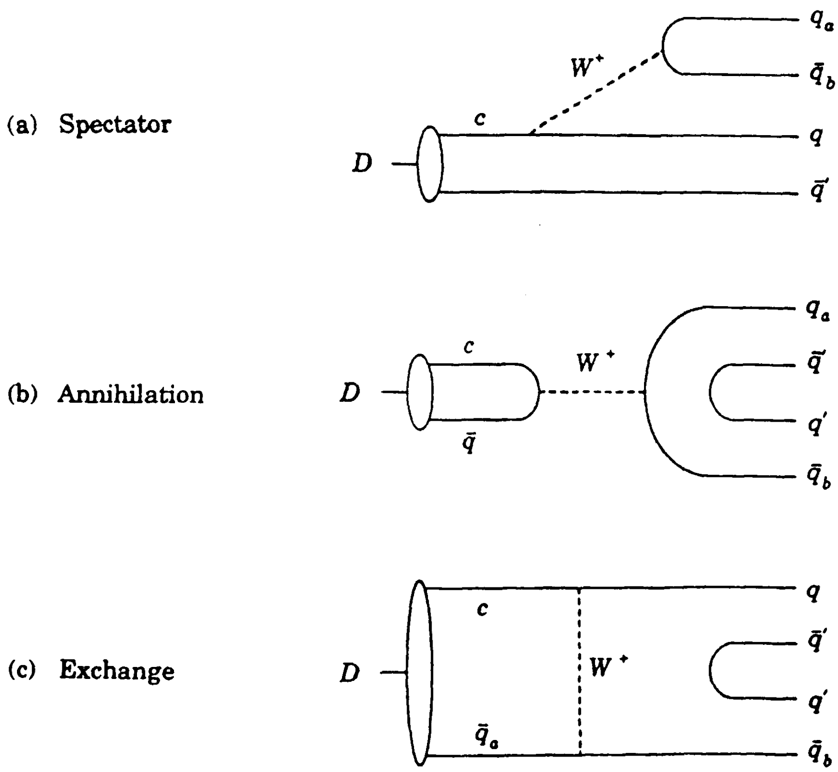

Figure 2.24 *Hadronic decay*

(iii) *Hadronic.* The weak decay of charmed mesons to exclusively hadronic final states may also occur via a spectator decay, as shown in Figure 2.24 (a). In this case, however, there are other diagrams which may contribute, involving annihilation and exchange; see Figure 2.24 (b) and (c). These last two processes, however, are helicity suppressed, and as a first approximation may be neglected.

2.11 The spectator model

Naive model

The spectator model [49] is motivated by the large mass of the charmed quark, which permits it to be treated as though it were essentially free, with the light spectator quark not contributing to the dynamics of the decay. The valence quark approximation is assumed, and the hadronisation of the quarks in the final state is not considered.

There is then a direct parallel between the charmed spectator decays seen above and muon decay (Figure 2.25). The invariant amplitude for muon decay is given by (from

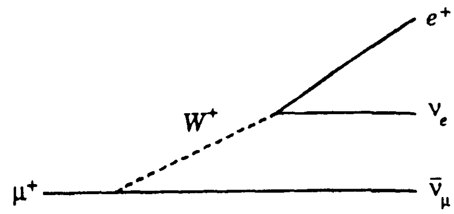

Figure 2.25 *Muon decay*

Equation 2.2):

$$\mathcal{M} = \left(\bar{e}\,\gamma^\nu \frac{1}{2}(1-\gamma_5)\,\nu_e\right)\frac{4G_F}{\sqrt{2}}\left(\bar{\nu}_\mu\,\gamma_\nu \frac{1}{2}(1-\gamma_5)\,\mu\right)$$

Equation 2.9 gives:

$$\Gamma_\mu = \frac{G_F^2\, m_\mu^5}{192\,\pi^3} \sim 4{\cdot}5\times 10^5\ \mathrm{s}^{-1}$$

In the naive spectator model, the decay rate for a process such as that illustrated in Figure 2.24 (a) is simply given by:

$$\Gamma_0 = \left(\frac{m_c}{m_\mu}\right)^5 \frac{1}{\mathcal{F}}\ |V_{cq}|^2\ |V_{ab}|^2\ \Gamma_\mu$$

where $\mathcal{F}$ is a 3-body phase space factor, with value $\sim 0{\cdot}5$. If the Cabibbo suppressed modes and non-charm masses are neglected, and we take $m_c = 1{\cdot}5$ GeV/c^2, then:

$$\Gamma_0 \sim 5\times 10^{11}\ \mathrm{s}^{-1}$$

The total rate is given by:

$$\Gamma_{TOT} = 5\,\Gamma_0$$

since there are 5 available final states, involving e, μ, and 3 colours for the quarks. Thus the predicted lifetime is:

$$\tau = \frac{1}{\Gamma_{TOT}} \sim 4\times 10^{-13}\ \mathrm{s}$$

The spectator model also predicts that the lifetimes of all weakly decaying charmed particles will be equal, and that the semileptonic branching ratio $B(D \rightarrow eX) \sim 20$ %, since semileptonic and hadronic decays are treated equivalently.

Experimentally, these predictions are quite good. The lifetimes of the D^0, D^+ and D_s mesons agree to within an order of magnitude, and are in the range 10^{-13}–10^{-12} s [50].

Furthermore [51]:

$$B(D^+ \to e^+X) \sim 17\ \%$$

close to the prediction. The agreement is not, however, perfect: the lifetimes of the charmed mesons are not exactly the same, but instead $\tau(D^+) > \tau(D^0) \approx \tau(D_s)$. Either the D^0 (and D_s) decay is enhanced compared with the spectator model prediction, or the D^+ decay is suppressed; unfortunately the lifetime prediction depends on the fifth power of the charmed quark mass, which is not accurately known, and therefore these possibilities cannot be distinguished from lifetime measurements alone.

QCD corrections

The spectator model is clearly too simple: the charmed quark is initially part of a hadron, and the final state is seen as hadrons, not free quarks. QCD corrections are necessary, to incorporate the effects of the strong interaction.

The Hamiltonian H for a process is related to the invariant amplitude $\mathcal{M}$ (such as that in Equation 2.2) by:

$$\mathcal{M}_{if} = \langle f \mid H \mid i \rangle$$

for a transition $i \to f$. Thus the bare spectator Hamiltonian for weak hadronic decays of charm is given by:

$$H_W^0\ (\Delta c = -1) = \frac{4G_F}{\sqrt{2}} \left[V_{cs}\,(\bar{s}c)_L + V_{cd}\,(\bar{d}c)_L \right] \left[V_{ud}\,(\bar{d}u)_L + V_{us}\,(\bar{s}u)_L + \bar{e}\nu_e + \bar{\mu}\nu_\mu \right]$$

The lowest order corrections may be separated into those involving self-energy or vertex corrections (illustrated in Figure 2.26 (a) and (b)) which may be absorbed into the renormalisation of G_F, and those involving hard gluon exchange (such as that shown in Figure 2.26 (c)), which affect only hadronic decays. The second class of contributions are logarithmically divergent, and imposing a cut-off at M_W yields [52] a first order correction to $H_W{}^0$ (for the Cabbibo allowed decays):

$$H_W^1 = -\frac{4G_F V_{cs} V_{ud}}{\sqrt{2}} \frac{3\alpha_s}{8\pi} \ln \left(\frac{M_W^2}{\mu^2} \right) (\bar{s}\lambda_a\, c)_L\, (\bar{d}\lambda^a\, u)_L$$

where μ is the scale of renormalisation, of the order of the charmed quark mass. The correction thus introduces a new operator with the same chiral and flavour structure, but involving the colour octet currents, λ_a. To see the physical effects we make a Fierz transformation [53]:

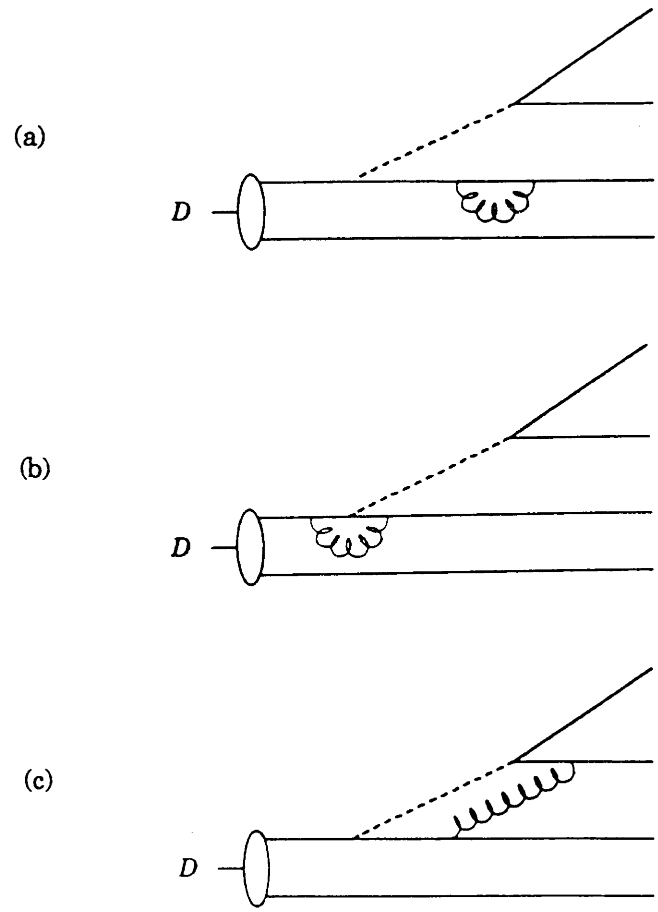

Figure 2.26 *QCD corrections*

$$(\bar{s}\lambda_a c)_L (\bar{d}\lambda_a u)_L = \frac{2}{3}(\bar{s}c)_L (\bar{d}u)_L + 2(\bar{s}d)_L (\bar{u}c)_L$$

Then the hadronic part of the Hamiltonian becomes:

$$H_W = H_W{}^0 + H_W{}^1 + \ldots$$
$$\approx \frac{4G_F}{\sqrt{2}} V_{cs} V_{ud} \left[\left(1 + \frac{\alpha_s}{4\pi} \ln \frac{M_W^2}{\mu^2} \right) (\bar{s}\,c)_L (\bar{d}\,u)_L - \frac{3\alpha_s}{4\pi} \ln \frac{M_W^2}{\mu^2} (\bar{s}\,d)_L (\bar{u}\,c)_L \right]$$

Defining the symmetric and antisymmetric linear combinations:

$$O_{\mp}\ (\Delta c = -1) = \frac{1}{2}\left[(\bar{s}\,c)_L (\bar{u}\,d)_L \pm (\bar{s}\,d)_L (\bar{u}\,c)_L \right]$$

we may write:

$$H_W = \frac{4G_F}{\sqrt{2}} V_{cs} V_{ud} \left[c_+ O_+ + c_- O_- \right]$$

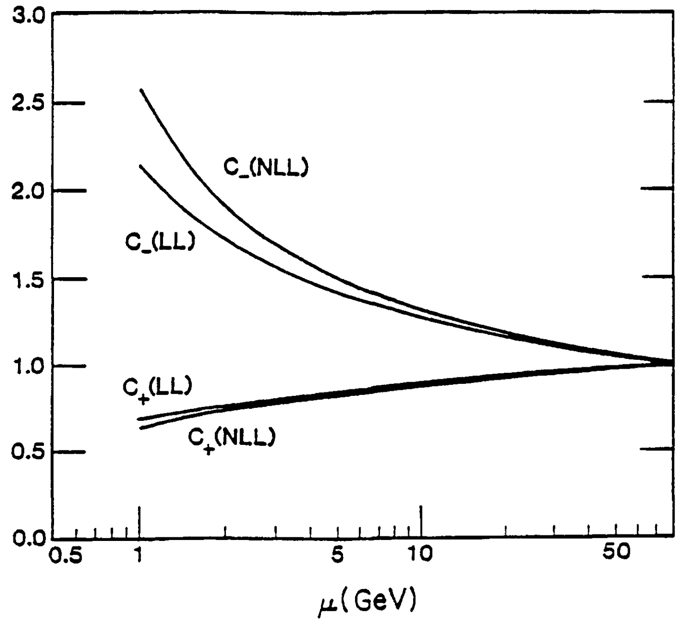

Figure 2.27 *QCD correction coefficients*

where the coefficients:

$$c_{\mp} = 1 \pm \frac{\alpha_s}{2\pi} \ln \frac{M_W^2}{\mu^2}$$

The bare spectator model is recovered in the limit $c_+ = c_- = 1$. These coefficients may be calculated to all orders in α_s (in the leading log approximation, *LL*) using renormalisation group methods [52]. Two loop corrections (next-to-leading log, *NLL*) have also been calculated [54], and are small, giving confidence in the procedure. The calculated values of the coefficients are shown in Figure 2.27, as a function of the scale μ. The effect of the QCD corrections may be seen by putting:

$$c_1 = \frac{c_+ + c_-}{2} \quad , \quad c_2 = \frac{c_+ - c_-}{2}$$

Then:

$$H_W = \frac{4G_F}{\sqrt{2}} V_{cs} V_{ud} \left[c_1 (\bar{s}c)_L (\bar{u}d)_L + c_2 (\bar{s}d)_L (\bar{c}u)_L \right]$$

and without corrections, $c_1 = 1$, $c_2 = 0$. Thus the QCD corrections are responsible for:

(i) shortening the charm lifetimes, as the non-leptonic decay width is enhanced [54]:

$$\Gamma_{NL} = (2\,c_+^{\,2} + c_-^{\,2})\,\Gamma_0$$

(ii) inducing an effective neutral current interaction, also known as the 'colour-suppressed' interaction, with coefficient c_2;

(iii) reducing semileptonic branching ratios. For example:

$$\Gamma\,(c \rightarrow s\,u\,\bar{d}) = (2\,c_+^{\,2} + c_-^{\,2})\,\Gamma\,(c \rightarrow s\,l\,\bar{\nu}_l)$$

therefore:

$$B\,(c \rightarrow e\,X) = \frac{1}{2 + 2\,c_+^{\,2} + c_-^{\,2}} \sim 15\,\%$$

These predictions are all in agreement with experiment, and represent a success for QCD. However, apart from small phase-space corrections, the lifetimes of all charmed mesons are still predicted as identical. This indicates that other, non-spectator, processes must be involved.

2.12 Non-spectator processes

The semileptonic branching ratio of the D^0 has been measured [51]:

$$B(D^0 \rightarrow e^+X) = 7{\cdot}5\,\%$$

in poor agreement with the spectator model prediction. With Equation 2.11, this gives:

$$\frac{B\,(D^+ \rightarrow e^+\,X)}{B\,(D^0 \rightarrow e^+\,X)} = 2{\cdot}3$$

But:

$$\frac{B\,(D^+ \rightarrow e^+\,X)}{B\,(D^0 \rightarrow e^+\,X)} = \frac{\Gamma\,(D^+ \rightarrow e^+\,X)}{\Gamma\,(D^+ \rightarrow all)}\,\frac{\Gamma\,(D^0 \rightarrow all)}{\Gamma\,(D^0 \rightarrow e^+\,X)} = \frac{\Gamma\,(D^+ \rightarrow e^+\,X)}{\Gamma\,(D^0 \rightarrow e^+\,X)}\,\frac{\tau\,(D^+)}{\tau\,(D^0)}$$

and from experiment [50]:

$$\frac{\tau\,(D^+)}{\tau\,(D^0)} = 2{\cdot}27$$

Thus the partial widths for semileptonic decay are the same for the D^0 and the D^+, and therefore the source of their differing lifetimes must lie in the non-leptonic decays.

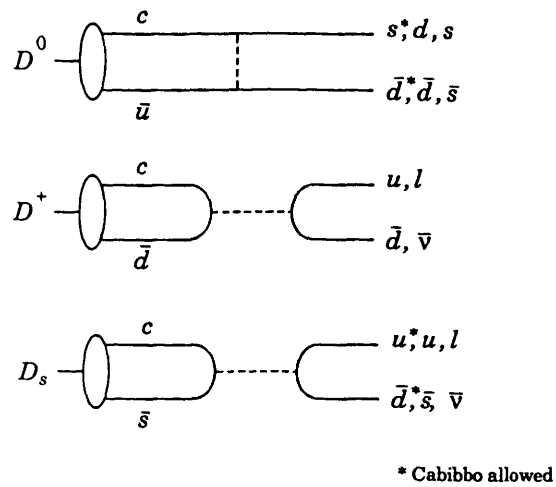

Figure 2.28 *Annihilation and exchange*

Annihilation and exchange

These processes were illustrated in Figure 2.24 (b) and (c). The possible final states for the D^0, D^+ and D_s are shown in Figure 2.28. This looks promising, as the D^+ hadronic decay is Cabibbo suppressed, unlike those of the D^0 and D_s. The decay rates depend on the overlap of the quark wavefunctions, and may be calculated in a manner analogous to the purely leptonic decays (see Equation 2.10), giving:

$$\Gamma_A = C\, G_F^{\,2} f_D^{\,2}\, m_D (m_a^{\,2} + m_b^{\,2})\, \mathcal{F}\, |V_{cq}|^2\, |V_{ab}|^2$$

where $\mathcal{F}$ is a phase-space factor, and C is a colour factor. The presence of a factor depending on the final quark masses is a result of the helicity suppression mentioned earlier. When the rates are calculated in this manner [55], they are found to be very small, e.g: $\Gamma_A(D^0) \sim 5 \times 10^{-3}\, \Gamma_0$.

The helicity suppression may be removed by the radiation of gluons from the initial state [56], as illustrated in Figure 2.29 (two gluons are required to ensure that the charged

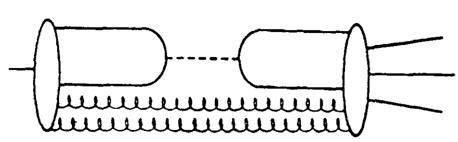

Figure 2.29 *Removal of helicity suppression*

current remains colourless). This allows the initial quark state to have spin 1, thus removing the suppression. A similar process is observed in strange-quark decays:

$$\frac{\Gamma(K \to e\,\nu)}{\Gamma(K \to \mu\,\nu)} = 2{\cdot}4 \times 10^{-5} \sim \frac{m_e^2}{m_\mu^2}$$

due to helicity suppression, but:

$$\frac{\Gamma(K \to e\,\nu\,\gamma)}{\Gamma(K \to \mu\,\nu\,\gamma)} = 2{\cdot}6 \times 10^{-3}$$

indicating that the emission of the photon reduces the suppression. The calculations for the charm decays are difficult, as the distribution of quarks in the mesons is not known, but indications are [57] that a lifetime ratio $\tau(D^+)/\tau(D^0) \sim 2$–$3$ can be achieved. However, a lifetime for the D_s that is longer than that of the D^0 is also indicated, disfavoured by experiment.

Final state interaction

The decay $D^0 \to \overline{K}^0\phi$ was originally proposed [58] as the 'smoking gun' test of the existence of non-spectator processes (see Figure 2.30 (a)), as the spectator contributions to this decay were expected to be strongly suppressed. It was in due course discovered [59], with a surprisingly large branching ratio of ~ 1 %. If the exchange process was responsible it would require an unexpectedly large wavefunction overlap.

An alternative explanation was advanced [60]—that of final state interaction, as illustrated in Figure 2.30 (b). Such re-scattering effects are required by unitarity, but whether they play a significant part in the weak decays of charmed mesons is an undecided question.

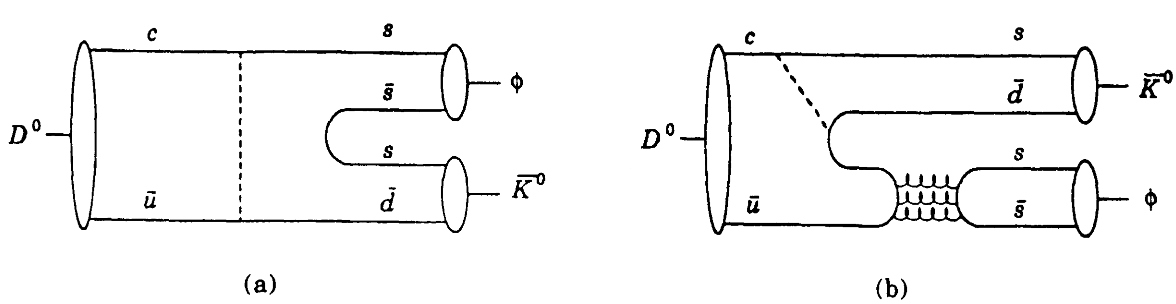

Figure 2.30 *Final state interaction*

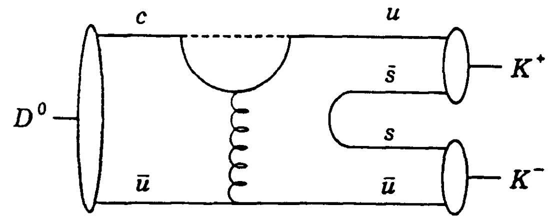

Figure 2.31 *Penguin diagram*

Penguin diagrams

A further lowest order QCD correction to the weak Hamiltonian is provided by the so-called 'penguin' diagrams, illustrated in Figure 2.31. Diagrams of this form are thought to play an important rôle in the $\Delta I = 1/2$ rule of K decays [61]. Their effect on charm decays is, however, strongly suppressed by the KM-matrix elements, and can only be significant for certain modes that are already Cabibbo suppressed.

Pauli interference

The amplitudes at the quark level from the spectator model Hamiltonian are shown in Figure 2.32. The four quark operators (from Equation 2.12) generate two distinct amplitudes for each charmed meson: one 'colour-allowed' with coefficient c_1, and the other 'colour-suppressed' with coefficient c_2. The latter results from the effective neutral current generated by the Fierz transformation, and is expected to be suppressed since the colour of the final state is completely determined by the initial state; a factor of 3 would be naively expected between the colour-allowed and suppressed amplitudes, as in the allowed case there are 3 colours available to the quarks forming the π.

We would therefore expect:

$$\frac{B\,(D^0 \to \bar{K}^0 \pi^0)}{B\,(D^0 \to K^- \pi^+)} = \frac{1}{2} \times \frac{1}{9} \approx 0{\cdot}055$$

where the extra factor of a half comes from isospin considerations, since:

$$\pi^0 = \frac{1}{\sqrt{2}}(u\,\bar{u} + d\,\bar{d})$$

But experimentally [62] the ratio is measured as ~ 0·45, compatible with *no* colour suppression. Theoretical motivation for the neglect of colour suppression comes from the '$1/N$-expansion' of decay matrix elements (where N is the number of colours). In this

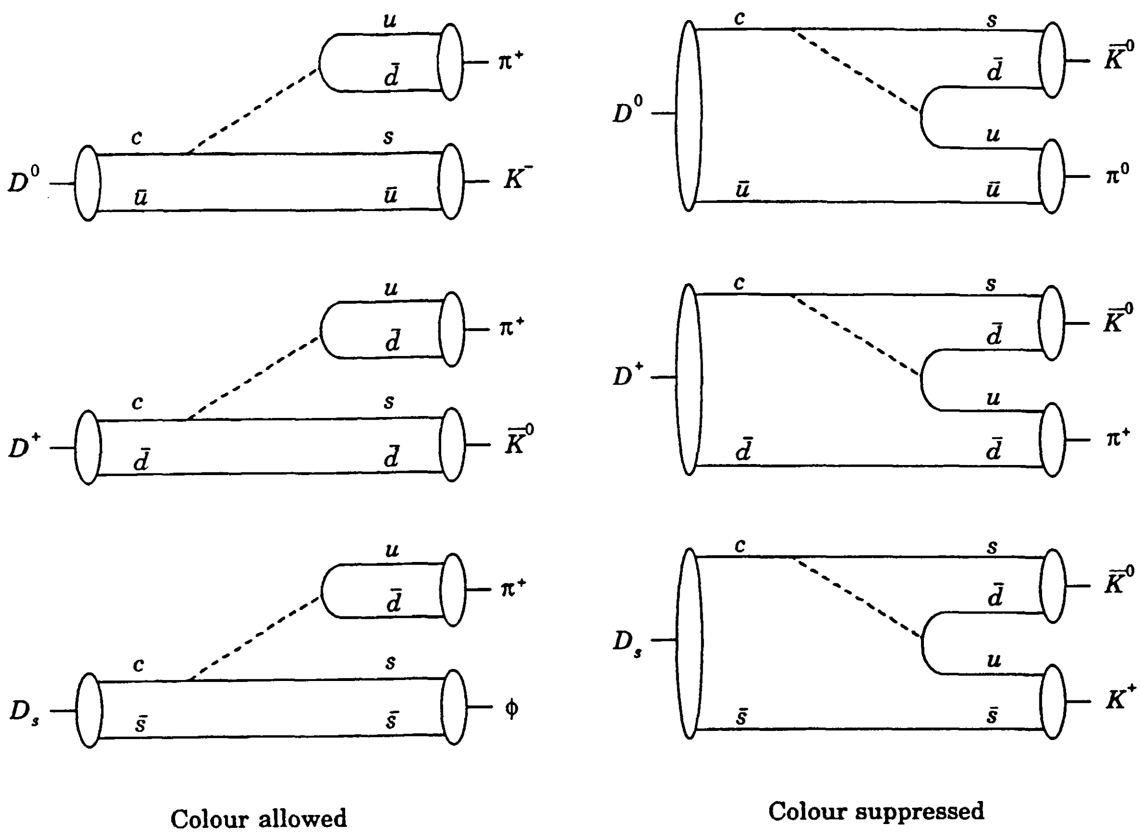

Figure 2.32 *Spectator decay amplitudes*

scheme [63], the limit as $N \to \infty$ is taken, providing simplifications which are then assumed to hold for the physical world (where $N = 3$). When the leading terms in the expansion are taken, the colour suppression is lost.

By inspection of Figure 2.32, the colour-allowed and suppressed amplitudes produce the same final state for the D^+ (but not for the D^0 or the D_s), including two identical fermions. Pauli interference is therefore expected between the two D^+ amplitudes, depending on the overlap of the wavefunctions. It has been shown [64] that maximal destructive interference occurs for reasonable values of the overlap, providing a theoretically favoured explanation for the suppression of the D^+ decay. A lifetime ratio of $\tau(D^+)/\tau(D^0) \sim 1{\cdot}5$ has been calculated, with an increased value if colour suppression is neglected.

IV Conclusions

As indicated in the previous sections, the fields of photoproduction, and the weak decay of charmed mesons, are a fertile area for theoretical endeavour. The large mass of the charmed quark results in relatively straightforward QCD calculations, and these phenomena therefore provide a suitable place for accurate tests of the theory. Furthermore, in areas where the QCD calculations are not simple, there exist a wide range of models to account for the data, and the lack of substantial experimental statistics makes the choice between theories difficult.

It is therefore important that further experimental data should be provided. The remaining part of this thesis will describe an experiment that was intended to fulfil this need.

Chapter 3

APPARATUS

This chapter begins with a description of the beam used by NA14. A discussion of the requirements of particle detection follows, and finally details are given of the principles and configuration of the detectors that make up the apparatus.

I The Beam

3.1 Coordinate system

The coordinate system chosen to describe the apparatus is Cartesian, with the x-axis lying along the beam direction, and the y-axis horizontal (see Figure 3.1). The origin is taken as the centre of one of the spectrometer magnets (the AEG) and corresponds approximately to the target position.

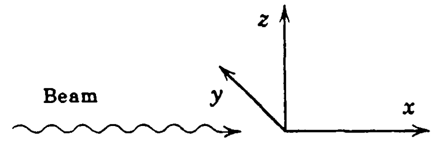

Figure 3.1 *The coordinate system*

For the data analysis, it is often convenient to describe the apparatus in terms of *projections*, i.e. the two-dimensional representations produced when the apparatus is viewed from particular directions. Most important of these are the (x,y) and (x,z) projections (i.e. those produced by viewing along the z- and y-axes). For the sake of brevity these will be denoted the Y-projection and the Z-projection respectively.

3.2 Beam production

The high energy photon beam is produced by an indirect process from protons accelerated to an energy of 450 GeV in the SPS at CERN. The acceleration takes about 12 s, and is followed by the extraction of the protons from the SPS ring by a kicker magnet that deflects them into an evacuated beam pipe towards the experiment. This *spill* takes approximately 2 s, and is followed by another cycle of acceleration, thus giving a burst structure to the beam seen by the experiment.

The beam is known as the 'Broadband Electron and Gamma' beam and uses the E12 beam line. It is produced using a three step process:

$$p \to \gamma \to e \to \gamma$$

This indirect scheme has the advantages that:

(i) The beam may be *tagged,* i.e. the energy of individual photons may be measured.

(ii) It produces a very pure photon beam, with low hadron contamination.

The production of the beam [65] is illustrated in Figure 3.2. The protons from the SPS are dumped into a production target (T10) consisting of a block of beryllium 100 mm in length. In a burst there are typically 2×10^{12} protons, of which about 20 % interact in the target. Amongst the interaction products are neutral pions, which decay electromagnetically:

$$\pi^0 \to \gamma\gamma$$

to give photons that are used in the next stage. The target material and length represent a compromise between the requirements that the protons should be used efficiently, implying a high probability of nuclear interaction, i.e. a short nuclear interaction length; and that the loss through electromagnetic interactions:

$$\gamma \to e^+e^-$$

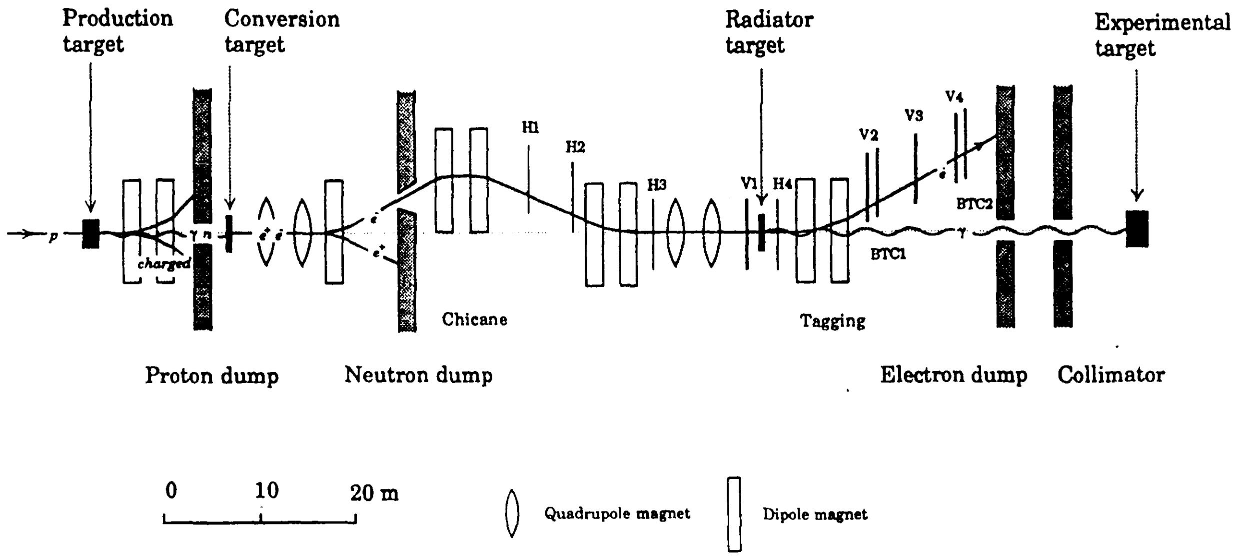

Figure 3.2 The beam line

of the produced photons should be minimised, implying a long radiation length. The ratio of radiation length to nuclear interaction length is largest for elements of low atomic number, such as beryllium (see Table 3.1). A further consideration in the choice of length of the production target is that the creation of muons forming the muon halo, a source of background to the experiment, is greater for longer lengths.

The products of the proton interactions pass through a pair of sweeping magnets that deflect all charged particles including those protons which have not interacted into a 4 m thick iron wall, the *proton dump*. The photons, and any other neutral particles (such as K^0s and neutrons) pass through an aperture and strike a conversion target consisting of a lead sheet 4 mm thick. About 40 % of the photons convert to give e^+e^- pairs. Here the requirements are an efficient conversion of the photons, but a minimisation of the

Material	Z	Density [g cm^{-3}]	Radiation length [g cm^{-2}]	Nuclear interaction length [g cm^{-2}]
Beryllium	4	1·85	65·2	75·2
Silicon	14	2·33	21·8	106
Lead	82	11·4	6·4	194

Table 3.1 Properties of materials

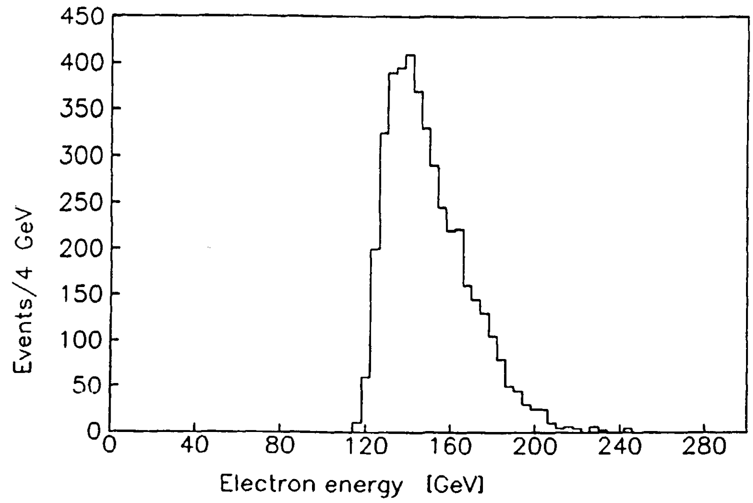

Figure 3.3 Electron energy

contamination from charged particles produced by the interaction of the neutral hadrons. A low ratio of radiation length to nuclear interaction length is needed, hence the choice of lead.

The electrons are selected using a series of five bending magnets in the form of a *chicane,* the neutral and positive particles being dumped into another iron wall, the *neutron dump.* The aperture through which the electrons pass has adjustable jaws, permitting variation of the momentum range selected; for a typical selection of 120–250 GeV/c there are about 10^8 electrons per burst, with a mean energy of 140 GeV (see Figure 3.3). Electrons rather than positrons are selected to reduce the muon contamination, since about twice as many μ^+ as μ^- are produced in the initial proton interactions.

The electron beam is focused with a pair of quadrupole doublets, and is incident on a radiator target, a 500 μm thick lead sheet. Here the electrons undergo *bremsstrahlung,* the emission of a photon as a result of deceleration in the electric field of a nucleus of the medium, in this case lead. About 10 % of the electrons radiate a single high energy photon, and it is these photons which provide the experimental beam. Increasing the radiator thickness would increase the photon yield, but also increase the probability of multiple bremsstrahlung which prevents the correct measurement of photon energy by the tagging system. The tagging magnets sweep all charged particles out of the beam, to be dumped in the *electron dump,* an iron wall. The photons are not deflected, and pass through an aperture in both the electron dump and a collimator, to reach the experimental target.

3.3 Tagging

The photon energy may be determined from the difference in the electron energy before and after it radiates, provided that only single bremsstrahlung has occurred. The electron energy is found from a measurement of its momentum through deflection in a magnetic field. Before radiating, this field is provided by the chicane magnets, and after by the tagging magnets. The position of the electron is determined using eight scintillator finger hodoscopes (discussed in Section 3.8) named H1–4 and V1–4 according to the horizontal or vertical orientation of the coordinate that they measure. Due to the high electron flux, the hodoscopes require fast time resolution and high segmentation to enable the trajectory of the radiating electron to be unambiguously measured. Also in the same region are the *Back Tagging Counters* (BTCs) which provide a time reference for the beam trigger.

An unambiguous solution to the tagging algorithm is found in about 30 % of events [66], whilst a further 15 % have ambiguous solutions due to multiple hits in the hodoscopes; for the remaining events the electron trajectory is not reconstructed. These efficiencies are low due to hardware problems experienced with the tagging system during data taking. The finger size of the hodoscopes limits their angular precision and gives rise to an uncertainty in the beam energy of about 3 GeV. The beam energy spectrum measured by the tagging is not, however, exactly the spectrum of energies seen by the apparatus due to the following effects:

(i) *Double bremsstrahlung*: The tagging assumes that all the energy lost by the radiating electron is taken by a single photon, so additional radiated photons will cause the tagging to over-estimate the energy;

(ii) *Random coincidence*: The photon causing the trigger may be in random coincidence with a different photon that is measured by the tagging.

These effects have been calculated using a Monte Carlo simulation [67], with the conclusion that (as a result of multiple bremsstrahlung or random coincidences) for 17 % of triggers the trigger photon is accompanied by a second photon of energy greater than 20 GeV. The tagging was tested using ψ-meson events, found in data taken with a muon trigger, looking for the decay:

$$\psi \rightarrow \mu^+\mu^-$$

Requiring that there are no other particles detected in the event other than the muon pair

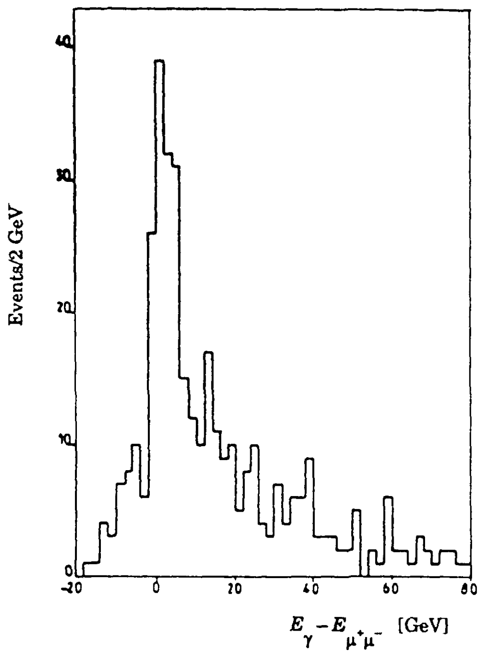

Figure 3.4 *Energy difference between beam photon and ψ-meson*

selects quasi-elastic production of ψ-mesons, for which the ψ energy should be equal to that of the photon. The difference between the tagging energy and the reconstructed ψ energy is plotted in Figure 3.4 [68]. As can be seen, the data display a peak at zero difference, of width determined by the finite resolution of the tagging, and a tail from the over-estimation of the energy due to double bremsstrahlung and random coincidences.

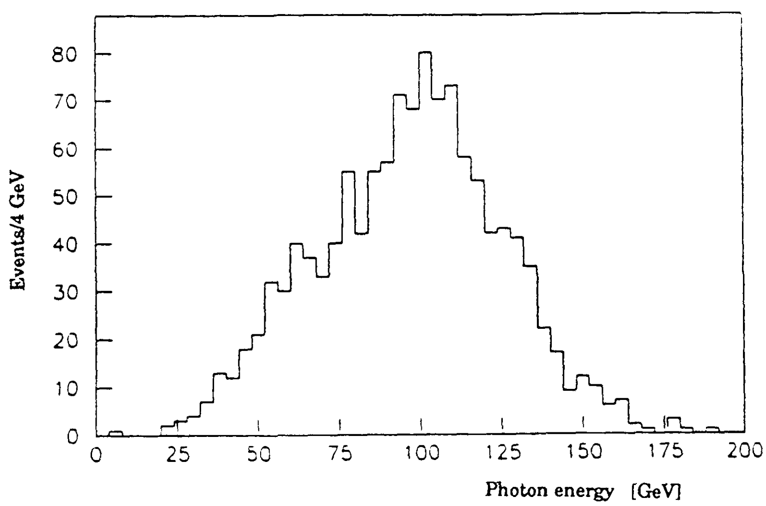

Figure 3.5 *Beam energy*

Beam	Particle	Flux [/burst]	Energy [GeV]	Mean energy [GeV]
Primary	p	2×10^{12}	450	450
Intermediate	e^-	10^8	120–250	140
Experimental	γ	10^7	40–180	100

Table 3.2 *Beam characteristics*

3.4 Beam properties

The energy spectrum of the beam measured by the tagging is shown in Figure 3.5, with a mean value of ~ 100 GeV. The flux of photons with energy greater than 40 GeV is typically 10^7 per 2 second burst; this and other characteristics of the beam are summarised in Table 3.2. The spatial dimensions of the beam may be determined from the distribution of vertices, formed using the tracks of charged particles reconstructed in the apparatus. This distribution is shown in Figure 3.6 for the two coordinates transverse to the beam; as can be seen the beam size is ~ 28×12 mm^2 (FWHM $y \times z$). It should be noted that the use of the active target in the trigger condition would influence these distributions if the area of the target included in the trigger was smaller than the beam size; this is not the case for

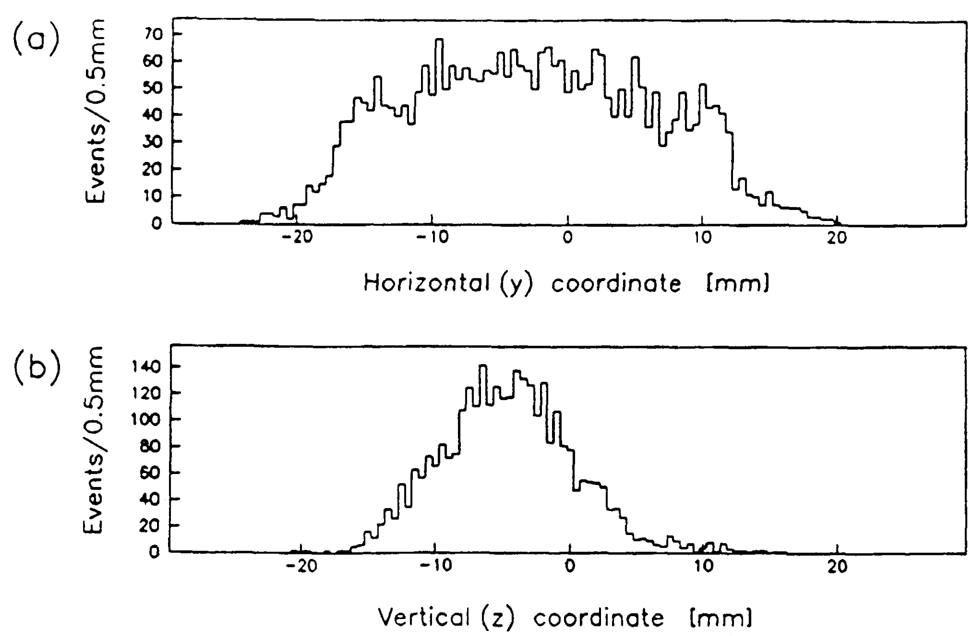

Figure 3.6 *Beam size*

the z-coordinate, but the clipped form of the profile indicates that it underestimates the beam width in y.

3.5 Sources of background

Hadronic

The photon beam is very clean of hadronic contamination, to the level of 1 part in 10^5. What contamination remains is a result of a small number of π^-s that accompany the electron beam with a ratio $(\pi/e) \sim 10^{-3}$. These pions are produced by the decay of neutral hadrons, principally Λ s and K^0s, and they are swept out of the beam by the tagging magnet, along with any charged particles that they produce through interaction in the radiator; however, any neutral hadrons produced will contaminate the beam, and result in a proportionally higher rate of background interactions in the experimental target.

Electromagnetic

The most serious source of background to the experiment is of electromagnetic origin. 98 % of the photons reaching the experimental target have energy less than 50 GeV: these low energy photons are the result of either bremsstrahlung in the radiator, or (for energies less than 10 MeV) *synchrotron* radiation caused by the deflection of the electron beam in the last magnets of the system. Every electron radiates on average six synchrotron photons and one bremsstrahlung photon towards the target, and the photons can convert in the target to form e^+e^- pairs, at a rate which would blind the apparatus if precautions were not taken.

To combat this source of background the experimental target is situated in a vertical magnetic field that is designed to sweep low energy (less than 250 MeV) pairs out of the acceptance of the apparatus, whilst not removing the higher energy interaction products that the experiment is designed to study. The pairs have opening angle α given by [69]:

$$\alpha = \frac{m}{E_\gamma} \log \frac{E_\gamma}{m}$$

where m is the electron mass and E_γ is the incident photon energy. Thus for $E_\gamma > 500$ MeV, $\alpha < 7$ mrad, i.e. the opening angle is very small. Thus the magnetic field

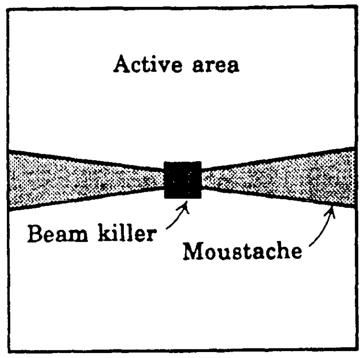

Figure 3.7 *Desensitised wire chamber regions*

sweeps the pairs that are of sufficient energy to remain inside the acceptance into a horizontal band. Detectors that would be adversely affected by the pairs are desensitised over a corresponding horizontal region; for example Figure 3.7 shows the desensitised regions of a wire chamber, known as the 'Moustache' for obvious reasons. The beam killer is required when a charged pion beam is used (see below).

The electromagnetic background is excluded at the trigger level by a requirement that more ionisation is deposited in the target than would be created by a single pair. Remaining pairs that are reconstructed may be recognised by their small opening angle in the non-bend (Z) projection.

Muon halo

Muons are created both in the production target and in the proton dump. They are highly penetrating, since being leptons they do not interact via the strong force, and as they are about 200 times as massive as electrons, they lose less energy radiatively. As a result there is a flux of about 10^6 $m^{-2}s^{-1}$ muons that penetrate the intervening material and reach the experimental apparatus. They are distributed asymmetrically over a large area transverse to the beam, and are most intense above and to the left of the beam. The flux could be reduced by changing the axis of the photon beam, but this would entail a tighter selection of the electron momentum, with a corresponding decrease in the beam intensity. The muon halo is excluded at the trigger level by the *muon veto,* a large scintillator array described in Section 3.8.

3.6 Alternative beams

One of the features of the NA14 beam line is its ability to run with different beams for purposes of alignment and calibration.

Pion beam

Pions are abundantly produced in the initial interaction of protons in the production target. They are selected by turning off both the sweeping magnet that follows the production target and the tagging magnets at the end of the beam line; the aperture of the neutron dump is narrowed and the chicane magnets are tuned to select π^-s of the chosen energy, usually 90 GeV; the conversion and radiator targets must be removed; and finally the BTCs and the *charge veto* (a scintillator detector, described in Section 3.8) are taken out of the trigger. Negative particles are chosen to prevent non-interacting protons from contaminating the beam, but there is a small component of K^-s and antiprotons. To avoid saturation of the detectors by the high flux of pions, the proton flux is reduced by the insertion of additional target material upstream of the production target, removing about 99 % of the protons; this has the side-effect of reducing the muon halo intensity.

Muon beam

This is produced by simply closing the apertures of the neutron dump and the collimator (see Figure 3.2), so that only the muon halo seen with the photon beam reaches the apparatus.

II The Detectors

3.7 Introduction

The reconstruction of an event requires knowledge of the particles that are produced in the interaction. The information about each particle that is of interest may be broadly separated into:

(i) *Identification*: the intrinsic properties, such as mass and charge;
(ii) *Kinematics*: the momentum and direction in space;
(iii) *History*: the point of creation, and of decay (if it occurs).

The identification of a particle may be achieved by a determination of its rest mass, its interactions, or in some cases its decay products. The kinematics and history are discovered primarily through *tracking,* the measurement of particle trajectories, and due to its importance this will be described first. The categories are not exclusive: for example, a particle may be identified through a knowledge of the kinematics of its decay, and the lifetime is obviously a characteristic of the particle type.

Most methods of particle detection depend on energy transfer to the medium through which the particle travels. For a charged particle this is principally through interactions with the electrons of the medium, causing ionisation or excitation of its atoms. The energy loss is described by the Bethe-Bloch formula [70], which gives the mean energy loss of a particle with charge z and velocity v travelling through a medium of atomic number Z and mass number A:

$$\frac{dE}{dx} = \frac{4\pi N_A z^2 e^2}{m v^2} \frac{Z}{A} \left[\ln \left(\frac{2 m v^2 \gamma^2}{I} \right) - \beta^2 \right] \tag{3.1}$$

where m is the electron mass, N_A is the Avogadro constant, x is the path length multiplied by the density of the medium, and I is an effective ionisation potential that depends on the material (~ 10 Z eV).

From this it may be seen that the rate of energy loss is only weakly dependent on the medium (since $Z/A \approx 0.5$ for most elements), and is independent of the incident particle mass; for nonrelativistic velocities it decreases as $1/v^2$, and then after passing through a minimum at $\gamma \sim 3$, increases logarithmically with γ. This is illustrated in Figure 3.8 [1], (where the momentum $p = \gamma M v$ for a particle of mass M).

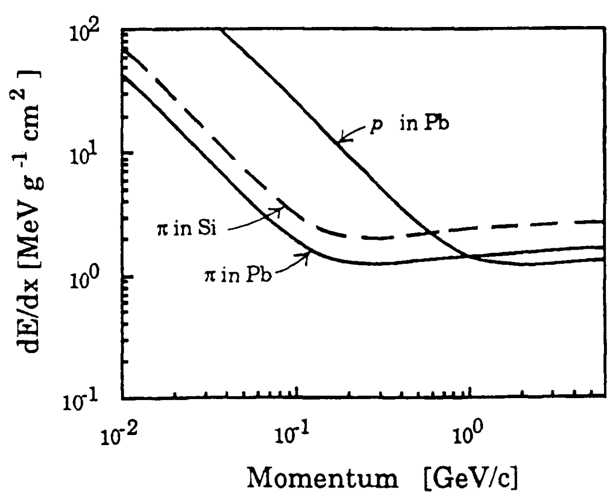

Figure 3.8 *Energy loss of particles in matter*

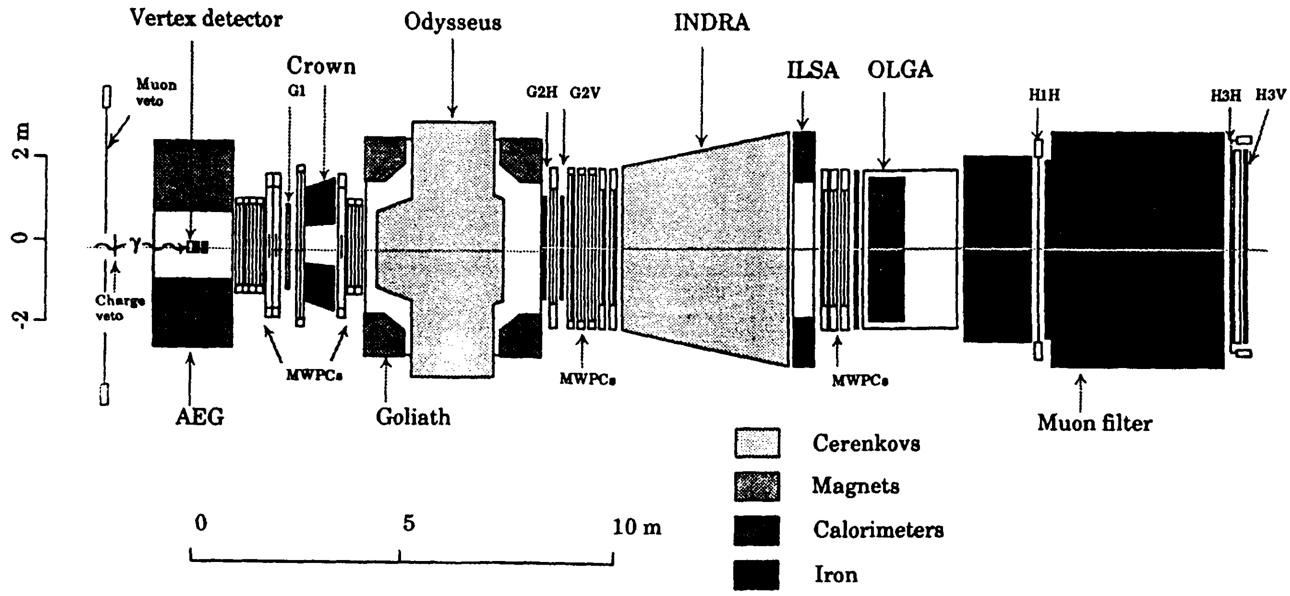

Figure 3.9 The apparatus of NA14

A particle is *minimum ionising* when its energy loss is close to its minimum value. Then the ionisation produced in a detector is known as I_{min}, and corresponds to about 2 MeV $g^{-1}cm^{2}$ in silicon for example.

No single detector is capable of determining all the properties of the interaction products that are of interest, so the apparatus of a high energy physics experiment is generally an assembly of different detectors, each measuring a subset of the properties. The information is then combined at the analysis stage. The detectors of NA14 will be described according to the property they are intended to investigate; they are arranged, as shown in Figure 3.9, into the form of a *spectrometer*, utilising magnets to deflect charged particles. Some parts of the apparatus are visible in Figure 3.10.

3.8 Particle kinematics

Tracking

The motion of the particles is not measured directly, and they are considered as *tracks*, the lines in space that they follow. The detection of tracks is central to high energy physics experiments, and has been achieved in a variety of ways. In the past, tracks were observed using *cloud chambers*, in which the ionisation caused by the passage of a

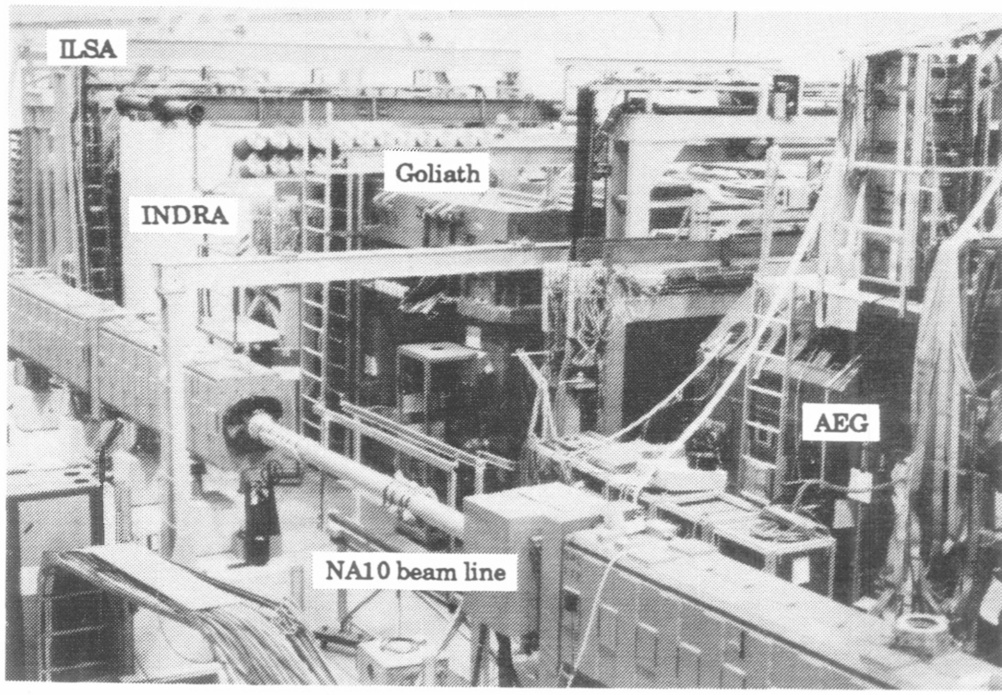

Figure 3.10 *View of the apparatus*

charged particle through a saturated vapour led to the formation of liquid droplets along the track; *Bubble chambers* operate in a related manner: the detector takes the form of super-heated liquid usually used as the experimental target, and the ionisation gives rise to bubbles of gas that may be photographed and so reveal the track; *Emulsions* represent one of the oldest techniques, but one that is still in use—stacks of photographic emulsion are exposed directly to the high energy particles, and reveal the tracks when developed. In electronically recorded experiments, on the other hand, track finding is achieved by the association of space points that are recorded as a result of the passage of a particle through digitised elements of the detectors.

Scintillator hodoscopes

Scintillating materials have the property that a small fraction of the energy gained by their atoms from ionising particles is lost through the emission of light, and furthermore the materials are transparent to their own luminescence. They may be classed as inorganic—of which sodium iodide (with suitable impurities) is the prime example—and organic, including various polystyrene based materials. One common arrangement for organic scintillator is to utilise excitation of molecular energy levels, which then decay

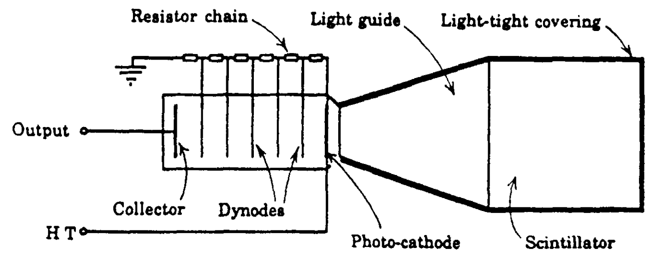

Figure 3.11 *Scintillation counter construction (schematic)*

with the emission of ultraviolet light, converted to blue by the fluorescent excitation of dye molecules incorporated in the primary scintillator medium.

The scintillation light is generally detected by a *photomultiplier*, a device which produces an electrical signal in response to light (see Figure 3.11). This is done using an alkali metal coated photocathode that emits photoelectrons when illuminated, with a typical efficiency of 10 % for photons of 450 nm wavelength. The *multiplier*, a chain of electrodes at progressively higher voltage (*dynodes*) gives a current amplification, typically of gain $\sim 10^8$, and the resulting pulse is large, permitting simple read-out.

Scintillation counters have the advantages of being robust, efficient and fast, with output signal widths as low as 10 ns providing accurate timing information, but their spatial resolution is obviously determined by the dimension of the scintillator, so for use in tracking they must be arranged into *hodoscopes* of thin fingers.

Scintillator hodoscopes of this nature have already been mentioned as part of the tagging system for the beam: H1–4, V1–4 and the BTCs. Their positions may be seen in Figure 3.2. H1–4 have vertically oriented fingers (giving measurement of the horizontal coordinate) and measure the energy of the electrons incident on the radiator target. H1 and H2 provide a measurement of the electron's trajectory before the last bending magnets of the chicane whilst H3 and H4 measure the trajectory after deflection. An electron of 150 GeV energy is deflected by about 17 mrad, and the two pairs of planes are about 5 m apart, so fingers with widths of the order of millimeters are required to give the necessary precision in energy measurement. The widths chosen represent a compromise between energy resolution and the number of channels of read-out electronics required; they may be seen in Table 3.3. The thicknesses (along the beam direction) are also a compromise, between the number of photoelectrons produced for good efficiency, and the requirement of transparency (since the electrons have not yet radiated, and so must not be significantly affected by the scintillator).

Hodoscope	No. of fingers	Thickness [mm]	Width [mm]	Height [mm]
H1	80	6	1·5	100
H2–4	64	6	1·5	100
V1	64	6	100	1·5
V2	34	8	100	3–10·5
V3	65	8	100	1·5–12
V4	72	8	100	1·5–12

Table 3.3 *Tagging hodoscope geometry*

V1–4 function in a similar fashion, with the deflection provided by the tagging magnets, in a vertical direction. Hodoscope V1 is like one of the H hodoscopes rotated through 90°; the other three are of a different type since they lie after the radiator target so the constraint of transparency is relaxed. The vertical width of their fingers is varied to ensure a constant precision in energy measurement, giving a quadratic dependence on the height from the beam axis. The BTCs provide a fast signal that serves as a time reference for the beam trigger. They cover the acceptance of the V hodoscopes, with only a few channels: 21 in total.

In the NA14 spectrometer there are three main scintillator hodoscopes, named G1, G2H and G2V. They are used primarily in the experimental trigger, to select hadronic events, i.e. events where the photon has interacted hadronically in the target (rather than electromagnetically). For further details of the trigger see Chapter 5.

Some parameters of these hodoscopes are given in Table 3.4; both G1 and G2V have their fingers oriented vertically, giving measurement of the y-coordinate, whilst for G2H the elements are horizontal. In all three there is a central horizontal gap in the area covered, to prevent the saturation of the detectors by electromagnetic pairs, as described in Section 3.5. In G1 the 80 fingers are arranged into four planes of 20, two above the beam and two below, with a separation of 27 mm along the beam direction. The others both have their elements arranged in single planes above and below the beam.

Also displayed in Table 3.4 are some parameters of three more hodoscopes that are part of a detector for muons. As this detector is used for the identification of particles it will be described in the next section. Scintillators are also used in the calorimeters both for position detection and as charge vetoes, as well as providing the active element in one

Hodoscope	Distance from target [m]	No. of elements	Element orientation	Element dimensions [mm^2]	Desensitised gap [mm]	Timing Resolution [ns]
G1	1·85	80	V	54×550	± 50	10
G2H	7·5	32	H	1200×70	± 50	15
G2V	8·3	24	V	200×750	± 60	10
H1H	18	36	H	1800×180	no	160
H3H	22	32	H	2190×180	no	160
H3V	23	72	V	180×1450	no	160

Table 3.4 *Spectrometer hodoscope geometry*

of them, but again these will be discussed with the calorimeters themselves.

The remaining uses of scintillators in the experiment are in a *muon veto* and *charge veto* that lie upstream of the target (i.e. at a lower x-coordinate). These are both used in the trigger: the muon veto is a large plane of scintillator ($1{\cdot}80 \times 1{\cdot}92$ m^2) 3·5 m upstream of the target that serves to prevent triggers from halo muons, whilst the charge veto is relatively small (100×100 mm^2), and is situated 1 m upstream of the target to prevent any charged particle that is coaxial with the beam from producing a trigger.

Wire Chambers

Multiwire proportional chambers (MWPCs) provide the main tracking detectors in many high energy physics experiments. They are constructed out of planes of parallel wires at a positive potential, lying between conducting surfaces in a gas filled container, as illustrated schematically in Figure 3.12. Electrons liberated from the gas by the passage of a charged particle drift towards the nearest wire, gaining energy from the electric field. If the energy gained exceeds that required to ionise the gas then further *secondary* electrons are produced, and an *avalanche* ensues. The *gas amplification*, the

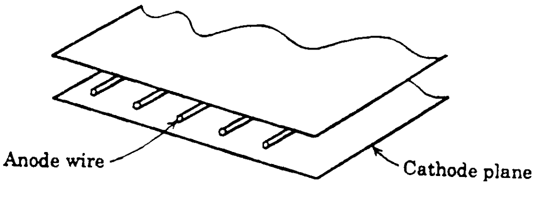

Figure 3.12 *Wire chamber contruction (schematic)*

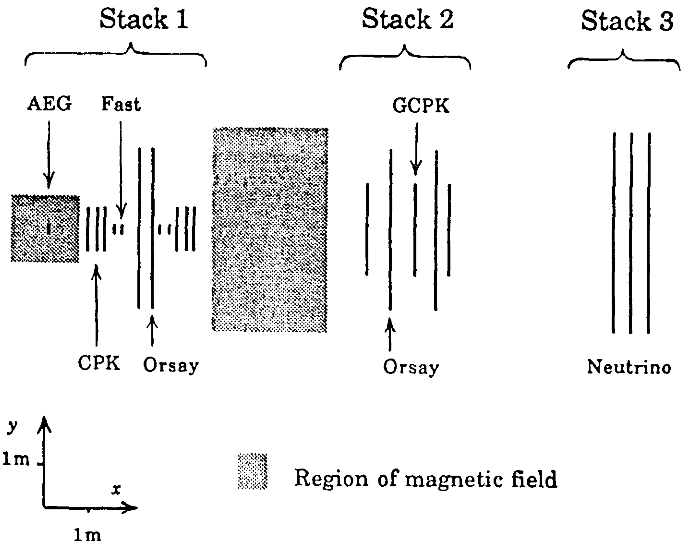

Figure 3.13 *Wire chamber layout*

number of secondary electrons produced per primary ion pair, is $\sim 10^5$. A typical arrangement is to have anode wires 20 μm in diameter with a 2 mm spacing, kept at 5 kV relative to the cathode planes, which are separated by 12 mm. The choice of gas is influenced by requirements including low operating voltage, high gain, fast recovery and long life. The noble gases have a low avalanche voltage and are suitably inert, with argon the standard choice; however if used alone the gain that may be achieved is severely limited by continuous discharge. This may be *quenched* by the addition of a polyatomic gas, and the gas used is generally a mixture such as argon-isobutane. By reading out the anode wires individually, the coordinate of the particle perpendicular to the wires may be determined.

MWPCs form the back-bone of the NA14 apparatus. There are 21 chambers, with a total of 73 planes of wires, distributed in three groups or *stacks* as illustrated in Figure 3.13. They are generally situated in regions free of magnetic field, to avoid problems of spiralling low energy electrons and the difficulties of track reconstruction in a strong field. An exception is the single chamber positioned within the AEG magnet to provide a track coordinate as close to the target as possible; it is small and has fast read-out to cope with the adverse conditions. Stack 1 contains two *Orsay* and six *CPK* chambers, all of which are desensitised in the median horizontal plane as described in Section 3.5. Four small *Fast* chambers are provided to cover this region, with fast read-out to combat the high rate of pairs. Stack 2 has five chambers, which along with

Chamber	No.	Distance from target [m]	Area ($y \times z$) [m^2]	De-sensitised region [mm]	Planes per chamber	Orientation* [°]	Wires per plane	Wire spacing [mm]	Gate [ns]
AEG	1	0·1	0·20 × 0·20	no	4	0 90 45 135	186 186 186 186	1	50
CPK	6	1·0 1·1 1·3 3·2 3·4 3·5	1·79 × 0·73	50 to 120	4	104 90 0 14	768 896 368 576	2	120
Fast	4	1·4 1·5 3·0 3·1	0·26 × 0·21	no	2	60 90 or 90 120	256 256 256 256	1	50
Orsay	4	1·7 2·1 8·1 8·8	3·60 × 1·50	5	4	90 60 120 90	1792 1536 1536 1792	2	120
GCPK	3	7·8 8·5 9·0	3·11 × 2·15	no	4	104 14 90 0	1024 896 1024 704	3	120
Neutrino	3	14·0 14·3 14·6	4·33 × 3·75	no	3	60 120 0	1232 1232 1232	3	120

* The angle is measured relative to the horizontal (y) axis, and the order follows the beam direction.

Table 3.5 *Wire chamber characteristics*

Stack 1 provide pattern recognition for tracks before and after the large Goliath magnet. Finally Stack 3, with three chambers, enhances the precision of momentum measurement for high momentum tracks. Some characteristics of the chambers are given in Table 3.5.

Silicon detectors

The use of silicon as a material for the construction of high resolution tracking detectors is a relatively recent development [71]. It has followed the creation of high resistivity silicon crystals, and the perfection of techniques of high spatial precision in the construction of the detectors. They use a wafer of silicon cut from a single crystal, of dimensions up to 5×5 cm^2. The silicon is treated as described below to produce diode strips, each of which acts as a separate detector element. The passage of a charged particle through a strip gives rise to a conduction charge in the material as a result of energy loss by ionisation. This charge is then collected at the electrodes of the diode to provide a signal.

The great advantage of using a silicon detector of diode construction is that by utilising the properties of the diode junction, the detector may be operated in a 'fully depleted' mode, for which the conduction charge in the detector volume is very small, even at room temperature. The charge produced by ionising particles is therefore readily detected.

The allowed energy levels of electrons in a crystalline material fall into bands, which may be separated by gaps of forbidden energy. In metals the band that is highest in energy is not filled, so that conduction is possible by electrons in that band. In other materials, however, in the absence of thermal excitation, the band of highest energy that contains electrons is exactly filled. This *valence* band contains the electrons responsible for the binding of the atoms to form the crystal structure. The next band, of higher energy, is known as the conduction band since electrons in it would be available for conduction, and it is separated from the valence band by a *band gap*. The only electrons that are in the conduction band are those that are thermally promoted from the valence band, with probability P given by [72]:

$$P \sim T^{3/2}\, e^{-(E_g / 2kT)}$$

where T is the absolute temperature, E_g is the band gap energy and k is the Boltzmann constant. The vacancy left in the valence band by the promoted electron acts as a positively charged particle, known as a *hole*. In the absence of an applied field these electron-hole pairs will recombine eventually, and an equilibrium concentration is achieved proportional to the rate of thermal excitation. This concentration is thus critically dependent on the band gap energy. For insulating materials, the band gap is large (~ 5 eV), whilst for semiconductors such as silicon the band gap is small enough (~ 1 eV) for an appreciable population of the conduction band to exist at room temperature.

In practice silicon is not used in this pure state, but instead small quantities of impurities are introduced into its crystal structure. Since silicon is tetravalent, if the

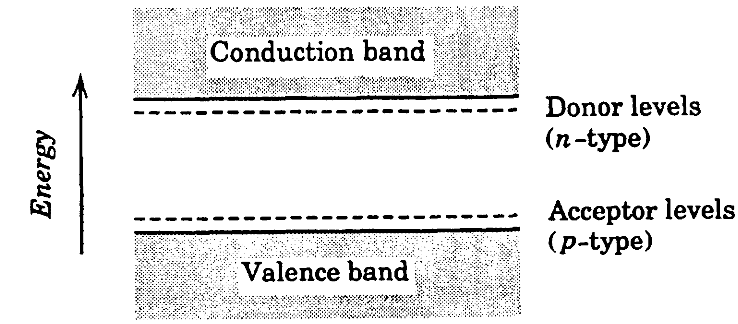

Figure 3.14 *Semiconductor energy levels*

additive is pentavalent then the electron of its atoms that is not required by the four bonds of the neighbouring silicon atoms in the crystal structure is only loosely bound, and lies at an energy level near the top of the band gap. This material, with its excess of negative charge carriers, is known as *n*-type. In a similar fashion, an atom of a trivalent impurity lacks an electron for bonding, and acts as a source of holes. Their energy level is at the bottom of the band gap, and the resulting material is known as *p*-type. See Figure 3.14.

If *n*-type and *p*-type silicon are brought into contact to form a *pn*-junction, the discontinuity in concentration of electrons and holes at the interface results in diffusion of the charge carriers across the boundary. In practice the *pn*-junction is achieved by the diffusion of trivalent impurities into an *n*-type substrate, or vice versa. As the charge carriers migrate they leave behind fixed charges in the crystal lattice, and thus a potential difference develops which eventually limits the flow. The electrons and holes that do migrate will recombine with the majority carriers in the material they have entered, leaving a region around the junction that is free of conduction charges, known as the *depletion layer* (see Figure 3.15). It is this region that forms the active area of the detector, and its thickness is usually enhanced by the application of a reverse bias; this increases the amount of charge deposited by an incident particle in the depleted region, and also decreases the capacitance of the detector, which helps reduce noise. For an applied voltage V, the depletion thickness d is given by [72]:

$$d = \sqrt{\frac{2\varepsilon\varepsilon_0}{eN}(V - V_0)}$$

where $\varepsilon\varepsilon_0$ is the dielectric constant, e is the electronic charge, N is the dopant concentration and V_0 is the built-in voltage of the junction (~ -0.6 V). If V is much greater than V_0, as is usually the case, we expect:

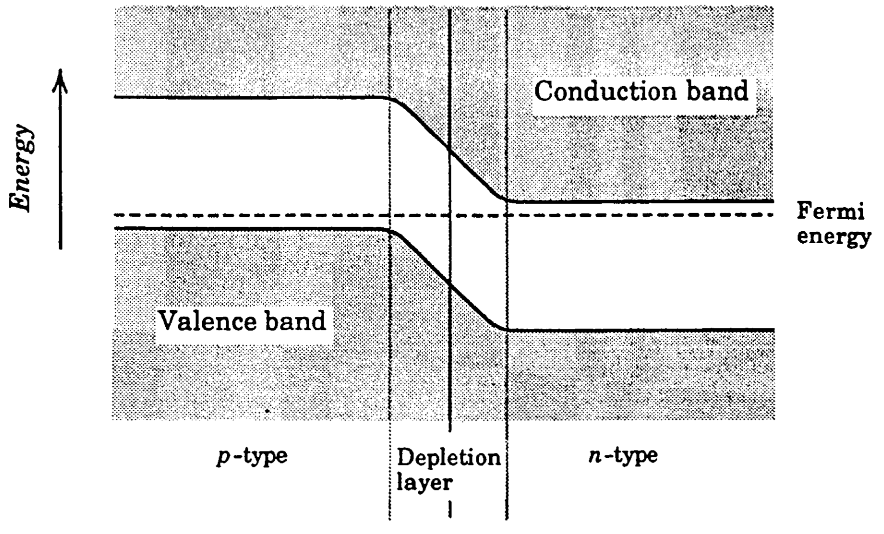

Figure 3.15 *pn-junction energy levels*

$$d \propto \sqrt{V} \tag{3.2}$$

The pn-junction acts as a diode since current may easily flow from n-type to p-type (i.e. electrons may pass from p-type to n-type) but not in the reverse direction.

The passage of a charged particle through the detector results in the creation of electron-hole pairs along the track. The average energy expended by the particle per electron-hole pair is about 3.6 eV, which improves significantly on the equivalent

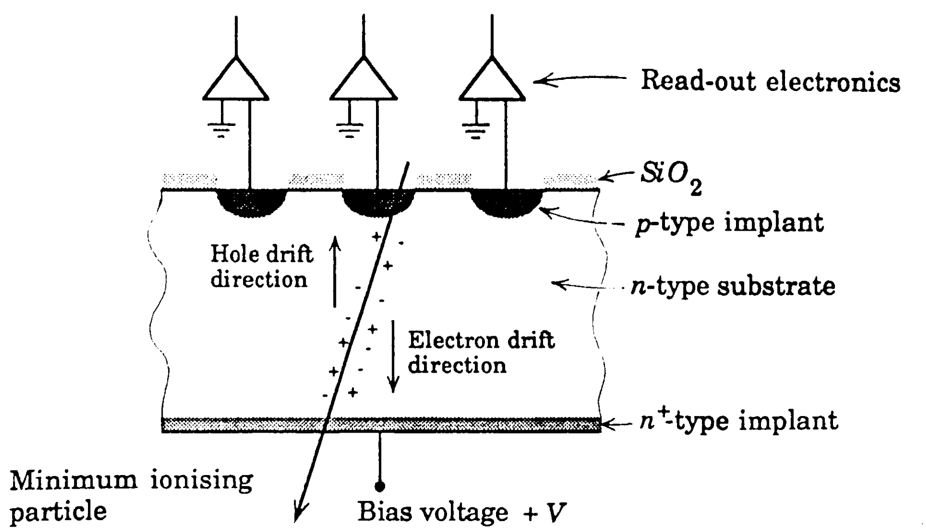

Figure 3.16 *Silicon strip detector operation (schematic)*

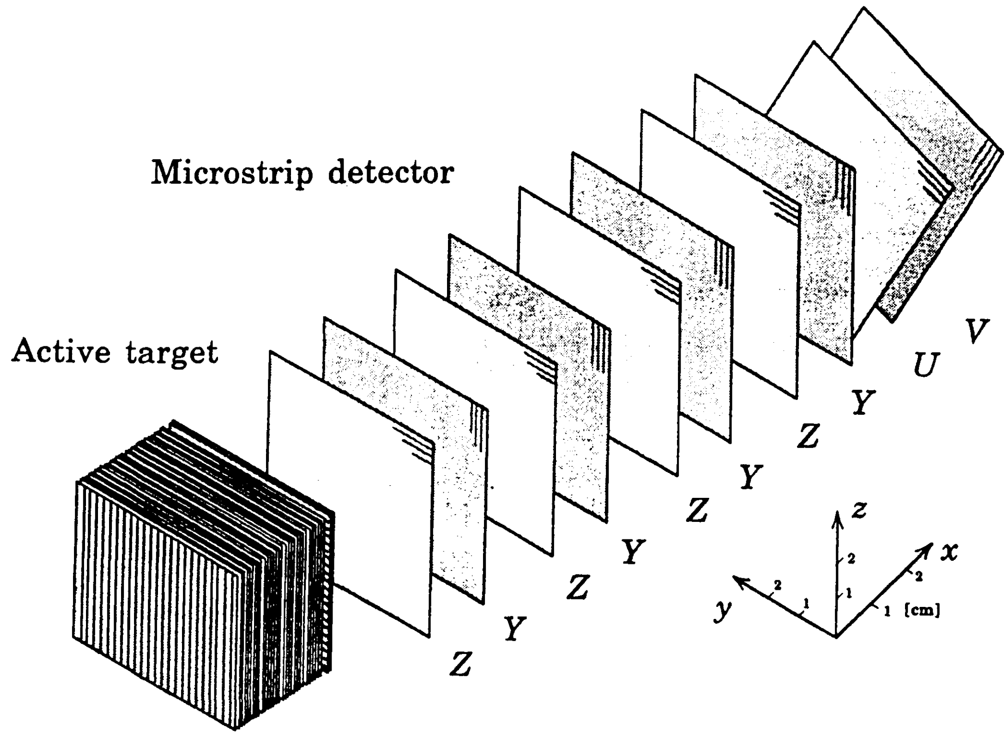

Figure 3.17 *The vertex detector*

energies in other types of detector, giving silicon detectors a high energy resolution. The charge is swept by the bias field towards the nearest electrode, where it is collected and detected by the read-out electronics (see Figure 3.16). The high field gives a high drift velocity, and since the distance the charge must drift is small, these detectors have a very fast response.

Silicon detectors are used in NA14 for the vertex detector. This is composed of an active target and a microstrip detector, as illustrated in Figure 3.17. Some parameters of the devices are given in Table 3.6; they will be described in more detail in the next chapter. A silicon *Quadrant Counter* was also installed, just downstream of the microstrips. It is a single plane, divided into four quadrants each of dimensions 1 cm $\times$ 1 cm. It was intended for use in the trigger, and was used in this manner during beam tests of the microstrip detector.

Momentum and Charge measurement

The momentum of charged particles may be measured through their deflection in a magnetic field. In a constant field $\boldsymbol{B}$, a charged particle with charge q and velocity $\boldsymbol{v}$ feels

	Active target	Microstrips
Number of planes	32	10
Plane orientation* [°]	90 (planes 1–30) 0 (planes 31,32)	0,90,0,90,0,90,0,90, 33,123
Plane dimensions ($y \times z$) [mm^2]	50×44	50×50
Silicon thickness [μm]	300	450
Number of strips / plane	24 (Y) 22 (Z)	1000
Strip pitch [μm]	2100	50
Read-out	Analogue	Digital

* Angle of rotation of strips about beam axis, relative to horizontal (y) axis.

***Table 3.6** Silicon detector characteristics*

a force:

$$\boldsymbol{F} = q\,\boldsymbol{v} \times \boldsymbol{B}$$

The particle therefore follows a helical trajectory, which in a projection orthogonal to the field is a circle of radius R, given by:

$$R = \frac{p \cos \lambda}{0{\cdot}003\, B\, q}$$

where λ is the angle of the track relative to the plane of the projection, and R is in units of cm, B in Tesla and p in GeV/c. The momentum of the particle may thus be determined from the magnitude of its deflection in the region of magnetic field, and the charge of the particle from the sense of the deflection. In practice the field is not exactly uniform, so the trajectories are not helical. The field is precisely mapped, and described in terms of a large number of coefficients: for example for one of the NA14 magnets, there are 27 coefficients, each determined at 39 separate sites from field measurements made using a Hall probe. The trajectories are then calculated using a Runge-Kutta method [73]. The procedure of track finding and propagation through the magnetic fields is performed by the program TRIDENT, and will be described in Chapter 6.

NA14 uses two magnets, as illustrated in Figure 3.9, both providing a dipole field with axis vertical. The first, named the AEG, surrounds the target. It is required to sweep the

	AEG	Goliath
B [T]	1·29	1·3
Distance from target [m]	0·0	5·5
Aperture ($y \times z$) [cm]	$\pm 65 \times \pm 25$	$\pm 120 \times \pm 60$
Acceptance ($y \times z$) [mrad]	$\pm 650 \times \pm 250$	$\pm 160 \times \pm 80$
$\int B \, \mathrm{d}l$ [Tm]	1·24	3·1

Table 3.7 Magnet characteristics

abundantly produced electromagnetic pairs out of the acceptance of the detectors, which would otherwise be rendered insensitive by the high rate. The AEG also provides momentum measurement for tracks that are outside the acceptance of the second magnet (which corresponds to tracks with energy less than about 5 GeV). The second, larger, magnet is named Goliath, and provides a precise momentum measurement for energetic particles, with:

$$\frac{\Delta p}{p^2} \sim 5 \times 10^{-4}\,\mathrm{GeV}^{-1} c$$

for tracks within its acceptance. The magnet parameters are given in Table 3.7.

For neutral particles, and charged particles that do not pass through the magnets, this technique of momentum measurement may not be used. If the particle decays into measured charged particles then its momentum may be reconstructed from the momenta of its decay products. This is necessary in particular for the short-lived charmed particles that we are intending to investigate. The momentum of photons and π^0s may be calculated using the calorimeter information.

3.9 Particle identification

From the multitude of particle types that are produced in a typical interaction, it is only those that are relatively long-lived that reach the detectors, and may be identified. The short-lived particles decay, and can only be identified from their decay products. This is also the case for some relatively long-lived neutral particles, such as K^0s and Λ s.

Of the long-lived particles produced in a hadronic interaction, the most abundant are pions, and also present in significant numbers are kaons, protons, electrons, photons and other neutrals. A number of different detectors are used to distinguish these particle types: the charged hadrons are identified using Cerenkov detectors, the electrons and photons are identified by the electromagnetic calorimeters, and for the muons there is a muon filter.

Cerenkov detectors

A Cerenkov detector is sensitive to the velocity of a particle. If the momentum of the particle is known, however, then its mass may be determined, providing identification. When a charged particle travels through a dielectric medium at a velocity greater than the speed of light in the medium, some of the light emitted by the excited atoms of the material appears as a coherent wave-front at a fixed angle to the particle trajectory. This *Cerenkov* light has a continuous spectrum of frequencies, peaked towards ultraviolet light. For particle velocity v and refractive index n, the condition for Cerenkov light to be produced is:

$$v > \frac{c}{n}$$

i.e:

$$\beta > \frac{1}{n}$$

See Figure 3.18.

A threshold Cerenkov detector is essentially a box of gas. The Cerenkov light created by a particle passing through the gas is collected using mirrors, and detected with photomultipliers. The trajectory of a particle through the Cerenkov detector is found using tracking information from other detectors, and the mirror through which the particle

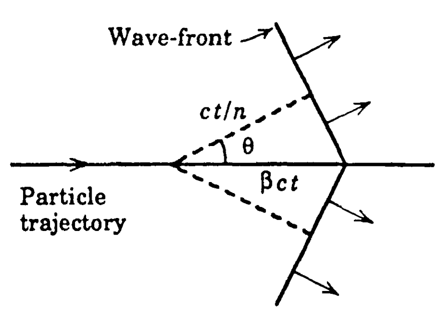

Figure 3.18 *Cerenkov light emission*

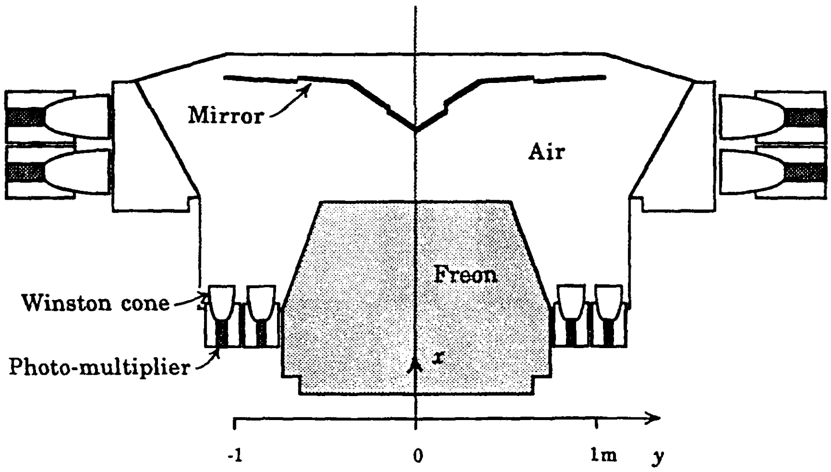

Figure 3.19 The Odysseus Cerenkov detector

passed is checked for light. As shown above, there is a minimum velocity for the production of Cerenkov light, which for a given particle type translates into a momentum threshold. Therefore if the particle momentum and the presence or absence of light are known, information is gained about the particle type.

NA14 has two Cerenkov detectors, named INDRA and Odysseus. A plan of Odysseus is given in Figure 3.19 to illustrate their construction. INDRA [74] has 48 mirrors, each with a photomultiplier. It is filled with dry air at room temperature and pressure, and has momentum thresholds as shown in Table 3.8.

The mirror size is influenced by the desire to keep all light from a single particle contained within a single mirror. From Figure 3.18, the angle of emission of the light is given by:

$$\cos\theta = \frac{ct/n}{\beta ct} = \frac{1}{\beta n}$$

Cerenkov	Gas	Refractive index	Momentum threshold [GeV/c]				
			e	μ	π	K	p
INDRA	Dry air	1·000297	0·021	4·34	5·73	20·27	38·52
Odysseus	Freon-12	1·001080	0·011	2·28	3·01	10·63	20·21

Table 3.8 Cerenkov detector characteristics

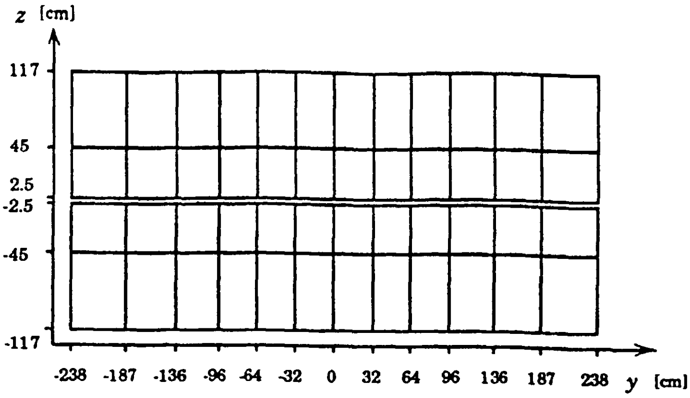

Figure 3.20 *The INDRA Cerenkov mirror layout*

After traversing a distance L through the Cerenkov detector, the cone of light has diameter given by:

$$d = 2\,L\,\tan\theta$$

For INDRA, $L \sim 3.5$ m, so for $\beta \sim 1$, $d \sim 170$ mm. The mirror size is limited by the conflicting requirement that no more than one track crosses any mirror in an event. This leads to a smaller mirror size near to the beam axis, as the density of particles is greater. The layout of mirrors for INDRA is shown in Figure 3.20. To avoid light from e^+e^- pairs, two horizontal opaque shields are fitted at height ± 25 mm. A similar shield is fitted vertically, along the beam axis, to further isolate regions of the Cerenkov.

The mirrors are oriented to reflect all the light towards their individual photomultipliers. To maximise the efficiency of light collection at the photomultipliers, each has a Winston cone light funnel.

The Odysseus detector was added to the apparatus to extend the momentum range of particle identification. It is filled with a different gas, giving different momentum thresholds. The gas chosen was Freon-12 (CCl_2F_2), and it fills a volume that accounts for approximately 60 % of the length of the detector, the rest being filled with air (see Figure 3.19). The detector has 32 mirrors, and lies in the 1·3 T field of the Goliath magnet, as that was the only available space for its installation. This, however, is the source of serious difficulties:

(i) The photomultipliers will not function in any magnetic field greater than $\sim 10^{-4}$ T. As far as possible they were kept out of the volume of the magnet, but extensive screening was required.

(ii) The tracks that are used in the analysis of the Cerenkov information are curved rather than straight, making the analysis more complex.

Odysseus was installed and tested in 1985, and was operational in 1986. Due to the problems mentioned above, it was not used for the analysis presented in this thesis; it will, however, be particularly useful in the study of channels containing protons, such as $\Lambda_c \rightarrow pK\pi$.

Calorimeters

A particle entering a dense medium will interact to produce secondary particles, which themselves interact producing further particles—generating a *shower*. In the case of electrons and photons, the interaction is electromagnetic. The process of showering is utilised by calorimeters, so named because most of the energy of the incident particle is absorbed and appears as ionisation or excitation in the medium.

Electrons and photons produce electromagnetic showers via the processes of bremsstrahlung and pair production, giving an initially exponential increase in the number of particles with depth. As the mean energy of the particles is reduced, ionisation loss becomes important and radiation ceases, giving a broad maximum in the number of particles, and then a gradual decline. The shower also spreads laterally via Coulomb scattering.

Electromagnetic calorimeters utilise materials with high atomic number as they have short radiation lengths, permitting the shower to be contained in a small volume. The calorimeters require an active component to allow the development of the shower to be measured. One technique is to use lead-glass (55 % PbO, 45 % SiO_2), and to detect the Cerenkov light caused by the relativistic electrons in the shower. Alternatively, the active and passive elements may be distinct, for example using alternate planes of scintillator and lead. From the development of their showers, electrons and photons may be distinguished from other particles.

The apparatus of NA14 includes three electromagnetic calorimeters, covering between them the angular acceptance. See Figure 3.21. OLGA [75] covers the forward region 0–80 mrad in the laboratory frame, ILSA [67] covers 80–150 mrad, around 90° in the centre-of-mass frame, and Crown [75] covers the backward region up to 275 mrad. All three detectors have the following structure:

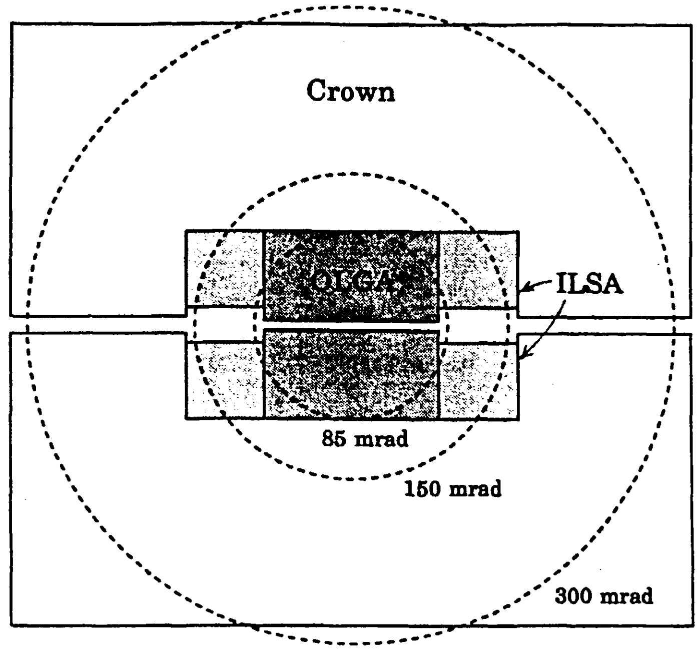

Figure 3.21 *Calorimeter geometrical acceptance*

(i) *Charge veto*: discriminates between charged particles and neutrals, and permits the rejection of charged particles for the analysis of photons;

(ii) *Preconverter*: initiates the showering of photons and electrons, and thus allows the measurement of the position of photons by the position detector. The thickness of the preconverter is determined by the requirements that all photons should be converted, but that the precision of the position measurement should not be degraded. A further incentive for keeping a low thickness is to assist in the rejection of neutral hadrons, since hadronic showers develop more slowly with distance than electromagnetic showers;

(iii) *Position detector*: determines the position of the shower in the calorimeter. The position detectors of all three calorimeters are of similar construction, of scintillator hodoscopes, each with two orthogonal planes of thin fingers. The problem of ambiguities encountered with such a system is helped by the low average track multiplicity in each detector, the segmentation of the calorimeter proper, and by comparison of the pulse heights in the two projections;

(iv) *Calorimeter proper*.

The calorimeters Crown and OLGA are quite similar in construction. See Figure 3.22. They are both essentially walls of lead glass blocks: Crown has 192 blocks, each of

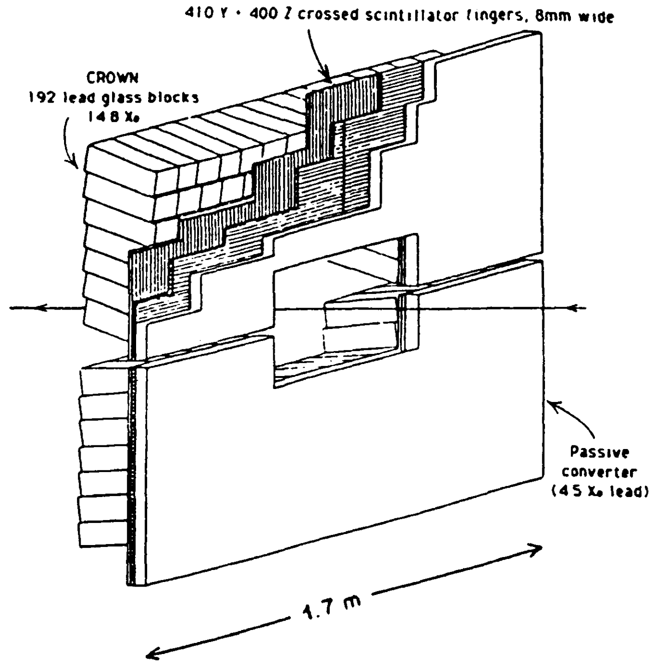

Figure 3.22 *The Crown calorimeter*

dimensions $9 \times 9 \times 25$ cm^3 and OLGA has 344 blocks of dimensions $14 \times 14 \times 47$ cm^3 —larger since it is further from the target. ILSA, on the other hand, is of lead/scintillator construction. It is composed of four separate quadrants, arranged symmetrically around the beam axis, each with four layers of 4 modules. The modules have dimensions 25×100 cm^2, and are constructed of 3 mm thick lead sheets interspersed with 5 mm thick scintillator planes. The layers in a quadrant are oriented alternatively vertical and horizontal; the first two have a thickness of 3·5 radiation lengths, whilst the last two are 5·5 radiation lengths. Finally there are two further layers of scintillator, used for triggering. Details of the calorimeters are given in Table 3.9.

Muon filter

Muons are remarkable for their ability, though charged, to penetrate matter with little loss of energy. This property is utilised in their identification, by detecting their passage through large thicknesses of iron at the downstream end of the experiment. See Figure 3.9.

The iron wall is 5·4 m in length, and is 20 m downstream from the target. The passage of charged particles through it is detected by three scintillator hodoscopes: H1H, H3H and H3V, the parameters of which were given in Table 3.4.

	OLGA	ILSA	CROWN
Distance from target [m]	15·5	13·5	2·35
Angular acceptance [mrad]	0-80	80-150	80-275 V 150-275 H
Construction	Pb-glass	Pb/scint.	Pb-glass
Cell size [cm^2]	14×14	25×25*	9×9
Number of radiation lengths	18·5	18	14·8
Minimum energy measured [GeV]	1·5	1·5	1
CHARGE VETO	Scintillator	Scintillator	Wire chamber
PRECONVERTER	Active	Active	Passive
Construction	Pb glass	Pb-scint.	Pb
Number of radiation lengths	3	4·5	5
POSITION DETECTOR	Scintillator	Scintillator	Scintillator
Width of fingers [cm]	1·5	1·5	0·8

* Cell size in each projection 25 × 100 cm^2.

Table 3.9 *Electromagnetic calorimeter characteristics*

3.10 Particle history

The history of a particle comprises its point of creation, its trajectory through the experimental apparatus, and if it decays, then its point of decay. The methods for determining the trajectory of the particle have been discussed in Section 3.8. The remaining information is provided by *vertex finding*. A vertex is the point in space at which two or more tracks intersect. If, for example, a charged particle decays into three charged products, and the tracks of all the particles are reconstructed, then a four-track vertex should be found. It is then inferred that the particles responsible for the downstream tracks are the decay products of the upstream particle, and information is obtained about this parent particle from the properties of its daughters. Obviously if some of the daughters are neutral, or their tracks are not reconstructed, then the recognition of such decays becomes more difficult.

The majority of the particles with which we are concerned are produced at the interaction of the beam photon in the silicon target. This point is known as the *production* or *primary* vertex. It is characterised by the existence of no incoming track, and typically about ten tracks are produced. However, the reconstruction of the primary vertex may prove difficult due to the presence of tracks not associated to it, coming either from decays or from errors in the track finding.

The vertices formed by particle decays may be broadly separated according to the lifetime of the decaying particle. For relatively long-lived particles, such as K^0s and Λ s, the vertex finding is simplified by the lack of other interfering tracks. For short-lived particles, the discovery of the *decay* or *secondary* vertex and its resolution from the primary vertex is a difficult problem, requiring a detector with high spatial precision. Just such a detector was used by NA14, and is described in the next chapter. The thorny problem of vertex finding is returned to in Chapter 7.

Chapter 4

VERTEX DETECTOR

The vertex detector is in two parts: a multilayer active target, and a microstrip tracking chamber. The information provided by the two components is complementary, as the active target gives a measurement of vertex position along the beam direction, whilst the microstrips are designed to give high transverse resolution. This chapter starts with a discussion of general considerations concerning signal creation and detection in silicon detectors. A description of the techniques of detector fabrication is then given, and finally the two devices are described.

I Silicon Detectors

4.1 Signals from silicon detectors

The Landau distribution

The signal deposited in a silicon detector consists of the electron-hole pairs created by the passage of an ionising particle. The Bethe-Bloch formula (Equation 3.1) discussed in Section 3.7 describes the macroscopic average of energy deposition in the material. However, if one is interested in the ionisation produced by the passage of an individual particle through a thin absorber, as is the case for the silicon detectors, then the statistical nature of the process must be considered. The distribution of energy loss in a thin

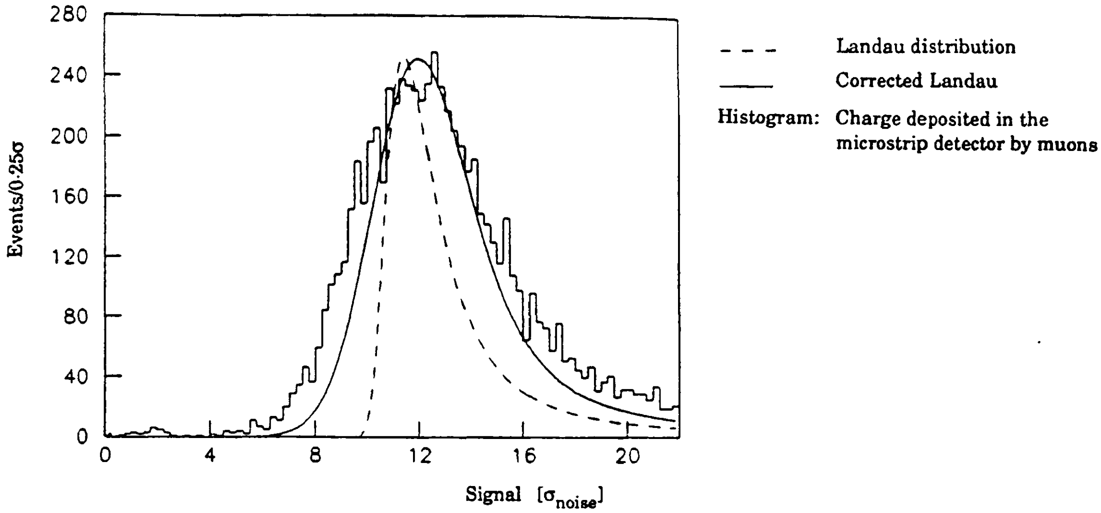

Figure 4.1 *Comparison of the Landau distribution with data*

absorber was first studied by Landau [76], so it is generally referred to as the Landau distribution. It is characterised by a long tail of high energy transfers. The calculation has been improved [77] by including the kinematic constraint on energy transfer, and by the incorporation of the fact that the electrons of the medium are not free. These corrections have the effect of broadening the peak of the distribution, and improve its description of the data (see Figure 4.1). The same general feature remains, however, that large fluctuations in the energy deposited are to be expected for thin absorbers.

Charge collection

The charge produced by the passage of an ionising particle through the silicon is deposited in a narrow tube around the track. It drifts under the influence of the electric field created by the bias voltage, towards the electrodes. The collection time is of the order of 10 ns for a 300 μm thick detector. The charge collection efficiency, i.e. the proportion of deposited charge that is seen at the electrodes of the detector, may be reduced by various factors, such as the recombination of electron-hole pairs, and the trapping of charge at imperfections in the crystal structure.

Charge sharing

Since the detectors have multiple channels on the same wafer of silicon, the possibility of charge sharing arises, where the charge deposited by an incident particle is shared amongst more than one channel. This arises for the following reasons [78]:

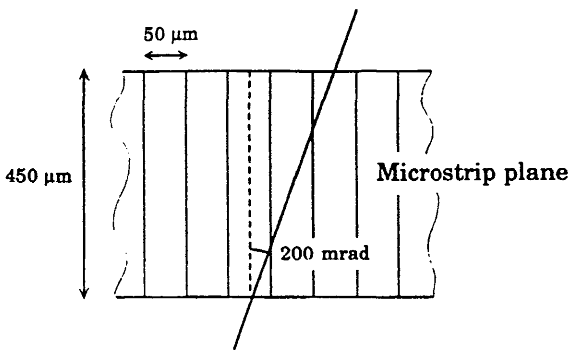

Figure 4.2 *Geometrical charge sharing*

(i) *The simple geometrical effect.* A track passing through the detector at an oblique angle may pass through more than one strip, and its charge will therefore be divided between the strips. For the microstrip geometry this can give rise to the charge being shared between up to 3 strips, for tracks originating in the target (see Figure 4.2).

(ii) *Diffusion.* Whilst the charge drifts under the influence of the electric field it spreads laterally due to diffusion. The transverse width of the charge distribution therefore increases during the drift time t_d, in a manner determined by the Diffusion equation. This leads to an *rms* width σ_D given by:

$$\sigma_D = \sqrt{2Dt_d}$$

where D is the diffusion constant, which has the value of 35 cm^2s^{-1} for electrons and 12 cm^2s^{-1} for holes in silicon. For a drift time of 10 ns this gives a width of about 5 μm at the electrodes, leading to the possibility that the charge spreads into the neighbouring strip.

(iii) *δ-rays.* These are electrons from the primary ionisation that have sufficient energy to cause secondary ionisation. A δ-ray of 100 keV will travel about 60 μm in silicon [79], and so may trigger the neighbouring strip in the microstrips.

Leakage current

The leakage current of a silicon detector is the (usually small) current that flows when the bias voltage is applied, in the absence of ionising radiation. If it becomes too large, then its fluctuations may be comparable to the signal charge. Leakage current is caused by the generation of electron-hole pairs in the silicon, the main sources of which are the following [80]:

(i) *Generation current*: generation of electron-hole pairs within the depleted region. The resulting current I_g is given by:

$$I_g = \frac{e n_i A d}{2\tau_0}$$

where n_i is the intrinsic carrier concentration, A is the junction area, d is the depletion thickness and τ_0 is the minority carrier lifetime. Using Equation 3.2, we therefore expect:

$$I_g \propto \sqrt{V} \tag{4.1}$$

(ii) *Diffusion current*: generation of minority carriers in the undepleted region of the detector. They may then diffuse into the depleted region and be swept away by the electric field. This contribution may be neglected in a fully depleted detector;

(iii) *Surface current*: generation of minority carriers at the silicon surface, which depends upon both the nature of the *Si-SiO$_2$* boundary, and surface contamination, in a complex manner. It is important that the surface be kept as clean as possible to minimise this source of leakage current.

Noise

Every system of measurement has an associated *noise*. This is the random background to the property being measured. If the magnitude of the signal is not large compared to the noise, then a random fluctuation in the noise may simulate a signal, degrading the performance of the system. For silicon detectors, the noise takes the form of fluctuations in the electrical read-out of each channel. It may be described in terms of the *Equivalent Noise Charge* (ENC), the amount of charge that would have to be deposited in the silicon to provide a signal of the same magnitude as the width of the noise distribution. The noise of the silicon detector arises from [72]:

(i) *Shot* noise, from fluctuations in the leakage current in the silicon.

(ii) *Johnson* noise, or thermal fluctuations, caused by series resistance such as poor electrical contact to the silicon.

These contributions to the noise, intrinsic to the detector, are usually small compared to the contribution from the read-out electronics. The signal must be amplified so that it is of sufficient magnitude to be registered by the data acquisition system. Since the signal deposited in silicon detectors is rather small (about 6 fC in the NA14 detectors), and has no intrinsic amplification, the amplification required of the read-out electronics is generally large. For the first stage of amplification, the contribution to the noise increases with increasing capacitance at the input of the amplifier. The amplification is therefore usually arranged to be a two stage process, with a preamplifier for each channel situated as close as possible to the detector, to reduce the capacitance provided by the connecting cables. The amplification from the preamplifier is sufficient for signals to travel a considerable distance to the main shaping amplifier, which need not then be close to the detector.

4.2 Detector fabrication

The creation of diode strips on wafers of silicon crystal, for use in high energy physics experiments, is a relatively recent development. The techniques used for the fabrication of these detectors have been adapted from the standard procedures used for integrated circuit construction. The general methods recounted here apply to both of the silicon strip devices in NA14, as well as others used elsewhere; the specific details are from the process used to fabricate the microstrip detector diodes.

The procedure utilises 'planar' technology [81], which involves the following steps. First a slice is cut from a doped silicon ingot. Its surface is *passivated* with a layer of silicon oxide, which is then etched using a technique of *photolithography* to reveal strips of silicon. These are then strongly doped with the opposite polarity to the bulk of the silicon.

The silicon wafers used for the microstrips were 500 μm thick, with a resistivity of 7500 Ω cm. They were doped n-type using a phosphorus additive at a concentration of about 10^{12} atoms/cm^3. One side was polished, becoming the front surface, and the other etched, and then *gettered*. This is a technique for the removal from the silicon of impurities, and of faults such as dislocations in the crystal structure that would form trapping centres. It is achieved by spraying the back surface of the wafer with 25 μm aluminium oxide particles, using a compressed air gun. The wafers were then heated to 1030 °C and exposed to a stream of oxygen and water vapour, which produces a uniform and pure layer of silicon oxide (SiO_2) on their surface, to a depth of 800 nm.

The strips were then etched using photolithography. Insoluble photoresist is applied to the surface of the wafer, and a mask defining the diode strip pattern is aligned with the

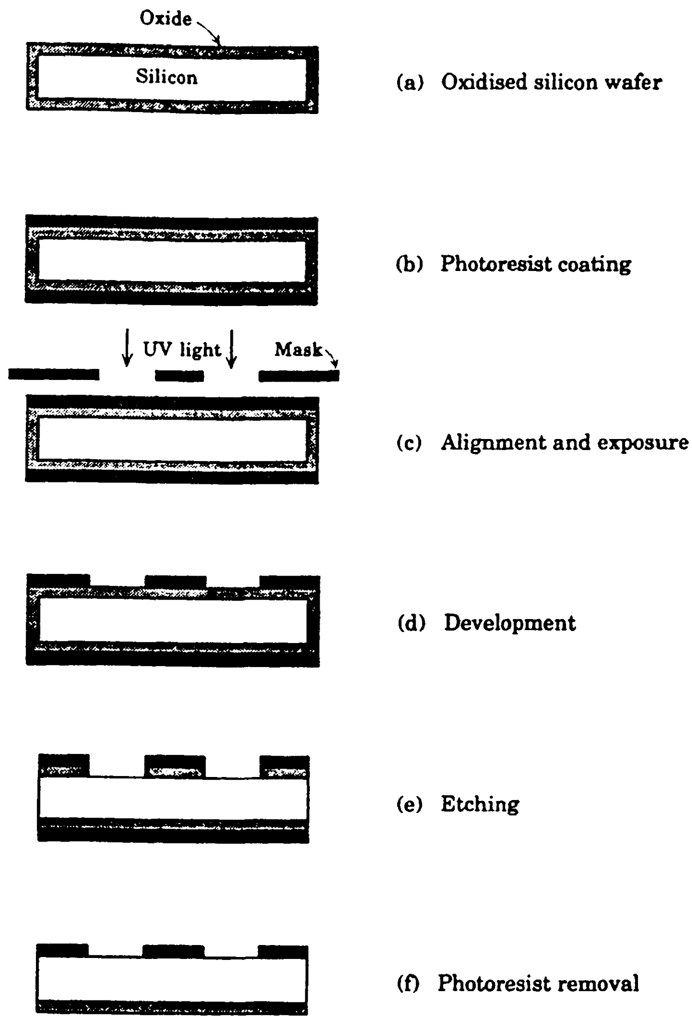

Figure 4.3 *Photolithography*

surface. It is then illuminated with ultraviolet light, which causes the exposed photoresist to become soluble, so that it may be removed by the application of a developing solution. This exposes the surface of the oxide layer, which is etched away with hydrofluoric acid to reveal the underlying silicon. Nitric acid is then used to remove the remaining, unexposed, photoresist. The steps of this process are illustrated in Figure 4.3.

The exposed strips must next be doped by the introduction of a p-type additive. For the NA14 detectors this is achieved using the technique of *ion implantation*. The wafers are irradiated with boron ions from an accelerator at an energy of 20 keV, using a dose of about 5×10^{14} cm^{-2}. The ions have a mean range of about 70 nm, and produce a junction depth (defined as the depth for equal concentration of n-type and p-type dopants) of about

250 nm. The back surface of the wafers is also ion implanted, with 60 keV arsenic ions at a dose of 5×10^{15} cm^{-2}, to produce a more heavily n-type doped layer (known as n^+) that gives good electrical contact. The ion implantation damages the crystal structure, so the wafers are annealed at 900 °C to remove the imperfections.

The electrical contacts to the front and back surfaces must next be made. A thin film of aluminium is deposited on both surfaces by electron beam evaporation. Photolithography is then used on the front surface to remove the unwanted metal from the oxide surrounding the strips. The negative of the original mask is used, and aligned to the strips to within 1 μm; slight over-etching ensures that the metal remains only on the silicon surface. Finally the completed planes are cut to size.

II The Active Target

4.3 Description

The active target [82] is constructed from 32 planes of silicon, each with an active area of 5·03 × 4·40 cm and 300 μm thick. The general lay-out was illustrated in Figure 3.17; the target may also be seen in a scale drawing of the vertex detector, Figure 4.4. The planes are separated by 512 μm along the beam axis, and are divided into parallel diode strips that act as particle detector elements as described in Section 3.8. The strips are 2 mm wide, with a pitch of 2·1 mm. For the first 30 planes there are 24 strips, and they are oriented vertically to provide measurement of the y-coordinate of tracks—they are known as Y-planes. The last two planes have 21 horizontally oriented strips (which measure the z-coordinate) and are known as Z-planes; they are used in the experimental trigger.

The dimensions of the target were imposed by the beam spot size, and are such that 90 % of beam photons are incident upon it. Apart from its obvious use for tracking, the segmentation is required for flux considerations, to reduce the signal rate in each channel to a level that can be handled by the read-out electronics (~ 2×10^6 s^{-1}). The material in the target constitutes about 10 % of a radiation length, and 3·2 % of a nuclear interaction length.

Each of the diode strips has analogue read-out, providing a direct measure of the

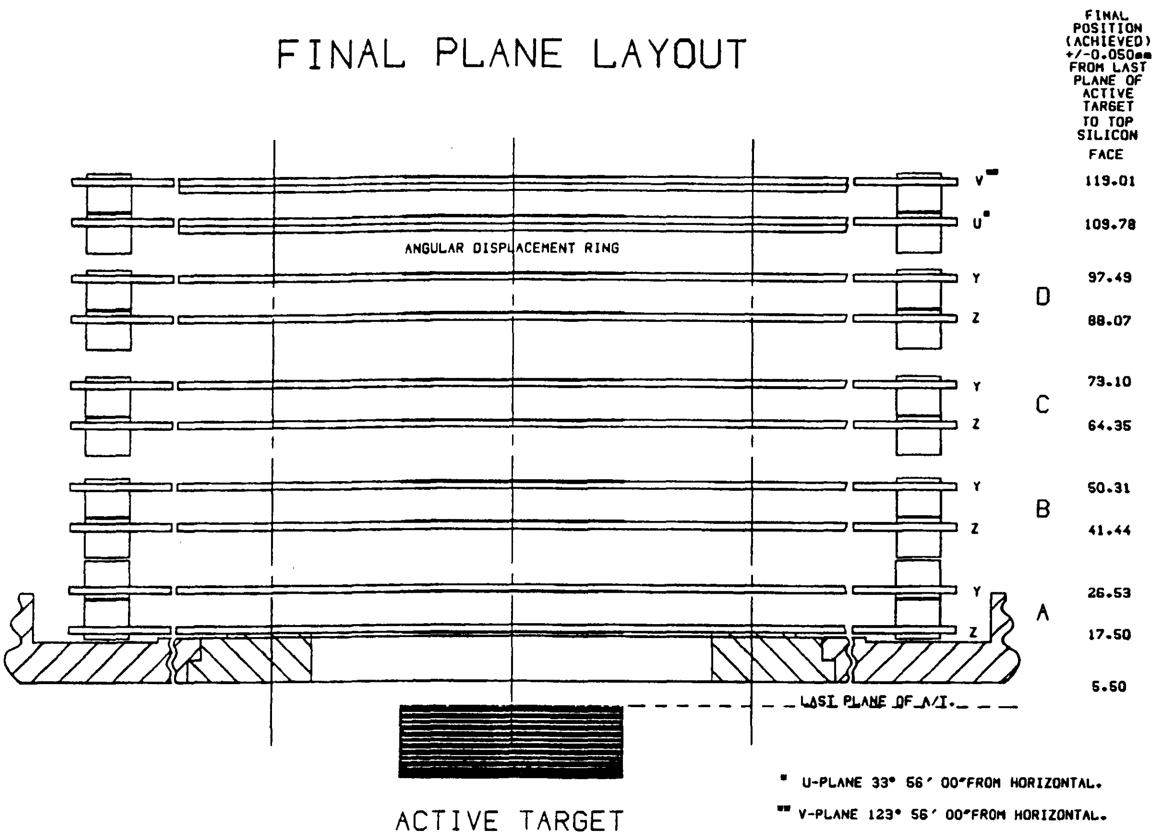

Figure 4.4 *The vertex detector (scale drawing)*

ionisation deposited in it. The strip width is such that the high energy products of a hadronic interaction in the target are typically contained within one or two strip widths throughout the length of the target. The particles will be approximately minimum ionising, so each deposits a similar amount of charge in traversing a strip, and the analogue read-out of the target thus permits a measure of the charged particle multiplicity. This is illustrated in Figure 4.5 where the pulse heights in the Y-strips of the target are displayed for a typical event, in units of I_{min}. The rectangle shown is the outline of the target, and the scale is marked in cm. The row of strips which show activity lie downstream from the production vertex, and are known as the *main road.* For clean events of this type the production vertex is easily localised—it lies in the first strip of the main road (circled in the figure). Note the high pulse height in the first strip, caused by the highly ionising nuclear recoil, which further aids in the determination of the production vertex position. Since the plane thickness is 300 μm, the x-coordinate of the vertex may be determined to within ± 150 μm.

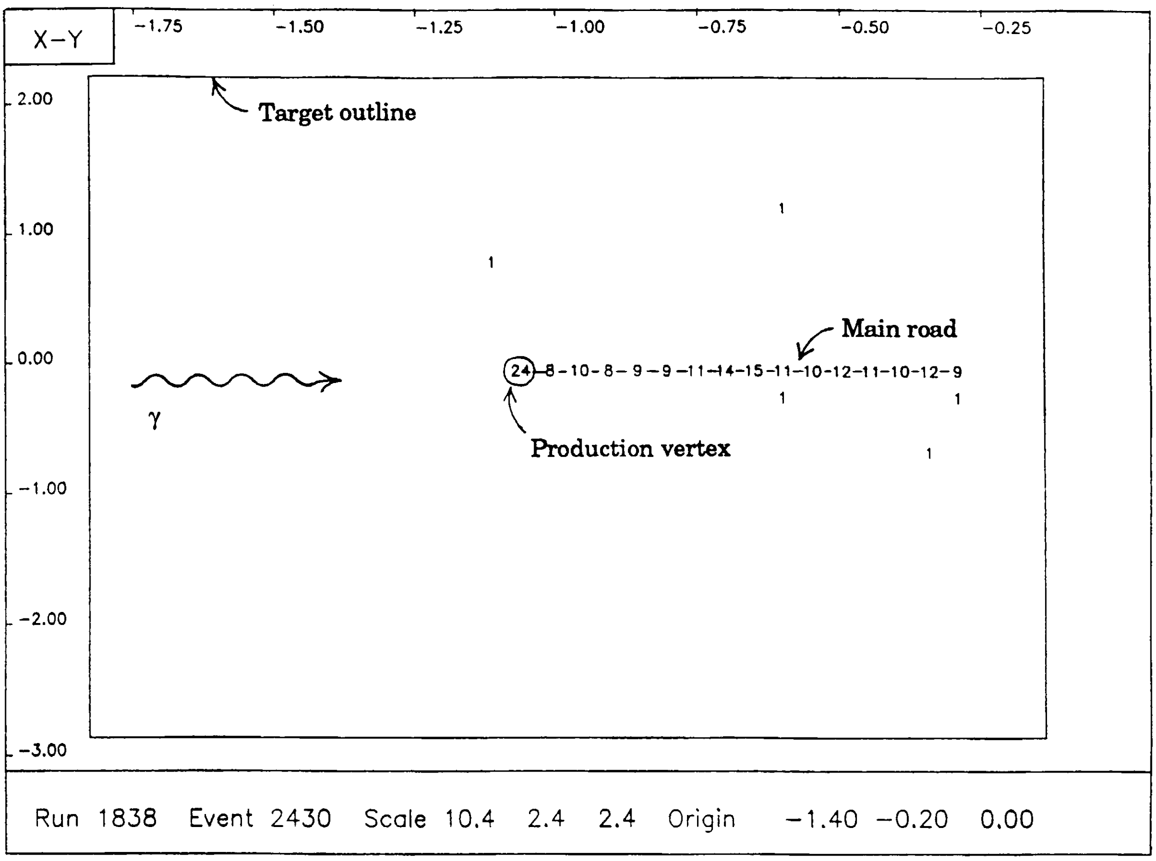

***Figure 4.5** A clean active target event*

A more complex event is shown in Figure 4.6. This is an example of an incoherent event, where there has been nuclear break-up, giving rise to grey tracks (indicated with lines in the figure, to guide the eye). They complicate the pattern recognition, but may be used to great effect in further localising the production vertex: the ionisation in the strips along the length of the grey tracks supply enough information for the tracks to be accurately reconstructed, and their wide angle gives precise information about the x-coordinate of the vertex.

It was originally intended that a study of the evolution of the charged particle multiplicity along the length of the main road would allow the detection of secondary, decay vertices. As shown schematically in Figure 4.7 (a), the decay of a particle to charged products will give an increase in multiplicity. Secondary vertices may therefore be detected by searching for a multiplicity step; this provided the basis for a fast filter to enrich the charm content of the data, as will be described in Chapter 6. A charm decay

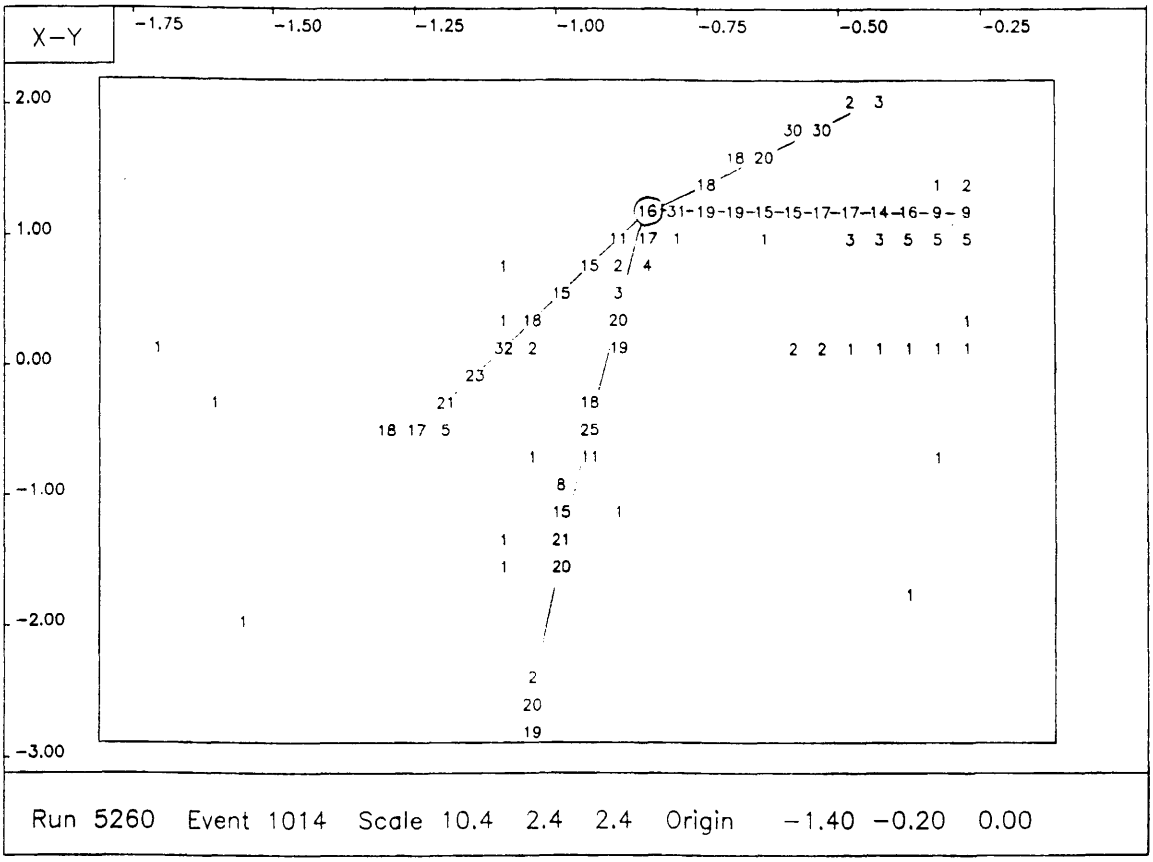

Figure 4.6 *An active target event with nuclear break-up*

found in this manner is shown in Figure 4.7 (b). Due to the fluctuations in the ionisation it is necessary to average the measured multiplicity over a number of strips, typically four. It was found that, even so, the technique was difficult—due mainly to photon conversion in the target simulating a secondary vertex. The photons come from both π^0 decay, and double bremsstrahlung, as mentioned in Section 3.3.

The target is also useful for the rejection of hadronic *secondary interactions* which might simulate a decay, i.e. where a particle from the production vertex has re-interacted in the target. These events may be recognised by a simple algorithm, described in Section 8.4. Finally the target information is used in the trigger, to enrich the data sample in hadronic interactions of photons, as described in Section 5.10.

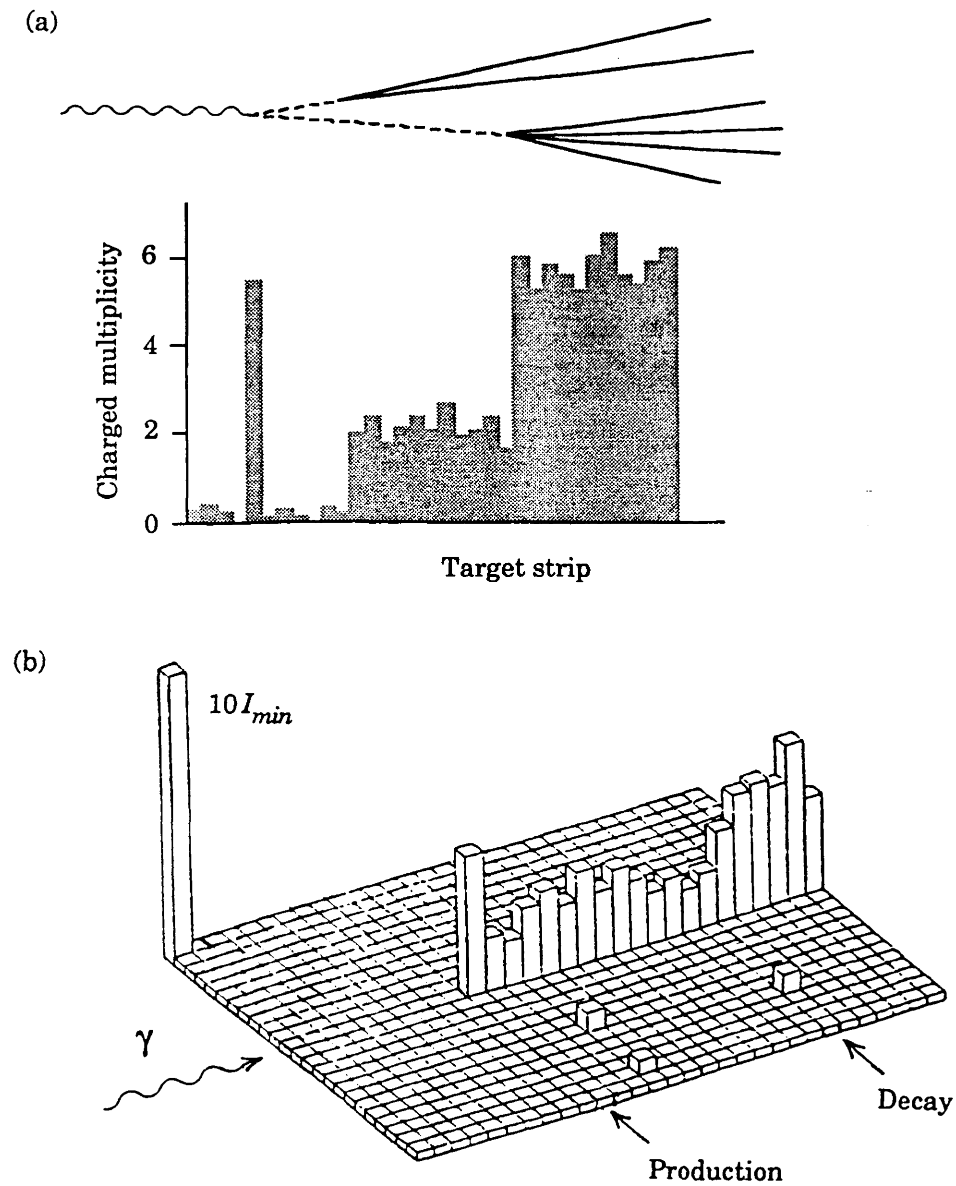

Figure 4.7 *Vertex detection with the active target*

4.4 Construction

The diodes of the target planes were fabricated by Enertec Schlumberger. The silicon planes are mounted on epoxy boards from which flexible fan-outs connect the signals to preamplifiers. A plane is shown in Figure 4.8, and the assembled detector can be seen in Figure 4.9. From the preamplifiers the signals travel about 90 m along twisted pair cables to line receivers, and are then read by charge-sensitive analogue-to-digital converters (ADCs) of the type LeCroy 2282.

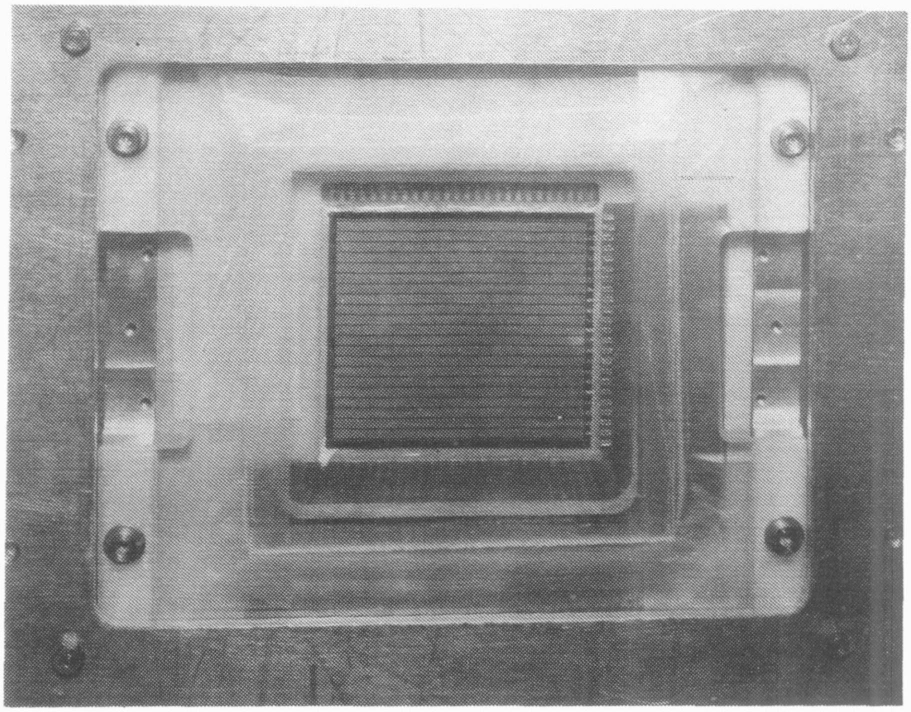

Figure 4.8 *An active target plane*

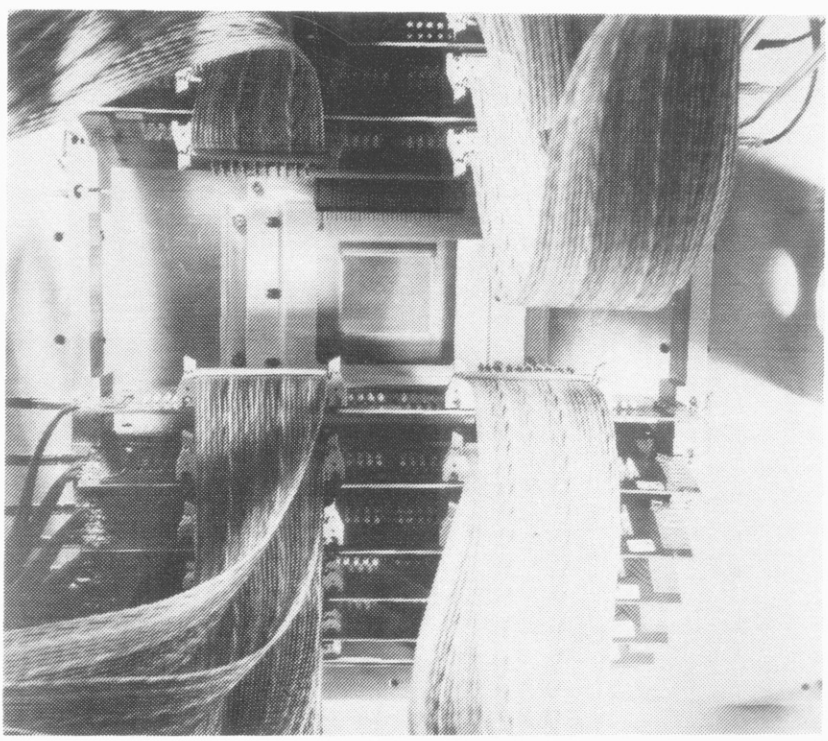

Figure 4.9 *The complete active target*

A minimum ionising particle traversing 300 μm of silicon deposits about 84 keV of energy, which compares well with the typical noise of $\sigma \sim 17$ keV for the read-out electronics. Leakage currents were about 54 nA per strip, giving a negligible contribution to the noise.

III The Microstrip Detector

4.5 Description

The microstrip detector [83] consists of 10 planes of silicon of dimensions 5 cm × 5 cm, and 450 μm thick. Each plane is divided into 1000 diode strips, with a 50 μm pitch, giving a total of 10,000 channels to be read out. The individual planes only provide two coordinates of a track passing through them: the x-coordinate of the plane, and a transverse coordinate from the position of the strip that is hit. The planes are therefore arranged in pairs, with the strips on the members of each pair orthogonal. A series of such pairs of planes will then give a *projection* of the track in both orthogonal views. However, when there is more than one track, the association of the track projections to form tracks in space is ambiguous. For this reason a third projection is required.

These considerations were satisfied for the microstrip chamber by the arrangement shown in Figure 4.4: the first four pairs of planes with their strips oriented horizontally and vertically, as (Z, Y) pairs, and the final pair (known as the U- and V-planes) rotated through approximately 33° about the beam axis. This scheme provides *redundancy* in both of the orthogonal views, and in the matching of the views. For example, tracks are straight lines in the Z-projection, and so could be specified by two points. However, if there is more than one track, the recognition of tracks using only two points would obviously become rather confused. Four point tracks, on the other hand, are much more likely to be real, so the system benefits from the extra information.

The area of the planes was the maximum that could be achieved with currently available 3 inch silicon wafers, and provides an acceptance of ± 250 mrad, which closely matches the acceptance of the AEG magnet in which the detector is situated. The use of the same plane design for all of the planes simplifies the construction of the detector, and is necessary due to the large spot size of the photon beam, which prevented a reduction in the size of the upstream planes. The strip width was chosen as the result of a Monte Carlo simulation which indicated that the resolution would be sufficient to recognise charmed particle decays. Monte Carlo studies were also used to choose the optimum positioning of the planes along the beam axis [84]. The main results of this work were that the first planes in each projection should be as close as possible to the target to give precision for the vertex reconstruction, and that otherwise the planes should be evenly spaced, with an overall length of 10 cm. If the length of the detector were increased then the acceptance would be reduced, and the reconstruction of tracks in the Y-projection (the bend plane of the magnetic field) would be more difficult at the filter level—since at this level the momentum is not known, so the tracks are approximated as straight lines. These considerations must be balanced against the corresponding increase in the lever arm for track reconstruction, which improves the accuracy at the vertex.

The microstrip detector is designed to give a high resolution for track finding close to the vertex. It therefore helps in the accurate reconstruction of events by the combination of its information with that from the rest of the spectrometer. It was also used to provide a fast filter for charmed events, by the recognition of tracks that are offset from the production vertex.

4.6 Construction

Silicon mounting

The silicon planes were fabricated by Micron Semiconductor (UK) Ltd, as described in Section 4.2. The signals from the diodes at a 50 μm pitch must be distributed or *fanned out* to the read-out electronics for each channel. A serious constraint for this is that the detector sits inside the AEG magnet, so the available space is limited by the AEG aperture. This also has the consequence that all materials used must be non-magnetic. The fanning out is achieved using conductive tracks on the surface of a fibreglass Printed Circuit Board (PCB) of standard 1·6 mm thickness. Each silicon plane is mounted in a 5 cm × 5 cm hole in the centre of a PCB, and is glued in position using epoxy. The diode strips are connected to fine tracks on the front face of the PCB by ultrasonically attached 25 μm aluminium wire bonds; these may be seen in Figure 4.10, which shows a magnified view of the edge of a microstrip plane. Consecutive strips on the silicon are connected on alternate sides of the plane, resulting in a bond separation of 100 μm. The tracks on the PCB were fabricated by Cicorel (Neuchatel) using a photolithographic

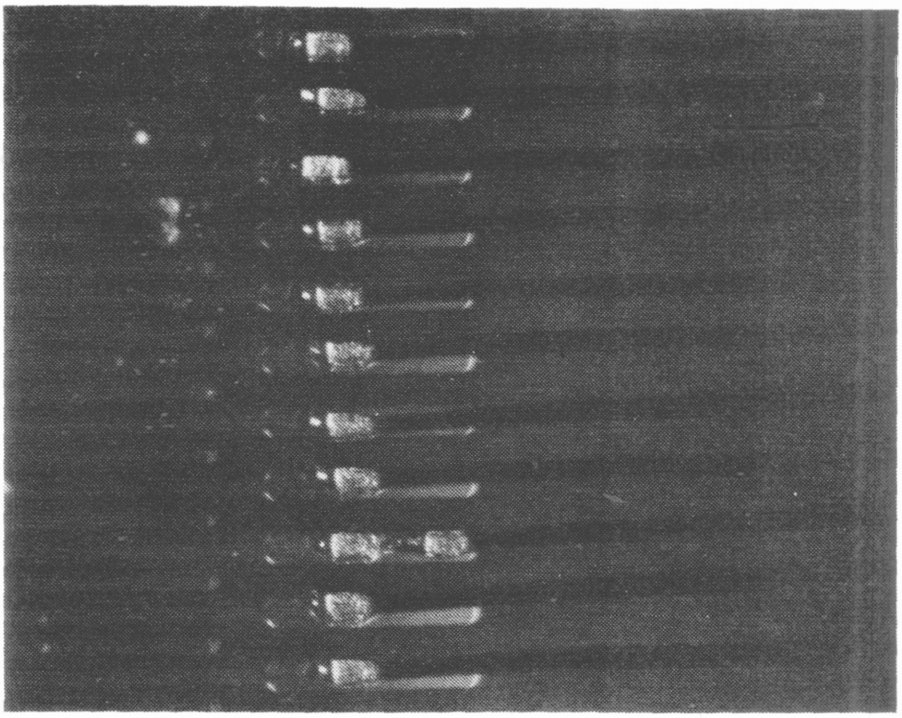

Figure 4.10 *Wire bonding to the silicon strips*

technique to etch the track pattern onto a coating of copper. The tracks were then electroplated with gold to provide a good electrical contact. They fan out from a pitch of 100 μm to 1/20 inch at the board edge, where they are soldered to commercial 50-way connectors (see Figure 4.11). The back plane of the PCB is coated with gold plated copper, and is maintained at earth potential. It is isolated from the back plane of the silicon (which is at the bias potential) by eight 4·7 nF capacitors. For the angled *U*- and *V*-planes it was not possible simply to rotate the PCB fan-outs, since they would foul the AEG pole pieces. Instead the central part of the PCB was retained, and triangular outer pieces were designed and built at Imperial College to maintain the same overall dimensions as the other boards. The inner and outer sections were glued to a fibreglass support, and their tracks connected using the same wire bonding technique as was used for the connection to the silicon.

Test pulse

The read-out system for the silicon strips is relatively complex. Even apart from the electronics involved, there are ten cable connections for every channel, each with a

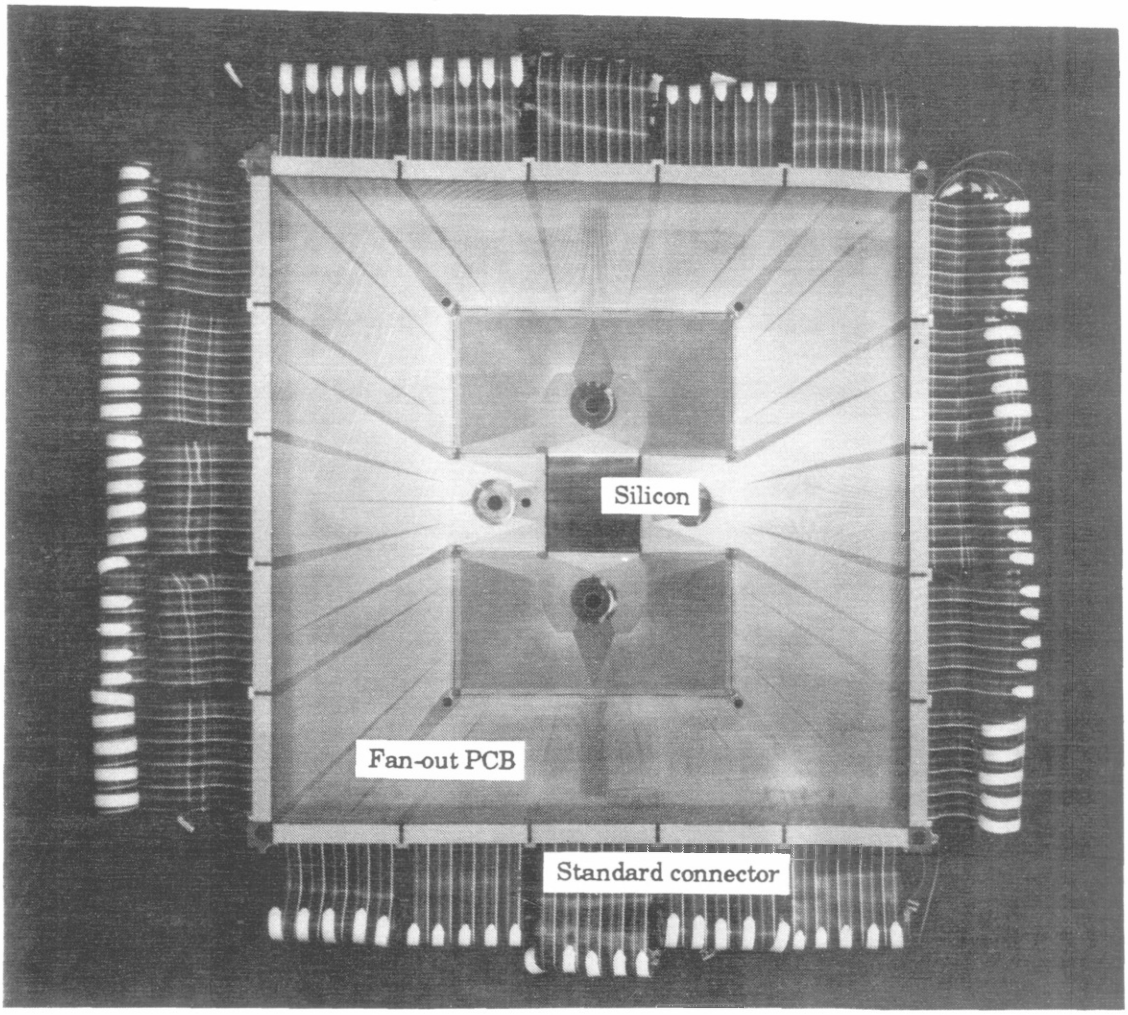

Figure 4.11 *A microstrip plane*

possibility of unsuccessful contact. It is therefore desirable to have a means of systematically testing the read-out chain, by the injection of a test signal into any chosen channel, with similar properties to a real signal. This also permits the amplifier gains and discriminator thresholds of individual channels to be checked.

The system chosen was a strip of copper laid across the fan-out tracks at each edge of the PCBs. The copper *test-strip* was 3 mm wide, and coupled capacitively to the PCB tracks, with a dielectric provided by a 100 μm thickness of Mylar (see Figure 4.12). The test pulse was implemented by the application to the test-strip of an attenuated NIM pulse (a negative going square pulse of standard 750 mV amplitude). The attenuation was such that the signal produced at the preamplifier input corresponded to the signal from a

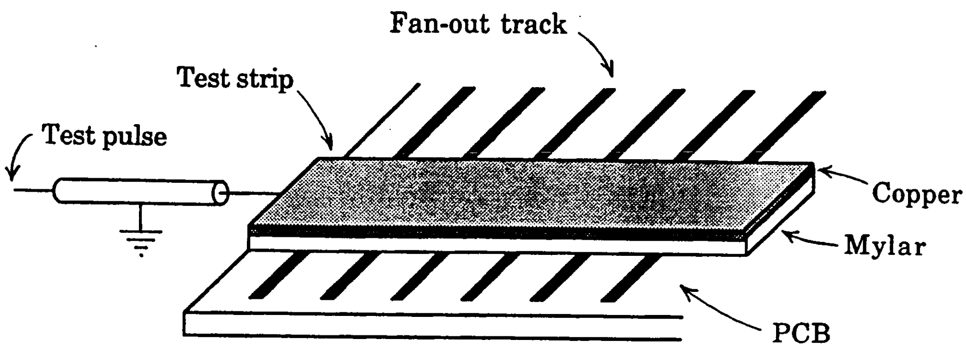

Figure 4.12 *Test pulse arrangement (schematic)*

minimum ionising particle. As the strips each covered one edge of a PCB, they each provided a test pulse for 250 channels, so a total of 40 strips were required.

Mechanical construction

The use of the microstrip detector for high precision tracking means that the relative alignment of the planes must be known to an accuracy of a few microns, and must be stable. The stability was achieved by mounting the PCBs on a stress-relieved 20 mm thick aluminium plate, to which the active target was also attached. The PCBs were supported by four 6 mm diameter stainless steel studs, which were threaded into a titanium block that was recessed into the aluminium plate. Titanium was used as it has a similar thermal expansion coefficient to the PCBs. The accurate assembly of the microstrip planes was achieved by the use of a high precision jig boring machine with attached microscope. The main plate was mounted on the travelling bed of the jig borer and the alignment of the strips to the direction of movement of the bed was observed using the microscope. The PCBs were attached to the studs with eccentric bushes, which could then be rotated to align the plane. This gave alignment of better than 3 μm over the 50 mm strip length, providing a high precision for the orthogonality and parallelism of the planes. Figure 4.13 shows the half assembled detector as the process of alignment was nearing completion. The relative displacement of strips from different planes was not measured at this stage, but was instead found from the reconstruction of particle tracks. To ensure that the first plane of each projection was as close as possible to the target, the first two planes were mounted 'face down', with the diode strips on the upstream side of the plane. This required the transfer of the strip orientation to the back face of the PCB as a cross hair mark, to permit the alignment. The U- and V-plane rotation was defined by an

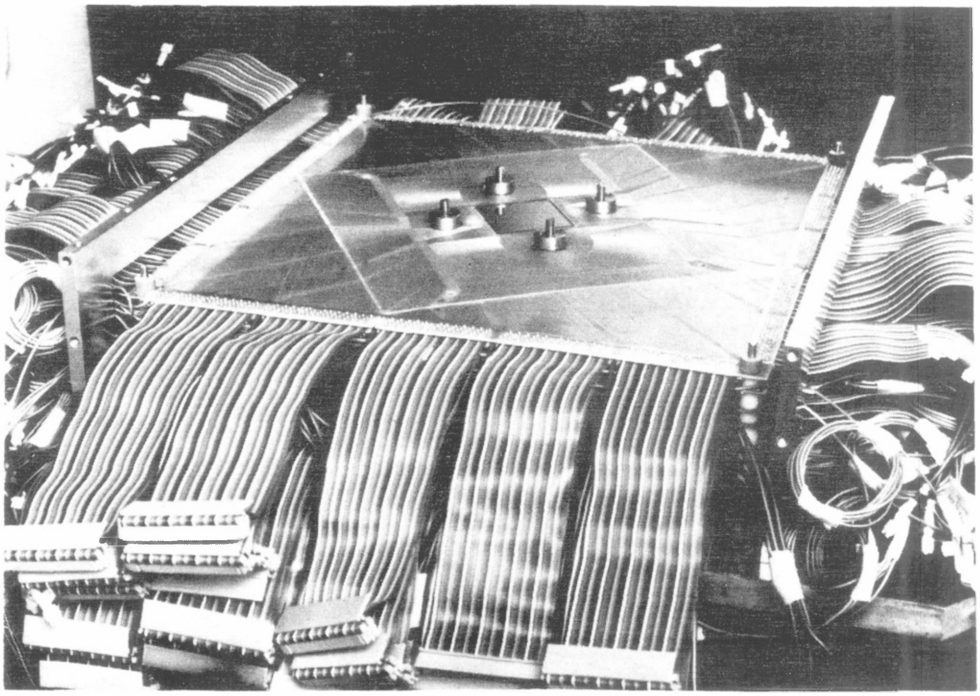

Figure 4.13 The microstrip detector during construction

angular displacement ring, that mounted on the studs and provided new, rotated, studs for the attachment of the planes.

The main plate was mounted on a wheeled *chariot*, which permitted the movement of the detector out from its inaccessible position inside the AEG magnet, for checks on the read-out cabling etc. Whilst data taking was in progress the chariot was locked in the correct position.

4.7 Read-out electronics

The signals from the silicon are fanned out along the tracks of the PCBs, and are then transmitted via 50-way cables to the preamplifiers. After the preamplification, the signals are further amplified, shaped and discriminated. This produces a digital output: a 'hit' if the signal is greater than the discrimination threshold, no hit if not. The choice of a digital rather than analogue read-out system was motivated by cost, bearing in mind the large number of channels.

The digital signals must then be fed into the data acquisition system, which

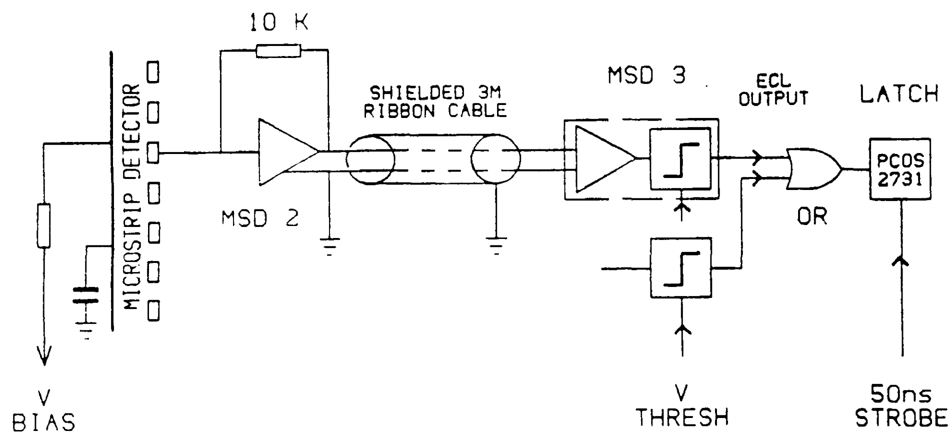

Figure 4.14 *Read-out chain for the microstrip detector*

interfaces them to the data-taking computer so that they may be recorded. The data acquisition system was the most expensive part of the detector system per channel, and financial constraints prevented the instrumentation of the full 10,000 channels. Instead, an OR-gate system was devised that permitted each channel of the data acquisition system to read two of the silicon strips. The total number of data acquistion channels required was thereby reduced by a factor of two. The read-out chain is illustrated in Figure 4.14.

Preamplifier

A minimum ionising particle passing through the 450 µm thickness of silicon of a microstrip detector plane deposits on average 130 keV of energy. Since it requires 3·6 eV to produce an electron-hole pair, this corresponds to a deposition of about 36,000 electrons' charge. The noise of the system must be sufficiently small that this signal may be detected. Since an incident particle may pass through two strips, the signal-to-noise ratio must be high enough to allow the discriminator threshold to be set at less than 50 % of the signal from a minimum ionising particle. The preamplifier must therefore have an equivalent noise charge less than ~ 2500 electrons.

The need to minimise the input capacitance requires the preamplifiers to be as close as possible to the detector. This results in a high packing density for the preamplifier channels, exacerbated by the large number of channels and the limited available space. The preamplifiers must therefore have low power consumption to avoid problems of heat

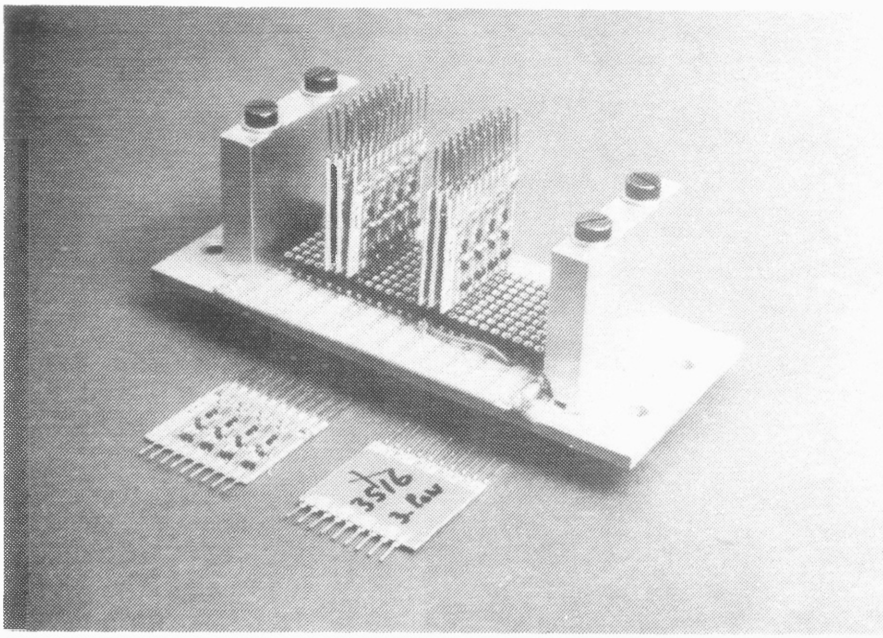

Figure 4.15 *Preamplifier hybrids in a miniblock*

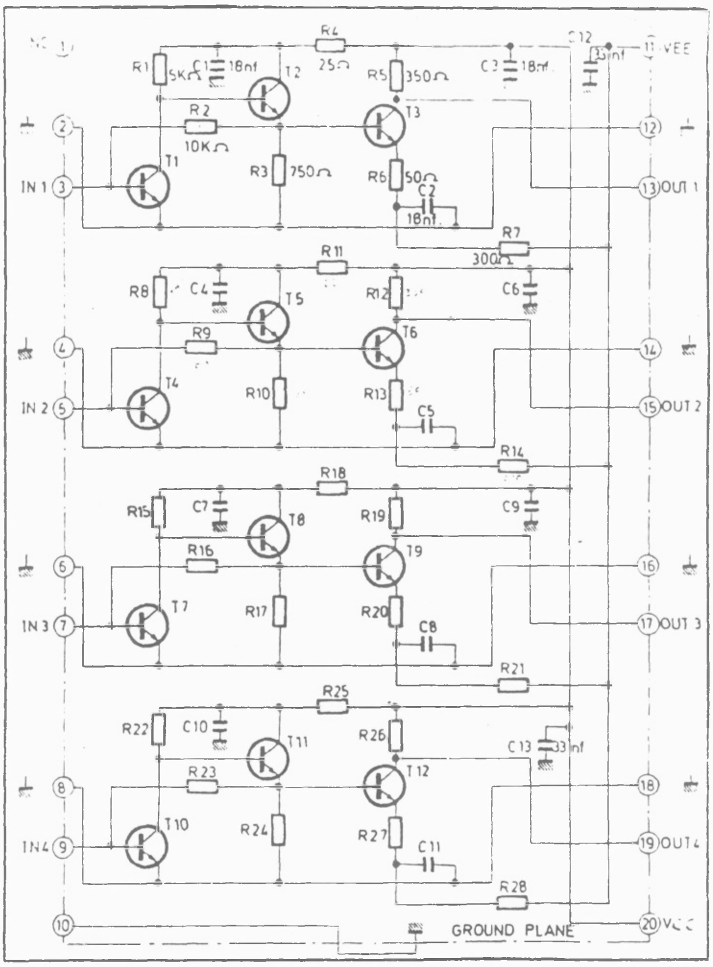

Figure 4.16 *MSD2 circuit diagram*

dissipation. Finally the high rate of electromagnetic background processes associated with the photon beam requires that the preamplifiers must have a fast shaping time, less than about 50 ns. These criteria were met by the *MSD2*, designed at CERN [85] and supplied by Laben (Milan). It is of *hybrid* construction, a combination of miniature active components and thick-film passive components, mounted on a 1 inch × 1 inch ceramic tile that carries four channels (see Figure 4.15). The MSD2s are current sensitive amplifiers, with a current gain of ~ 200, and hybrids were selected with gain within 10 % of the sample mean. They have a rise time of ~ 10 ns and a shaping time of ~ 15 ns; the circuit diagram is shown in Figure 4.16. Their low power consumption of about 20 mW/channel permits them to be closely packed, separated by 0·1 inch, suitable for standard connectors. They were grouped together to form 'miniblocks', consisting of 25 hybrids, arranged to accept two input 50-way cables. The 100 miniblocks necessary to supply 10,000 channels were arranged in groups of 25 to form four 'maxiblocks', each taking the channels from one side of the detector. A maxiblock is shown in Figure 4.17. They were mounted on the detector chariot to minimise the cable length to the preamplifier inputs—20 cm of ribbon cable was required. The detector with maxiblocks attached may be seen in Figure 4.18.

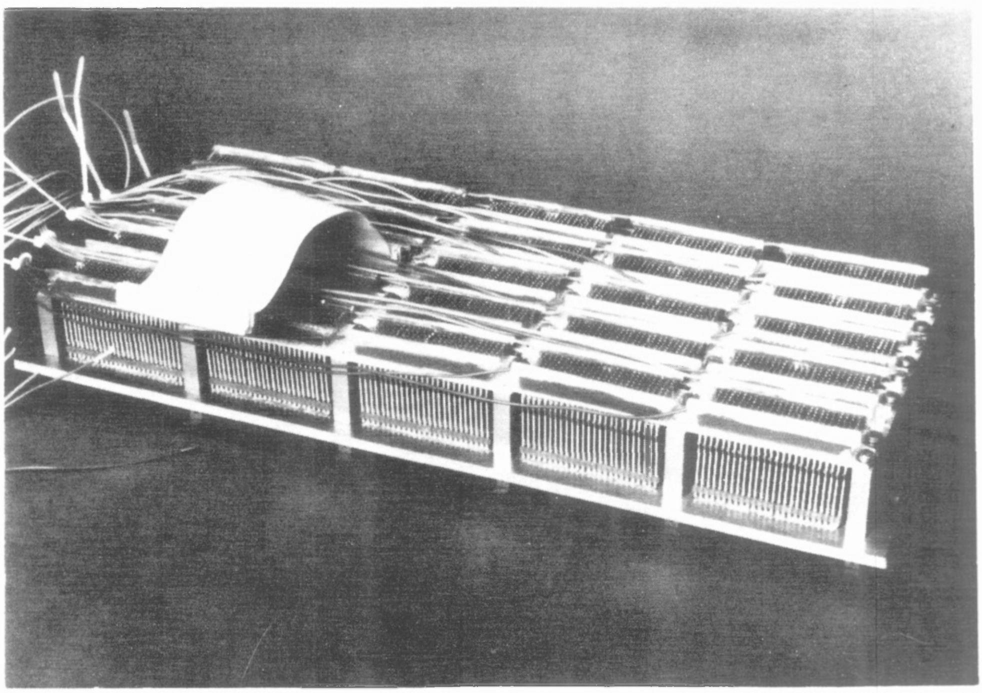

Figure 4.17 *A maxiblock of preamplifiers*

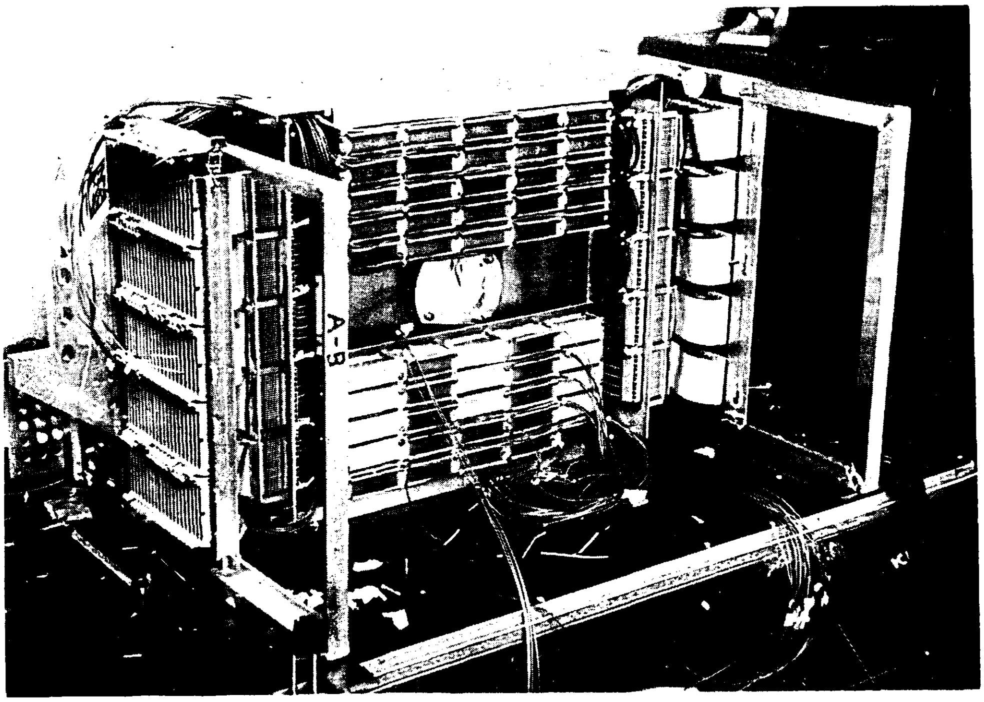

Figure 4.18 *The microstrip detector nearing completion*

Amplifier / discriminator

The limited space close to the detector required the next stage in the read-out chain, the amplifier/discriminator, to be situated at some distance from the preamplifiers. A short length of 50-way cable joined the preamplifier outputs to a bulkhead connector, where the signals were transferred to a further 3 m length of 50-way cable connected to the main amplifiers. This arrangement provided both strain relief and a common ground for the long cables, each of which carried 25 signals and their grounds. The cables were individually wrapped in aluminium foil to provide screening from electrical pick-up.

The amplifier/discriminator was designed at CERN [86] for use in conjunction with the MSD2, and is known as the *MSD3*. It is also of hybrid construction, shown in Figure 4.19, with a voltage gain of ~ 40; the circuit diagram is given in Figure 4.20. Each hybrid has four channels, so they were mounted on boards in groups of 13, to give 50 channels per board (with 2 channels unused). There were therefore two input cables per board, and two output cables. The hybrids on each board were selected to have uniform gain and offset voltage, so that they could all be supplied with the same discriminator threshold.

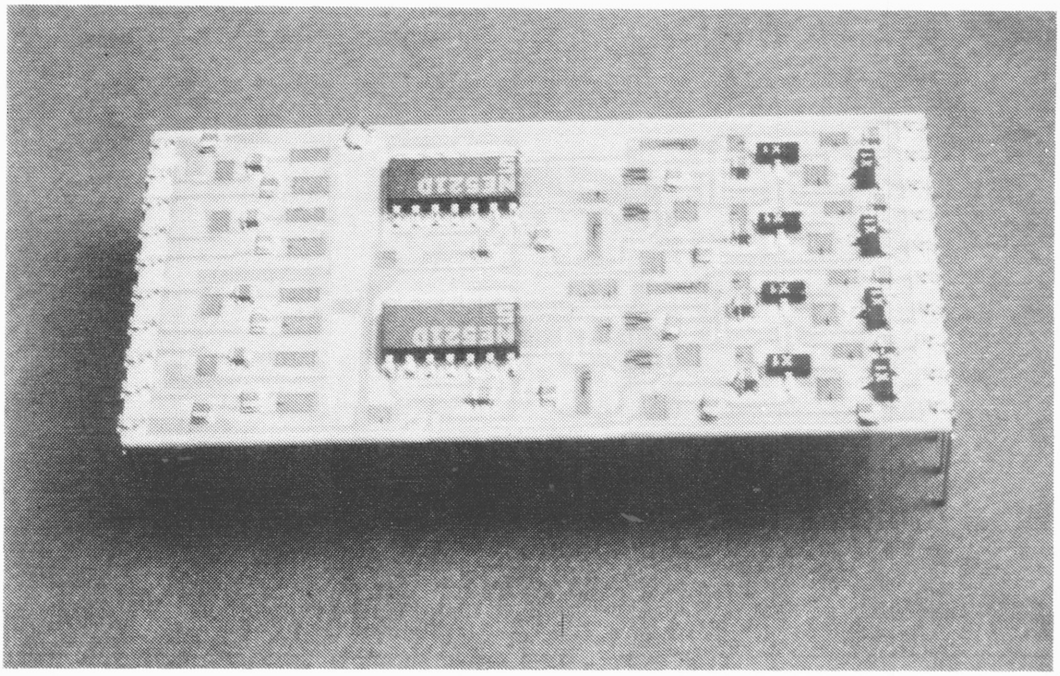

Figure 4.19 *An amplifier / discriminator hybrid*

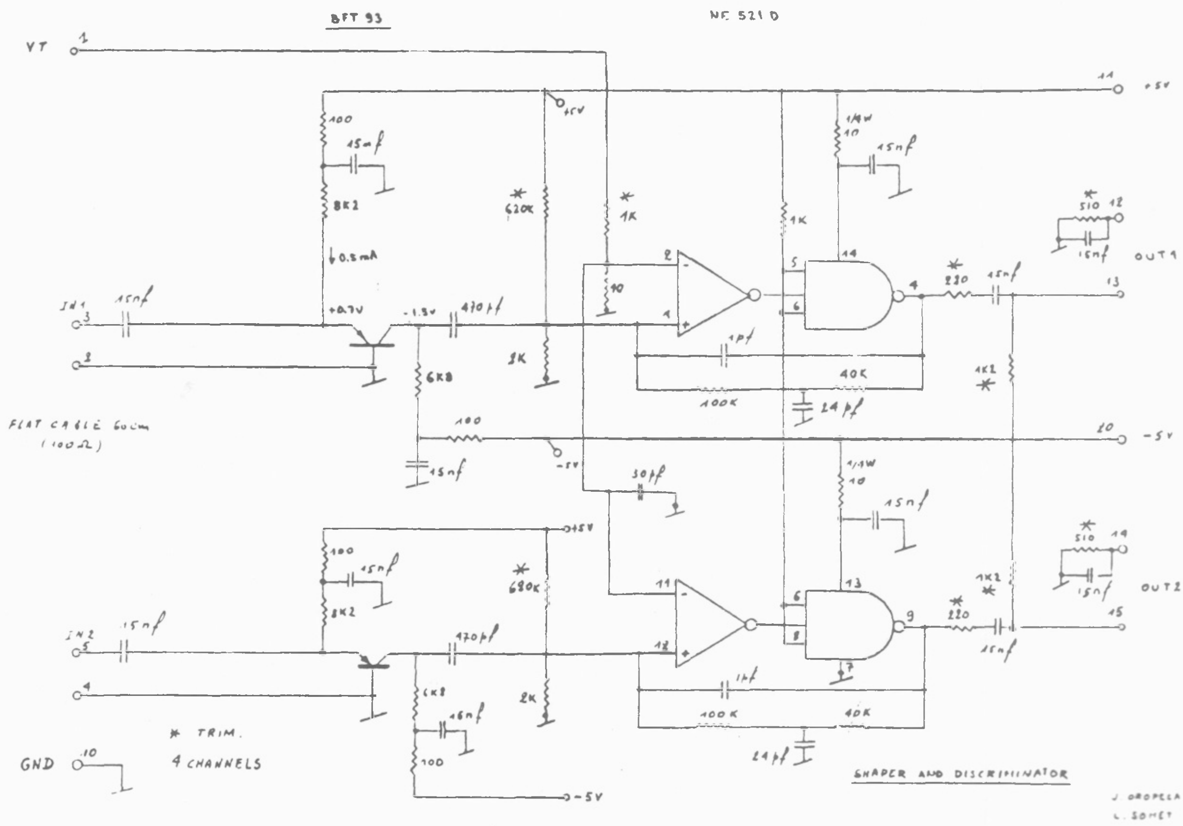

Figure 4.20 *MSD3 circuit diagram*

The digital discriminator output must be suitable for input to the data acquisition system. The system used required *ECL* inputs. ECL (Emitter-Coupled Logic) is one of the standards for logic signals in electronics, with 'high' and 'low' voltage levels of about -0.8 V and -1.6 V respectively. The voltage levels of the output from the MSD3s were changed to balanced ECL by additional circuitry mounted on the boards.

OR-gate

The digital signals were passed from the MSD3s to another set of electronics boards, performing the *OR*-gating. For each pair of input channels, the logical *OR* of their digital signals is taken, and fed into a single output channel. The effect of the *OR*-gate is that for every real hit, an 'image' hit is produced, elsewhere in the detector. There is clearly a danger that these image hits might confuse the track finding programs, and result in the reconstruction of nonexistent (*'ghost'*) tracks. The decision of which channels to pair was made using a Monte Carlo simulation [78], and the scheme chosen was the one that minimised the production of ghost tracks: this involved the *OR*-ing of channels from different regions of the orthogonal planes.

The *OR*-gate boards were purpose-built at the Saclay institute. Each board takes four input 50-way cables (100 channels) and provides three 34-way output cables each carrying 16 channels (giving a total of 48 channels), suitable for the data acquisition system. The remaining two channels per board were collected together to make up further cables.

Data acquistion system

The data acquistion system serves as an interface between the signal processing electronics and the on-line computer. It has various tasks. The channels from the detector must be *multiplexed*, since the system has 5000 parallel inputs, which must be converted into a single serial output; as the inputs are mostly empty, it is desirable that zero-suppression should be performed, to speed up the processing of the data.

A commercially available system was chosen, designed for the read-out of MWPCs: 'Proportional Chamber Operating System' (PCOS III) manufactured by LeCroy. It is a modular system, consisting of crate mounted units, under the control of *CAMAC* (Computer Automated Measurement and Control)—an international standard for modular systems of data processing that specifies a standard data highway for the communication of modules and the connection to an on-line computer, and also sets out mechanical and electrical specifications [87].

The PCOS III system consists of three different types of module, shown in Figure 4.21 (photographically in (a) and schematically in (b)). Firstly there is a delay and latch module designated the 2731. Each 2731 module accepts 32 input channels (and their grounds) in two 34-way flat cables. The input signals are delayed by a solid-state programmable delay, which may be set for each module over the range 300–680 ns, in 1·5 ns steps. This delay is required whilst the trigger logic (described in Section 5.10) decides whether the event should be recorded. The delay is produced by the 'Ripplethru' circuit of LeCroy, which unlike earlier monostable delays does not generate a dead time equal to the delay, but instead may operate at greater than 10 MHz rates. It replaces the usual cable delays, and has the advantage of being more flexible, since the relative timing of the input signals and the trigger decision may be modified at will.

If the trigger algorithm is satisfied by the event, a *gate* is produced, a short pulse sent to the data acquisition system to initiate the reading of the event; a 70 ns gate was used. For the duration of the gate the delayed signals are *latched* by the 2731 modules, i.e. if a hit is received on a channel as an ECL 'low' from the discriminator, then the information is retained by holding the level of the channel low. This provides time for the *addresses* (i.e. locations within the system) of the hit channels to be read. The hit-channel information is stored in the latch as a 32 bit word (one bit per input channel). The 2731 modules also provide a voltage level to be used for setting the discriminator threshold. The voltage is produced by an 8-bit digital-to-analogue converter, giving an available range of 0–7·5 V under computer control. The level is sent down one of the remaining pair of wires of the 34-way input cables which do not carry a signal, and in our set-up was read at the *OR*-gate board and distributed to the MSD3s.

The latch modules are mounted in CAMAC crates. A connector at the rear of each module plugs into a corresponding socket in the crate, which provides power for the module, and connects it to the other elements of the system. Each crate has space for 25 single-width modules: 23 of these *slots* are filled by latches; the remaining two are occupied by a double-width dedicated controller known as the 2738, which controls the read-out the modules in its crate. The controller communicates with the latches by 32-bit data transfers, at 10 times the maximum rate defined by the CAMAC standard. It scans the status of the latches, and only those modules that have been hit are read out, at a speed of about 100 ns per module. The data from each latch are then encoded by the controller, to give a 16-bit address for each hit channel—the information of 'hit' or 'no hit' of all the

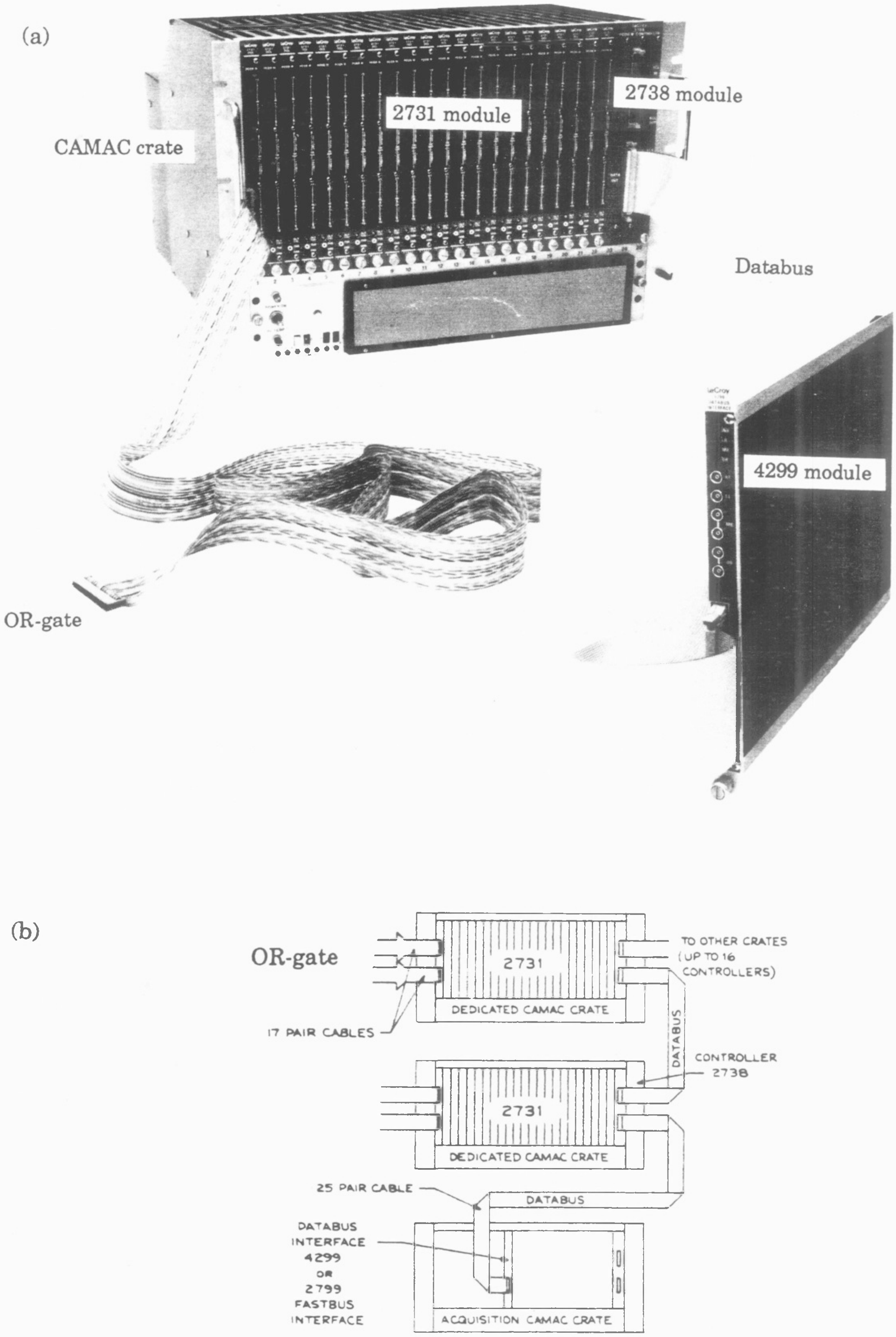

Figure 4.21 *The PCOS III data acquisition system*

inputs is thus translated into a series of unique addresses for the hit channels. The controller is *double-buffered*, allowing a second latch to be read whilst the output from the first is being encoded. The encoded addresses of the hit channels are loaded into the 1 K × 16-bit memory of the controller, ready for subsequent CAMAC read-out.

The 23 latch modules in a single crate give a total of 736 inputs. To cover the full 5000 channels of the experiment seven crates were therefore required, each with a controller; the crate controllers are read out via a 50-way 'Databus' cable which allows 16-bit parallel word transfer. The final module of the PCOS system is the LeCroy 4299 Databus interface, which occupies a single slot in a standard CAMAC crate. It has a 4 K memory, and permits the data on the Databus to be read using CAMAC commands via a standard CAMAC crate controller. The data are then passed to the on-line computer.

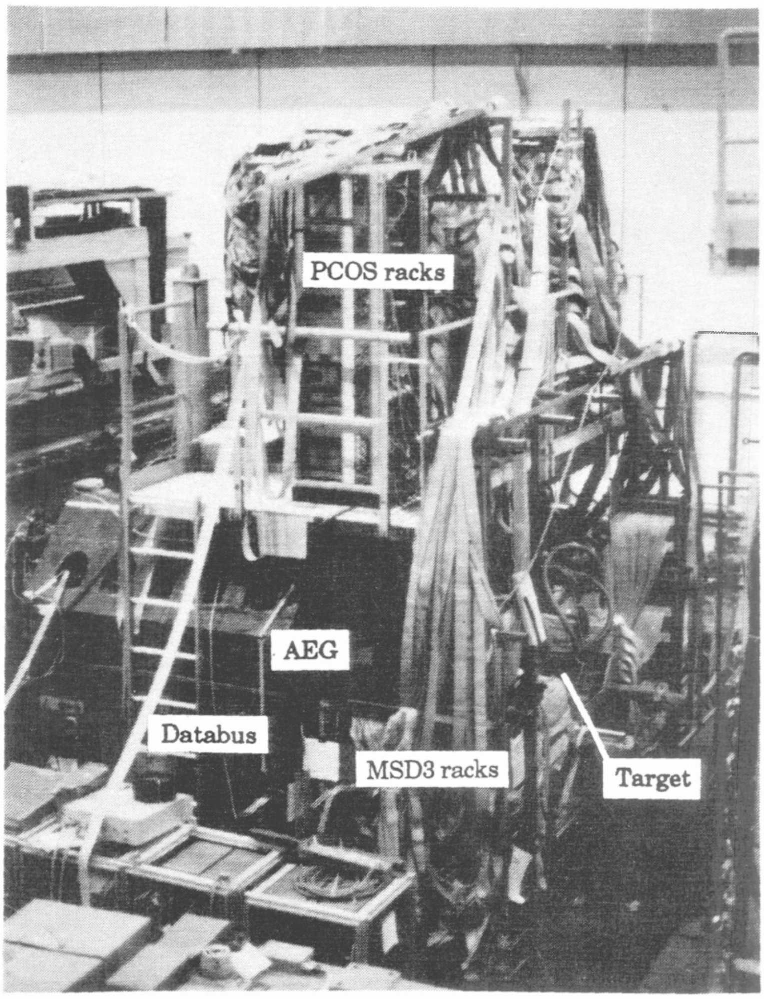

Figure 4.22 *Microstrip detector system installed*

One useful feature of the system is a facility for the down-loading of a 32-bit test pattern of choice to each latch module. The pattern is stored close to the inputs of the modules, and can be read back in a similar manner to real input signals. This facility may thus be used to perform systematic tests of the data acquisition, and proved invaluable in setting up the system.

The completely assembled microstrip detector system is shown in Figure 4.22. The detector itself lies within the magnet aperture, and is overwhelmed in volume by the associated cabling and racks of the read-out electronics.

4.8 Vertex detector display

The main features of the vertex detector may be seen in event displays, such as Figure 4.23. The Y- and Z-projections of a typical event are shown. The box to the left of each frame represents the outline of the active target, and the vertical marks within the target denote the strips for which the pulse height was greater than 1 I_{min}. Note the evidence for wide angle tracks in the Y-projection. The microstrip detector planes are shown as vertical lines to the right of the target (the beam enters from the left). Only the relevant planes of each projection are displayed, and the U- and V-planes are not shown at all. The angled marks on each plane represent the microstrip hits; the angling of the marks is purely an artifice of the display—the marks for hits on consecutive strips of a plane are progressively rotated through 90°, so that the effective resolution of the display is improved, and clusters may be more easily recognised. Underneath each plane the total number of hits is given.

The tracks that have been reconstructed for the event are displayed, and to the right of each track information is provided, giving the track index, and the particle identification (if any). At the edge of each frame is a scale, marked in cm. Note that on each of the tracks that have been found there are hits at almost all of the microstrip planes. Note also the substantial number of hits seen in the outer parts of each plane, not associated to tracks; these are due to the *OR*-gate, and are the *OR*-images of the true hits on the tracks.

The event display program will be described in Section 6.4. In the next chapter, meanwhile, the taking of data is discussed, with some specific details concerning the microstrip detector.

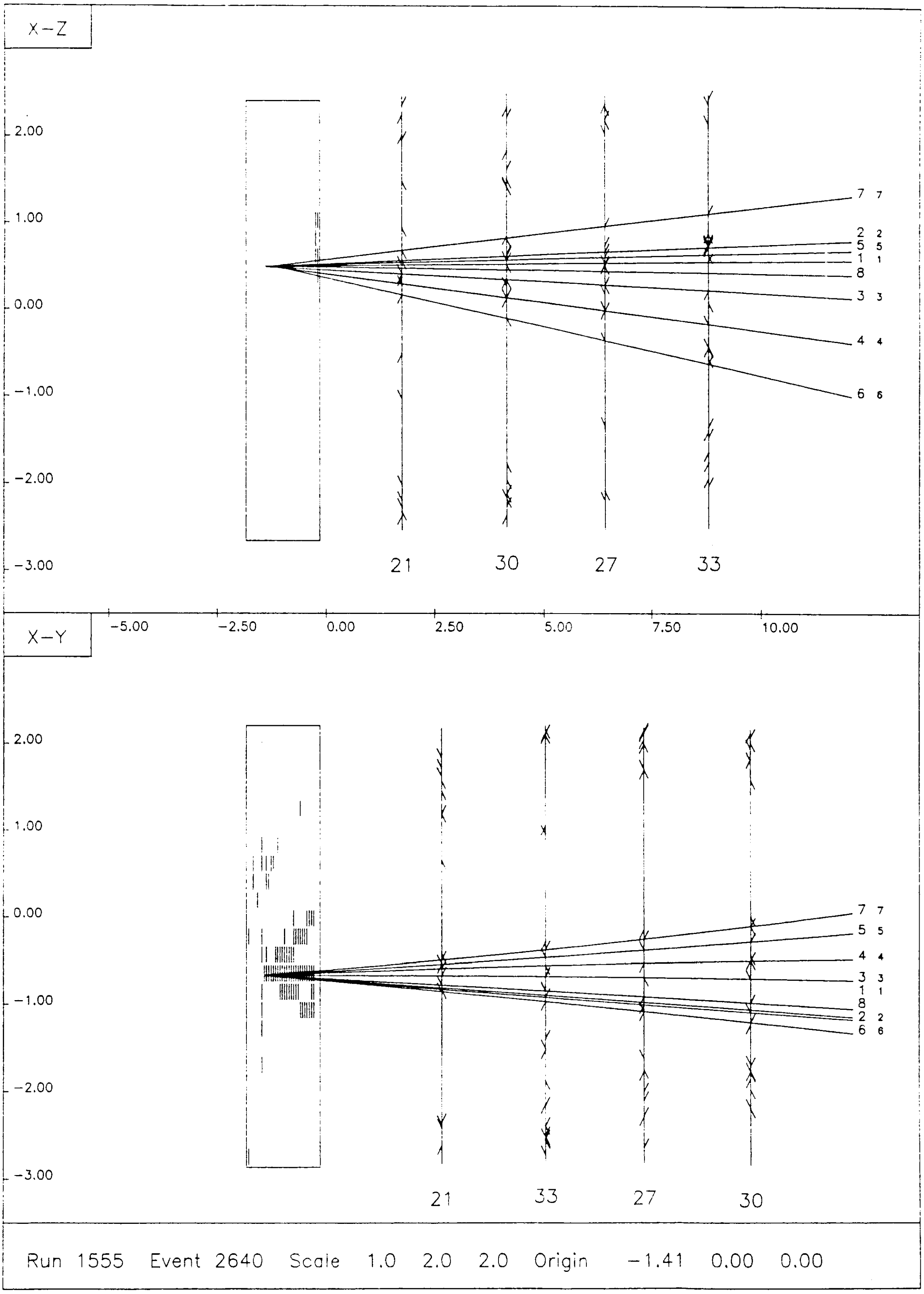

Figure 4.23 *Vertex detector event display*

Chapter 5

DATA TAKING

In this chapter, a description is given of the tests of the microstrip detector for which I was responsible, during the development and construction of the device. The preparations for the data taking are discussed, and details are given of the trigger and the data-taking periods. Finally the performance of the microstrip detector is described.

I Microstrip Detector Tests

5.1 Leakage currents

An apparatus was assembled to measure the leakage currents of individual diode strips on the microstrip detector planes. A switch board was used that could be connected to one of the 50-way connectors on the PCB fan-out of a plane, with a set of switches that allowed any one of the channels to be connected to an ammeter, sensitive to 0·1 nA. The leakage currents of all strips were measured, and the ten planes with the most uniform currents and the largest number of operational strips were selected for use in the detector.

A typical distribution of currents from the strips on a single silicon wafer is shown in Figure 5.1. These data were taken with a bias voltage of 90 V. As can be seen, most strips have a leakage current of ~ 2·0 nA/strip (which corresponds to ~ 80 nA cm^{-2}), but a few strips are found with anomalously high leakage currents, up to ~ 1 μA; the high currents

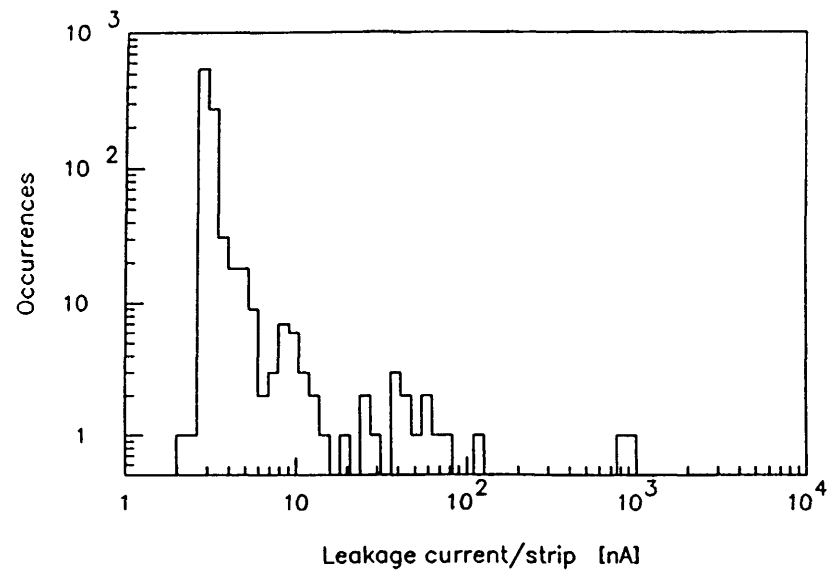

Figure 5.1 *Microstrip leakage currents*

are caused by imperfections in the silicon crystal structure, or faults in the processing. Such strips are useless for particle detection as any signal would be obscured by fluctuations in the leakage current. They were therefore stabilised by the insertion of a 10 MΩ resistor in the connection to the preamplifier, to prevent the current drawn becoming so large that the bias could no longer be applied. Other faults that were detected included strips that were shorted together, and others which were open circuits. These problems were often traced to faults on the high resolution section of the PCBs, and were corrected with the use of a scalpel and a soldering iron. A few remained that could not be corrected, due to faults in the silicon. Strips that remained shorted together would share the charge from an ionising particle between two read-out channels, so in these cases one of the read-out channels was severed, effectively leaving a strip of 100 μm width. After this effort, there were typically 995 operational strips out of 1000 on each plane.

The variation of leakage current with bias voltage is shown in Figure 5.2, both for normal strips and for a strip with a high leakage current. Note that for low voltages the leakage current is approximately proportional to V^n, where n is constant, but $n \sim 0{\cdot}7$ instead of the value of 0·5 which would be expected if the dominant contribution to the leakage current was Generation current (see Equation 4.1). Diffusion current or Surface current must therefore make a significant contribution to the total.

The leakage currents drawn by each of the silicon planes of the microstrip detector

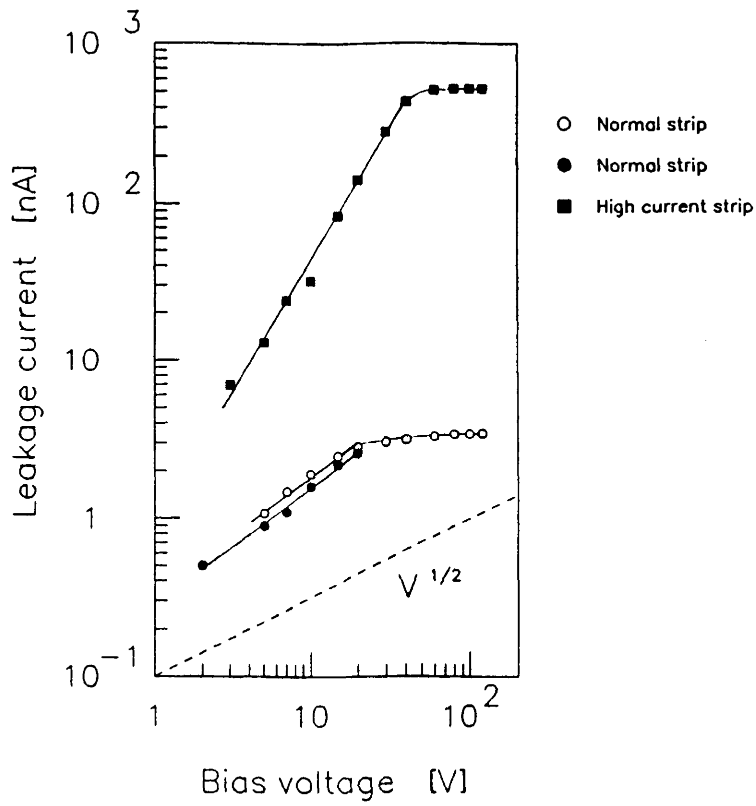

Figure 5.2 *Variation of leakage current with bias voltage*

were monitored, and the variation of the leakage current of one of the planes during the operation of the detector is shown in Figure 5.3. As can be seen, the current rose during exposure to the beam, but after each run it fell to the original level. The increase in leakage current is due to radiation damage to the detector planes [88]. The normal operation of silicon detectors requires a near-perfect crystalline lattice, to avoid defects that can trap the charge carriers and cause incomplete charge collection. Exposure to ionising radiation causes disruption of the lattice, most commonly through the creation of *Frenkel* defects, where atoms are displaced from the lattice. This gives rise to the following effects:

(i) Increase of leakage current due to damage to the bulk silicon;

(ii) Decrease in charge collection;

(iii) Decrease in effective dopant concentration, which may distort the internal electric field;

(iv) Damage to the oxide passivation layer.

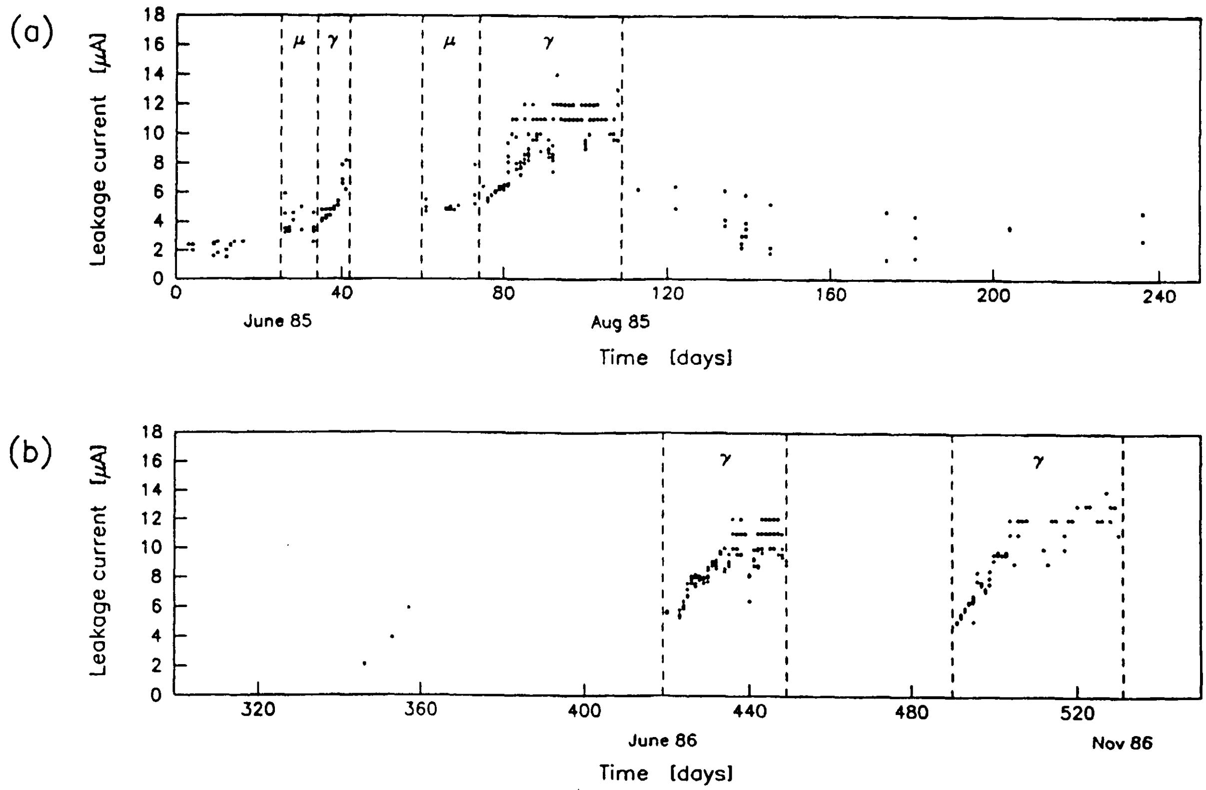

Figure 5.3 *Variation with time of the leakage current of a microstrip plane*

During exposure to the beam the leakage current increased by a factor of about 5. The decrease of the current in the period after exposure is thought to be due to room temperature self-annealing of the silicon, which repairs the radiation induced lattice defects. The total flux of minimum ionising particles during the running of the experiment was about 4×10^{11} cm^{-2}. There was no noticeable degradation of the performance of the detector as a result of exposure to the beam.

5.2 Test pulse development

The scheme for the provision of a test pulse facility for the read-out electronics of the microstrips has been described in Section 4.6. It was necessary to test the system, to check that the coupling of the test-strip to the read out channels was capacitive, and was of a suitable magnitude. A test apparatus was constructed, using a section of a fan-out PCB with conductive tracks on its surface, and test-strips of various widths. The strips were cut from Mylar-backed copper, using a scalpel and a steel rule. Their widths were

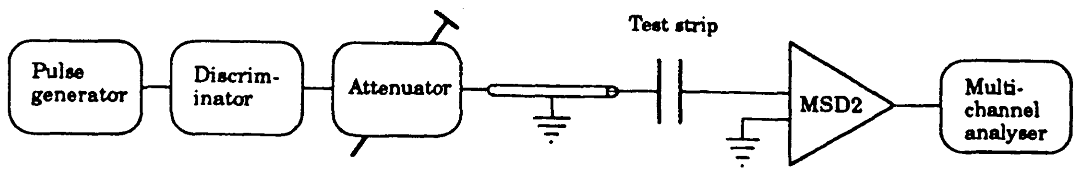

***Figure 5.4** Apparatus for test pulse investigations*

measured with a travelling microscope, to an accuracy of ± 2 μm. The measurement was made at each end of the strips, and any with varying width were rejected. The strips were glued to the board using double-sided adhesive tape; firm pressure from a blunt spatula ensured uniform adhesion.

The apparatus used for the test is shown in Figure 5.4. An attenuated pulse was applied to the strip, and any signal picked up by a fan-out track was amplified using an MSD2, and then digitised with a multichannel analyser. Using a 0·8 V pulse, with 51 dB attenuation, and with strips of different widths, the data shown in Figure 5.5 were taken. From the definition of capacitance:

$$C = Q / V$$

where V is the applied voltage and Q is the measured charge, it can be seen that the

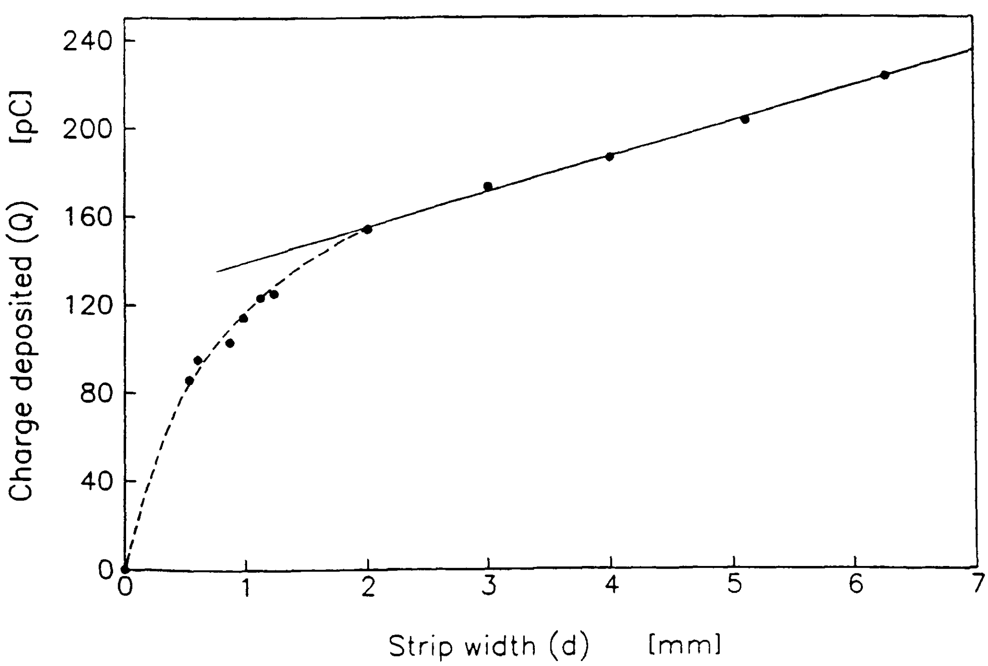

***Figure 5.5** Variation with strip width of charge deposited by the test pulse*

capacitance depends linearly on strip width, for widths above about 2 mm. This is as expected from a parallel plate capacitor approximation:

$$C = \frac{\varepsilon \varepsilon_0 A}{d}$$

where ε is the permittivity of the dielectric (adhesive tape and Mylar), ε_0 is the permittivity of free space, d is the thickness of the dielectric, and A is the area of the capacitor plates, in this case the product of the strip width and the track width. For strip widths less than 2 mm the data fall below the straight line, as expected when edge effects become important.

In a further test, the thickness of the dielectric was varied. This was achieved simply by the inclusion of additional layers of adhesive tape between the strip and the track. A strip of 3 mm width was used. If a stray capacitance C_s (from the connecting wires etc) is assumed, and the parallel plate approximation for the test-strip system is valid, then:

$$Q = C\,V = (C_s + \varepsilon \varepsilon_0 A / d)\,V$$

For n thicknesses of adhesive tape, we may put:

$$d = d_0 + n\,d_a$$

where d_0 is a constant (due to the Mylar) and d_a is the thickness of the tape, measured

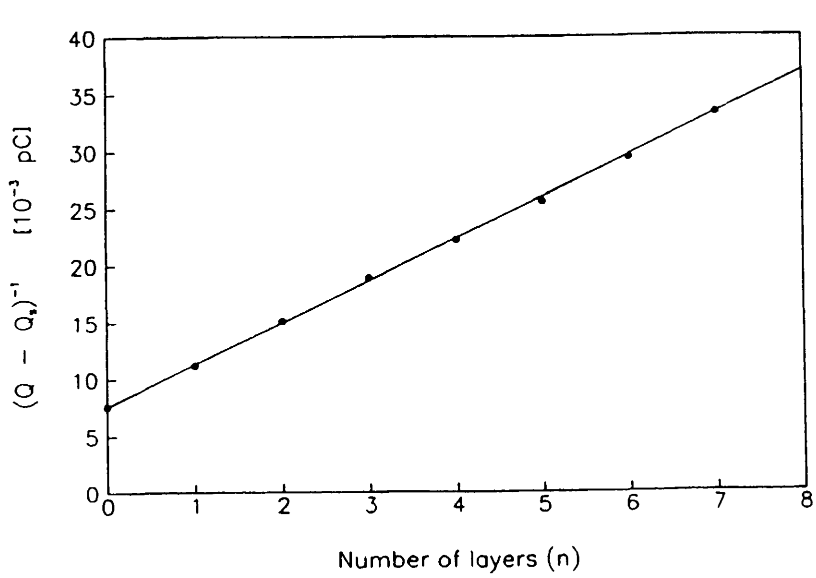

Figure 5.6 *Test of capacitive coupling of the test-strip*

with a micrometer to be about 100 μm. Thus we expect:

$$Q = Q_s + k \,/\, (d_0 + n\, d_a)$$

where $Q_s = C_s\, V$, and k is a constant. Rearranging this gives:

$$(Q - Q_s)^{-1} \propto d_0 + n\, d_a$$

See Figure 5.6. As can be seen, the relationship is accurately linear, indicating that the coupling is indeed capacitive. The intercept of $(Q - Q_s)^{-1} = 0$ at $n \sim -2$ indicates that $d \,/\, \varepsilon$ for the Mylar layer is approximately twice that for the adhesive tape.

5.3 Analogue read-out tests

Preamplifier tests

The apparatus shown in Figure 5.7 was used to measure the noise and the gain of all the MSD2 channels. For the measurement of the noise, no signal was applied, and the output was switched to the RMS meter; to measure the gain, the signal was applied, and the output was switched to the oscilloscope. The four channels on a hybrid could be independently tested using another switch system. Hybrids were selected for use in the detector that had gain within 10 % of the sample mean, and an ENC of less than 2000 electrons, measured with an input capacitance of 22 pF and a 50 ns gate.

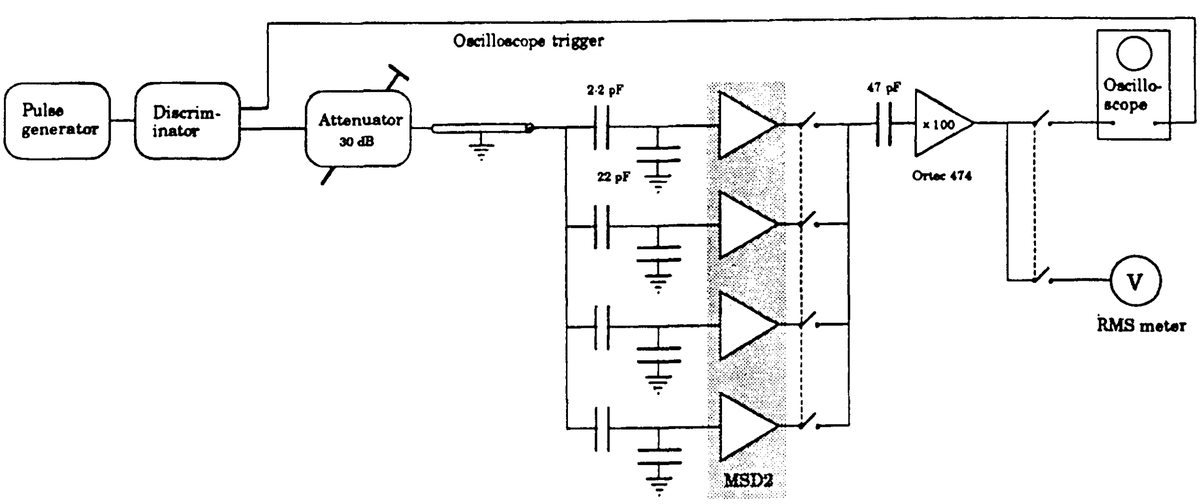

Figure 5.7 *Apparatus for preamplifier tests*

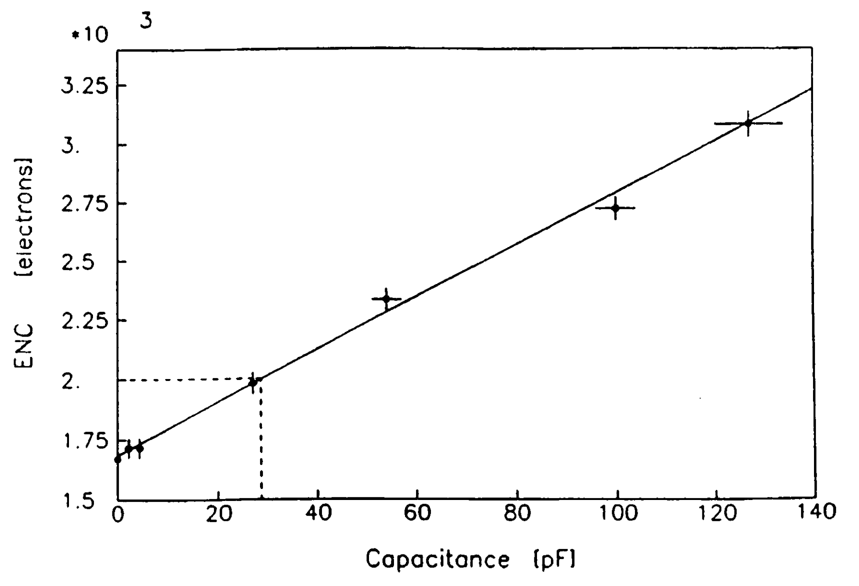

Figure 5.8 *Variation of MSD2 noise with input capacitance*

The variation of the ENC of the MSD2s with input capacitance was measured [84] (see Figure 5.8). In the microstrip detector there are contributions to the input capacitance from the silicon, the PCB, and the 20 cm ribbon cable to the MSD2 inputs. These contribute about 4 pF, 11 pF and 12 pF repectively, making a total of ~ 27 pF, and hence an ENC of ~ 2000 electrons.

ADC instrumentation

The microstrip detector was partially instrumented with MSD2s and installed in the experimental hall at CERN. Another experiment, NA10, was running at this time, and halo muons from the beam of the NA10 experiment were used to test the performance of the detector with high energy particles. For these tests ADCs were used for the read-out, to provide analogue information about the signal, permitting the measurement of such

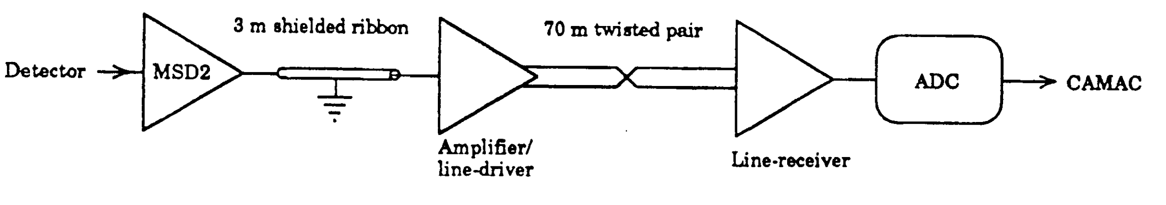

Figure 5.9 *Apparatus for analogue tests of the microstrip system*

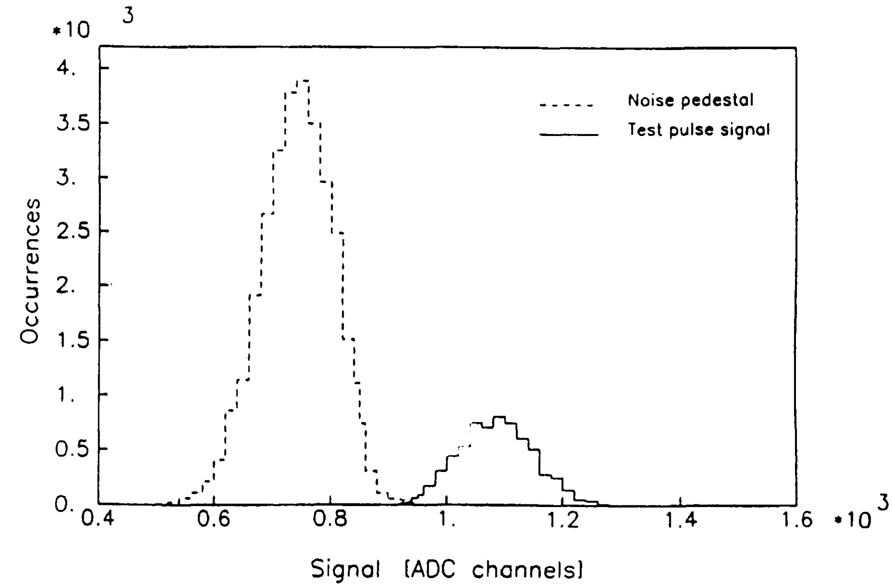

Figure 5.10 *Pulse height spectrum from the test pulse*

quantities as charge sharing and the signal-to-noise ratio. The read-out chain is shown in Figure 5.9. 240 channels were instrumented, chosen so that they covered similar regions in all four planes of a projection: the choice was respectively 24, 24, 96 and 96 channels on the four planes.

The pulse height spectrum from a typical channel when the test pulse is used is shown in Figure 5.10. Shown in the figure are the peak (or 'pedestal') at low channel number (i.e. low measured charge) due to noise when the test pulse was not active, and the peak at higher charge due to the test pulse signal. The separation of the peaks provides a measure of the signal from the test pulse.

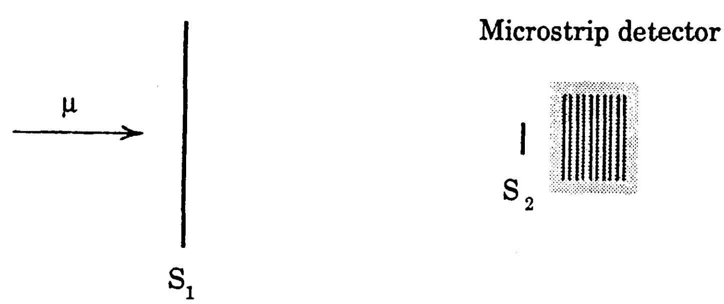

Figure 5.11 *Scintillator trigger arrangement*

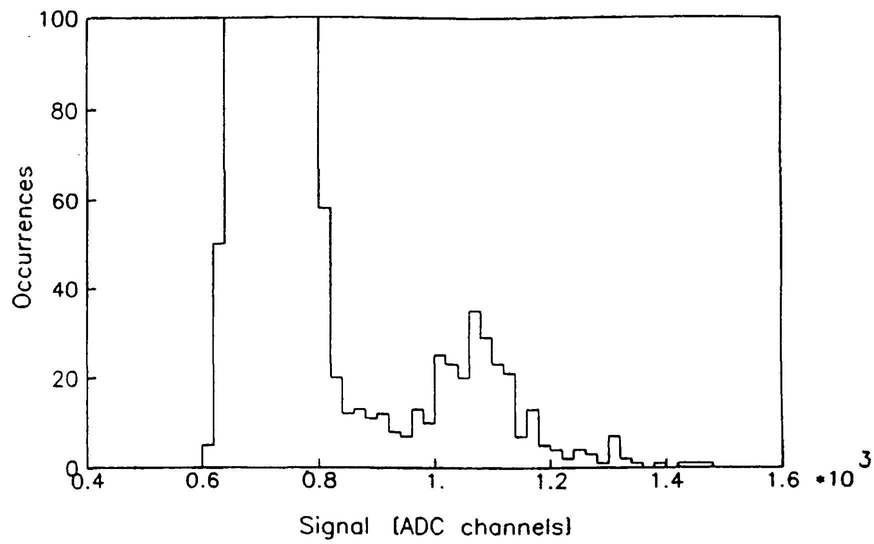

Figure 5.12 *Pulse height spectrum from minimum ionising particles*

To observe the signals from particles, a scintillator trigger was used, as illustrated in Figure 5.11. The trigger was formed from the coincidence of the two scintillators S_1 and S_2. The pulse height spectrum of a typical channel is shown in Figure 5.12, for a silicon bias of 90 V. Now the noise pedestal is contributed to every time a particle satisfies the trigger but does not pass through the strip being read out. A distinct signal peak can be seen, due to the particles. The signal-to-noise ratio was calculated for all the instrumented channels using plots such as this. The signal is measured by separating

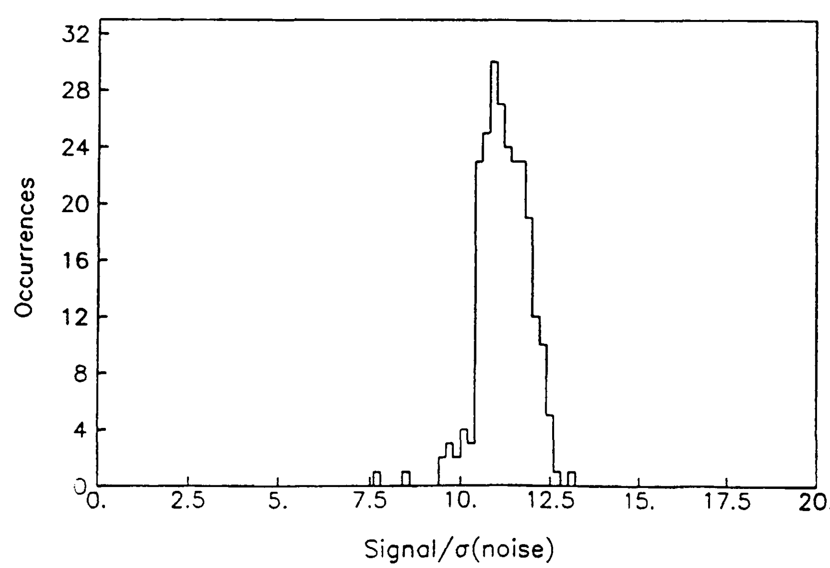

Figure 5.13 *Signal-to-noise ratio for the microstrip detector*

the signal peak from the pedestal and taking its mean, whilst the noise is taken as the *rms* width of the pedestal. See Figure 5.13. As can be seen, the channel-to-channel variation of the signal-to-noise is low, less than about 10 %, and the average value is ~12.

Using this value and the measurement of 2000 electrons for the noise of the MSD2, the collected charge may be estimated as about 24,000 electrons. This may be compared with the expected charge deposition of a minimum ionising particle of 36,000 electrons, indicating approximately 70 % charge collection. This is, however, thought to be an underestimate, as the amplifiers used for the signal-to-noise measurement were not specially tuned, and the resulting overshoot in the signal gave a value for the ratio that was about 15 % low.

The variation of the signal-to-noise ratio with bias voltage V_B is shown in Figure 5.14. From Equation 3.2 we expect the depletion depth to vary approximately as ${V_B}^{1/2}$ up to full depletion. The signal is proportional to the depletion depth, and the contribution of the silicon to the input capacitance (and hence to the noise) is insignificant for all but the smallest depletion depths, so we expect the ratio to vary as ${V_B}^{1/2}$. This is found to be the case, up to $V_B \sim 90$ V, where the curve flattens off, indicating that the silicon is fully depleted. An operating bias of 90 V was therefore chosen for the detector.

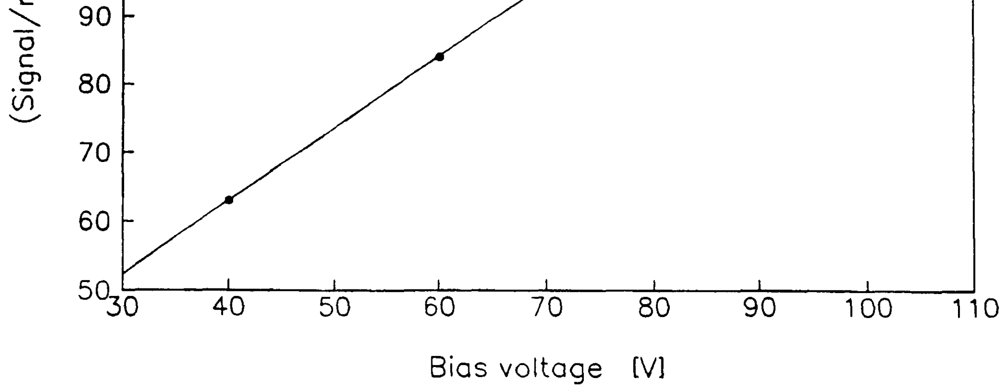

Figure 5.14 *Variation of the signal-to-noise ratio with bias voltage*

5.4 Digital read-out tests

MSD3 tests

The MSD3s were tested using the apparatus shown in Figure 5.15. The pulse generator was set at a frequency of 10 kHz, under CAMAC control. The attenuator was adjusted to give a test signal comparable to that expected from a minimum ionising particle in the final detector set-up. Then the MSD3 discriminator threshold was varied, also under CAMAC control, whilst the output rate was measured with a scaler. The variation of the measured rate with discriminator threshold is shown in Figure 5.16, with test pulses of two different amplitudes, and with no test pulse applied. The behaviour can be understood with reference to Figure 5.10: when the threshold is large no signals can trigger the discriminator, so the measured rate is zero. For a lower threshold, the largest test pulse signals trigger the discriminator, and as the threshold is further reduced a point is reached at which all of the signals exceed it, and a plateau is seen. Then the noise pedestal is reached and the rate increases dramatically.

A comparison of the threshold voltages required to reduce the measured rate to half the input rate at two different values of the attenuation (41 and 47 dB) gave a measure of the gain and the DC offset for each channel. The system was automated using CAMAC, permitting the rapid and reliable testing of all the MSD3 channels.

During the setting up of this test, problems were experienced with *oscillation* of the electronics. In this state the output becomes an uncontrollable high frequency oscillating

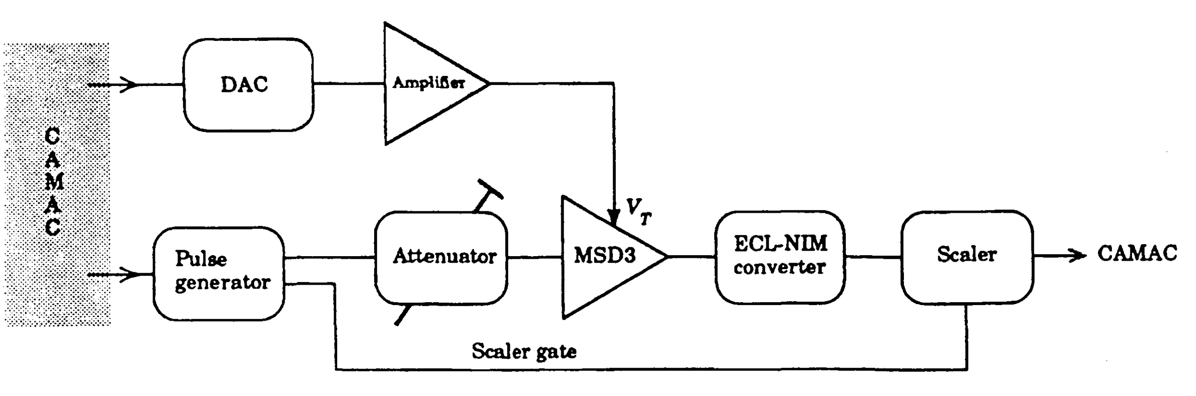

Figure 5.15 *Apparatus for amplifier / discriminator tests*

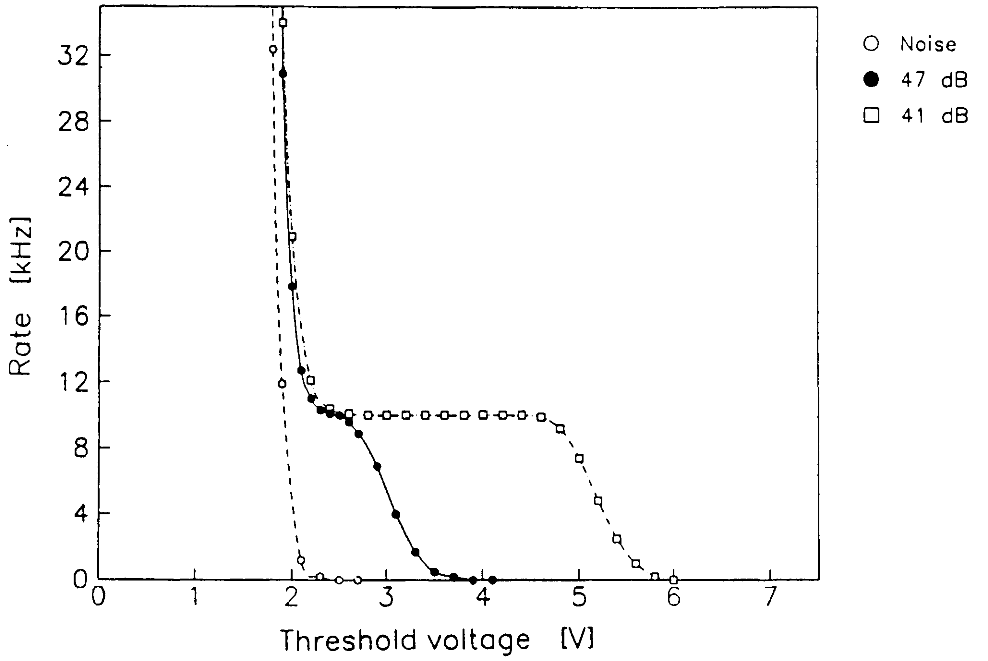

Figure 5.16 *Variation of rate with threshold voltage in MSD3 test*

waveform, and the system is useless for the amplification of signals. It is a problem that goes hand-in-hand with high gain, low noise electronics, and is a symptom of unwanted positive feedback. The input of the MSD3 was found to be particularly sensitive, and thorough screening was required for stability. Oscillation problems plagued the setting up of the full detector read out, as will be described below.

PCOS tests

A small test system was arranged to test the PCOS system and to gain familiarity with its operating procedures. It used a single crate of latch modules read out using CAMAC under the control of a minicomputer, an LSI-11. Programs were written to perform the various functions of the system: to set and measure the programmable threshold and delay, to down-load and read back test patterns, and to read in test inputs. As a result of these tests, various faults of the system were identified, and remedied.

The symptoms of a problem with the data acquisition are in some respects rather difficult to trace back to the underlying fault. Since the system is digital, either a hit or no hit is read at the monitoring computer for each channel. If a hit is spurious, due to a marginal effect such as crosstalk from a different channel, it cannot be distinguished from a valid hit. One can only compare the hits recorded with those that were expected. In a test arrangement this is straightforward, as specific channels may be injected with a signal. In the experimental situation, however, one does not know which channels *should* register a hit. One can only verify that the address of the hit is valid: that it corresponds to a real channel, and that no channel has more than one hit in any event. It is for this reason that the test facility of PCOS was so useful. A program was written that would down-load a random test pattern that simulated real data, and then read it back and compare the read pattern with the pattern that was set.

Using the techniques described above, it was found that the PCOS controller 2738 modules had a fault that gave rise to repeated hit addresses in the data; this was remedied by the manufacturers with a minor modification to the electronics of the modules. Another fault that was detected was the intermittent generation of hits, as a result of the use of nonstandard crates for the PCOS latch modules. The crates had been constructed at Saclay using a wire wrap technique for the Dataway lines, and the wiring was such that significant crosstalk existed between the lines of separate modules. Rewiring the crates solved this problem. When the full system of seven crates of latches was assembled, it was found that correct termination of the Databus was essential, to avoid the dropping of words. Finally, faults in individual latch modules were discovered by the systematic use of the test pattern, and the modules were repaired or replaced.

5.5 Prototype run

In the Summer of 1984 the first data were taken with a photon beam. A prototype microstrip detector was used which had only eight planes of silicon, arranged as three (Z, Y) pairs and one (U, V). The silicon thickness for the prototype was 300 μm. The number of channels that could be instrumented was limited by the availability of MSD3s, to 2800 channels.

Serious problems were experienced with oscillation, which became more severe as further channels were instrumented. The stability of the system depended critically on the positioning of the cables connecting the MSD2s to the MSD3s. The oscillation was thought to be due to capacitive coupling between the outputs and inputs of the MSD2s.

From the experience gained with the prototype run, the following modifications to the microstrip detector were implemented:

(i) The MSD2 mounting was modified to provide a good common ground for the inputs;

(ii) The Bulkhead was introduced between the MSD2s and MSD3s, giving a common ground for the earths of the cables carrying the signals to the MSD3s;

(iii) The cables to the MSD3s were individually wrapped in aluminium foil to provide electrical screening;

(iv) Additional circuitry was introduced on the MSD3 boards to give balanced ECL conversion for the outputs;

(v) A further two planes of silicon were incorporated, to assist the track reconstruction through the increase of redundancy;

(vi) The thickness of the silicon wafers was increased to 450 μm, so that a greater signal would be produced by a particle, and therefore a higher discriminator threshold would be possible for the same detection efficiency;

(vii) The discriminator threshold was raised to a high value (7 V) in the periods between bursts. This has the effect of killing any oscillation that might have started during the previous burst, and so assists in maintaining the stability of the system.

As a result of these modifications, few problems with oscillation were experienced in the subsequent periods of data taking.

5.6 Preparation for data taking

The improved detector and read-out electronics were installed at CERN in the Spring of 1985. The full 10,000 channels of MSD3s were now available, so the entire system could be instrumented.

Setting a threshold

A beam test was carried out using muons from NA10, in a similar manner to the ADC tests mentioned above, using the same trigger. The correct timing for the signals was simply found using the programmable delay of PCOS: the threshold was set to 1·8 V, and then by sweeping through the values of the delay, a curve such as that shown in Figure 5.17 (a) was produced, from which the correct timing could be chosen. The width of the PCOS strobe was 70 ns. A similar timing curve for the test pulse is shown in Figure 5.17 (b).

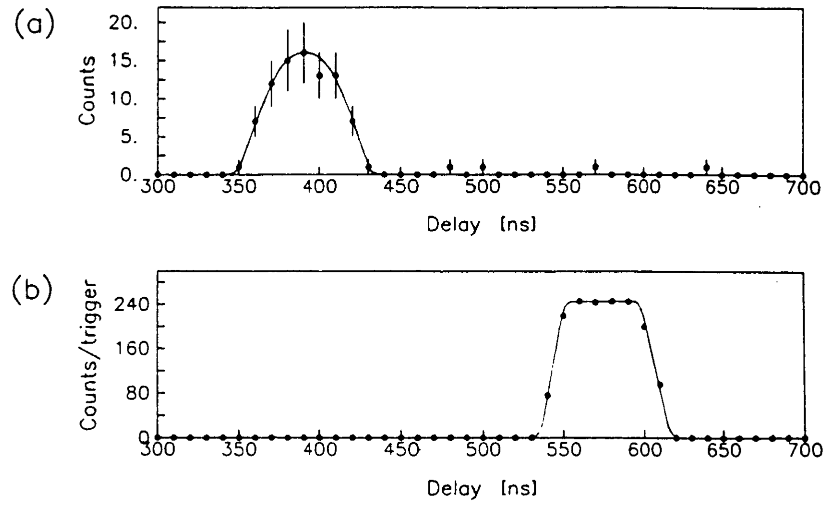

Figure 5.17 *Timing curves*

A threshold scan could then be produced by scanning through the discriminator threshold using the programmable facility of PCOS, with the correct timing set (determined from the delay scan). The results for one of the test pulses are shown in Figure 5.18, which exhibits the same features as the curve from the MSD3 test described in

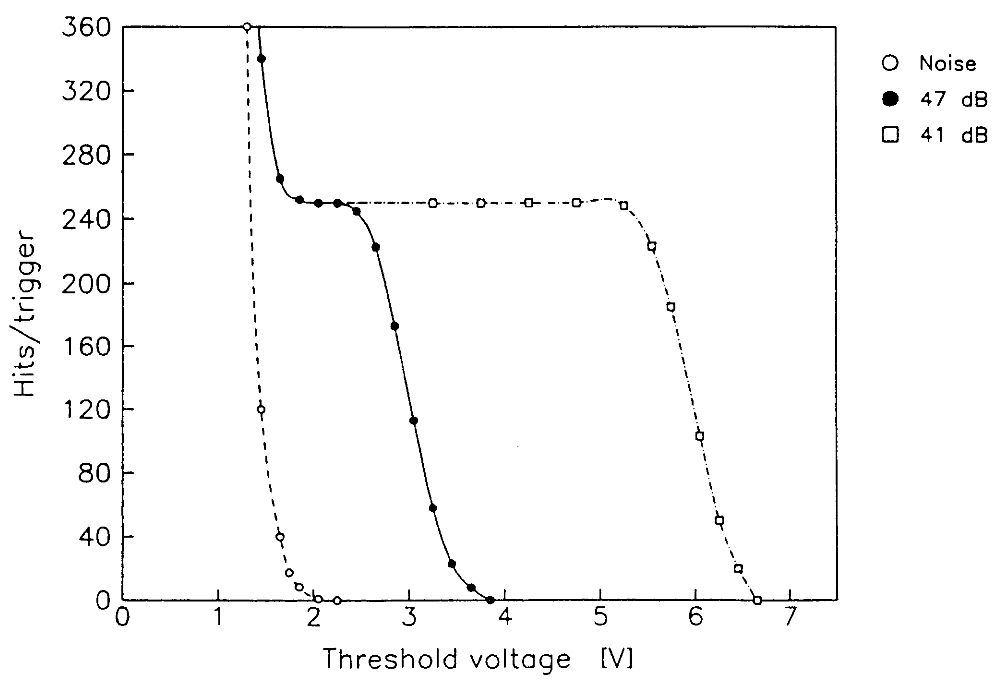

Figure 5.18 *Threshold scan with test pulse*

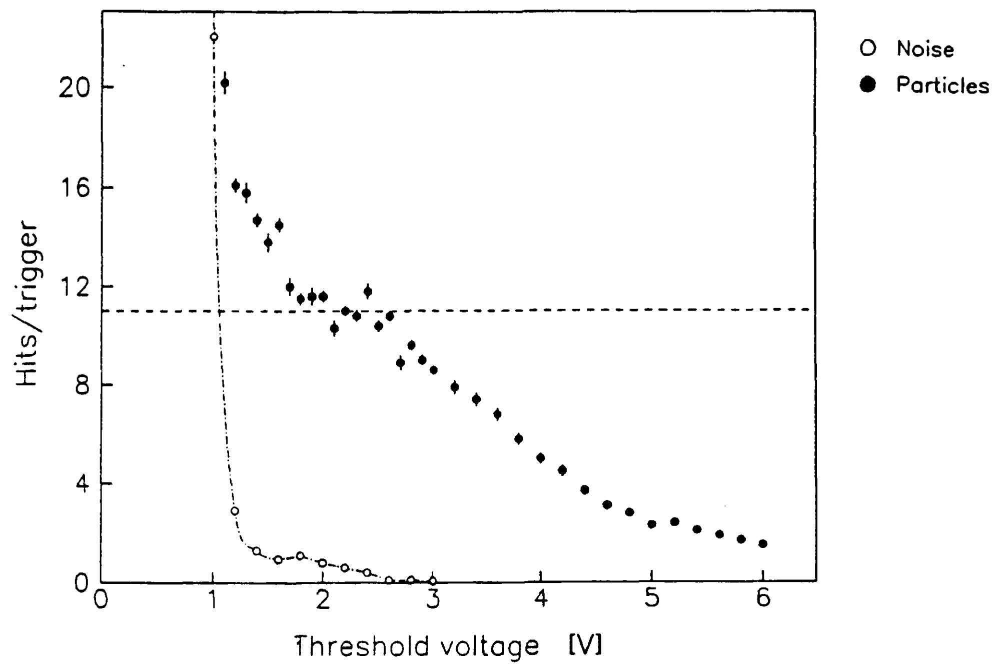

Figure 5.19 Threshold scan with particles

Section 5.4. The plateau now occurs at 250 hits/event, as expected, since each test-strip covers 250 fan-out tracks. A threshold scan produced with particles is shown in Figure 5.19. An out-of-time curve is also shown, which indicates the response to noise. At a threshold of 1·5 V there is about 1 noise hit in the detector per event. For the in-time curve, one would therefore hope for a plateau at 11 hits per event, corresponding to a hit from each of the 10 planes of the detector, and one noise hit. As can be seen, there is some evidence that this is the case.

The threshold for the discriminators must be set low enough to give a high efficiency for particle detection, whilst maintaining a low number of noise hits. A threshold of 1·6 V was chosen. It was possible to run at a lower threshold, but then there were signs of the onset of oscillation. The magnitude of the threshold may be determined in terms of the signal deposited by a minimum ionising particle (I_{min}) by inspection of the test pulse threshold curve. From the ADC spectra it was found that a test pulse with 47 dB attenuation corresponded to about 70 % of the signal from a minimum ionising particle. The threshold voltage for this test pulse at which only half the channels give a signal greater than threshold is about 3·0 V. Thus the threshold of 1·6 V corresponds to about 35 % of I_{min}. This was also verified by a cluster size analysis of muon data taken with the ADC read-out [84].

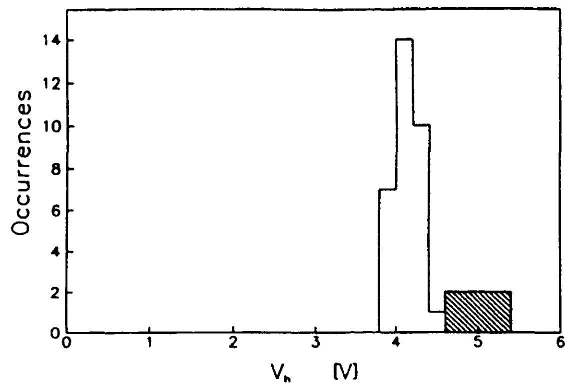

Figure 5.20 *Strip-to-strip uniformity of test pulse*

Uniformity of the test pulse

The uniformity of the test pulse was investigated using discriminator characteristics such as those shown in Figure 5.18. For a given test strip, a measure of the average magnitude of the test pulse is given by the threshold voltage V_h for which half of the channels respond per event. This was measured for the 40 test strips, and the results are shown in Figure 5.20. Most of the test strips gave pulses of closely similar magnitudes. A few, however, gave significantly larger pulses, shaded in the figure. They were found to be the strips on the inclined planes, and the larger pulse heights were understood: the special fan-out PCB sections for the inclined planes were manufactured at Imperial College and had slightly wider tracks than those of the other, commercially produced, boards. The capacitance formed by the test strip and the tracks was therefore greater, and the test pulse larger. Apart from this effect, the pulses were uniform to better than ± 10 %.

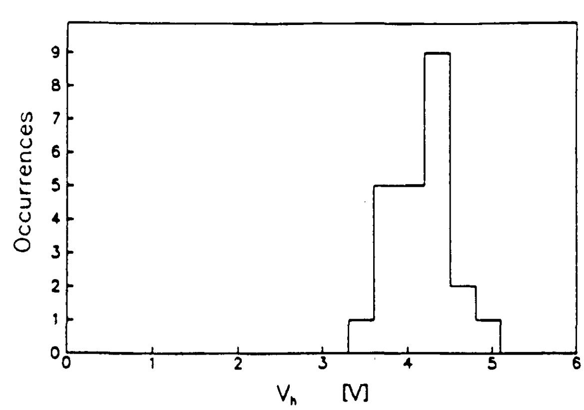

Figure 5.21 *Channel-to-channel uniformity of test pulse*

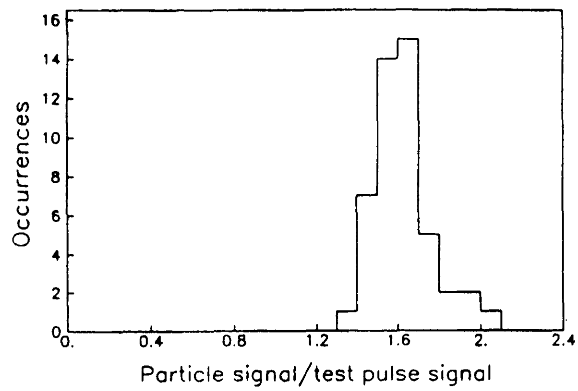

Figure 5.22 *Ratio of signals from particles and test pulse*

What spread is found could be due to many sources: different widths of the strips, non-uniform application of the strips to the PCBs, variation in the amplifier gains etc. A similar investigation was made of the channel-to-channel uniformity of test pulses within a test strip, shown in Figure 5.21. This was also checked using the ADC data, by calculating the ratio of the signal from particles and the signal from the test pulse for the same channel, so that the channel gain does not influence the distribution. See Figure 5.22. In all cases, a uniformity of about ± 10 % was found.

These measurements also indicate that the channel-to-channel variation of the gain is small. As a result, a common discriminator threshold could be applied to all the channels of the detector. Although the facility for application of individual threshold values to channels exists in the PCOS system, the use of a single value was obviously a substantial simplification.

5.7 Preparation of other detectors

MWPCs

The MWPCs were aligned using the data from special runs taken with a muon beam. As described in Section 3.6, the muon beam is created by closing the apertures of the neutron dump and the collimator in the beam line. Muons are particularly suitable for alignment work as they are highly penetrating, and form straight tracks.

INDRA Cerenkov

The Cerenkov had to be calibrated before it could be used in the data analysis. To recognise light incident on a mirror of the Cerenkov, it is necessary for photoelectrons to be generated at the associated photomultiplier, and then for the signal produced in the read-out ADC to be distinguished from the noise pedestal. The calibration therefore involves the following steps [74]:

(i) Measurement of the ADC pedestals;

(ii) Measurement of the ADC gain: the signal produced in the ADC per photoelectron. This is achieved using light emitting diodes (LEDs) that are mounted within the detector, and are supplied with a pulsed current that produces short bursts of light. By adjusting the current that passes through each LED, the intensity of the light that is emitted may be varied. In the analysis of data taken with the LEDs, peaks are seen in the pulse height distributions of the ADCs due to discrete numbers of photoelectrons, and the gain may be calculated (typically 25 ADC channels per photoelectron);

(iii) Determination of the number of photoelectrons produced by the passage of a minimum ionising particle through the detector. This may be calculated from a knowledge of the signal seen, and the gain; it is typically 10 photoelectrons per particle.

II Data Taking

5.8 Data structure

The data of an event take the form of 16-bit digital words. Each word may either be a record of a signal in one of the detector channels, or a formatting word that either delimits a given group of data or gives information about the group. In a typical event from the NA14 apparatus there are about 2000 words. They are organised according to the detectors in the apparatus, with a *block* of words from each detector. The first word in the block is a unique identifier for the detector; it is followed by a *header*, a descriptive sequence of words that includes information such as the number of words in the block; then finally the data proper.

Microstrip data format

The data from PCOS for an event take the form of words encoding the addresses of the PCOS channels that have received a signal. The data from each crate are output in sequence, followed by a delimiter word that gives the crate address. Due to the complicated cabling through the various stages of the read-out chain, the PCOS address of a channel is not simply related to its position on the silicon. Since it is the position on the silicon that is of interest for the analysis of the data, it is therefore necessary at some point to translate the addresses to give strip coordinates. To avoid having to do this repeatedly, a module was introduced into the data acquisition system that provided on-line translation. It is known as the *CAC* (Contrôleur Autonome de Chassis), and consists of an EPROM memory that is programmed with a look-up table for the conversion of the addresses. The positions of hit strips were therefore available for use by the on-line monitoring programs. To guard against failure of the CAC module, both the raw PCOS data and the CAC-converted data were recorded, so that if the converted data was suspect then the conversion could be checked. In practice it was found that this was only necessary in a very few events.

The microstrip data therefore had the following structure: the block identifier, followed by a header which gave the number of words in the block, and a CAC conversion status indicating whether the converted data existed; then the raw PCOS data, with the delimiters suppressed, followed by the CAC-converted data, giving the hit silicon strip numbers (running from 1 for the first strip of the first plane, to 10,000 for the last strip). Due to the *OR*-gate, the CAC generated two converted words for each raw PCOS word.

5.9 Monitoring

The data acquistion of the experiment was controlled by a PDP 11/45 computer. This computer was dedicated to reading the various subsystems of the apparatus via CAMAC, and writing the data to magnetic tape. It is obviously essential that whilst the data are recorded they should be monitored, to ensure that the apparatus is correctly set up, and that the detectors are performing efficiently. The 11/45 does provide a limited degree of monitoring, giving the values of various scalers that measure trigger rates etc, and histograms of some variables such as hit multiplicities. However, as it is dedicated to the efficient read-out of the apparatus and recording the data to tape, there is little processing

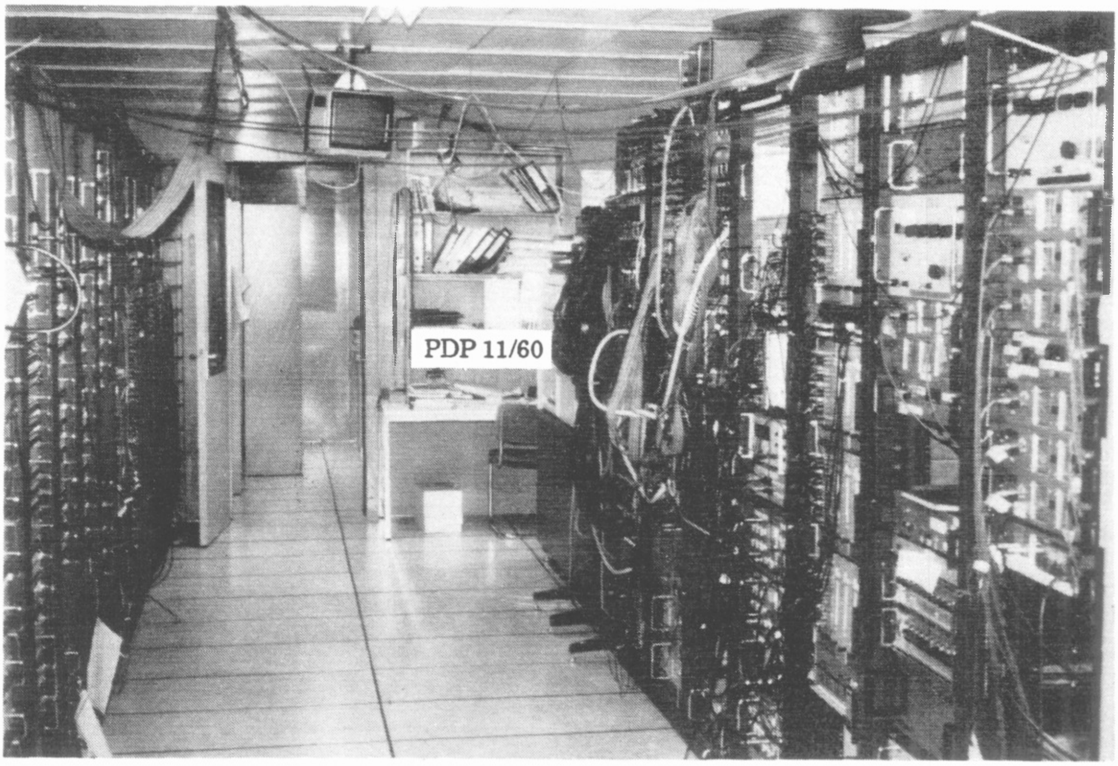

Figure 5.23 *Inside the NA14 counting room*

time available for monitoring. Instead the monitoring is handled by other on-line computers, and off line.

In the NA14 counting room, in addition to the PDP 11/45 there are two PDP 11/60 computers. They were dedicated to the monitoring of various detectors. The one operated by Imperial College (visible in Figure 5.23) was responsible for the monitoring of the microstrip detector and ILSA, one of the calorimeters. The 11/60s received data from the 11/45 via a CAMAC controlled 'Link', that permitted events to be transferred from the 11/45 to an intermediate memory module, without interfering with the recording of the events to tape. The 11/60s could then share the events from the memory, to use for their monitoring. When the Link was not functioning it was always possible to take one of the recently written 11/45 tapes to read at the 11/60. During the periods when the experiment was running, a shift system was operated so that there were always physicists 'on shift' with the responsibility of checking the monitoring, and responding to any problems.

Another person on shift was responsible for the off-line monitoring. This was known as the 'bicycle shift' as tapes had to be regularly transferred to the main CERN computer so that standard monitoring jobs could be run. The greater processing power of the main computer permitted more complicated checks to be made of the data. The output from these jobs was returned to the counting room for evaluation by the physicists on shift.

Microstrip monitoring

The monitoring system run on the Imperial College 11/60 was of a standard CERN form, using a *skeleton* structure. All of the standard procedures such as reading in the data and filling histograms are handled by the provided skeleton routines, and the user needs only to supply routines that are specific to the monitored system. The skeleton arrangement allows many tasks to be run simultaneously, and is controlled at the terminal with a tree structure of command menus. The histograms that are filled by tasks may be inspected at any time.

The monitoring tasks that were written for the microstrips were as follows. Some examples of the histograms produced by these tasks are shown in Figure 5.24.

(i) *Raw event dump*. This displayed the data as it was received, and was useful for investigating very basic problems, such as corruption of the data;

(ii) *Display of PCOS information*. The addresses of the hit channels in the PCOS system were decoded from the data, and histogrammed to produce a channel-by-channel profile. An overall profile was also produced, with the signals from the channels of each module summed and entered into one bin. See Figure 5.24 (a). This allowed the rapid recognition of serious problems such as power failure on a PCOS crate. The rather irregular appearance of the profile is caused by the complex fan-out of the detector channels. This can be seen by comparison with Figure 5.25, a corresponding profile produced from the Monte Carlo simulation of the detector. The channel-by-channel profile gave useful information for the recognition of read-out problems. Failure at different points in the read-out chain gave characteristic irregularities in the profile: if the *OR*-image of a dead channel was also dead then the problem was probably after the *OR*-gate in the chain, whilst groups of four dead channels, for example, were generally caused by the failure of an MSD3 hybrid;

(iii) *Display of hit strips*. An aggregate profile was produced for each plane of the detector, with ten strips per bin. Due to the *OR*-gate, these profiles do not show the true profile of hits in the silicon, since for each true hit an image hit is produced on a different plane. See Figure 5.24 (b);

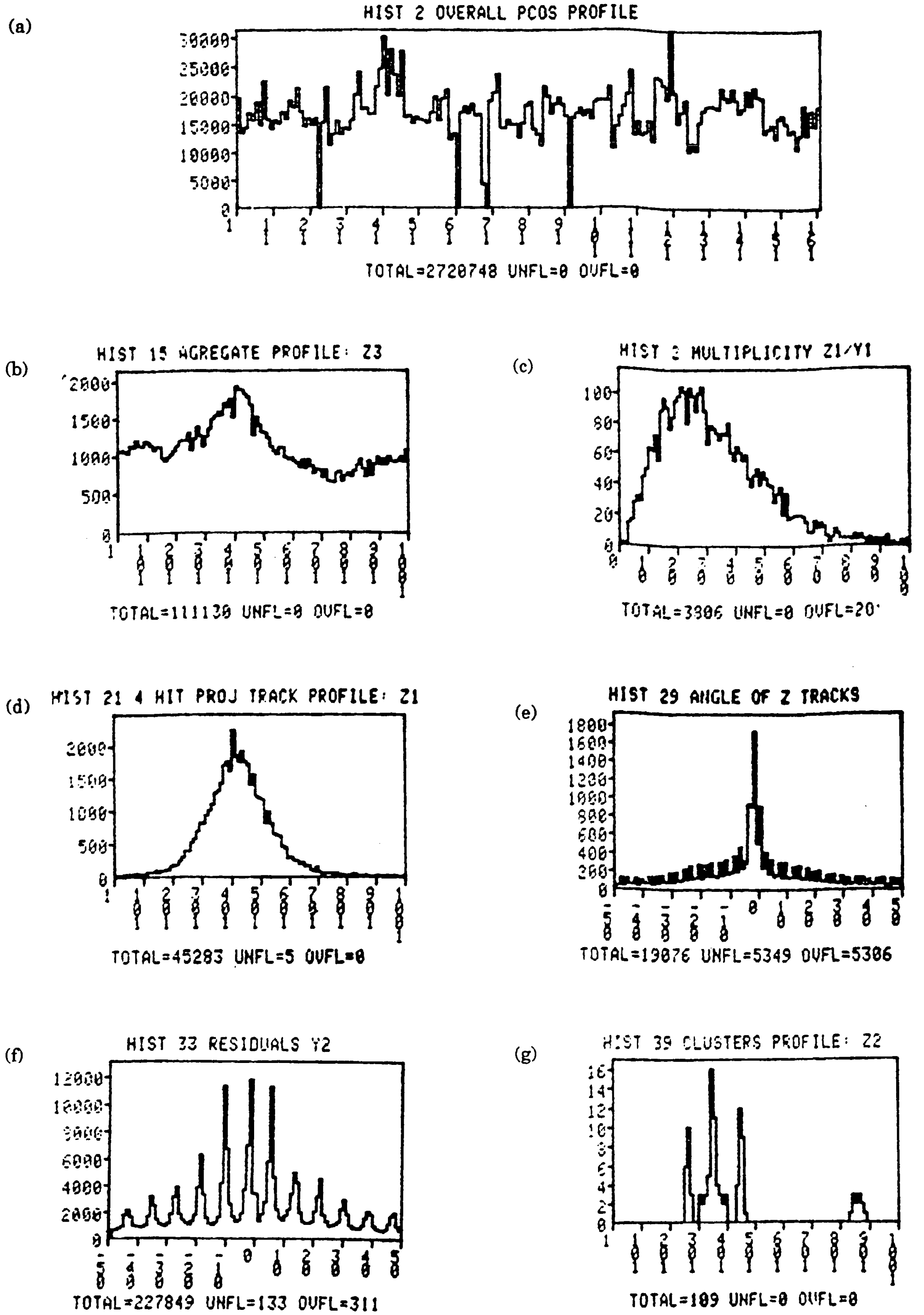

Figure 5.24 *Histograms from the microstrip detector online monitoring system*

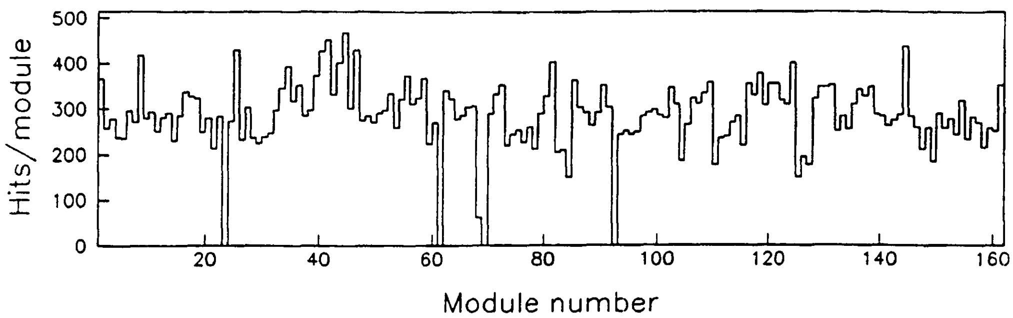

Figure 5.25 Hit frequency profile from Monte Carlo simulation

(iv) *Multiplicities.* The total hit multiplicity was histogrammed, and after the data had been decoded histograms were produced of the multiplicity of hits in each plane. See Figure 5.24 (c). Note that due to the effect of the *OR*-gate, pairs of planes have the same multiplicity;

(v) *Display of hits on fitted tracks.* To remove the obscuring influence of the *OR*-gate, a simple track fit was performed, finding four point tracks in each projection. It could then be confidently assumed that the hits on the tracks were true hits rather than image hits, and they were histogrammed to produce an aggregate profile for each plane, with ten strips per bin. See Figure 5.24 (d). Other information from the track fit was also displayed, such as the track angles (Figure 5.24 (e)) and the fit 'residuals' (discussed in Section 5.14, see Figure 5.24 (f));

(vi) *Oscillation monitor.* Oscillation in the read-out electronics of the detector appears in the data as large numbers of hits in groups of channels. Due to the arrangement of the cabling, oscillation in consecutive channels of the MSD2s (the most frequent type) is seen as hits in every fourth consecutive channel of the detector. A task was written to search the decoded data for such a pattern of hits. If the number of hits in the candidate 'oscillation' was greater than a user defined threshold, then the hit channels were entered into an aggregate profile. See Figure 5.24 (g). In this manner, a check could be kept on the overall incidence of oscillation, and whether it was localised in any part of the detector;

(vii) *Event display.* This provides a overall impression of how well the detector is performing, and is particularly useful for the recognition of the onset of oscillation. A display of a normal event is shown in Figure 5.26 (a), with tracks from the simple fit of the profiling task mentioned above. In Figure 5.26 (b) an event is shown where oscillation can be seen.

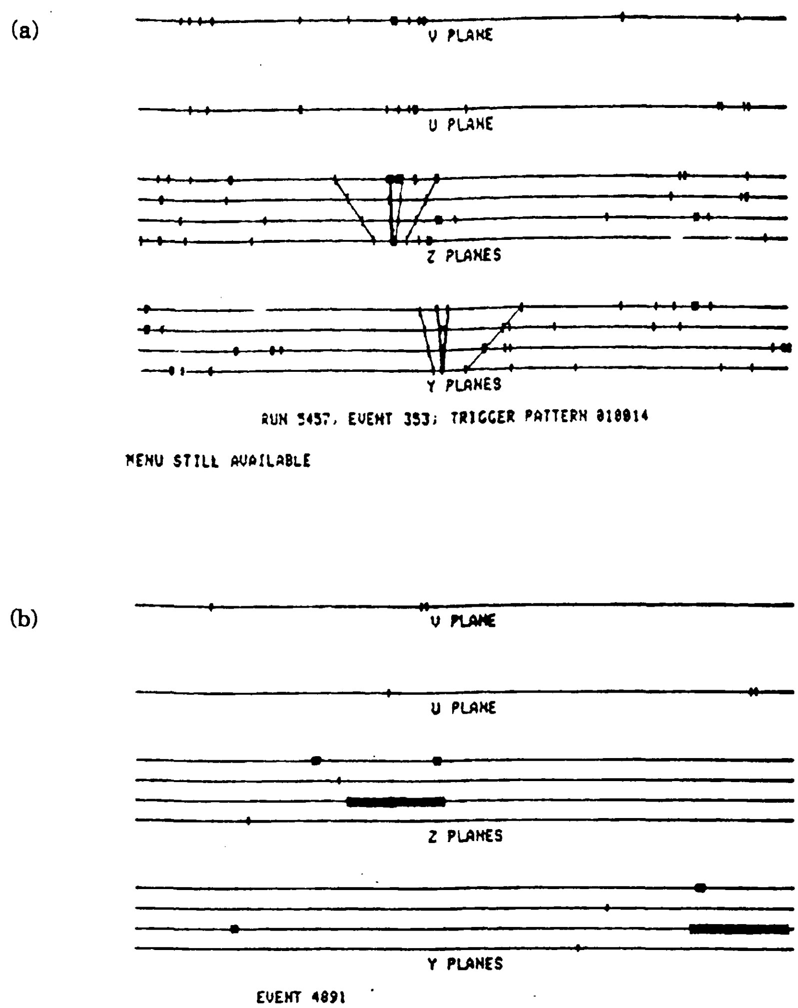

Figure 5.26 *Online microstrip event display*

The monitoring of some of these tasks was automated: for the overall multiplicity and PCOS profile, the contents of the histogram bins were compared with default values, and if the disagreement exceeded a user-defined limit then an alarm was sounded. This helped to ensure a quick response to any serious failures of the system.

Recovery of dead channels

The Imperial College 11/60 was also used to control the read-out of the microstrip detector in periods when the 11/45 was inactive, such as when the beam was off. This was simplified by the use of two Databus interface modules, one dedicated to each computer. To switch between the two computers was then simply a matter of transferring the PCOS

Databus cable from one interface to the other, and switching over the triggering system. With the detector read-out under the control of the 11/60, various tests could be run. Use was made of both the test pattern facility of PCOS, and the test pulse, to detect dead channels. A lot of effort was expended on their recovery, usually with one person at the computer console, whilst a second investigated the fault in the zone, in communication via an intercom system. In this manner dead channels were identified, and recovered if possible, and for the majority of the time during which the experiment was running there were 9927 out of the total 10,000 strips operational. Of the remaining 73, most of the faults were those discovered during the DC tests, and therefore could not be remedied.

PCOS problems

Various problems concerning the PCOS data acquisition system had been met when a test arrangement was operated, as described in Section 5.4. However, when the full system was assembled, further difficulties were experienced. The symptoms of trouble were the production of data words that corresponded to nonexistent addresses, the repetition of words, the creation and loss of data words, and the corruption of the data delimiters. Some of these faults were found to be specific to modules, which were repaired or replaced, but for others no conclusive diagnosis was formed. Instead it was found that by moving a troublesome module to a different slot in its crate would often cure the fault. Some time was spent before the run started finding a stable arrangement for the modules. This appears to have been successful, as no evidence for problems of this sort have been found in the data that were taken.

5.10 The experimental trigger

The trigger of a high energy physics experiment is the algorithm that is used to determine whether an event should be recorded. It is used to select events that are interesting, since they exhibit evidence of those properties that the experiment is investigating. Given the limited rate at which the data acquisition system can record data, this is important, if only to ensure efficient use of the beam time. It also gives a reduction of storage and handling problems, and reduces the off-line analysis task.

The trigger is generally a combination of calculations using information from different detectors in the apparatus. The more complicated decisions generally take a longer time. If an event fails any of the decisions it is rejected, and the data acquisition systems of the detectors are cleared, ready for the read out of the next event. The time taken to process an event that is subsequently rejected contributes to the *dead-time* of the system. In order to reduce this dead-time, it can be advantageous to separate the constituent decisions that make up the final trigger according to their duration. The fast, simple, decisions are made first, and only if they are satisfied are the more lengthy calculations begun. This procedure may be extended to produce many levels of trigger.

In NA14 the trigger is designed to select hadronic interactions of the beam photon. There are two levels of trigger, a pretrigger and the final trigger, the elements of which are described below.

Pretrigger

The pretrigger is constructed from the following components:

BEAM • ACT • HODO • DT

where • implies a logical *AND*. The components have the following meaning:

BEAM — The tagging counters indicate that a photon of energy greater than 40 GeV is incident on the experimental target.

ACT — An interaction has occurred in the active target. Discriminators attached to some of the target read-out channels are used to provide this information. The discriminator threshold is set to 2·5 times the signal from a minimum ionising particle, I_{min}. This helps to reject the electromagnetic background, where an e^+e^- pair is produced, since then a signal of only 2 I_{min} would be seen. The channels used for the trigger were the central 15 vertical strips on the last two Y-planes (planes 29 and 30), and the central 13 horizontal strips on the first of the Z-planes (plane 31). A hit above threshold must be registered in each of the planes for the trigger condition to be satisfied. The central strips on Y- and Z-planes were chosen to avoid interactions at the edge of the target (for which tracks would be lost from the microstrips) whilst the number of strips in the trigger was chosen to give a trigger rate that saturated the data acquisition.

HODO — This is a combination of signals from the scintillator hodoscopes of the apparatus, designed to increase the hadronic content of the trigger. In more detail, the requirement was:

$$\left((\overline{\mu V} \bullet G1 \bullet G2V \bullet G2H)_{top} \bullet G2H_{bot} \right) \mid \left((\overline{\mu V} \bullet G1 \bullet G2V \bullet G2H)_{bot} \bullet G2H_{top} \right)$$

where | implies logical *OR*; G1, G2V and G2H are the hodoscopes described in Section 3.8, and μV is the muon veto. The *top* and *bot* subscripts refer to the top and bottom halves of the detectors.

DT 'Dead Time': this is the signal from the 11/45 that it is ready to read in an event.

Final trigger

The final trigger only differs slightly from the pretrigger. It is the following:

$$PT \bullet DARM$$

where the elements have the following meaning:

PT The pretrigger.

DARM 'Double Arm': a more restrictive requirement for the hodoscopes than HODO. It is designed to select events with a track in both the upper and the lower halves of the apparatus. This further enhances the hadronic content of the trigger. In more detail the requirement is:

$$(\overline{\mu V} \bullet G1 \bullet G2V \bullet G2H)_{top} \bullet (\overline{\mu V} \bullet G1 \bullet G2V \bullet G2H)_{bot}$$

The trigger is illustrated in Figure 5.27.

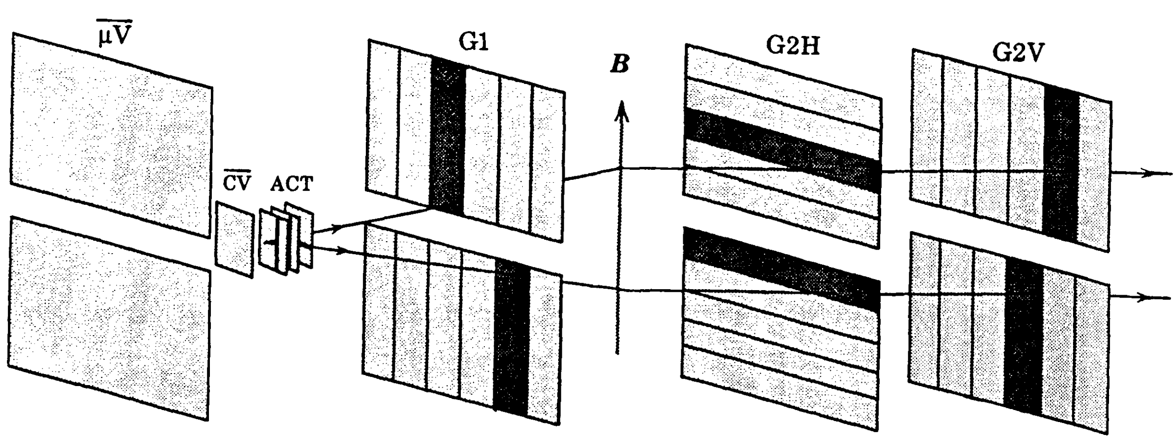

Figure 5.27 *The experimental trigger (schematic)*

In the 2 s burst of the experimental beam, there were typically 220 pretriggers, and 95 final triggers, from which 80 events were written to tape. The dead-time of the data-acquisition system is determined by the time taken to read the registers (~ 5 ms) and the time taken by a fast clear (~ 5 μs). From a scan of events, the trigger was found to be about 95 % hadronic. Monte Carlo studies indicate that it enriches the charm content of events by a factor of about 2, compared with all photon induced hadronic interactions (see Section 9.9).

5.11 The data sample

Following the prototype run in 1984, data was taken in three runs during 1985 and 1986. In the Summer of 1985, the experiment ran for 35 days, and 5·2 million triggers were recorded. In the Summer and Autumn of 1986 a further 70 days of running yielded 12 million triggers. A total of 17·2 million triggers were therefore taken by the experiment. This is equivalent to about 2500 raw-data tapes.

Assuming that the charm cross-section is about 1 % of the total hadronic cross-section, and bearing in mind the trigger enrichment factor of 2, a total of about 300,000 charm events are expected in the data sample. For a decay channel with a product of cross-section and branching ratio that is 1 % of the charm cross-section, and assuming a combined filter and reconstruction efficiency of 30 %, we expect to measure about 1000 decays.

III Microstrip Detector Performance

5.12 Noise

The number of noise hits in the microstrip detector, measured with an out-of-time strobe, was typically 6 per event in 10,000 channels. This compares with about 120 hits from a typical photon interaction in which 10 charged tracks were produced. The hit multiplicity is shown in Figure 5.28 (taking the *OR*-gate into account, i.e. taking half the number of hits seen by the data acquisition).

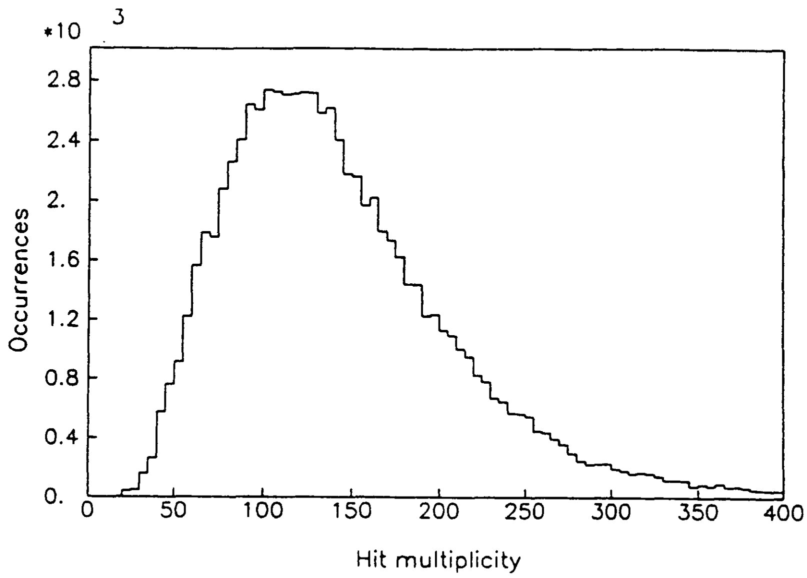

Figure 5.28 Microstrip hit multiplicity

5.13 Charge sharing

The sharing of charge from an ionising particle amongst channels in the silicon manifests itself as clusters of hits. The cluster size distribution observed for tracks produced by photon hadronic interactions is shown in Figure 5.29. As can be seen, about

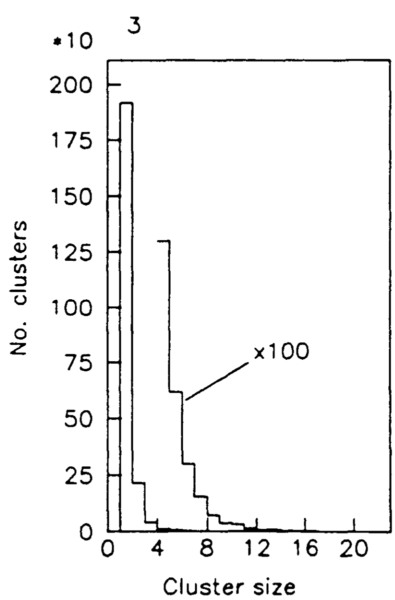

Figure 5.29 Cluster size distribution

90 % of clusters are single hits, indicating that charge sharing is low. Clusters of two and three hits are compatible with the mechanisms described in Section 4.1. The occasional very large clusters are thought to be the result of particle re-interaction occuring in the microstrip silicon planes.

5.14 Alignment

Internal alignment

The separation of the microstrip planes was accurately measured during the construction of the detector. The transverse alignment, on the other hand, was performed using the reconstruction of tracks. For the four planes in each projection, tracks are found using hits on three of the planes, and a prediction made for the position of the hit on the remaining plane of the projection. The distance of the nearest hit to the predicted point, the *residual*, is histogrammed to produce plots such as that in Figure 5.30. The existence of a clear peak in the distribution indicates that tracks are being successfully found. The internal alignment of the planes is achieved by adjusting their relative offsets so that the peak is centred on zero. For the inclined planes, tracks found in the Y- and Z-projections are used to predict the position of hits, and a similar procedure is followed.

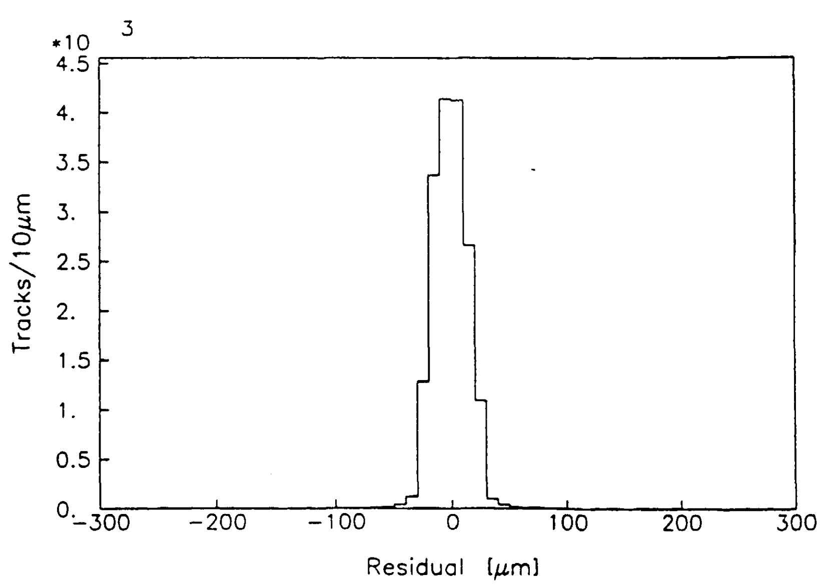

Figure 5.30 *Residual distribution (four-point tracks)*

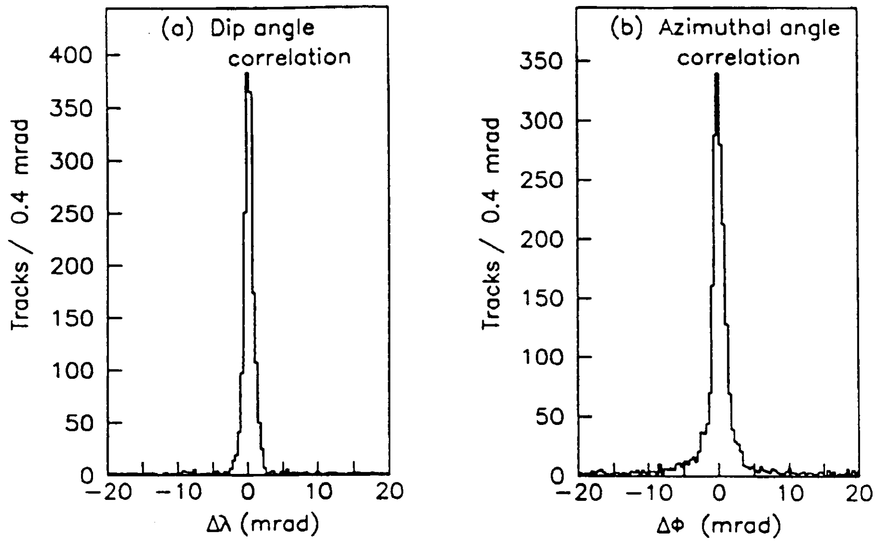

Figure 5.31 Angular matching of microstrip and spectrometer tracks

During the periods that data was taken the alignment was checked, and found not to change. This indicates that the relative movement of the planes was less than ~ 2 μm.

Alignment to the spectrometer

The alignment of the microstrip detector to the spectrometer is essential to permit the association of tracks found in the two systems. This is important, as it allows the combination of the spatial precision of the microstrips with the momentum resolution and particle identification capability of the spectrometer. The association of the tracks is achieved by the comparison of their angles: two angles define the track direction, the dip and azimuthal angles (λ and ϕ) which are defined in Section 6.9. The distributions of the difference in angle of tracks found in both systems is shown in Figure 5.31. As can be seen, the matching of the tracks is clear, with an *rms* width to the peak of ~ 0·7 mrad.

5.15 Spatial precision

Since the microstrip detector is designed for vertex detection, with the task of recognising short-lived decays, the spatial precision is clearly an important property. It is measured by determining the residual on the tenth plane of tracks that pass through hits on each of the other nine planes of the detector, validated with the spectrometer. The validation is

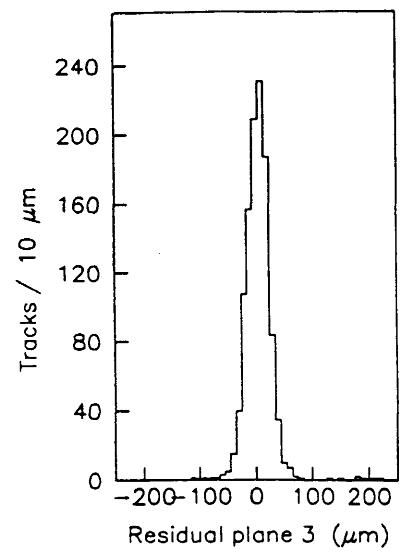

Figure 5.32 *Residual distribution (ten-point tracks)*

achieved by requiring that a spectrometer track matches the dip and azimuthal angles of the microstrip track to within 2·5 mrad. A typical residual distribution is shown in Figure 5.32. The width of the residual gives the spatial precision, which was measured to be ~ 16 μm *rms* for all planes, independent of angle up to ~ 150 mrad. This measurement was made using photon interaction products, in normal conditions. The theoretical limit σ_t to the resolution of a detector with strip pitch w is given by:

$$\sigma_t = \frac{w}{\sqrt{12}}$$

So for a 50 μm strip pitch, $\sigma_t \sim 14{\cdot}4$ μm. The measured value of 16 μm is close to this limit.

The *pull* function of the track fit is shown for one of the planes in Figure 5.33. The pull is defined as follows:

$$\frac{y_m - y_f}{\sqrt{\sigma_m^2 - \sigma_f^2}} \tag{5.1}$$

where y is the track coordinate and σ is the corresponding error; the subscripts m and f refer to *measured* and *fit* quantities respectively. The fit was calculated using $\sigma_f = 16$ μm, and the pull function is a Gaussian distribution with *rms* width of about 1·0, indicating that the nominal resolution is a good description of the data.

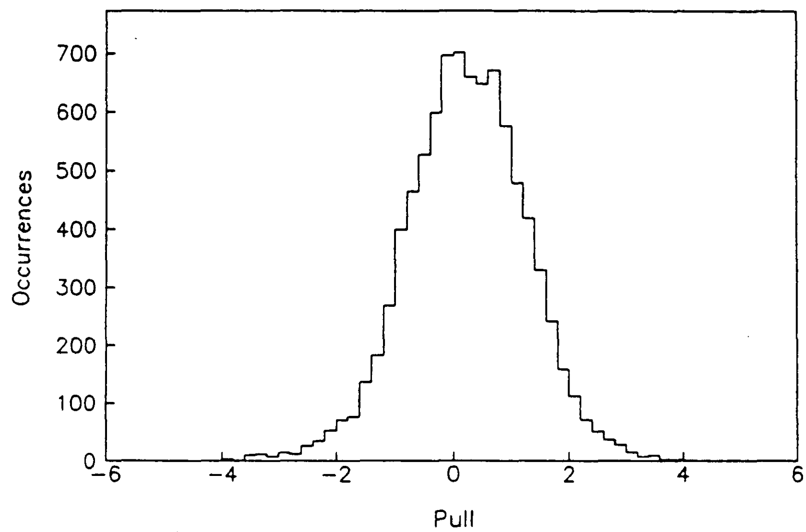

Figure 5.33 Pull distribution from track fit

5.16 Plane efficiency

The per-plane efficiency of the microstrip detector may be determined from the distribution of the number of hits on a reconstructed track. This is plotted in Figure 5.34, for tracks with momentum greater than 5 GeV/c that pass through all 10 planes of the

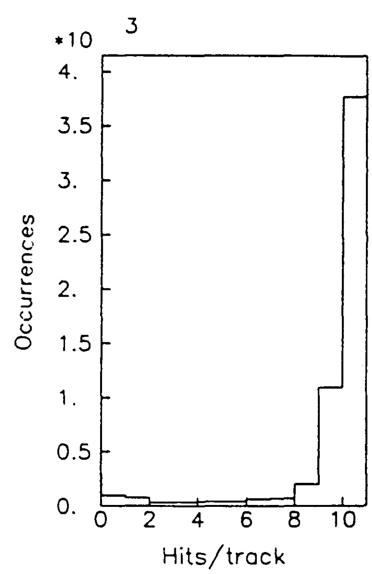

Figure 5.34 Number of microstrip hits on spectrometer tracks

detector. From the ratio of 9-point to 10-point tracks R, the efficiency ε may be calculated, since the number of 10-point tracks:

$$N_{10} \propto \varepsilon^{10}$$

and the number of 9-point tracks:

$$N_9 \propto 10\,(1-\varepsilon)\,\varepsilon^9$$

so:

$$R = \frac{N_9}{N_{10}} = \frac{10\,(1-\varepsilon)}{\varepsilon}$$

and therefore:

$$\varepsilon = \left(1 + \frac{R}{10}\right)^{-1}$$

From the distribution, $R \sim 0{\cdot}29$, giving an efficiency of 97 %. This is found for all the planes, and no fall in efficiency is seen for traversal angles up to 150 mrad. See Figure 5.35. This indicates that the discriminator threshold is at a suitably low level, since for a particle at 100 mrad (for example), the average signal deposited in a strip is only 70 % of that at normal incidence. The value measured for the efficiency includes losses due to dead channels, and due to the software clustering algorithm.

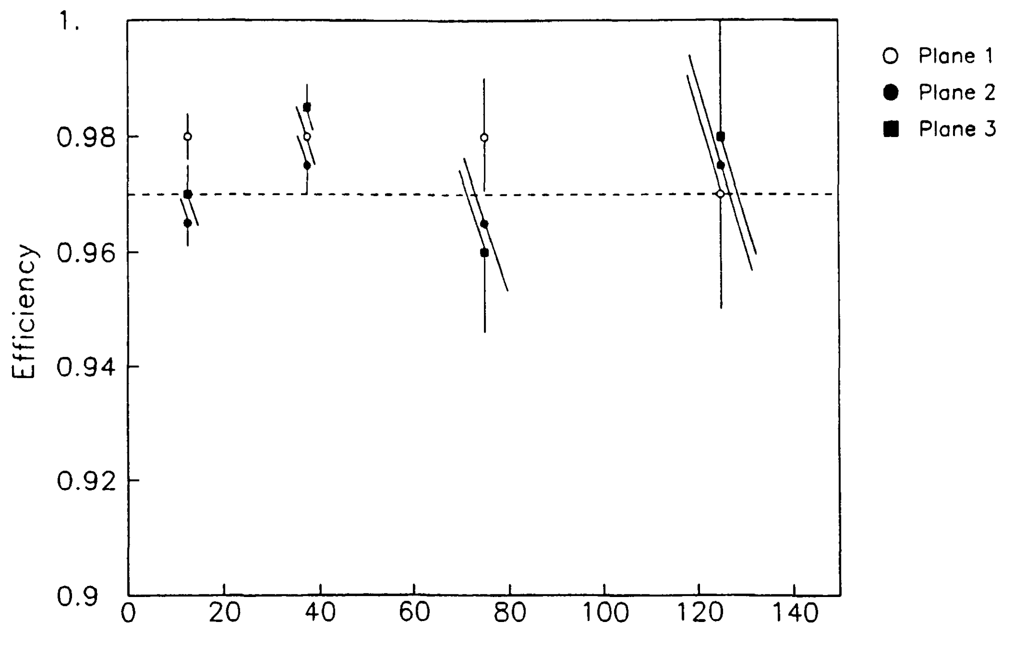

Figure 5.35 *Per-plane efficiency of the microstrip detector*

IV Summary

The experiment ran for a total of 105 days during 1985 and 1986. Over this period 17·2 million triggers were taken, selecting hadronic interactions of the photon.

As a result of experience gained during a prototype run in 1984, the microstrip detector was modified to improve the stability of the read-out electronics for the data-taking runs. The upgraded detector was operated successfully during the runs, with 9937 of its 10,000 channels operational. The noise and charge sharing were low, and the measured spatial resolution of ~ 16 μm is close to the ideal value for a 50 μm strip pitch. The per-plane efficiency was ~ 97 %, and the detector functioned reliably throughout the data taking periods.

In the following chapter, the first stages in the analysis of the data taken will be described, including the data reduction, and the reconstruction of tracks in the spectrometer.

Chapter 6

DATA PROCESSING

The raw data from the experiment are written to tape, as described in the previous chapter. The data take the form of *digitisings*—wire addresses, digitised pulse heights and so on—that are read from the apparatus. To analyse the events, it is necessary to reconstruct the kinematic variables of the tracks that gave rise to the digitisings, and then to identify the particles concerned. This comprises the data processing. The physics analysis may then proceed, using mass combination calculations and so forth, as will be described in later chapters.

The reconstruction of charged tracks in the full apparatus, known as the *production*, is a complex task. It is consequently rather slow, and requires substantial computer resources. Instead of running the production on all of the data, a *filter* may first be run, to select events of interest. It is also useful to have a fast version of the production, or *preproduction*. These various features of the data processing are discussed in this chapter.

I Computing

The use of computers is widespread throughout the whole of high energy physics. This is due partly to the nature of the data involved (which take the form of a large set of numbers for each event) and also to the complexity of the operations that must be performed on the data. For example, a particle passing through the apparatus may generate 70 or more digitisings, and the associated track fit will require a correspondingly complex calculation, to reduce the number of parameters to the few required for the track definition (the coordinates of a point on the track, and its vector momentum). There are also an enormous number of repetitive calculations, both within each event and because consecutive events are treated in essentially the same manner. Digital computers are perfectly suited to operations of this nature.

6.1 Programming

The standard programming language used throughout the subject is FORTRAN. The programs tend to be large, and once developed they are often used by many people with only minor modifications. A program handling and editing facility is therefore useful, allowing the selective modification of small parts of a program by individuals, without affecting the other users. This need is filled by various schemes, one of which, *PATCHY*, is used for the NA14 software.

The basic structures of PATCHY are the *pam-file*, a collection of all the standard code, stored in a special format, that is accessible by many users; and the *cradle*, created by each user, which contains control cards to select and modify code from the pam-file, along with any additional code that is required.

The most important pam-files used by NA14 are the following:

GEANT — The Monte Carlo. Separate pam-files are used for the standard GEANT routines, the user-specific routines, and the fragmentation routines.

TRIDENT — The production program.

TYPHON — The preproduction program.

NEPTUN — Everything else (more or less). NEPTUN is the main pam-file of the experiment, with about 100,000 lines of code. It is divided into sections (or *patches* in PATCHY terms) that deal with the analysis of information from each of the detectors that make up the apparatus. Of particular interest to the analysis of this thesis are ACTANL, responsible for a stand-alone active target analysis, and INDANL, providing an analysis of the INDRA Cerenkov.

Data are transferred between the programs in one of two formats: either 'raw-data', as written by the data acquisition computer, or 'EPIO', a CERN standard format designed to ease data analysis where transfer between different computer systems is involved. Generally the data were kept in raw-data format until they were processed through TRIDENT, at which point they were translated to EPIO.

Within each program, the data are read event-by-event, decoded, and stored internally using *ZBOOK*, a dynamic data storage and handling package that stores the information in a one-dimensional array, with associated pointers to the beginnings of sequences (or *banks*) stored in a second array. A particular bank may be simply accessed by determining the required pointer, and then reading from that position onward in the first array.

6.2 Computers

The computer resources required for an experiment are typically divided amongst the following activities: program development, producing Monte Carlo events, running filters, preproduction, production and physics analysis jobs. For NA14, the overall time used was dominated by the production.

The computers available to the collaboration for offline work are distributed amongst the various associated institutes. The IBM 3090 computer at CERN is important because of its central situation. Another of these machines is available at the CCPN institute for the use of our French collaborators, and was used for a large proportion of the production. At Imperial College, the IBM 4341 is less powerful, and was not suitable for extensive production. Instead it was used for program development, and for some of the final analysis of the data.

Recently an *emulator* facility has become available for our use at CERN. An emulator has the processing power of the computer that it emulates, whilst having much reduced *I/O* facilities, and consequently being much less costly. The *I/O* is handled by a *host* computer. At CERN, a *farm* of seven 3081/E emulators is used, all under the control of the same host, an IBM 4361. This facility has a processing power of about twice that of the main CERN IBM, and is dedicated solely to its user, whilst the central computer is a multi-user system; the production of NA14 takes about 0·85 s per event on the emulators [89], compared with 1·8 s on the main CERN IBM. Although the facility was available too late for the production of the filtered data, it has been used to run the production on some raw data for a determination of filter efficiencies and biases.

The timing of programs will be given in terms of the time taken on the main CERN IBM. This corresponds to a power of about 5 standard IBM 168 units.

6.3 The Monte Carlo

A Monte Carlo is essentially a simulation of the experiment that is run on a computer. Information about the apparatus and the underlying physics events is incorporated into the simulation, and random numbers are generated by the computer to simulate those parameters of the events which are not specified.

Monte Carlo events may be used to measure the performance of the experiment, both during the design of the apparatus, and for optimisation of the software used in the data analysis. The underlying event may be arranged to simulate whatever property is under investigation, or equally to simulate the background, and the efficiency of event selection criteria may be determined from a comparison of the results. The Monte Carlo is also used for the measurement of detector efficiencies, and acceptances, and may be used to predict physics results (as seen in Section 2.9).

The event generation is of either hadronic (non-charm) events or charm events. The non-charm events are produced in line with the Vector Meson Dominance model of photon interactions: the photon materialises as vector meson (via a quark-antiquark pair of up or down quarks) which then interacts with the target nucleon, as illustrated in Figure 6.1. The generation of charm events proceeds via gamma-gluon fusion, as

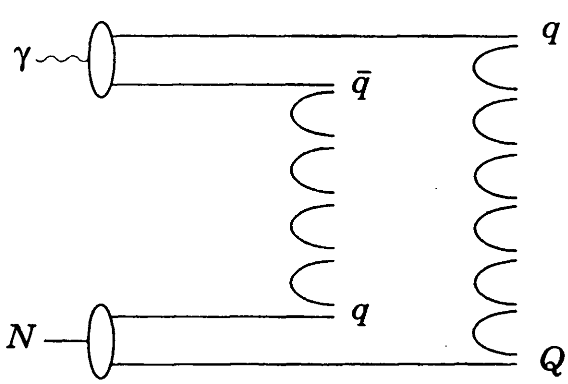

Figure 6.1 *Non-charm event production*

discussed in Section 2.7. The hadronisation of the interaction products is simulated using the Lund Monte Carlo [41] (the JETSET pam-file, version 6.01). For both classes of event simulation the beam energy spectrum is taken into account, and for gamma-gluon fusion the dependence of the charm cross-section on energy is considered.

The interactions take place in the target, and the products are tracked through the other detectors of the apparatus. The Monte Carlo used by NA14 for detector simulation is GEANT [90] (version 2). This is a large, standard program, which has provision for user-defined routines that describe the materials and layout of the apparatus. Multiple scattering and electronic noise are included in the simulation. Other features include the generation of grey tracks in the target, charge sharing in the microstrips, and the effect of the OR-gate used in the microstrip detector read-out electronics. A simulation of the experimental trigger (Section 5.10) may also be used.

Events with a specific charmed particle may be produced by generating gamma-gluon fusion events and selecting only those events in which the particle is present, for tracking through the apparatus and output to tape. The decay mode may be specified by choosing suitable branching ratios for the simulated decay. This allows the response of the detector to a particular channel to be studied efficiently.

6.4 Display programs

The visual scanning of events is an important part of the analysis. It permits the direct interpretation of the data, and gives an insight into such processes as track and vertex finding. Unusual occurrences (such as a Monte Carlo track that is not reconstructed due to an error in the track finding routines) may be displayed and the cause readily determined. The visualisation of event topologies is useful for suggesting new approaches to follow in the analysis: in particular, candidate events of the 'signal', either from real data or Monte Carlo, may be compared with the events that form the background, and suitable cuts chosen.

Tektronix display

Some of the displays produced with the Tektronix event display package have already been shown (Section 4.8). The package was created to display the information from the vertex detector: the microstrip detector and the active target. It is based on standard

HPLOT [91] routines, that handle the manipulation of a special Display file in which the pictures are stored, and provide a limited set of graphics facilities, such as the drawing of specified straight lines and numbers. These are organised into a modular set of routines, designed to be used as a program library for NEPTUN analysis jobs. Each routine has a well defined purpose, such as initialisation, the drawing of the detector outlines, or the drawing of tracks. A sequence of calls to these routines within a NEPTUN job then causes the creation of the required display. This arrangement allows the user to select which events are of interest within the NEPTUN job, and then to write them out. The created Display file is either viewed in a straightforward manner on a Tektronix graphics terminal, or printed using a Benson plotter.

The displays are made of the detectors in projection—the Y- and Z-projections are used. There are the facilities of both 'zoom' and 'pan': an arbitrary origin and independent scales for the two axes of the pictures may be specified. Various types of display were developed:

(i) *Overall view of the detector.* This has already been described (Figure 4.23). It gives a hit/no-hit display of the target information;

(ii) *Active target display.* The pulse height of each strip recorded, in units of I_{min} as was seen in Figures 4.5 and 4.6;

(iii) *Vertex display.* See Figure 6.2. The calculated positions of the primary vertex and any secondary vertices are shown, along with the corresponding errors; the vertices are marked with an error ellipse that represents 1 σ. The tracks that belong to each vertex are drawn so that they start at the x-coordinate of the vertex; in the event displayed in Figure 6.2, the secondary tracks are marked dashed, and the 'charm' track (Section 8.2) dotted. The active target hits are also marked, with the pulse height written below each hit. The procedures used to find the vertices will be described in the next chapter.

As more use was made of the displays it became clear that a different philosophy for the package would be more suitable. The turn-around time of a NEPTUN job is often substantial, typically 10 minutes or more even for a simple job. If an event display was found to have features of interest, it was often desirable to produce more displays, to investigate those features further. To do this more efficiently, the display package was reorganised to give interactive control of the displays. Instead of directly producing a display file in the NEPTUN job, a 'Picture' file was created instead, which contained all the relevant information for each event that was to be displayed: the number of tracks, the

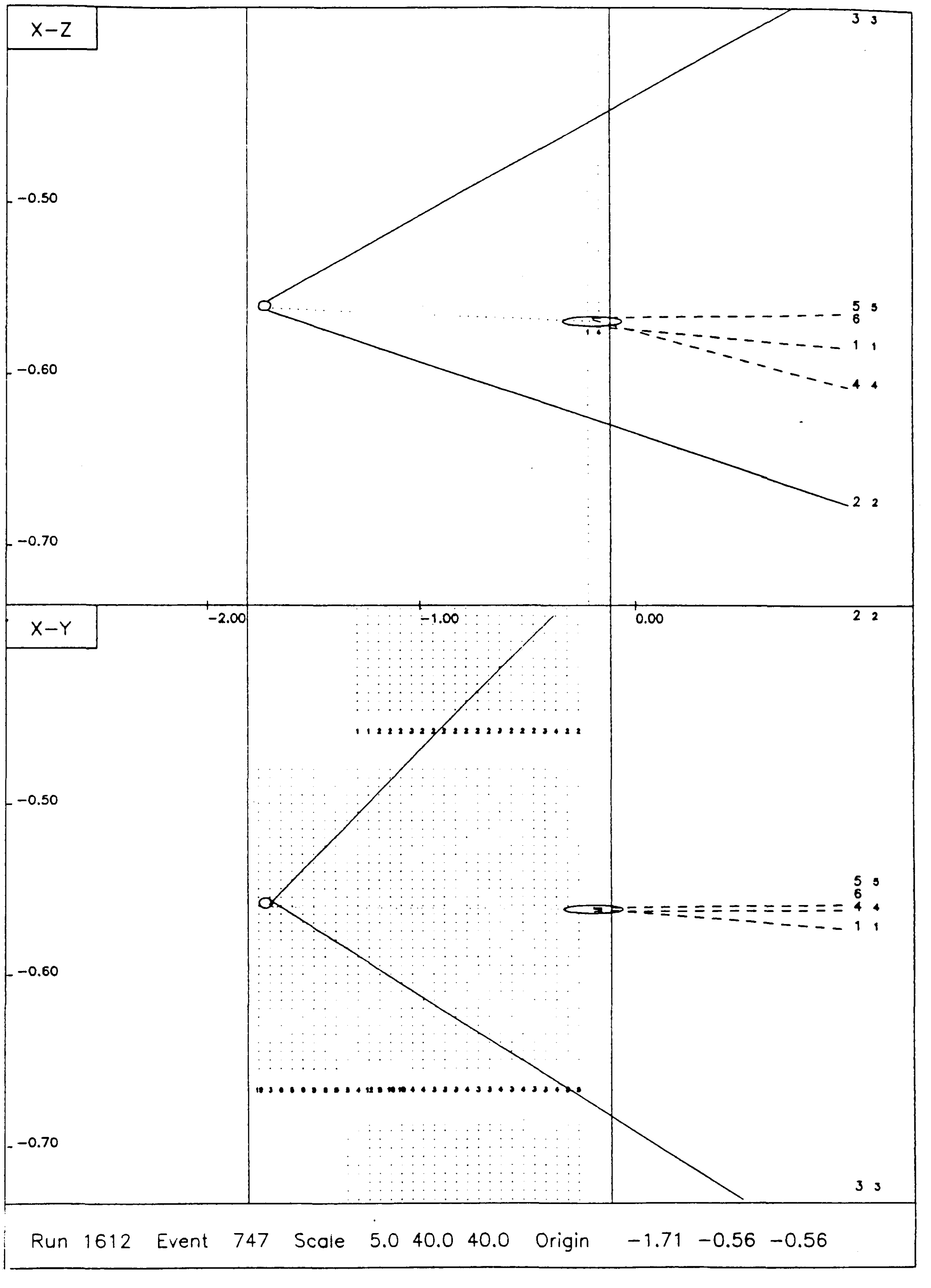

Figure 6.2 *Vertex display of a D_s candidate*

microstrip hit coordinates, and so on. This file could then be read by a stand-alone display program, which is run on a Tektronix terminal and uses the display package routines. The parameters such as the type of display and the scale are entered interactively, and the picture that is created is immediately displayed. Any modified display that is required may then be produced without delay.

Megatek display

An event display package was also developed for use with a Megatek system [92]. It uses a similar philosophy as the interactive Tektronix display package, with a Picture file (created by a NEPTUN job) that is transferred to the Megatek for the interactive display of events; the same Picture file as for the Tektronix display is used.

The advantages of the Megatek include its three-dimensional capability, and a colour display. The three-dimensional facility allows the user to 'rotate' the display in real time, relatively smoothly, under joy-stick control. This is often an aid to the visualisation of the event topology. The colour display enables different features to be easily distinguished: for example the microstrip hits that are the OR-images of hits on tracks may be indicated in a different colour. Some disadvantages were that the level of zoom available was limited, resulting in a poor resolution for vertex analysis; and there was only a single Megatek available, whilst the other package could be run on any of the common Tektronix terminals at Imperial College or CERN.

6.5 Preproduction

The first operation carried out on the tapes of data recorded by the on-line computer is to copy them to high density tape. They are originally recorded at a density of 1600 *bpi*, so copying to 6250 *bpi* allows about 3 times the number of events to be stored on a single tape. It also allows the data to be compressed, if the low density tapes were not completely filled due to the premature ending of runs.

As noted above, the running of the production on the full data-set was not feasible, so at this stage various filters were run on the data. They will be described in the next part of the chapter. Some of them utilise a fast version of the full production, known as TYPHON, that does a simplified pattern recognition using a subset of the wire chambers.

For the runs in 1986, sufficient computing resources were available for TYPHON to be run on *all* of the data. This was performed at the same time as the compressing job, so that the high density tape, when written, included the results of the TYPHON analysis as an additional block appended to the data. It was possible to run the preproduction sufficiently quickly that it kept pace with the data taking.

The operation of TYPHON is discussed in Section 6.10. First, the various filters used by the experiment are described.

II Filters

The rôle of a filter is rather similar to that of the experimental trigger. It is responsible for the selection of events that are of interest for a particular line of analysis. The obvious difference, however, is that an event rejected by the trigger is not recorded, whilst an event rejected by any particular filter is still available on tape for later use.

Filters are necessary since the production takes about 2 s per event on the CERN computer, so to process the entire data-set on that machine would take about a year of uninterrupted processing. This would result in unacceptably slow analysis of the data, and was beyond the resources of the collaboration. Instead, filters are run on the full data-set, and only those events that pass their requirements are written to the output tapes. They are designed to give a fast decision, and to select events of interest to a particular line of analysis. The output tapes are then processed through the production.

A number of different filters were used by the NA14 collaboration. Some were quite specific: for example the electron filter, designed to select events with an electron in the final state, for the study of semileptonic decays of charm. Others were less specific, such as the microstrip filter described below, which used the general property of offset tracks to identify events with short lived decays. A description follows of the two filters which are of direct relevance to the analysis presented in this thesis, and a brief sketch is given of the others.

6.6 The kaon filter

The information from the preproduction permits the construction of a simple filter to select events with kaons in the final state. This is useful because, as shown in Chapter 2, there is a high probability that a charmed quark will decay to give a strange quark. Events containing charm are therefore expected to exhibit enhanced strangeness, which is generally seen as kaon production: examples include $D^0 \rightarrow K\pi$, and $D^{\pm} \rightarrow K\pi\pi$. The filter criteria were as follows:

- at least two good TYPHON tracks
- at least one TYPHON identified kaon

'Good' tracks for this purpose are tracks that have been reconstructed on both sides of the Goliath magnet. They are known as 'flag 4', where the track flags of TYPHON follow the same definitions as those of TRIDENT (given below in Section 6.9). A TYPHON identified kaon is defined as a track of TYPHON flag 3 or 4 that passes through the INDRA Cerenkov, gives no light, and has momentum in the range 6–50 GeV/c. This wide momentum range (compared with that used in the standard INDRA Cerenkov analysis, Section 6.11) is necessary due to the relatively poor momentum resolution of TYPHON compared with TRIDENT. It also results in the inclusion of candidate protons in the filtered data sample.

This filter was run on the full data-set of 17 million events, and passed ~ 7 % of the data, giving ~ 1·2 million events output. It took about 100 ms per event, taken mainly by the running of TYPHON. The efficiency of the filter was determined [93] using events that were known to contain kaons (they had been selected to contain ϕ-mesons, with $\phi \rightarrow K^+K^-$), and was found to be ~ 75 %.

6.7 The microstrip filter

The purpose of a microstrip filter is to recognise events with short-lived decays by utilising the accurate tracking information of the detector at the vertex. The decay may be recognised either by the offset of the decay tracks from the primary vertex, or by a reconstruction of the secondary vertex, and its separation from the primary.

The microstrip filter run at Imperial College [84] was designed to be independent of the rest of the apparatus. In particular, no information from the MWPCs is required. The first requirement of the filter is therefore pattern recognition, to recognise the tracks passing through the detector. Then the tracks must be fit, a vertex formed, and the offset of the tracks from the vertex investigated.

As the program is to run as a filter, it is essential that it is fast. Exhaustive pattern recognition is therefore impossible, and instead a compromise must be reached between track finding efficiency and speed. Rather than a full error analysis, in the calculation of separations in space used in the filter the coordinates concerned were weighted according to the associated uncertainty: the weights used $x : y : z$, were 0·05 : 0·5 : 1. Although the intrinsic spatial precision for the y- and z-measurements is the same (~ 16 μm), the factor of 2 between their weights reflects the loss in precision of the trajectory in the Y-projection due to the momentum being unknown, since the production has not been run at this stage. This affects the Y-projection since it is the bend plane of the magnetic field.

Tracks in projection

The microstrip hits are *clusterised*: clusters of 2 or 3 hits are merged to give a single point for the pattern recognition, as they can arise from a single track in a well understood manner; larger clusters are not merged. The *OR*-image of clusters of greater than 2 hits are removed, but those of 2 hit clusters are not, due to the significant probability of random formation. In the Z-projection, tracks are fitted as straight lines. They are found by taking pairs of hits on the first and last planes of the projection and looking for hits in the intermediate planes within 80 μm of the predicted position.

In the Y-projection, a similar procedure is used, but with a wider cut of 200 μm, to allow for the magnetic bending of tracks. A parabolic fit to the hits is used, with a 145 μm cut on the sagitta (see Figure 6.3). This corresponds to rejecting tracks with energy less than about 1·5 GeV, which (due to multiple scattering) are likely to give a false offset when extrapolated back to the primary vertex. A parabola is used rather than a circle, as it is faster to compute.

Tracks in space

The tracks found in the two projections are matched using the inclined U- and V-planes. For each pair of tracks, a hit position is predicted on the U-plane and the V-plane. If a hit

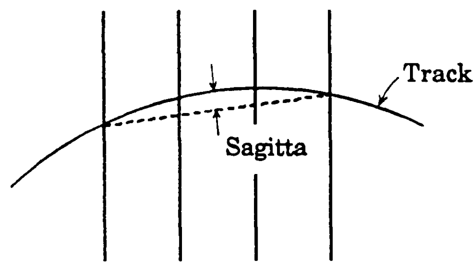

Figure 6.3 The sagitta of a track

is found within 110 μm on the U-plane and 150 μm on the V-plane, then the projection track pair is flagged as 'validated', and is likely to be the result of a real space track. There is, however, generally more than one track of the orthogonal projection with which any given projection track might be matched. One of these possibilities must be chosen. This is achieved by entering into an *assignment matrix* the residual calculated (from the hit found relative to the predicted position) on the inclined planes. When the residuals from all the validated track pairs have been entered, the matrix is diagonalised [94] to provide the most likely matching of the track projections. With the track projections that remain, matching is attempted using either one of the U- or V-planes.

Primary vertex

The next step of the filter is to construct a primary vertex using the space tracks that have been found. This will then be used to distinguish offset tracks, which may be due to short-lived decays. It is vital that the x-coordinate of the primary vertex is accurate, as otherwise offset tracks are found that are not physical, as illustrated in Figure 6.4. The

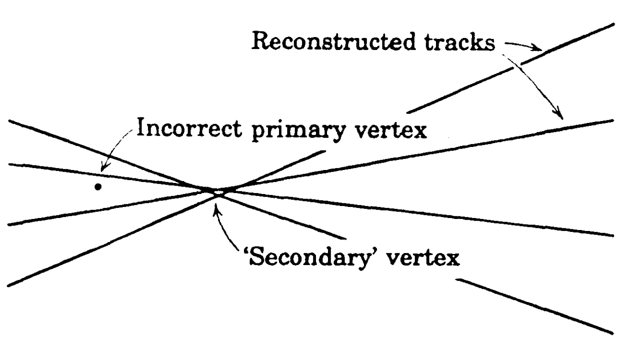

Figure 6.4 Consequence of incorrect vertex finding

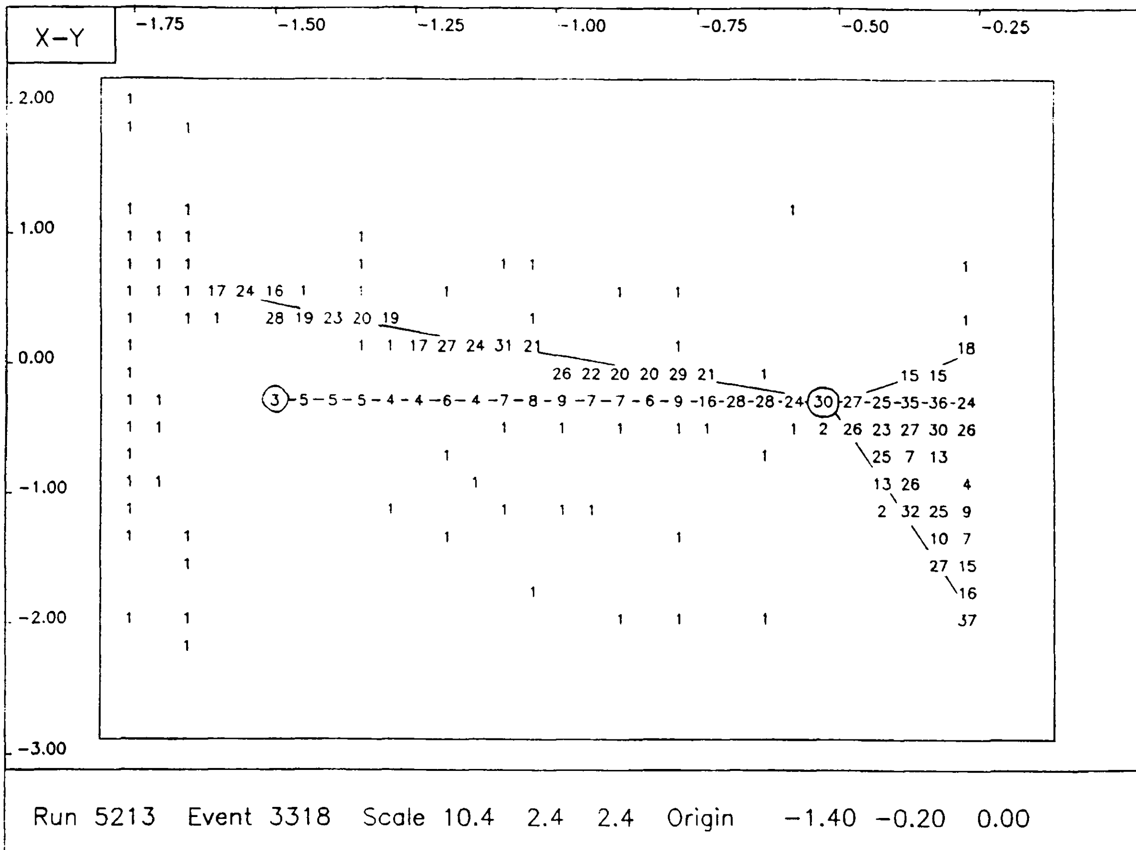

***Figure 6.5** Active target activity in an event with a backward grey track*

tracks from the microstrips are generally at a small angle to the beam axis, and therefore have poor accuracy in the x-coordinate for the reconstruction of the vertex. Instead, the active target was used. If the primary vertex is found in the correct plane of the target, then the x-coordinate is accurate to $\pm$ 150 µm. This, however, is not always the case: it was found that for a significant proportion of events the information from the active target is complicated, and the correct reconstruction of the vertex is difficult. One example of this is where a backward grey track exists, mimicking an upstream primary vertex. See Figure 6.5.

To avoid some of these problems, only those events that passed a simple algorithm for the active target analysis were used by the filter. The algorithm was fast, and selected events such as those shown in Figure 6.6, with a well defined main road that has a large pulse height in the first strip (> 9 I_{min}) due to nuclear recoil, and not too much confusion caused by grey tracks [84]. The x-coordinate of the vertex for these events was more

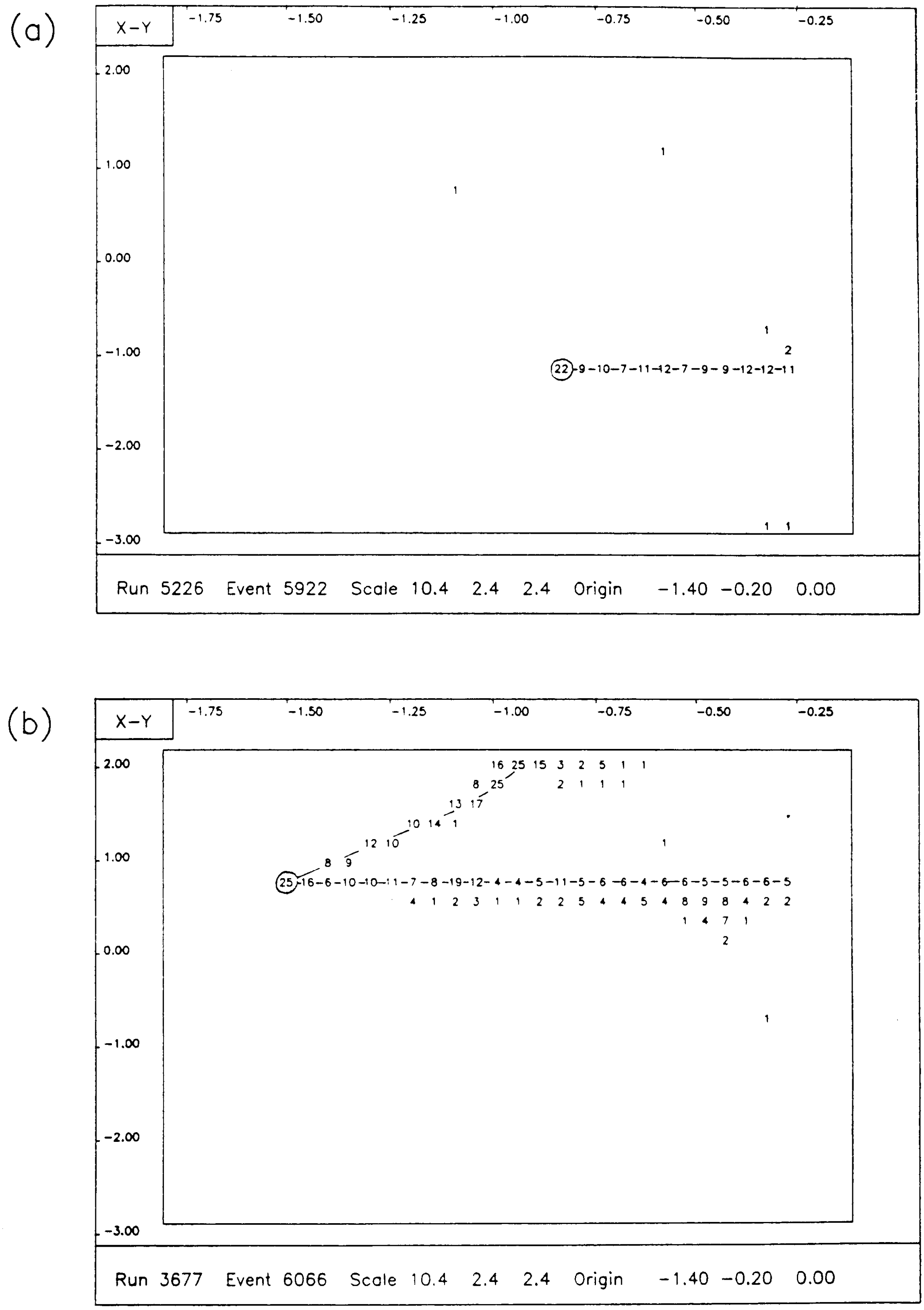

Figure 6.6 *Typical events passing the active target algorithm*

reliable than that of the remaining events, analysed with the full target analysis (ACTANL). This was checked using events with pairs of wide angle (> 50 mrad) microstrip tracks, the intersection of which gives an accurate measure of the x-coordinate of the vertex. This was found to agree more frequently with the active target measurement of the vertex x-coordinate for events that passed (rather than failed) the target algorithm. For events that passed the algorithm, the difference between the two measures of the vertex x-coordinate exceeded 2 mm in ~ 9 % of events, whilst for other events the corresponding figure was ~ 15 %. The target algorithm selected ~ 23 % of the data.

The y- and z-coordinates of the vertex were then found by taking the average of the corresponding coordinates of the tracks, at the x-coordinate of the vertex. If any track was offset from the vertex by more than 60 µm, then the most offset track was rejected from the vertex calculation, and the vertex position recalculated. The offset of tracks from the primary vertex in the two projections is shown in Figure 6.7.

Secondary vertex

Offset tracks were defined as any track that passed more than 80 µm from the primary vertex. Secondary vertex reconstruction could then be attempted using an offset track plus any other track (or another offset track, according to the filter criterion). The weighted distance of closest approach was measured for the pair of tracks, and the criterion for a valid vertex was satisfied when the track separation was less than 135 µm. The vertex

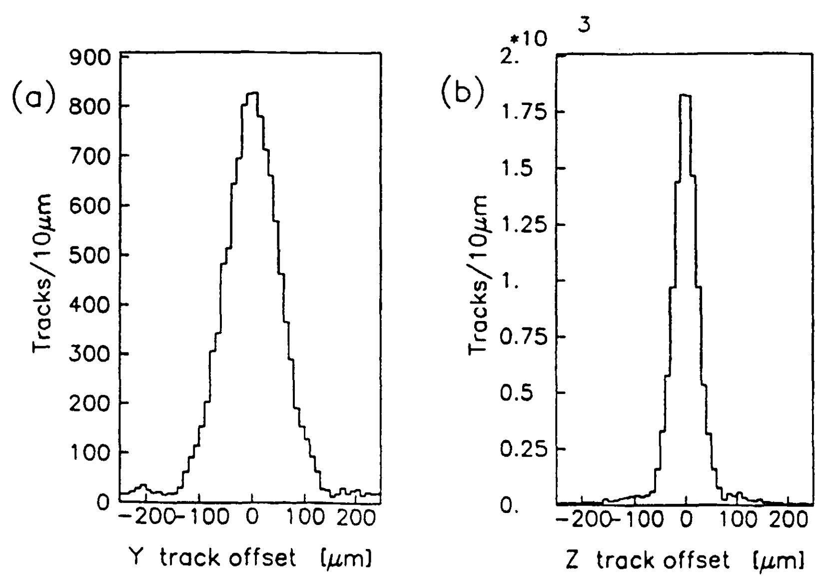

Figure 6.7 *Offsets of projection tracks from primary vertex*

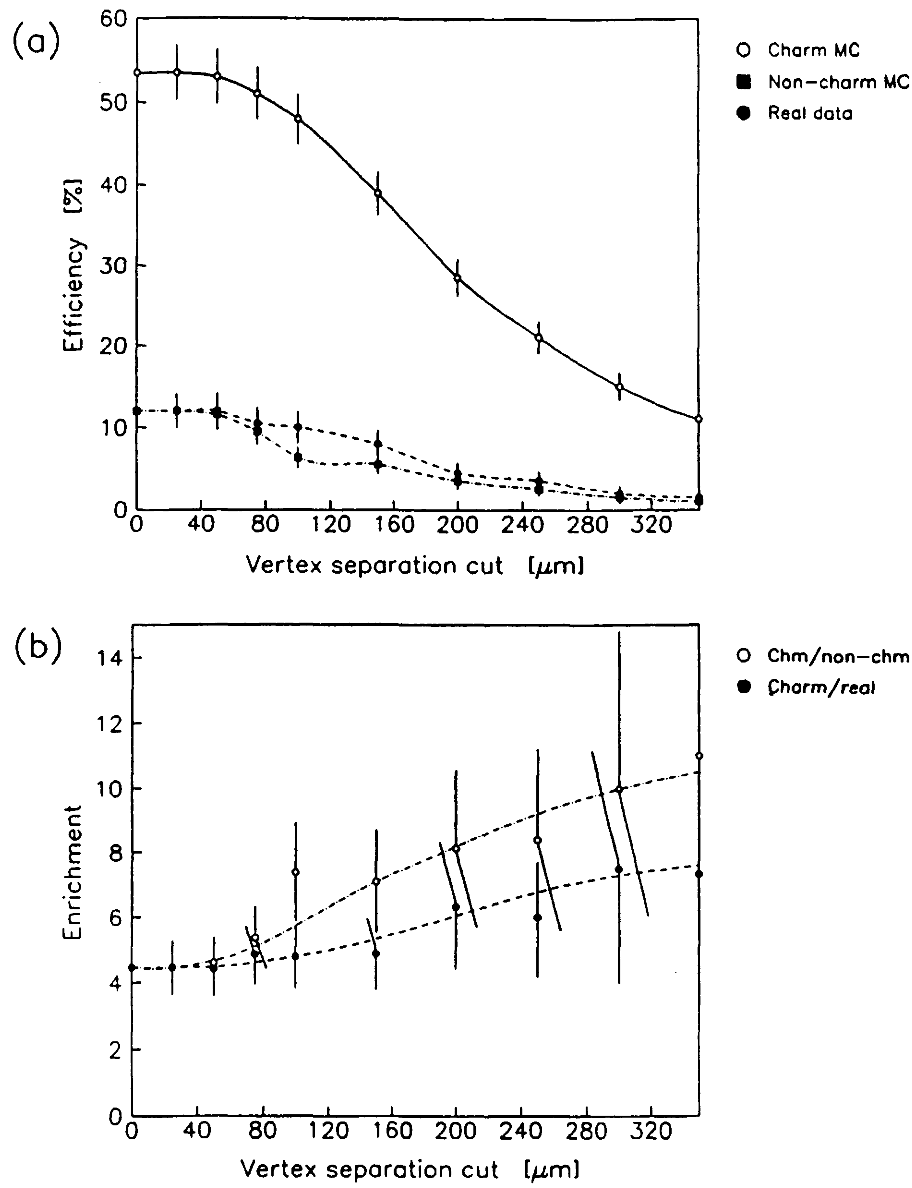

Figure 6.8 *Influence of vertex separation cut on filter performance*

coordinates were taken as the mean of the coordinates of the tracks at the point of closest approach. A cut was then made to ensure that the intersection was not compatible with the primary vertex: the weighted separation in space of the vertices had to be greater than 100 μm, with the secondary vertex downstream from the primary (i.e. at a more positive x-coordinate).

The various cuts used in the filter were tuned using Monte Carlo. Charmed and non-charmed events were run through the filter: the fraction of charmed events that are passed gives the *charm efficiency,* and the ratio of the fractions of charmed and non-charmed events that are passed gives the *charm enrichment*. For example, the influence on the charm efficiency and enrichment of the separation of primary and secondary vertices cut is shown in Figure 6.8. The charm enrichment increases as the cut is increased, and at the chosen value of 100 μm for the cut the requirement does not severely reduce the charm efficiency.

Filter criteria

Various filter criteria were tested using the Monte Carlo, involving different combinations of offset tracks and secondary vertices. The filter chosen represented a compromise between the requirement of a high charm efficiency and maintaining a reasonably high charm enrichment. It was the following:

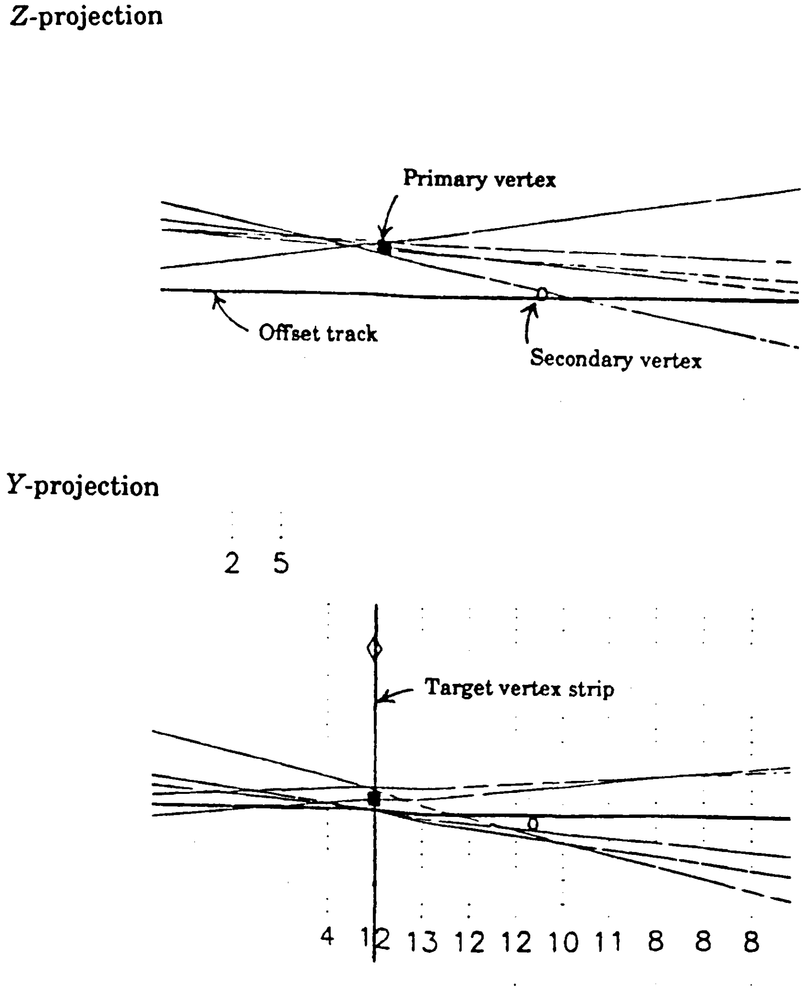

Figure 6.9 *Typical event passing the microstrip filter*

- at least one secondary vertex, formed between an offset track and any other track of the event.

A typical selected event is displayed in Figure 6.9. The charm efficiency for this filter was ~ 40 %, and the enrichment ~ 3. About 12 % of the data passed the filter.

Kaon selection

When the filter was first run, the volume of data passed was still too great for running production rapidly on the Imperial College computer. As the charm channels analysed first would contain a kaon, it was decided to incorporate a further filter to select events with at least one kaon in the final state. This reduced the data-set by a further factor of about 2. The filter was operated in a similar manner to the kaon filter of Section 6.6, using the MWPCs of Stack 2 to provide track segments at the INDRA Cerenkov. When more computer time was available later, the events that failed this kaon selection filter were also run through the production.

The full data-set from the run in the Summer of 1985 was run through the microstrip filter. This corresponded to ~ 5·2 million events. About 160 thousand events were passed by the microstrip filter, and this was further reduced to ~ 72 thousand by the kaon selection. These events remained to be passed through the production. As the raw data tapes were stored at CERN, the filter was run on the CERN computer, and took ~ 10 ms per event.

6.8 Other filters

Post-TYPHON microstrip filter

The microstrip filter described above was designed for use when no information was available from the rest of the spectrometer. For the runs in 1986, however, the preproduction TYPHON was run on all events, so this was no longer the case, and a more comprehensive use could be made of the information available. A filter that was similar in principle to the original microstrip filter was created for this purpose by our Orsay collaborators. It was similarly designed to select events with a complex vertex topology, but now used tracks in the microstrips which were matched to tracks from the spectrometer. The filter was run on the data of the 1986 runs, and ~ 16 % were passed.

Clean target filter

The clean target filter used the active target alone. It was designed to select events in which the information from the target was relatively simple. In particular, a well defined main road was required, unaffected by heavily ionising tracks. These events were suitable for a search for the multiplicity step signature of secondary vertices, and also provided a data-set enriched by coherent production on the silicon nuclei of the target. About 8 % of the data passed the filter.

Electron filters

Run using two of the calorimeters, OLGA and Crown, the electron filters were designed to recognise the presence of an electron in an event. Semileptonic decays of charm could then be investigated. About 6 % of the data passed the filters.

η-filter

The OLGA calorimeter was used to select events that contained an η candidate, for use in the study of channels such as $D_s \to \eta\pi$, $\eta\pi\pi^0$. The η candidates are selected from pairs of photons seen in the calorimeter, with energy greater than 2 GeV and an invariant mass that did not correspond to a π^0. About 6 % of the data was passed by this filter.

The events that were output by these various filters were then passed through the production program, TRIDENT, described in the next section.

III Production

6.9 TRIDENT

TRIDENT is the program responsible for charged track reconstruction in NA14, using the MWPCs and the microstrips. It was developed from a multipurpose program that was originally written for the Omega spectrometer [95].

The hits in the wire chambers are associated to form space points, using groups of planes that are adjacent along the beam direction, but have wires at different orientations, such as a (Y, Z, U, V) arrangement. The space points are then associated to form 'roads' in the spectrometer. In the field-free regions of the apparatus, the tracks are straight lines, and fits are done in the various stacks of chambers: Stack 1 between the AEG and Goliath magnets, and Stacks 2 and 3 after Goliath (as was shown in Figure 3.13). The association of the straight-line segments with one another or with a vertex (by extrapolation through the magnetic fields) gives a momentum measurement. A Runge-Kutta method [73] is employed to swim the tracks through the magnetic fields, for which there are detailed maps.

Incorporating the microstrips

The TRIDENT program had already been used for the pre-upgrade NA14 experiment. With the addition of the microstrip detector, the program was modified [93] to use the new information. The matching of the spectrometer tracks with the microstrips is achieved as follows:

(i) Three and four point tracks are found in projection in the microstrips, using the extrapolated spectrometer tracks. If the momentum is known, it is used for the track finding in the Y-projection (the bend plane). The tracks in projection are then matched using the inclined U- and V-planes (trying first to find hits in both inclined planes, and then to find a hit in either).

(ii) Matched tracks that do not point to the vertex are released, so that their hits may be used again, and they are then refitted using looser cuts.

(iii) The remaining tracks in projection are dropped if they cross matched tracks, or if they do not point to the vertex. Those that are left are matched using the matching of the spectrometer tracks, if they lie outside the acceptance of the inclined planes.

Using this technique, ~ 90 % of the well measured tracks, found both before and after the Goliath magnet (flag 4, see below), are matched with the microstrips.

The results of the TRIDENT processing are output as an extra block of data on tape. This block consists of a vertex bank, giving the coordinates of any vertex found as described below, and a track bank, providing a description of the tracks found. For each track, the information given is sufficient to specify the trajectory. The coordinates of a point on the track are given, along with the two angles that define the trajectory at that point (see Figure 6.10). The *dip* angle λ is the angle of the track about a horizontal axis perpendicular to the track, whilst the *azimuthal* angle ϕ is the angle in the Y-projection.

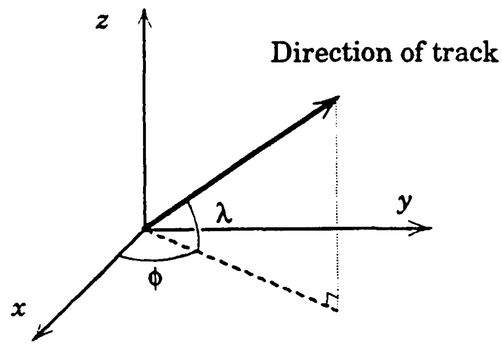

Figure 6.10 *Track angles*

The particle momentum is also specified. It is then possible to calculate the coordinates of the track at any x-coordinate, by following the trajectory of the track, so long as the value of any magnetic field encountered is known. The basic track parameters are thus $(y, z, 1/p, \lambda, \phi)$ at a specified x-coordinate.

The track parameters each have an associated error. Since these errors may be correlated, they are described using a square matrix that gives the value of the error associated with each pair of parameters. The inverse of the momentum, $1/p$, is used rather than p in the track parameterisation, because it is $1/p$ that has a Gaussian error.

Vertex association

The well measured tracks reconstructed by TRIDENT (flags 4, 22, 23 and 24, see below), are used to form a vertex. An attempt is then made to associate all tracks with the vertex, and those which are compatible with it are flagged as 'fitted'. The remainder, which may either be poorly reconstructed or valid offset tracks (due to halo muons or electromagnetic background for example), are flagged as 'extra' tracks.

Track flag	2	3	4	12	13	22	23	24
$\Delta p / p^2$ [10^{-4} GeV^{-1} c]	60	20	5	–	–	20	3	4
Fraction [%]	17	5	6	9	4	25	4	30

Table 6.1 *Momentum precision of tracks*

TRIDENT track flags

Each track found by TRIDENT is given a track flag, that indicates the manner in which it was formed. The meaning of the TRIDENT track flag is as follows:

2	Track segment is found in Stack 1 only. The momentum is measured by the association of the track to the vertex, using the bending of the AEG field.
3	Track segments are found in Stacks 2 and 3 only. The momentum is measured by the association of the track to the vertex, using the bending of both the AEG and Goliath fields.
4	Track segments are found in all stacks. The momentum is measured by the association of track segments on either side of the Goliath magnet, using the bending of the Goliath field, improved when possible by the association of the track to the vertex, using the bending of the AEG field.
12, 13	As for flags 2 and 3 respectively, but with no association to the vertex, so no momentum measurement.
22, 23, 24	As for flags 2, 3 and 4 respectively, but in addition a track segment is found in the microstrips. The momentum measurement for tracks of these flags is therefore most accurate of all (see Table 6.1). They form the basis of most of the subsequent analysis.

There are typically twelve TRIDENT tracks found per event, with ~ 50 % fitted. The relative abundance of tracks with the different flags is shown in Table 6.1. Note that the microstrip matched tracks (flag greater than 20) account for ~ 60 % of all the tracks found. A reconstructed event is shown in Figure 6.11, with tracks of different flags (pre-microstrips) marked.

TRIDENT takes about 1·8 s per event.

6.10 TYPHON

TYPHON was written specifically for NA14. It is designed to provide fast reconstruction of charged tracks using the hits in 45 of the MWPC planes. The technique used is similar to that of TRIDENT (described above), but it is faster, both due to the use of fewer planes of the detectors, and because the analysis of the track propagation through magnetic fields is simplified: the fields are approximated using a thin-lens type formula. As a result the

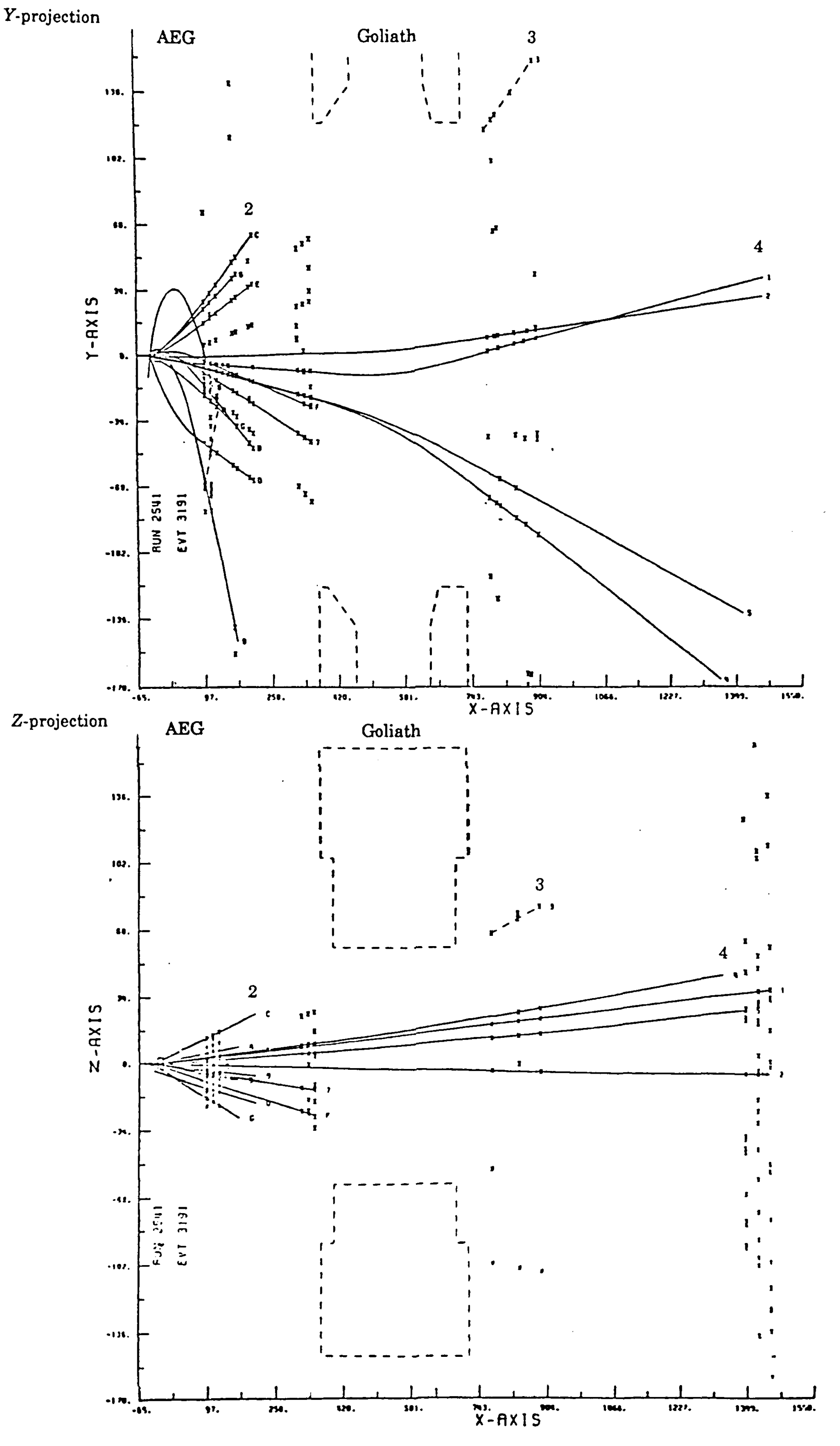

Figure 6.11 *Reconstructed event after TRIDENT processing*

momentum precision is lower than that of TRIDENT, with:

$$\frac{\Delta p}{p} \sim 0{\cdot}05\,p\ \ \mathrm{GeV}^{-1}c$$

The microstrips are not used by TYPHON. Instead, it assumes that the vertex is at the centre of the AEG, in order to provide a momentum measurement for flag 2 tracks (which do not pass through the Goliath magnet).

TYPHON takes ~ 90 ms per event.

6.11 The Cerenkov analysis

Analysis of the information from the INDRA Cerenkov takes place in the INDANL patch of NEPTUN. The charged track reconstruction must already have been performed. The tracks are associated with the Cerenkov data to give particle identification, and the results of the analysis may then be written to the output tape. There are two approaches to the use of the Cerenkov information, either threshold or probability mode.

Threshold mode

The threshold mode is the simpler and faster of the two, and was used for the analysis presented in this thesis. The mirror of the Cerenkov through which each track passes is

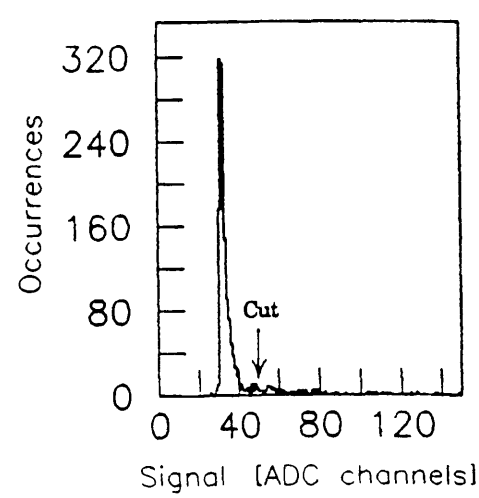

Figure 6.12 *Cut for the definition of light in INDRA*

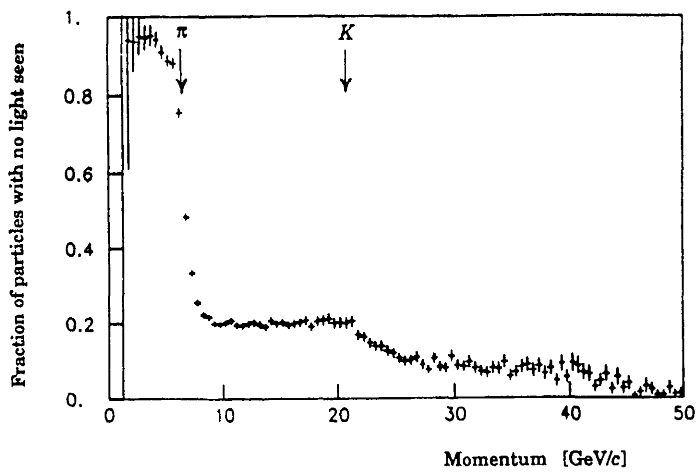

Figure 6.13 *Variation with momentum of the fraction of particles giving no light*

identified, and the ADC of the corresponding photomultiplier is checked to see whether there is a signal. The light signal is determined using the pedestal and gain of each ADC channel from the calibration. Light is defined as:

$$(data - pedestal) > 13 \text{ channels}$$

This corresponds to a cut at about 0·5 photoelectrons. See Figure 6.12. The production of Cerenkov light by a particle depends on its velocity (as explained in Section 3.9), and each particle type has a characteristic threshold momentum, listed in Table 3.8. The variation with momentum of the proportion of particles giving no light is shown in Figure 6.13 for the INDRA Cerenkov. The thresholds for light production by pions and kaons are clearly visible. The particle type may thus be determined from a knowledge of the momentum of the particle, and whether light has been produced, using the assignments shown in Table 6.2.

	e	π	K	p
Light	0–4 *	6·5–19		
No light		0–5	6·5–20	21–38

* Momentum limits in units of GeV/c

Table 6.2 *Standard particle type assignments*

	e	π	π/K	K	p
Light	0–6 *	6–20	> 20		
No light		0–5	5–6·5	6·5–21	> 21

* Momentum limits in units of GeV/c

Table 6.3 *Extended-kaon particle type assignments*

The identification of kaons is important for many charm channels, as discussed in Section 6.6. In the standard, unambiguous, assignments of Table 6.2 there is only a restricted region over which kaons are identified. Alternative assignments were proposed that improve the efficiency of kaon recognition, with an extended kaon definition, shown in Table 6.3. A new class of identification is introduced, the ambiguous kaon, π/K. Particles assigned this identification are used in the analysis as either pion or kaon. Particles that are outside the acceptance of the Cerenkov are classed as pions, as they are the most abundant particle type.

Confusion may arise when more than one track passes through the same mirror, and these events are flagged accordingly. Even then, information is still available, for example if no light is recorded in the mirror, then clearly *none* of the particles have generated light.

Probability mode

The probability mode involves a more detailed study of the generation and detection of the Cerenkov light. A Monte Carlo technique is used to predict the distribution of light at the photomultipliers of the detector produced by a track, assuming that it is each of the common particle types (e, μ, π, K, p) in turn. Then a statistical analysis of the probability of each particle type giving rise to the observed signal is performed. This technique is slower than the threshold analysis, and produced no convincing improvement in efficiency, so was not used here.

The data that have passed the various filters, and have been run through the production, are now ready for charm analysis. One of the most important aspects of this is vertex finding, the subject of the next chapter.

Chapter 7

VERTEX FINDING

This chapter describes the techniques employed for vertex finding. The microstrip detector gives a high precision measurement of tracks close to the target, and we wish to reconstruct the vertex (or vertices) from which the tracks originate. A thorough description of the vertex finding procedure is given here, both due to the importance of the subject, and because I was responsible for writing and developing the vertex finding algorithms.

The vertex structure of an event is the most important characteristic used in the analysis to identify charmed particles: the short-lived particles give rise to decay vertices that may be resolved from the production vertex. It is this property that was exploited in the microstrip filters to enrich the data-set with charmed events, as explained in the previous chapter. Accurate vertex reconstruction is, therefore, an essential part of the analysis. It was found that the careful adjustment of the vertex fit parameters was the most critical operation for enhancement of charm signals.

In the course of the data analysis, two approaches to vertex finding were developed; both will be described as each was found to have features of merit:

(i) *The 'Intersection' vertex:* the algorithm that was initially developed. The vertex is found using the pairwise intersections of tracks. It has the advantage of simplicity, and was found to be suited to the analysis of events that pass the microstrip filter.

(ii) *The 'Constraint' vertex:* this was originally developed to improve the mass resolution, and was then extended to form a complete vertex package. It involves constraining the tracks (with reference to the errors on their parameters) to pass through a common point, which is then taken as the vertex; it gives a consistent use of the errors on the track parameters, and makes optimal use of the available information, at least at the single vertex level.

One of the most difficult problems of the charm analysis is deciding which tracks originate from any particular vertex. In a typical charm event, a charmed quark and antiquark are produced at the primary vertex and form short-lived charmed particles that decay, giving rise to two secondary vertices. In addition, there are further tracks from the primary vertex; and there may be spurious ghost tracks caused by incorrect pattern recognition in the tracking detectors. See Figure 7.1. The study of a particular charmed particle therefore involves the correct selection of the tracks that form its decay vertex. Furthermore, the correct choice of tracks from the primary vertex must be made, so that the separation of the decay vertex from the primary vertex can be determined. It is therefore necessary to reject offset tracks from the calculation of the primary vertex. In particular, the tracks from the 'second charm' (i.e. the charmed particle that has not had its decay vertex reconstructed) will tend to pull the primary vertex downstream from its true position, towards the secondary vertex.

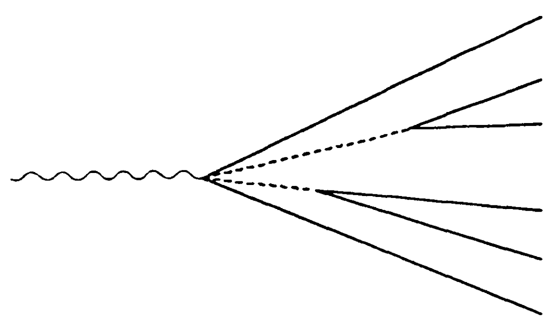

(a) Underlying event

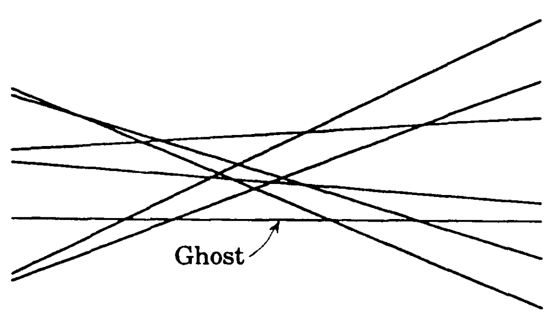

(b) Reconstructed tracks

Figure 7.1 The task of vertex reconstruction

The choice of tracks to be used for the reconstruction of a given vertex is difficult. It is deeply involved with the strategy for the enrichment of the charm signal, and that discussion is left to the next chapter, when the charm analysis will be described. Here a description is given of the vertex finding algorithms, assuming that the track selection has been made. The vertex finding algorithm uses the selected tracks to form a vertex, and provides some measure of its success. If the vertex formed is considered unsatisfactory, then the track that is least well associated with it may be rejected, and a new calculation made.

First it is necessary to describe the tracks that will be used in the analysis.

I Tracks

The charged track reconstruction is performed by TRIDENT, as described in Section 6.9. The hits in the microstrips are used, as well as those from the wire chambers, so that the spatial precision of the microstrips is matched with the momentum measurement and particle identification capability of the rest of the spectrometer. In the course of reconstruction, TRIDENT uses the tracks found to form a vertex, which is used in turn to improve the momentum measurement of the tracks, where possible.

The TRIDENT vertex is not suitable for use in the charm analysis, since the tolerance on the track offset for acceptance in the vertex calculation is sufficiently loose that tracks from short-lived particle decays are accepted, rendering the vertex inaccurate. It is also important that the tracks which are to be used in a particular vertex calculation may be freely selected.

The tracks reconstructed using TRIDENT are not used directly in the analysis. When TRIDENT was modified to incorporate the microstrips, the early versions used the vertex in the track fit, thus potentially distorting offset tracks; in later versions, there were problems with the procedure for matching track segments in the microstrips with those in the spectrometer, which gave rise to tracks that were badly fitted in the microstrips. A refit procedure was therefore introduced, to ensure that the microstrip fit was good.

7.1 Trajectory calculation

The tracks that are found by TRIDENT are specified using the parameters $(y, z, 1/p, \lambda, \phi)$, as discussed in Section 6.9. This will be referred to as the TRIDENT parameterisation. The parameters are defined at the first measured point on the track, which for a track that has been matched in the microstrips is the first microstrip hit. In the course of the analysis it is necessary to calculate the track parameters at different points along the track, so the relationship between the parameters at different x-coordinates must be determined.

If we take the starting values at x-coordinate x_0 as $(y_0, z_0, 1/p_0, \lambda_0, \phi_0)$, then we wish to calculate the values $(y, z, 1/p, \lambda, \phi)$ at arbitrary x. If energy loss processes are neglected, which is a good approximation in the vertex detector, the momentum is independent of x. Therefore:

$$1/p = 1/p_0$$

The variation of the other parameters may be found using the equation of motion:

$$\boldsymbol{F} = \frac{\mathrm{d}\boldsymbol{p}}{\mathrm{d}t}$$

The force on a particle of charge q travelling through a magnetic field $\boldsymbol{B}$ with velocity $\boldsymbol{v}$ is:

$$\boldsymbol{F} = q\,\boldsymbol{v} \times \boldsymbol{B} = \frac{q}{m}\boldsymbol{p} \times \boldsymbol{B}$$

Therefore:

$$\frac{\mathrm{d}\boldsymbol{p}}{\mathrm{d}t} = \frac{k\,q}{m}\boldsymbol{p} \times \boldsymbol{B} \tag{7.1}$$

where the constant k is introduced to permit the use of suitable units: if p is in GeV/c, B in Tesla, m in GeV/c^2 and q is the sign of the charge (± 1), then $k \sim 0{\cdot}003$.

Referring to Figure 6.10, we may put:

$$p_x = p \cos\lambda \cos\phi \tag{7.2}$$

$$p_y = p \cos\lambda \sin\phi \tag{7.3}$$

$$p_z = p \sin\lambda \tag{7.4}$$

The dependence of the angular parameters on x is found by substituting these equations into the components of Equation 7.1. One finds:

$$\frac{\mathrm{d}}{\mathrm{d}x}(\sin\lambda) = -\frac{kq}{p}(B_y - B_x \tan\phi)$$

$$\frac{\mathrm{d}}{\mathrm{d}x}(\sin\phi) = \frac{-kq}{p\cos\lambda}\left[\tan\lambda\,(B_y \sin\phi + B_x \cos\phi) - B_z\right]$$

In the region of the vertex detector, the magnetic field (from the AEG magnet) is approximately constant, and oriented along the z-axis. So $B_x = B_y = 0, B_z = B$. Then:

$$\frac{\mathrm{d}}{\mathrm{d}x}(\sin\lambda) = 0$$

$$\frac{\mathrm{d}}{\mathrm{d}x}(\sin\phi) = \frac{kqB}{p\cos\lambda}$$

Integrating these equations with respect to x gives:

$$\lambda = \lambda_0 \tag{7.5}$$

$$\sin\phi = \sin\phi_0 + \frac{kqB}{p\cos\lambda}(x - x_0) \tag{7.6}$$

The dependence of the spatial parameters on x is found using Equations 7.2–4. Taking the ratios p_y/p_x and p_z/p_x leads to:

$$\frac{\mathrm{d}y}{\mathrm{d}x} = \tan\phi$$

$$\frac{\mathrm{d}z}{\mathrm{d}x} = \frac{\tan\lambda}{\cos\phi}$$

Integrating these equations with respect to x gives:

$$y = y_0 + R\left[\cos\phi_0 - \sqrt{1 - \left(\sin\phi_0 + \frac{(x - x_0)}{R}\right)^2}\,\right] \tag{7.7}$$

$$z = z_0 + R\tan\lambda\left[\sin^{-1}\left(\sin\phi_0 + \frac{(x - x_0)}{R}\right) - \phi_0\right] \tag{7.8}$$

where:

$$R = \frac{p\cos\lambda}{kqB}$$

These equations are used in the analysis to follow the trajectories of the tracks.

7.2 Track refit

The basic principle of the refit is to determine which microstrip hits lie on a given TRIDENT track, and then to use those hits in a new track fit. It is important to use the TRIDENT tracks rather than to do pattern recognition using the microstrip hits alone, since the matching of the microstrip track segment to the rest of the spectrometer is maintained, providing a measurement of the momentum and reducing the number of ghost tracks found.

In the first pass, only those tracks are used for which TRIDENT finds a matching between the spectrometer and the microstrips, i.e. those with flag greater than 20. To find the microstrip hits, the coordinates of the trajectory at each of the microstrip planes must be determined. This is achieved using the tracking equations, as described in the previous section. Using the parameters provided at the first measured point, the trajectory is followed to each of the microstrip planes, and the distance from the predicted point to the nearest hit is determined. If the separation is less than a given cut, then the hit is accepted as lying on the track. The cut was determined from residuals such as those in Figure 5.32, and had the value of 60 μm for planes 1 and 2, and 50 μm for the others. If two hits are found within the cut, then the point used in the refit is taken as the mean of the two hit coordinates. At least 3 hits are required in each of the Y- and Z-projections for the refit. This is achieved for ~ 99 % of the tracks, consistent with the microstrip efficiency (Section 5.16).

If the requisite number of hits has been found, then the track fit is performed in both projections. To use the full tracking equations in the fit would be complicated. Instead the situation is simplified by approximating the track as a straight line in the Z-projection, and a parabola in the Y-projection. A power series expansion of the equations for the y- and z-parameters (Equations 7.7 and 7.8) gives:

$$\Delta y = \tan\phi_0\,\Delta x + \frac{1}{2R\cos^3\phi_0}\,\Delta x^2 + O(\Delta x^3) \tag{7.9}$$

and:

$$\Delta z = \frac{\tan\lambda}{\cos\phi_0}\,\Delta x + O(\Delta x^2) \tag{7.10}$$

where $\Delta x = (x - x_0)$ etc. The approximation corresponds to neglecting the $O(\Delta x^3)$ terms in the equation for Δy, and the $O(\Delta x^2)$ terms in the equation for Δz. For tracks of reasonable

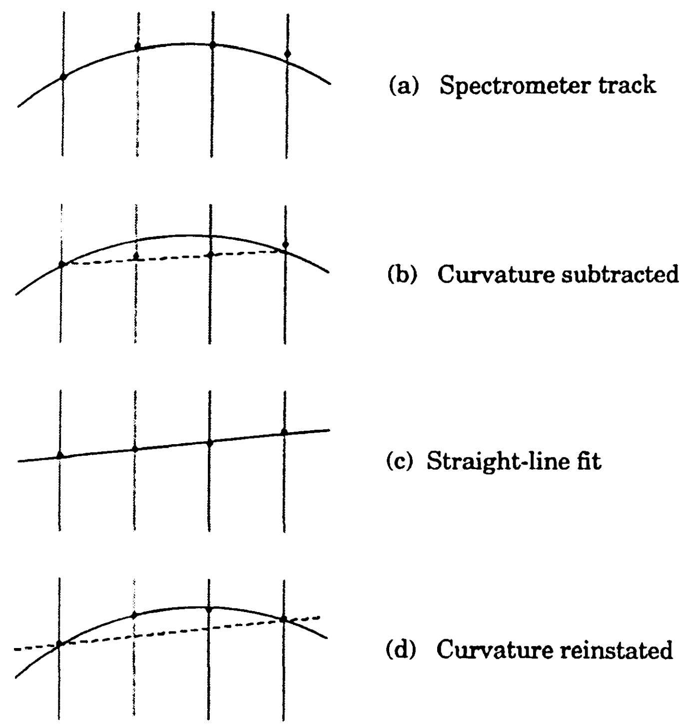

Figure 7.2 Procedure for Y-projection track fit

momentum (greater than about 1 GeV/c), and over the distances that the approximation will be made (a few cms), the error introduced by this approximation is small compared to the contributions from the intrinsic spatial resolution of the microstrips, and from multiple scattering.

The refitted tracks are parameterised as follows:

$$y = a_y x^2 + b_y x + c_y$$
$$z = a_z x + b_z$$

In the Z-projection the track fit is accomplished using a least-squares fit to a straight line. In the Y-projection, the curvature of the parabola is taken from the momentum, using (from Equation 7.9):

$$a_y = \frac{1}{2R\cos^3\phi_0} = \frac{kqB}{2p\cos\lambda\cos^3\phi_0}$$

The procedure is illustrated in Figure 7.2: the hits on the track are found (a), and the contribution of the curvature to the hit coordinates is subtracted (b), so that a least-squares

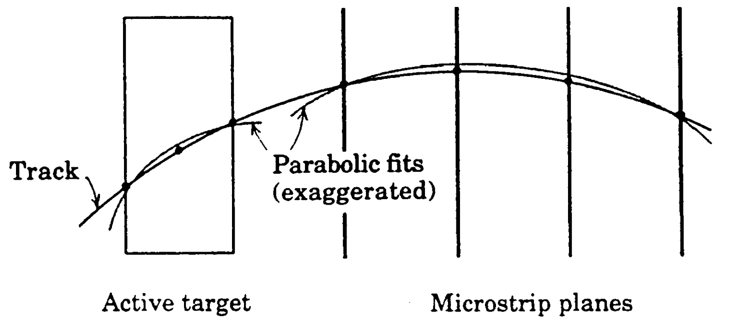

Figure 7.3 *Definition of track parameterisation at the vertex*

fit to a straight line may be used (c). The curvature is then added once more, to give the fitted track (d).

The region of interest for vertex calculation is in the active target. If the tracks are extrapolated from the microstrips to the target using the parabolic parameterisation then the systematic errors introduced become significant. Instead, the track parameters are transformed back into the $(y, z, 1/p, \lambda, \phi)$ parameterisation using (from Equations 7.2–4):

$$\phi = \tan^{-1}\left(\frac{\mathrm{d}y}{\mathrm{d}x}\right) = \tan^{-1}(2\,a_y\,x + b_y)$$

$$\lambda = \tan^{-1}\left(\cos\phi\frac{\mathrm{d}z}{\mathrm{d}x}\right) = \tan^{-1}(a_z\cos\phi)$$

calculated at the centre of the microstrip detector. The trajectory may then be accurately calculated, using Equations 7.5–8.

For the vertex calculation, however, more fits must be accomplished, so a parabolic parameterisation is again convenient in the Y-projection. A parabola is therefore defined in the target by finding the coordinates of the track at the front, middle and back of the target, and calculating the parameters of a parabola that passes through the three points. See Figure 7.3. The multiplicity distribution of tracks that have been successfully refitted is shown in Figure 7.4; the mean is ~ 7 tracks per event.

7.3 Error calculation

The least-squares fits of the previous section (and elsewhere in the analysis) require the specification of the errors associated with each measurement that is used in the fit. The

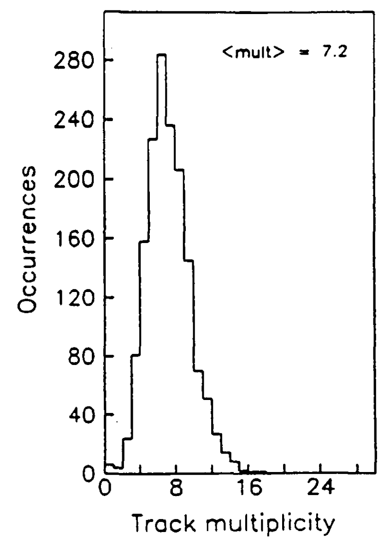

Figure 7.4 Multiplicity of refitted tracks

error is necessary for the calculation of the weight that is to be given to each measurement.

Calculation of weights

If there are several independent measurements X_i of a physical quantity, with standard deviations σ_i, then the weighted mean is given by:

$$\bar{X} = \sum_i w_i X_i$$

The variance of this mean is:

$$V(\bar{X}) = \sum_i w_i^2 \sigma_i^2$$

To calculate the correct weights, we wish to find the minimum variance with respect to the weights w_i, subject to the condition:

$$\sum_i w_i = 1$$

Define:

$$\chi = V + \lambda\left(\sum_i w_i - 1\right)$$

where a Lagrange multiplier λ has been introduced. Then the minimisation becomes:

$$\frac{\partial \chi}{\partial w_i} = 2 w_i \sigma_i^2 + \lambda = 0$$

giving:

$$w_i = -\frac{\lambda}{2}\left(\frac{1}{\sigma_i^2}\right)$$

From the constraint:

$$\sum_i w_i = -\frac{\lambda}{2}\sum_i \left(\frac{1}{\sigma_i^2}\right) = 1$$

Hence:

$$w_i = \left(\frac{1}{\sigma_i^2}\right) \Big/ \sum_i \left(\frac{1}{\sigma_i^2}\right)$$

Thus the weight given to a measurement should be proportional to the inverse-square of its associated error.

Errors for the refit

The errors on the microstrip hits that are used as points for the refit are taken from the spatial resolution given in Section 5.15, i.e. an *rms* value of 16 μm on each point, or 32 μm when the mean coordinate from a two hit cluster is used.

The curvature of the parabolic fit in the Y-projection is determined using the momentum from TRIDENT, as explained in the previous section. This introduces a further error, the error on the measurement of the momentum, which can be read from the TRIDENT bank. Each of the track parameters calculated by TRIDENT has an associated error, and the errors on the different parameters are not necessarily independent, so they must be specified using a matrix: the *covariance* matrix. For two variables X_i and X_j the covariance is defined as follows [96]:

$$C_{ij} = E\Big(\big(X_i - E(X_i)\big)\big(X_j - E(X_j)\big)\Big)$$

where $E(x)$ represents the expectation value of x. The elements C_{ij} constitute a matrix. For independent variables it is diagonal, and the diagonal elements give the variances:

$$C_{ii} = \sigma^2(X_i)$$

In the case of the track parameters from TRIDENT, the variables $\boldsymbol{X} = (y, z, 1/p, \lambda, \phi)$; the error on the momentum for use in the refit may be calculated from the variance of the inverse momentum, $\sigma^2(1/p)$, read from the error matrix.

Propagation of errors

In the refit calculation it is necessary to transform the parameters used to describe a track from one set of variables to another. For example, the parameters provided by the fit are in the $(a_z, b_z, a_y, b_y, c_y)$ parameterisation; whilst to follow the trajectory to the target, the $(y, z, 1/p, \lambda, \phi)$ parameterisation is used. When such transformations are made, the errors of the transformed parameters must be calculated using those of the original set.

If $\boldsymbol{X}$ is a set of variables with covariance matrix $\mathbf{C}_X$, and $\boldsymbol{Y}$ is the set of transformed variables, i.e. $Y_i = Y_i(\boldsymbol{X})$, then if the transformation functions are linear (or are well approximated by the linear terms of a Taylor expansion), the covariance matrix of $\boldsymbol{Y}$ is given by [96]:

$$\mathbf{C}_Y = \mathbf{T}\,\mathbf{C}_X\,\mathbf{T}^{\mathrm{T}}$$

where $\mathbf{T}$ is the matrix of derivatives:

$$\mathrm{T}_{ij} = \frac{\partial Y_i}{\partial X_j} \quad (at\, \boldsymbol{X} = \bar{\boldsymbol{X}})$$

A particular use of this procedure is when the transformation is simply the calculation of the parameters at a different x-coordinate. For example, for the propagation of the errors on the TRIDENT parameters of a track from x-coordinate x_0 to x_1:

$$\boldsymbol{Y} = (y_1, z_1, 1/p_1, \lambda_1, \phi_1) \quad (at\; x = x_1)$$

and:

$$\boldsymbol{X} = (y_0, z_0, 1/p_0, \lambda_0, \phi_0) \quad (at\; x = x_0)$$

The matrix of derivatives $\mathbf{T}$ is a (5×5) matrix which may be calculated using Equations 7.7–8:

$$\mathrm{T}_{11} = \frac{\partial y_1}{\partial y_0} = 1$$

$$\mathrm{T}_{12} = \frac{\partial y_1}{\partial z_0} = 0$$

$$T_{13} = \frac{\partial y_1}{\partial (1/p_0)}$$

$$= p\left[\frac{\left(\sin\phi_0 + \frac{(x_1 - x_0)}{R}\right)(x_1 - x_0)}{\sqrt{1 - \left(\sin\phi_0 + \frac{(x_1 - x_0)}{R}\right)^2}} - R\left(\cos\phi_0 - \sqrt{1 - \left(\sin\phi_0 + \frac{(x_1 - x_0)}{R}\right)^2}\right)\right]$$

etc. As can be seen, the expressions can be quite complex. The propagated errors may then be found by simple matrix manipulation. In this manner the track errors can be calculated at any position along the track.

Routines were written to transform the error matrix between the TRIDENT and the parabolic parameterisations, and also from either of these to a linear parameterisation that will be used at the vertex.

For the errors from the refit, a covariance matrix is constructed using the errors from the parameters of the linear fits, and the error on the curvature term:

$$\begin{bmatrix} a_y a_y & 0 & 0 & 0 & 0 \\ 0 & b_y b_y & b_y c_y & 0 & 0 \\ 0 & c_y b_y & c_y c_y & 0 & 0 \\ 0 & 0 & 0 & a_z a_z & a_z b_z \\ 0 & 0 & 0 & b_z a_z & b_z b_z \end{bmatrix}$$

where each element is labelled with an obvious notation. The errors are then propagated to the TRIDENT parameterisation, using a (5×5) matrix of derivatives. The element of the transformed error matrix that corresponds to $\sigma^2(1/p)$ is forced to take the value of $\sigma^2(1/p)$ read from the TRIDENT bank.

The errors on the various refit parameters at the middle of the microstrips are shown in Figure 7.5. The entries at higher values for the error are from tracks with fewer than the full four hits in each projection.

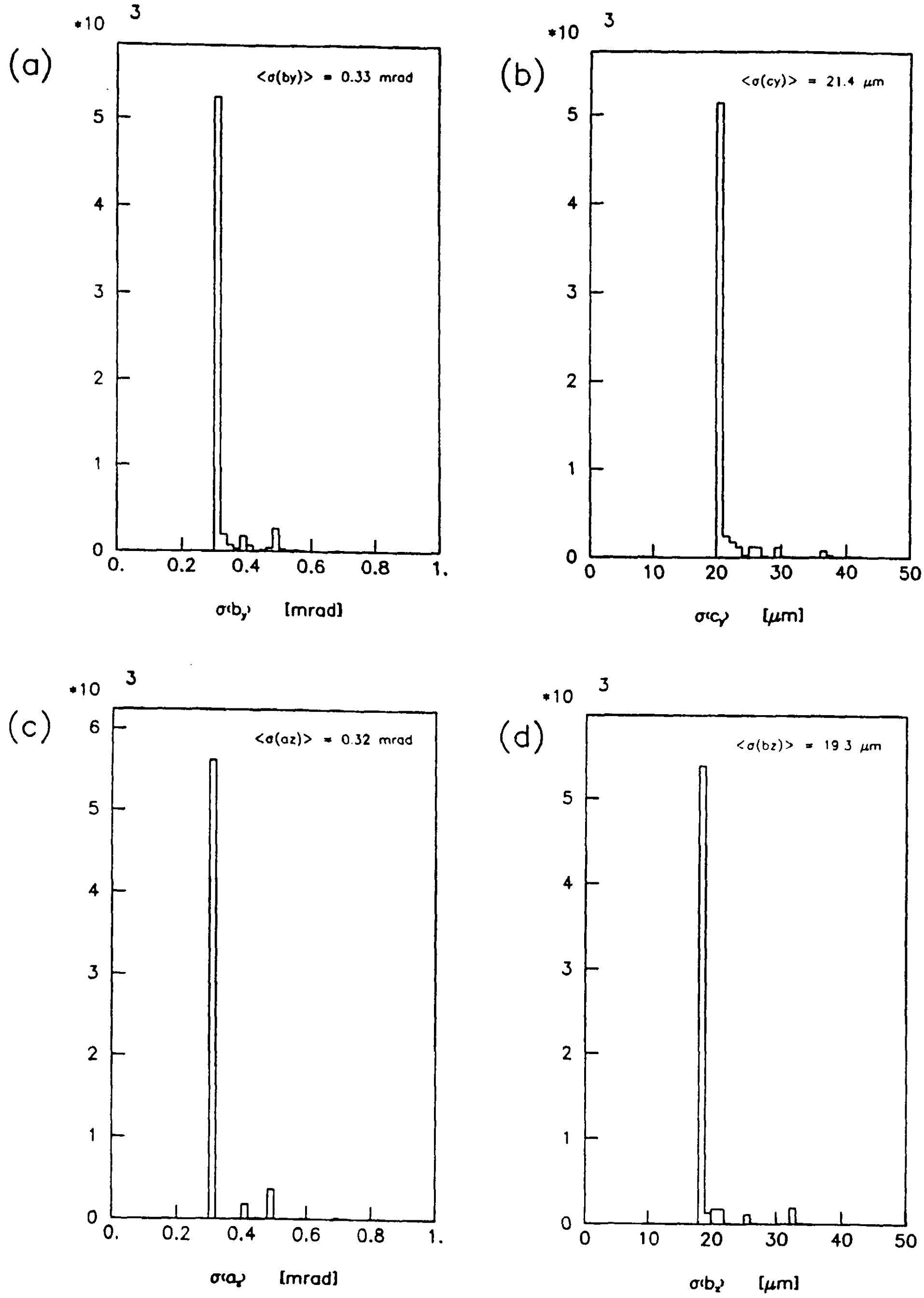

Figure 7.5 *Errors on refit track parameters at the middle of the microstrips*

Multiple scattering

A charged particle passing through matter undergoes Coulomb scattering, due to its electromagnetic interaction with the charged components of the material. The individual interactions typically cause a small and effectively random change in the direction of the particle trajectory, and the total deflection caused by the material is found by summing these changes over many scatterings.

Multiple scattering is particularly important for this analysis when the track measured in the microstrips is extrapolated back into the active target to find the vertex. The passage of the track through the target material will have introduced some (unknown) deflection due to multiple scattering, so when the extrapolation is performed, the errors on the track parameters must be increased to accommodate this uncertainty.

For a thin layer of traversed material, the expectation of the square of the scattering angle in space *per unit length* can be approximated by [97]:

$$\Theta_0^2 = \alpha^2 \frac{\left(m^2 + p^2\right)}{p^4 \beta^2 X_0} \left[1 + \frac{1}{9} \log \left(\frac{x}{X_0} \right) \right]^2 \quad (10^{-3} < x/X_0 < 10)$$

where m is the mass of the incident particle, p is its momentum and β is its velocity; X_0 is the radiation length of the traversed medium and x is its thickness; α is a constant with a value of about 21 MeV.

For the purposes of this analysis, $p \gg m$, $\beta \sim 1$, and neglecting the logarithmic term, we may put:

$$\Theta_0^2 \sim \frac{\alpha^2}{p^2 X_0}$$

Note that the average scattering angle depends upon the inverse of the momentum, so the effect of multiple scattering is particularly important for low momentum tracks.

The variance of the projected scattering angle, θ_y, is determined by:

$$\frac{d\,\sigma^2(\theta_y)}{dx} = \frac{\Theta_0^2}{2}$$

and considering the scattering effect as white noise it follows [97] that the expectation of the projected scattering angle is given by:

$$E(\theta_y^2) = \frac{\Theta_0^2}{2} x$$

Similarly for the projected transverse scattering distance:

$$E(y^2) = \frac{\Theta_0^2}{2} \frac{x^3}{3}$$

and for the correlation between the two:

$$E(y,\theta_y) = \frac{\Theta_0^2}{2}\frac{x^2}{2}$$

The active target is constructed from a stack of silicon wafers, each 300 μm thick, separated by about 200 μm of air. For the purposes of the calculation of multiple scattering, the material is considered as homogeneous, and an average radiation length is calculated. Using the radiation length of silicon from Table 1.1 (~ 9·36 cm), the average radiation length may be calculated: $X_0 \sim 15{\cdot}8$ cm.

To include the effect of multiple scattering on the error calculations, the distance Δx that has been travelled through the target is determined. The multiple scattering gives a contribution to the covariance matrix for the track parameters: if C_{ij} is an element of the covariance matrix at a given x-coordinate, in the TRIDENT parameterisation $(y,z,1/p,\lambda,\phi)$, then the corrected covariance matrix is given by:

$$C_{ij} \rightarrow C_{ij} + \varepsilon_{ij}$$

where ε is the covariance matrix for the multiple scattering:

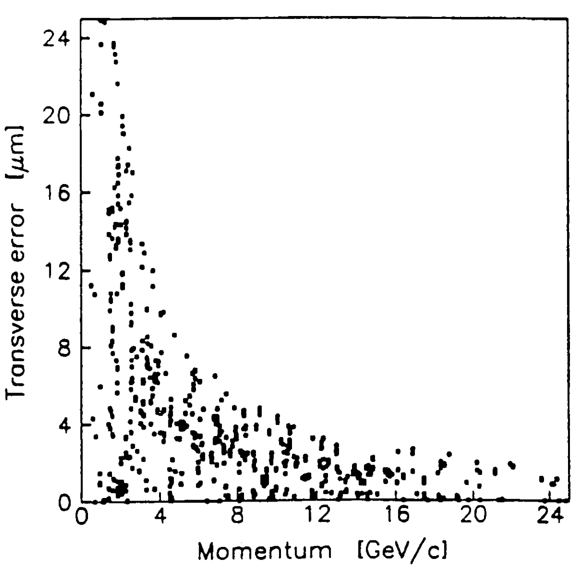

Figure 7.6 *Variation with momentum of multiple scattering contribution to track error*

$$\varepsilon = \frac{\Theta_0^2}{2}\begin{bmatrix} \Delta x^3/3 & 0 & 0 & 0 & \Delta x^2/2 \\ 0 & \Delta x^3/3 & 0 & \Delta x^2/2 & 0 \\ 0 & 0 & 0 & 0 & 0 \\ 0 & \Delta x^2/2 & 0 & \Delta x & 0 \\ \Delta x^2/2 & 0 & 0 & 0 & \Delta x \end{bmatrix}$$

The effect of the multiple scattering is illustrated in Figure 7.6, where its contribution to the transverse error of the tracks (σ_{yy} and σ_{zz}) at the vertex is plotted against the track momentum. The multiple scattering in the planes of the microstrip detector is neglected.

The errors on the transverse track coordinates at the vertex are shown in Figure 7.7. Using the non-charm Monte Carlo events, the transverse offset of tracks from the true vertex may be determined (see Figure 7.8 (a) and (b)). If the error analysis is accurate, then the ratio of the offset and its error (the 'normalised' offset) should be normally distributed, i.e. follow a Gaussian distribution with *rms* width of 1·0 (see Figure 7.8 (c)). The distributions are indeed of Gaussian shape, but the widths are slightly greater than 1·0, indicating that the errors have been underestimated. This can be caused by the

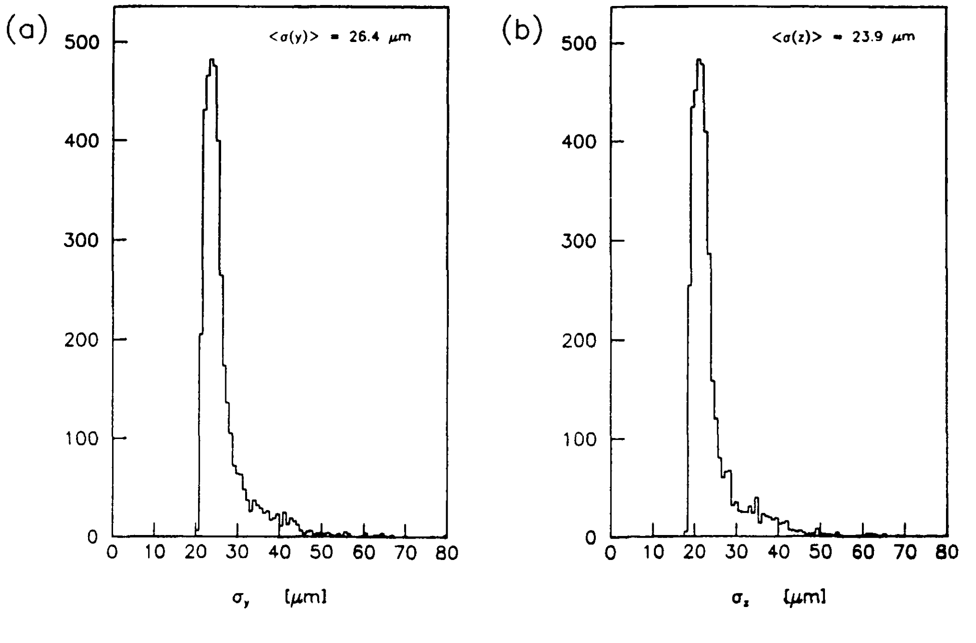

Figure 7.7 *Error on transverse coordinates of tracks at the vertex*

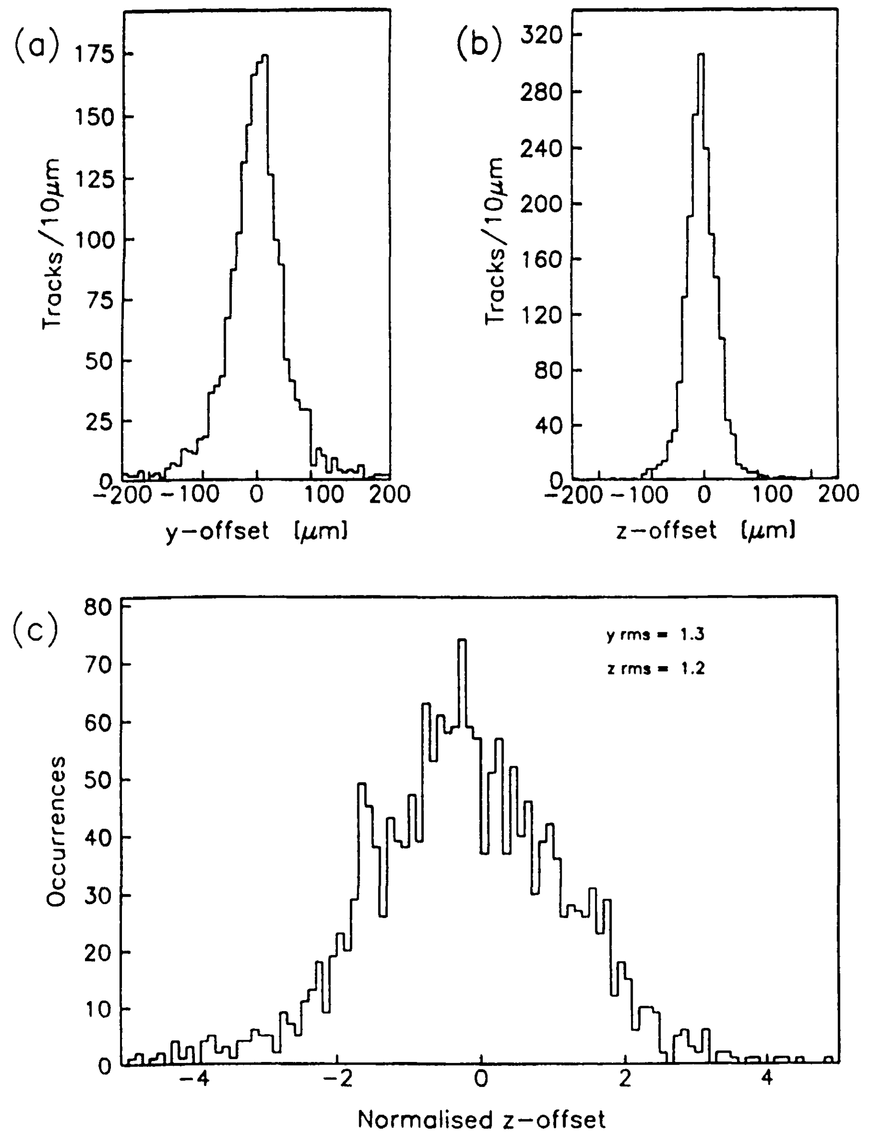

Figure 7.8 *Offset of tracks from the vertex (Monte Carlo)*

incorrect assignment of hits to tracks, due to the presence of clusters, or by ghost tracks. To compensate for these effects, a correction factor of (1·3, 1·2) was introduced into the calculation of the errors for the (Y, Z) tracks.

7.4 Additional tracks

The tracks from TRIDENT that have been used for the refit do not account for all of the hits in the microstrips. The average microstrip hit multiplicity is (from Figure 5.28) about 140. The multiplicity of tracks from TRIDENT with flag greater than 20 (i.e. matched in the microstrips and suitable for use in the refit) is about 7. If we assume that each track has 10 microstrip hits, this only accounts for about half of the total number of hits. The number of noise hits that are expected in an event is small (as was shown in Section 5.12), typically 6 hits per event, and may be neglected in this argument. Clusters account for a few more hits, but a significant number remain—they are from tracks in the microstrips which have not been reconstructed by TRIDENT. This may be due to the tracks being outside the acceptance of the wire chambers, or due to inefficiencies in the chambers and the track reconstruction.

If these 'additional' tracks are outside the acceptance of TRIDENT, they will tend to have low momentum, so multiple scattering will be serious. Furthermore, since the tracks are not reconstructed in the rest of the spectrometer, the momentum will not be measured, so the error from the multiple scattering will be unknown. However, the precision in the x-coordinate of a vertex is greater for wide angle tracks, so the additional tracks may be useful for vertex finding.

They are found by pattern recognition in the microstrips alone. As mentioned above, this would be unsuitable for the recognition of all tracks, using all of the microstrip hits. However, the search for additional tracks is only made *after* the refit has been performed. The hits which lie on the refitted tracks can therefore be excluded from the search; the OR-images of these hits are also excluded. In Figure 7.9, an event is displayed after the refit has been performed; in Figure 7.10 the same event is shown with the refit hits and their OR-images not displayed: the remaining hits indicate the presence of additional tracks.

The remaining microstrip hits are clusterised: each cluster (of hits in consecutive strips on a plane) is replaced by a point at the centre of the cluster, for use in the pattern recognition. The width of the cluster will be used to determine the error on the point for the track fit. Tracks are searched for in each of the Y- and Z-projections.

Z-projection

The tracks in the Z-projection are fit as straight lines. They are found by taking each combination of hits in the first plane and the last plane of the projection (i.e. planes 1 and 7), and calculating the line that passes through them both, to give a candidate track. The offset in z of the candidate track from the TRIDENT vertex is determined (see

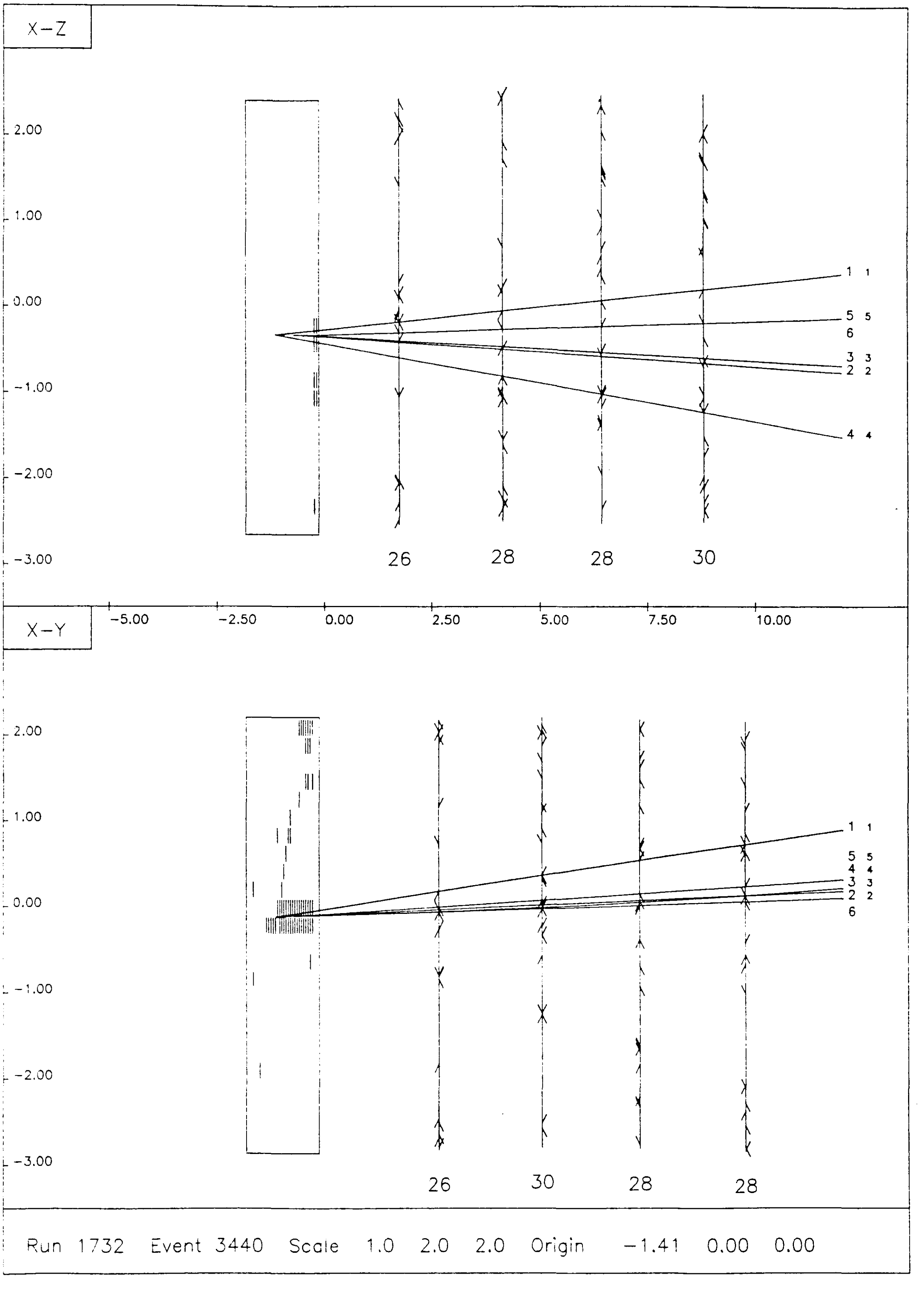

Figure 7.9 *Event displayed after refit performed*

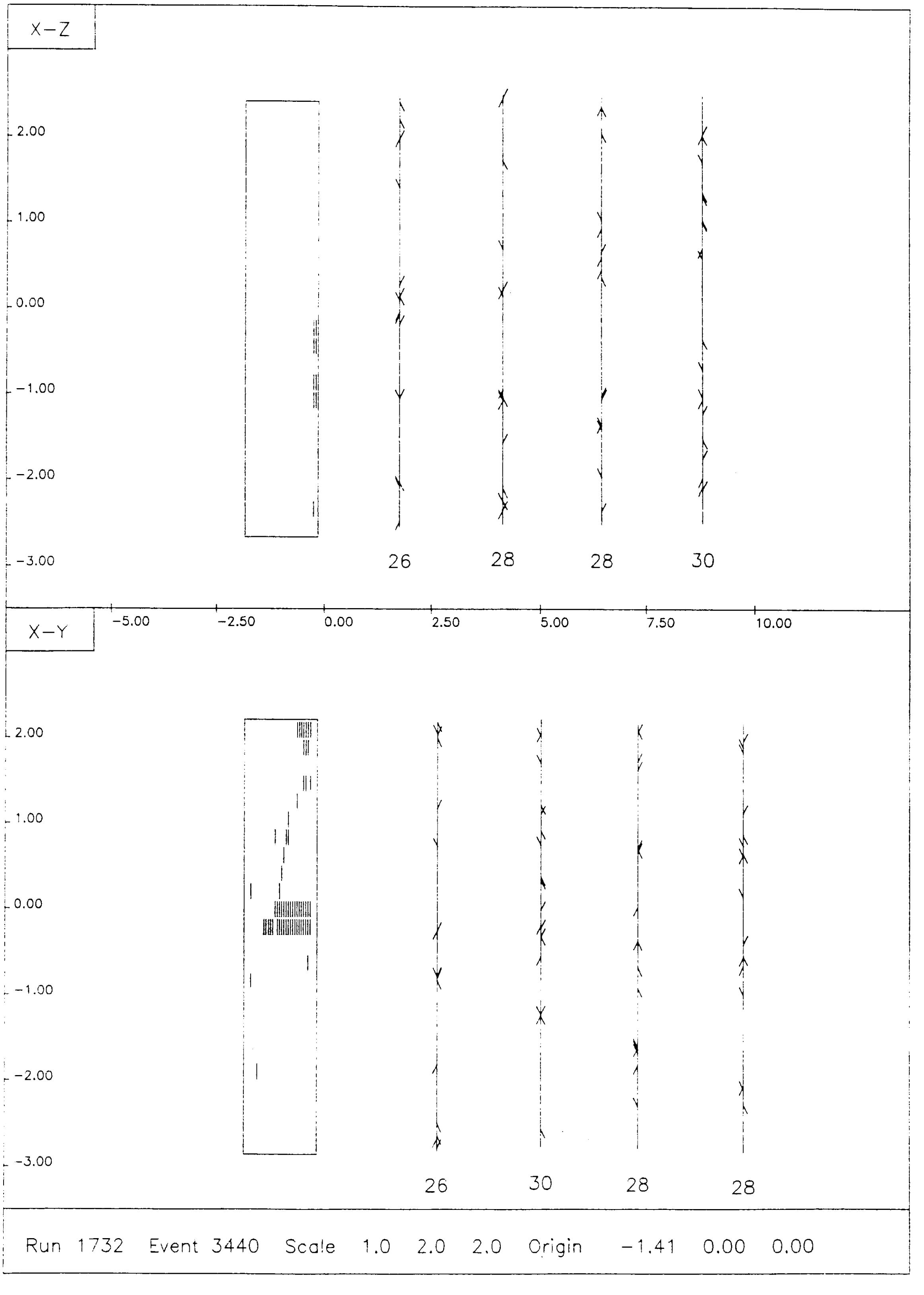

***Figure 7.10** Event displayed without refit hits and their OR-images*

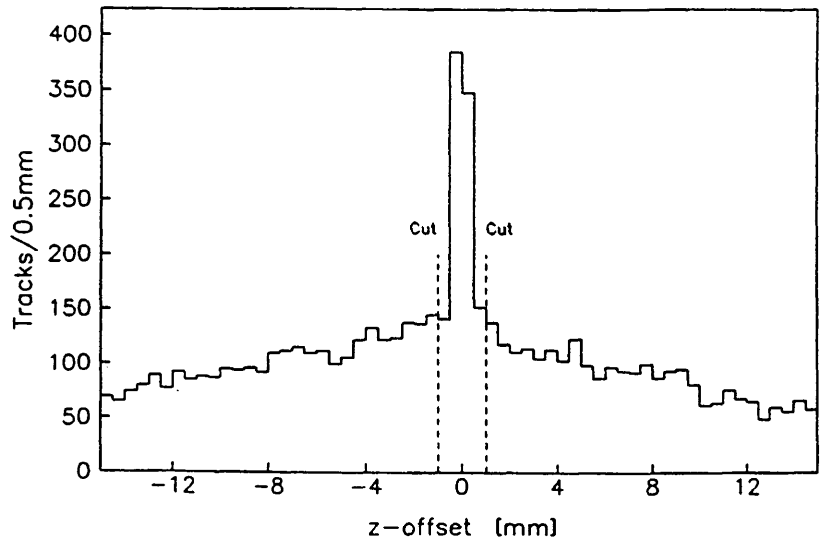

Figure 7.11 *Raw offset of candidate additional tracks from the TRIDENT vertex*

Figure 7.11). The presence of a clear peak at small offset indicates that real tracks are being found. A loose cut of ± 1 mm is made on the offset, to select tracks that point toward the vertex. The cut is loose, since the TRIDENT vertex is not very accurate, and it is important that the vertex position does not bias the track fit.

The points at which a hit is predicted are calculated on the intermediate planes, and the nearest hit selected. Only four-point tracks are used. A least-squares fit to a straight line is made using the four points, and only those tracks for which the fit is good are accepted. This is achieved by making a cut on the *probability of chi-square* for the fit. The chi-square of a fit to N measurements is defined as:

$$\chi^2 = \sum_{i=1}^{N} \left(\frac{\delta_i}{\sigma_i} \right)^2$$

where δ is the offset of a measurement from its predicted value, and σ is the error on the measurement. If the offsets are normally distributed about their true values, this quantity should follow a *chi-square* distribution [98] with the appropriate number of degrees of freedom, N_{dof}, given by:

$$N_{dof} = (\textit{no. of constraints}) - (\textit{no. of free parameters}) \tag{7.11}$$

As every measured point contributes a constraint equation, there are therefore two degrees of freedom for the four-point straight-line fit.

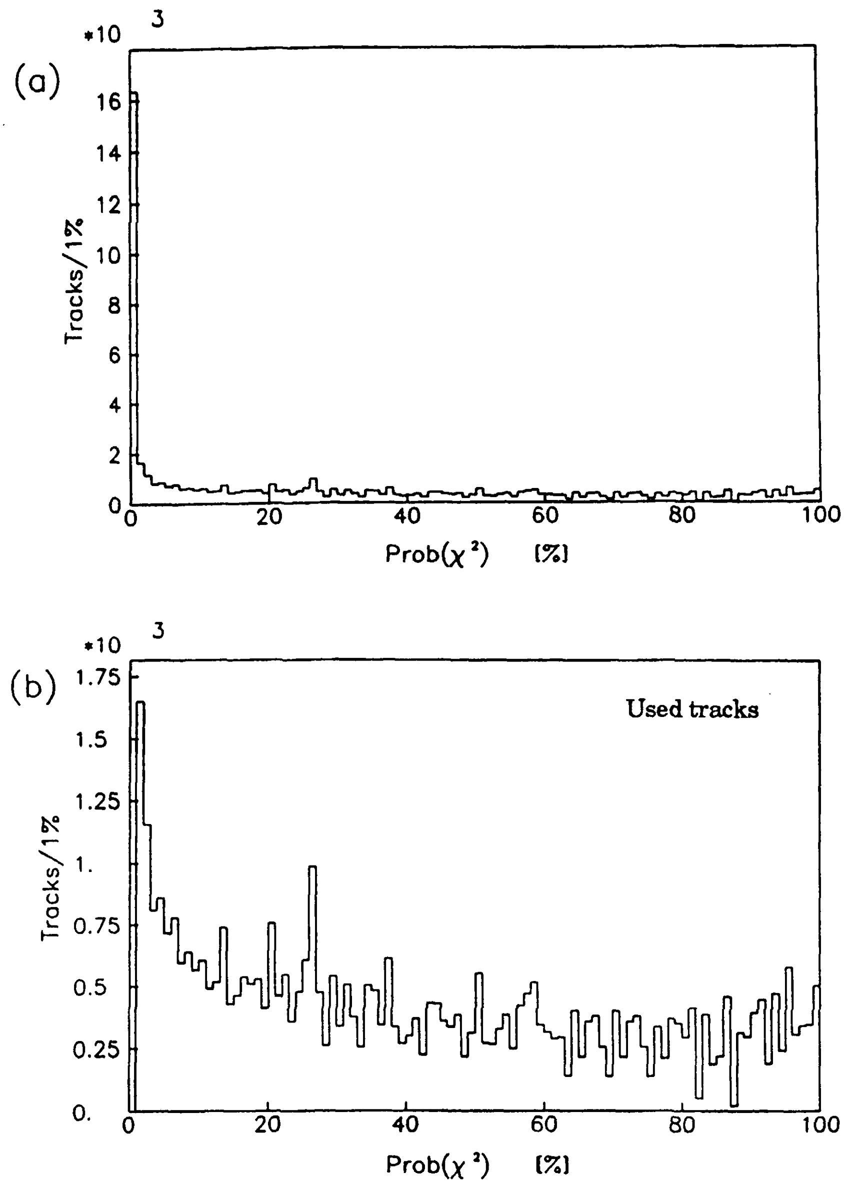

Figure 7.12 *Probability of chi-square for the additional track fit*

The probability *Prob* (χ^2) that a value chosen from a true chi-square distribution (for a given number of degrees of freedom) would exceed the chi-square calculated, is determined using a routine from the CERN program library [99]. If the hypothesis is correct, i.e. the variable under investigation does follow a chi-square distribution, then *Prob* (χ^2) should be a flat distribution, with all values from 0–1 equally populated.

If the fit for the additional track is poor, then the chi-square will be large, and the

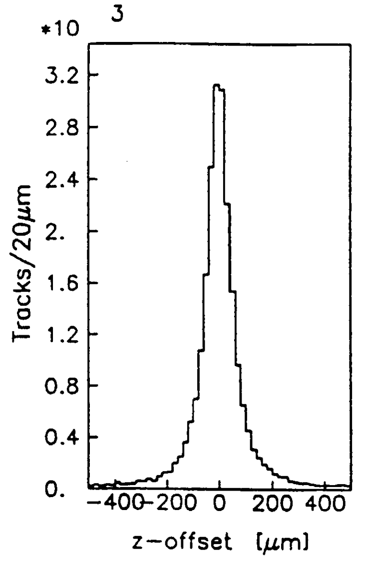

Figure 7.13 *Offset of Z-projection additional tracks from the TRIDENT vertex*

Prob (χ^2) distribution will have a spike at low probability. A cut is made, to select only tracks with *Prob* (χ^2) > 1 %. See Figure 7.12, where the probability distribution is shown both before the cut (a) and after (b). The offset of the fitted tracks from the TRIDENT vertex may again be calculated, and is shown in Figure 7.13. As can be seen, the peak is narrow compared with the earlier cut, indicating that the cut did not bias the track finding.

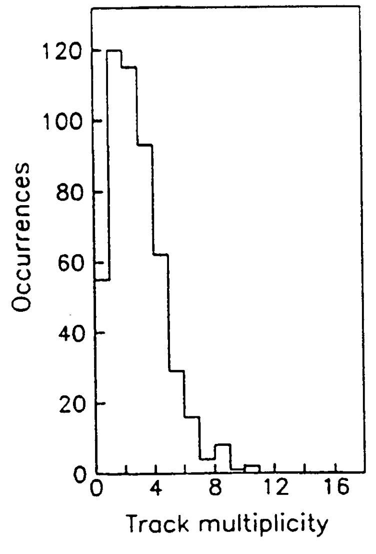

Figure 7.14 *Multiplicity of Z-projection additional tracks*

The multiplicity of tracks found in this manner is shown in Figure 7.14; the mean is about 2·5 tracks per event. The number of additional tracks is more significant than it might at first appear, since although there are on average 7 refit tracks, if a charm decay is under investigation for which there are three charged decay products, such as $D_s \rightarrow KK\pi$, then there remain only 4 tracks from the primary vertex. The additional tracks can therefore make a significant contribution to this calculation. The remaining excess of microstrip hits includes three-point tracks, where a hit has been dropped due to the microstrip per-plane efficiency being less than 100 %, or due to tracks outside the acceptance of the downstream planes. These three-point tracks could also be found, but due to the increasing uncertainty in the track fit, their usefulness in the vertex finding is questionable, and their reconstruction was not pursued.

The angular distribution of the additional tracks found is compared with that of the refit tracks in Figure 7.15; as can be seen, they do indeed have a flatter distribution, apart from an enhancement at low angle due to pairs—these are rejected at the charm analysis stage (Chapter 8). The accuracy of the additional tracks in the x-coordinate of the vertex was checked using the Monte Carlo. Non-charm events were used, and the x-offset of the tracks from the Monte Carlo vertex position is shown in Figure 7.16. Also shown is the

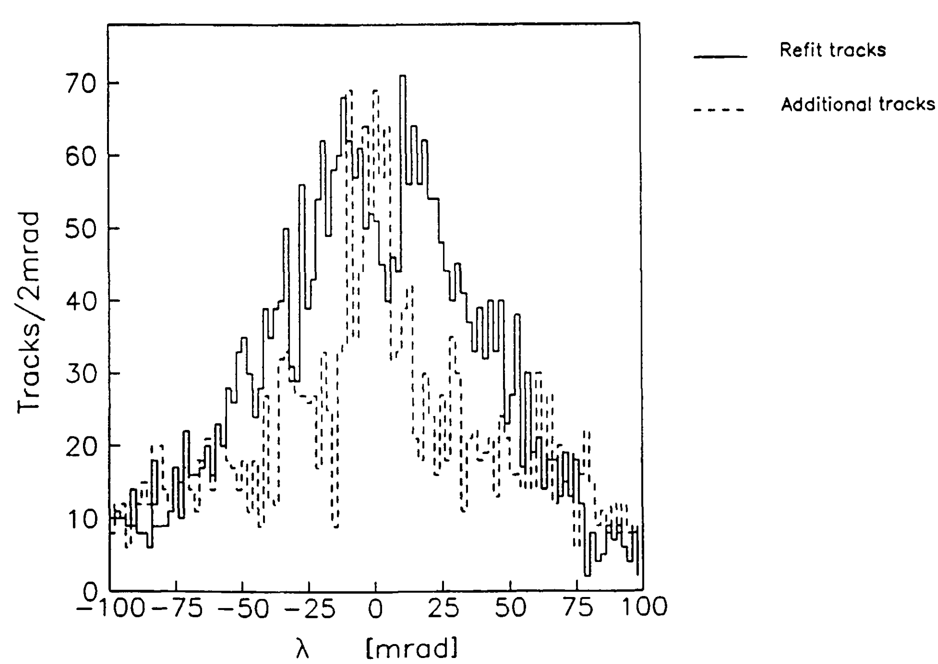

Figure 7.15 *Angular distributions of tracks*

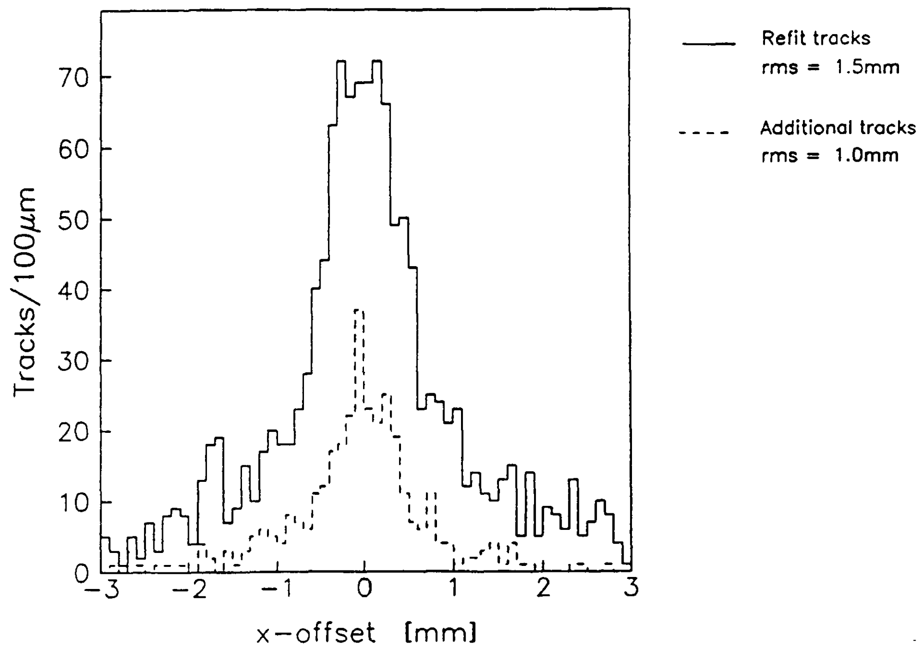

Figure 7.16 *x-offset of tracks from the Monte Carlo vertex*

offset calculated with the refit tracks. The distribution for the additional tracks is narrower, indicating their usefulness for vertex calculation.

Y-projection

For the recognition of tracks in the Y-projection, the lack of information about the momentum is more serious, because the tracks are curved (since the Y-projection is the bend plane of the magnetic field), but the curvature of the tracks is unknown. Four-point tracks are again used, but a parabolic rather than linear fit is employed. A candidate track is made using hits on the first plane and the last plane in the projection (planes 2 and 8), and then a hit on the second plane of the projection is used to define a parabola. A cut is made on the sagitta of this parabola, at 500 μm (see Figure 7.17), which corresponds to rejecting tracks with momentum less than 0·5 GeV/c (that would be highly inaccurate due to multiple scattering). The candidate track is required to point towards the TRIDENT vertex, with a 1 mm cut as for the Z-projection.

The parabola is used to predict a point on the remaining plane of the projection, and the nearest hit is taken for use in a parabolic least-squares fit. The probability of chi-square is calculated for the fit, this time with one degree of freedom; the same cut of

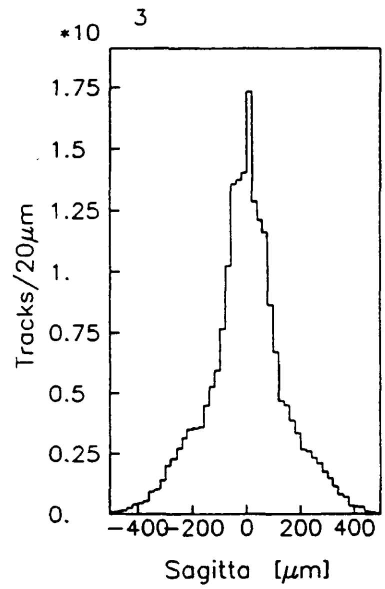

Figure 7.17 Sagitta of Y-projection additional tracks

Prob $(\chi^2) > 1$ % is applied, as for the Z-tracks. The offset of the tracks from the TRIDENT vertex after this cut is shown in Figure 7.18. The mean multiplicity of additional tracks found in the Y-projection is about 2·3, which is reassuringly similar to that of the Z-projection tracks. In Figure 7.19, the same event as was shown in Figure 7.9 is displayed, after the additional track search has been performed, with the additional tracks found marked dot-dashed.

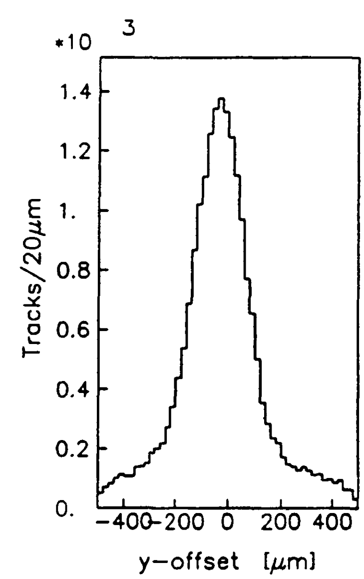

Figure 7.18 Offset of Y-projection additional tracks from TRIDENT vertex

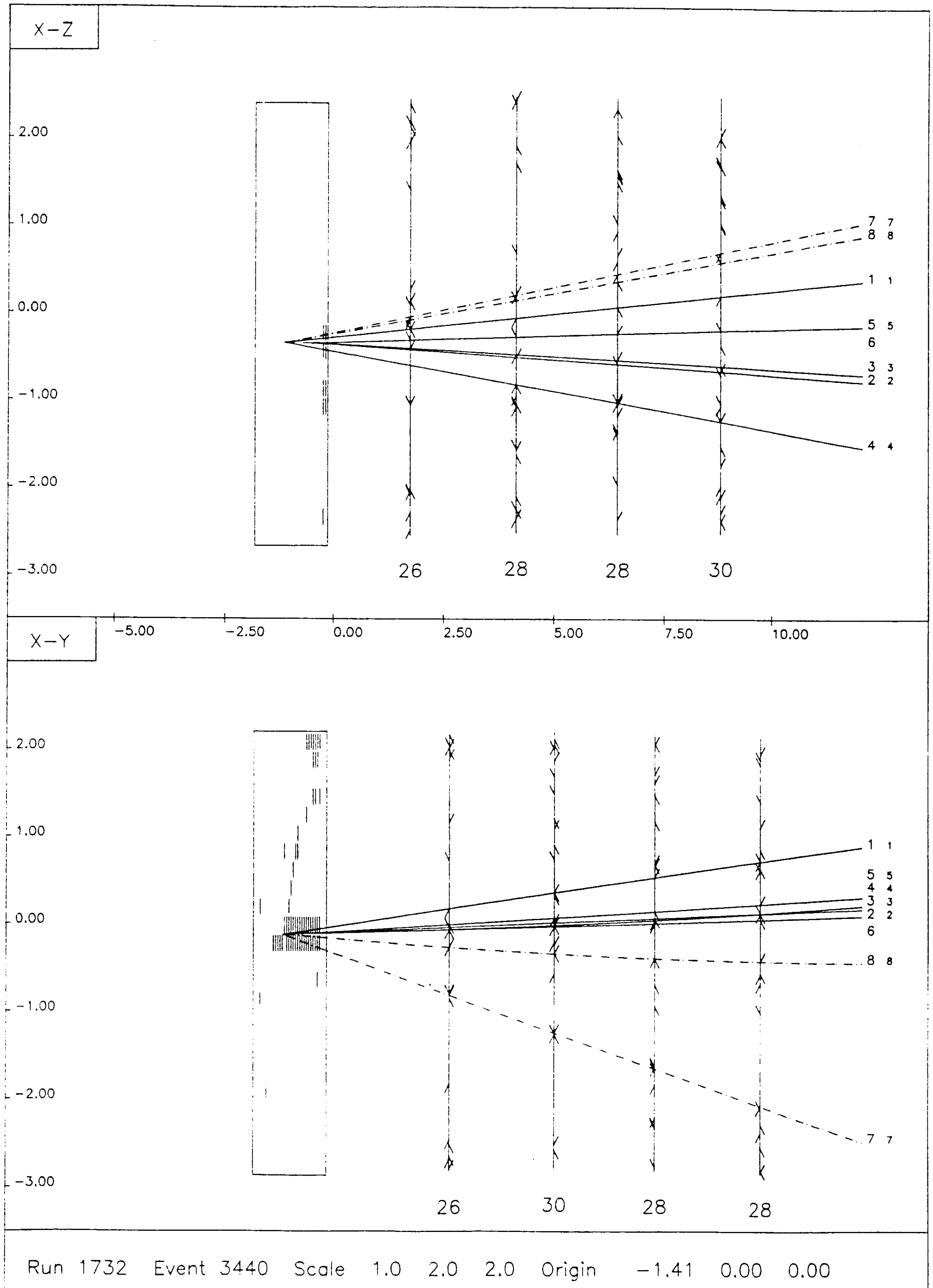

***Figure 7.19** Event displayed after additional track search*

II Vertex finding schemes

7.5 Intersection vertex

The Intersection vertex is formed using the pairwise intersections of tracks. It represents a stage in the development of vertex finding from the simple approach such as is used in the microstrip filter (Section 6.7), where no error analysis is done, to the fully consistent error analysis used in the 'Constraint' vertex (described in the next section). This vertex scheme is of interest, as it was found to give good charm signals in the analysis of some channels. It is particularly suited to use in conjunction with the active target information, as will be explained.

Intersections

The tracks from the refit are used, i.e. TRIDENT tracks with flag greater than 20 which have been refitted in the microstrips. The tracks that are to be used in a particular vertex search are chosen, as will be described in the next chapter. For each pair of tracks, the point of closest approach in the transverse (y-z) plane is found. The transverse separation s of a pair of tracks is given by:

$$s = \sqrt{(y_1 - y_2)^2 + (z_1 - z_2)^2}$$

where the subscript distinguishes the tracks. As explained in Section 7.2, the refit tracks are parameterised as parabolæ in the target. Substituting:

$$y_1 = a_1 x^2 + b_1 x + c_1$$
$$z_1 = d_1 x + e_1$$

and similarly for track 2, gives:

$$s = \left[\Big((a_1 - a_2)\, x^2 + (b_1 - b_2)\, x + (c_1 - c_2) \Big)^2 + \Big((d_1 - d_2)\, x + (e_1 - e_2) \Big)^2 \right]^{1/2}$$

The point of closest approach is found by minimising this separation, which is equivalent to minimising its square:

$$\frac{\mathrm{d}\, s^2}{\mathrm{d} x} = 0$$

leading to a cubic equation for x:

$$2\,\Delta a^2\,x^3 + 3\,\Delta a\,\Delta b\,x^2 + (\Delta b^2 + 2\,\Delta a\,\Delta c + \Delta d^2)\,x + \Delta b\,\Delta c + \Delta d\,\Delta e = 0$$

where $\Delta a = (a_1 - a_2)$ etc. The roots of this cubic equation are found using a routine from the CERN program library [100]. The root is chosen that lies within the target; if there are more than one, then the root that gives the smallest separation is taken. This gives the x-coordinate of the intersection. The y- and z-coordinates are calculated as the average of the two track coordinates at that x.

The error on the separation of the tracks must next be found. The track errors are propagated to the point of intersection, in the $(y, z, 1/p, \lambda, \phi)$ parameterisation, and the elements of the covariance matrices concerning the y- and z-coordinates are combined to form a new matrix:

$$\begin{bmatrix} y_1y_1 & y_1z_1 & 0 & 0 \\ z_1y_1 & z_1z_1 & 0 & 0 \\ 0 & 0 & y_2y_2 & y_2z_2 \\ 0 & 0 & z_2y_2 & z_2z_2 \end{bmatrix}$$

Using Equation 7.12, the derivatives of s with respect to the four parameters (y_1, z_1, y_2, z_2) may be calculated, to give a (4×1) derivative matrix. Finally the error propagation is performed using this matrix, to give the error σ_s on s. The ratio s/σ_s gives a measure of the quality of the intersection. If the ratio is large, then the tracks are probably not from the same vertex (or one of the tracks may be a ghost), and the intersection should be excluded from the vertex calculation. A cut on the separation is applied, accepting intersections that satisfy:

$$\frac{s}{\sigma_s} < 3{\cdot}0$$

See Figure 7.20. The usefulness of this cut can be demonstrated using charm events from the Monte Carlo: the separation is calculated for tracks that belong to the same vertex, or different vertices. The rejection of the cut is greater for tracks from different vertices than for those from the same vertex, as can be seen in Figure 7.21.

Vertex calculation

The vertex coordinates are taken as the weighted means of the intersection coordinates. For the sake of consistency, it is necessary that all mutual intersections of the tracks used

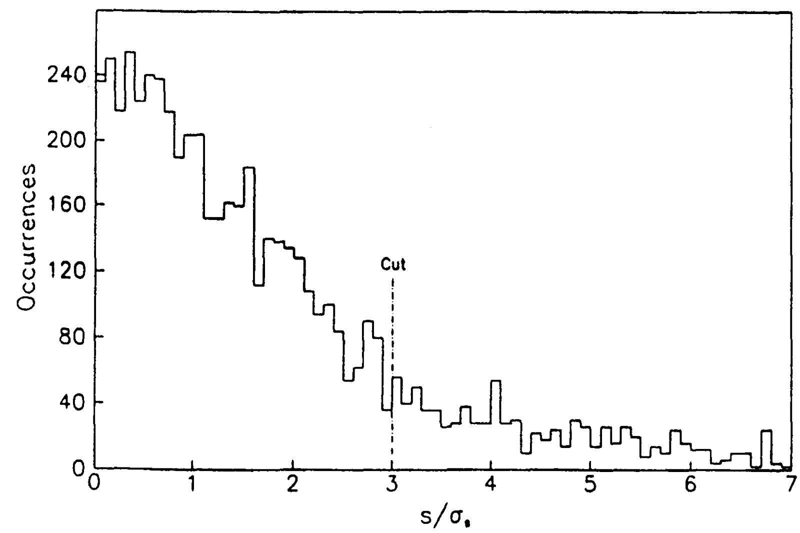

Figure 7.20 Cut on track pair separation

in the vertex calculation should be acceptable. If an intersection is unacceptable, then this indicates that one of the two *tracks* used to form it is unacceptable, and the other intersections of that track should also be rejected. Therefore, if unacceptable intersections exist between the tracks being used, the track with the highest number of unacceptable intersections is rejected, and the process repeated until all intersections of used tracks are acceptable.

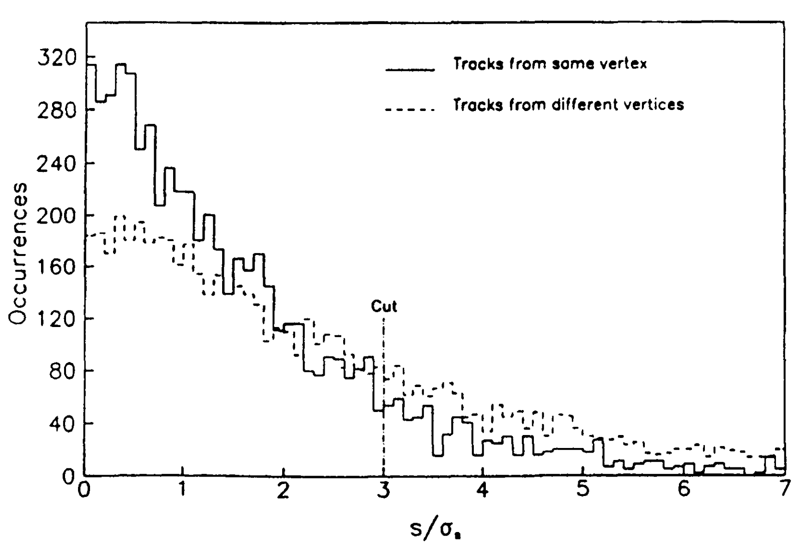

Figure 7.21 Cut on track pair separation (Monte Carlo)

The error on the intersection coordinates must be determined. Due to the complex nature of the expression for the x-coordinate of the intersection, the calculation of the derivative matrix for error propagation cannot be simply performed. Instead, a new parameterisation is introduced for the tracks at the intersection: a linear approximation, calculated for the Y-projection as the tangent to the parabola. That is:

$$y = a_y' x + b_y'$$
$$z = a_z' x + b_z'$$

with:

$$a_y' = 2\, a_y\, x_I + b_y$$
$$b_y' = c_y - a_y\, x_I^2$$
$$a_z' = a_z$$
$$b_z' = b_z$$

where x_I is the x-coordinate of the intersection. The track errors are propagated to the intersection point in the TRIDENT parameterisation, and then transferred to the (a_y', b_y', a_z', b_z') parameterisation, giving a (4×4) covariance matrix $\mathbf{C}'$ for each track. These are combined to give the (8×8) matrix:

$$\begin{bmatrix} \mathbf{C}_1' & 0 \\ 0 & \mathbf{C}_2' \end{bmatrix}$$

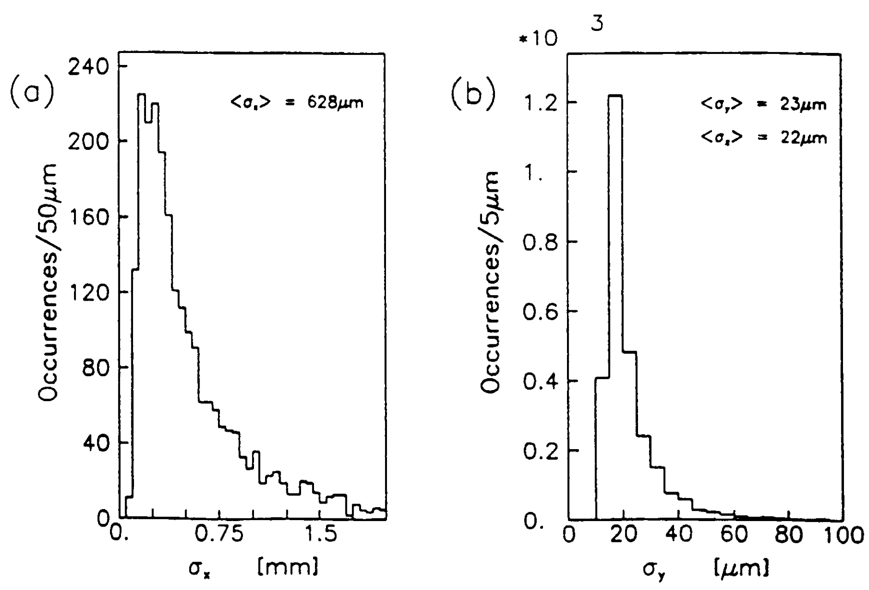

Figure 7.22 *Intersection coordinate errors*

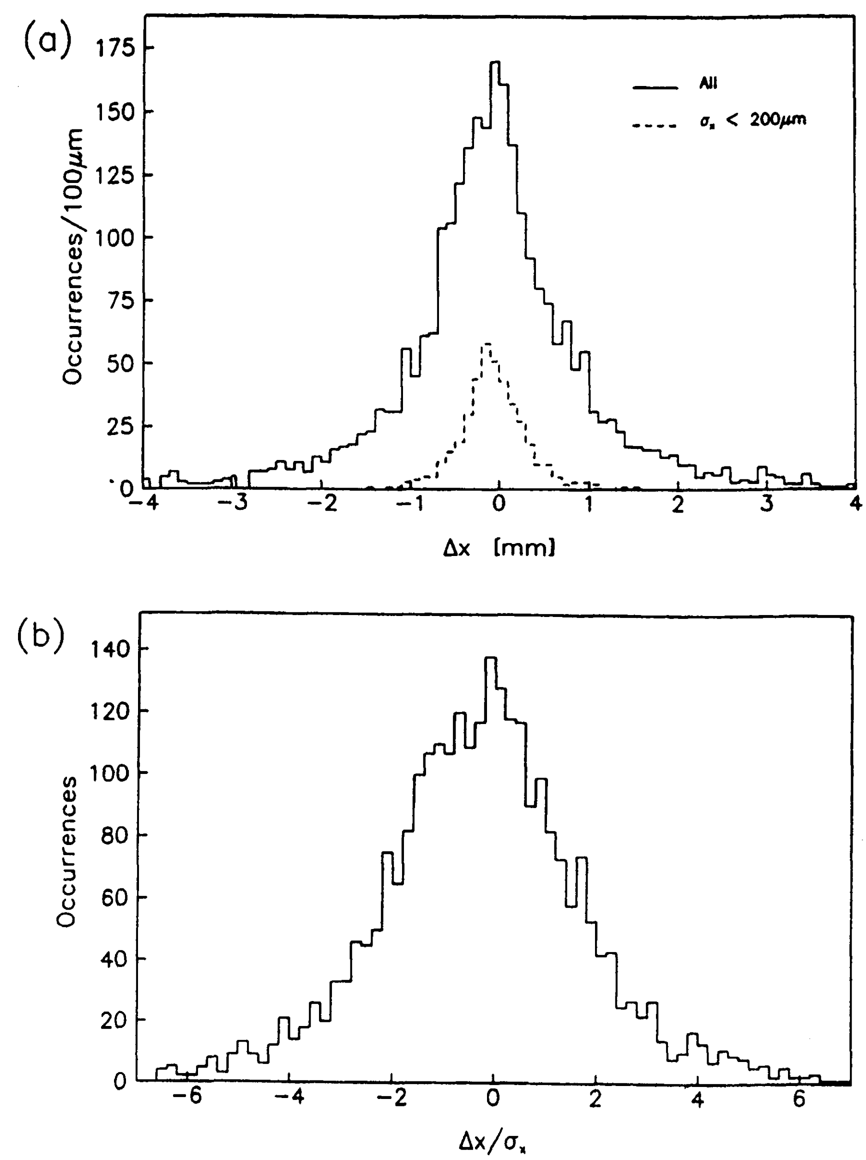

Figure 7.23 *x-offset of intersections from the vertex (Monte Carlo)*

where **0** represents the (4×4) null matrix (the track-track correlations are zero). With the linear parameterisation of the tracks, x_I may be solved for, and the elements of the (8×3) derivative matrix that is used to transfer the errors to (x_I, y_I, z_I) may be calculated. Thus a (3×3) error matrix, e^I, is determined for each intersection.

The errors on the intersection coordinates are shown in Figure 7.22. In Figure 7.23 (a) the offset in x of the intersections from the true vertex position is shown for non-charmed Monte Carlo events. The distributions are given both when all intersections are used, and also when only those intersections with error $\sigma_x < 200\ \mu\text{m}$ are included; as can be seen, for these intersections the distribution is narrower, indicating that the error calculation is sensible. The normalised offset is shown in (b).

The calculation of the weighted mean of the intersection coordinates will now be described. The weight of an intersection is given by:

$$\mathbf{w}^I = (\mathbf{e}^I)^{-1}$$

Then the weighted sum of the intersection coordinates x^I is:

$$M_j = \sum_I \sum_i x_i^I \mathrm{w}_{ji}^I$$

where the indices (i, j) run over the 3 spatial coordinates, (x, y, z). The sum of the weights is:

$$\mathbf{S} = \sum_I \mathbf{w}^I$$

and the error on the vertex is:

$$\mathbf{E} = (\mathbf{S})^{-1}$$

Finally, the vertex coordinates are given by:

$$X_i = \sum_i \mathrm{E}_{ij} M_j$$

The candidate vertex found in this manner may not be good: the intersections with the other tracks of a track that does not belong to the vertex may be acceptable, but offset from the vertex position, as illustrated in Figure 7.24. It is therefore necessary to check if

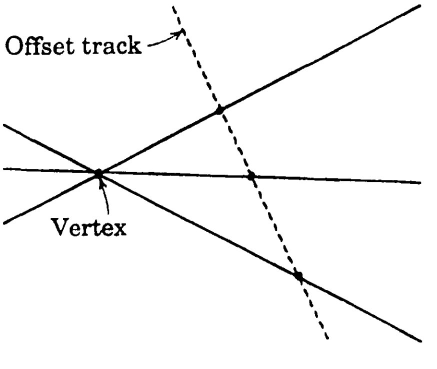

Figure 7.24 *Possibility of intersections not belonging to the vertex*

the intersections used are compatible with the vertex that has been calculated. The offset of each intersection in space from the candidate vertex is found using:

$$R^I = \left[\sum_i \left(x_i^{\,I} - X_i \right)^2 \right]^{1/2}$$

The error on this offset, σ_R, is calculated by transferring the errors from the vertex and the intersection, in a similar manner to the calculation of the error on the track separation, although now the vertex and intersection have 3 parameters each, so their combined covariance matrix is (6×6), and the transfer matrix has 6 elements. The normalised offset is checked, and if all intersections satisfy:

$$\frac{R}{\sigma_R} < 3{\cdot}0$$

then the vertex is accepted. Otherwise, the most offset intersection is found; once again, it is a track rather than the intersection which must be rejected, so for the two tracks that form the intersection the partial chi-square is calculated:

$$\chi^2 = \sum_I \left(\frac{R^I}{\sigma_R} \right)^2$$

The track with the larger partial chi-square is rejected, and the procedure iterated. The normalised offset of intersections (for real data) is shown in Figure 7.25, where the offset is measured relative to the first calculated vertex.

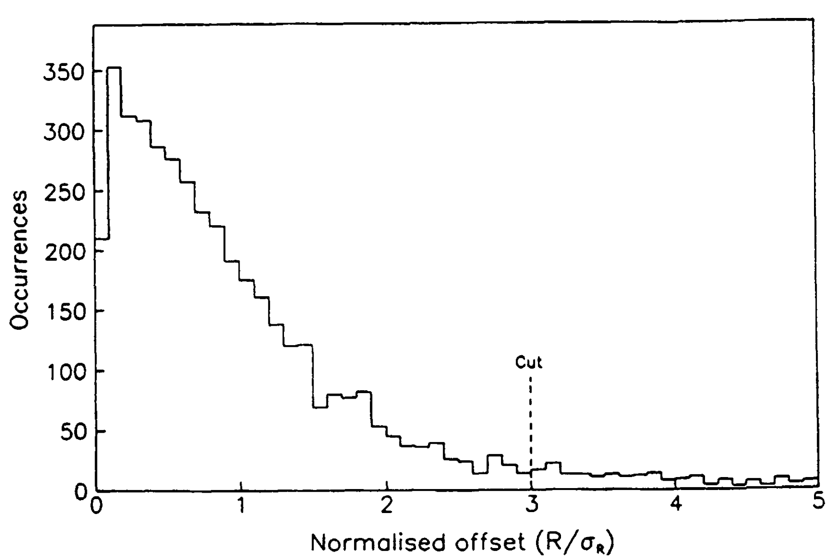

Figure 7.25 *Normalised offset of intersections from the vertex*

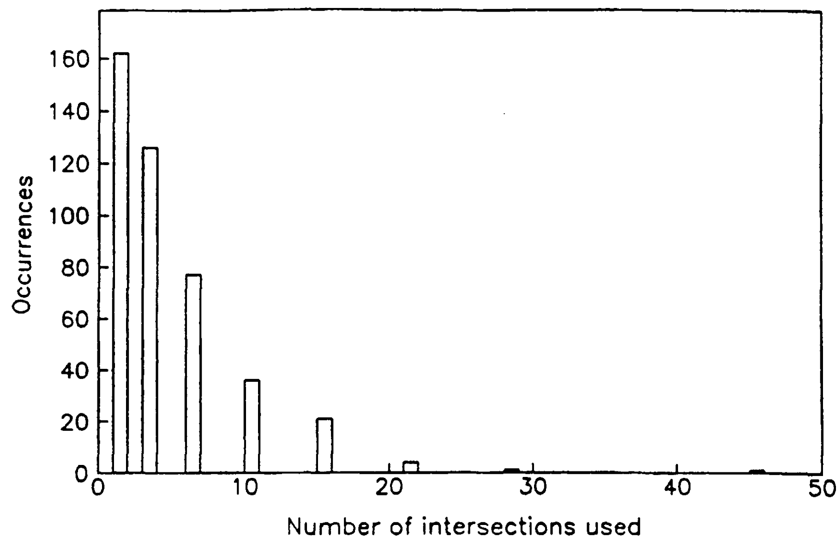

Figure 7.26 *Number of intersections used in the vertex*

The number of intersections used in the vertex is shown in Figure 7.26. The discrete nature of the distribution is forced by the consistency requirement that all the mutual intersections of used tracks are acceptable. This ensures that for n tracks there are $n(n-1)/2$ intersections used. The errors on the coordinate of the vertex are shown in Figure 7.27. The multiple peaked structure is a result of the different numbers of intersections used in the vertex calculation, as indicated. The Monte Carlo can be used to

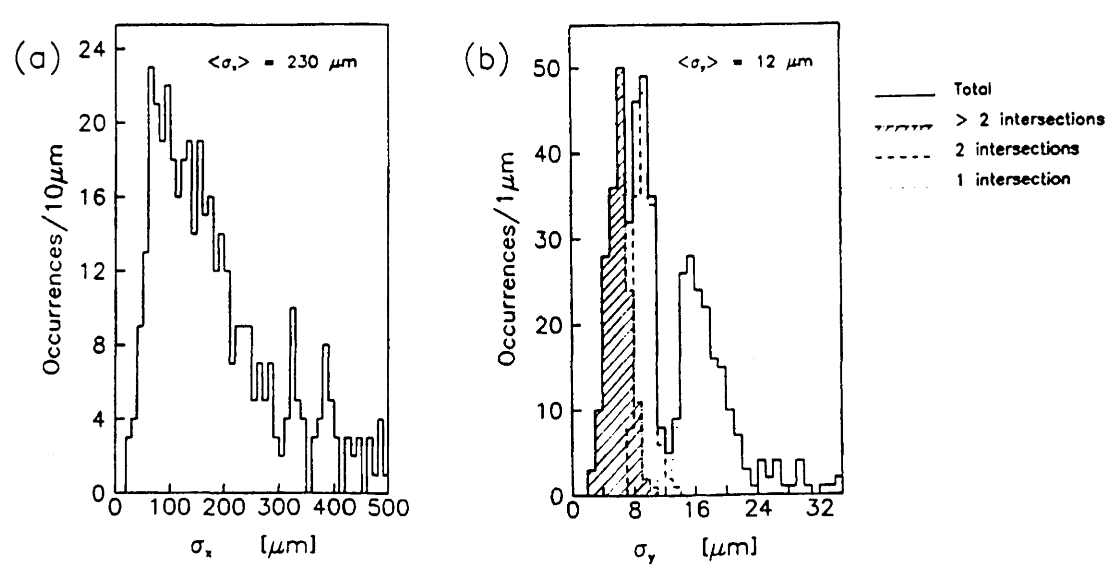

Figure 7.27 *Intersection vertex coordinate errors*

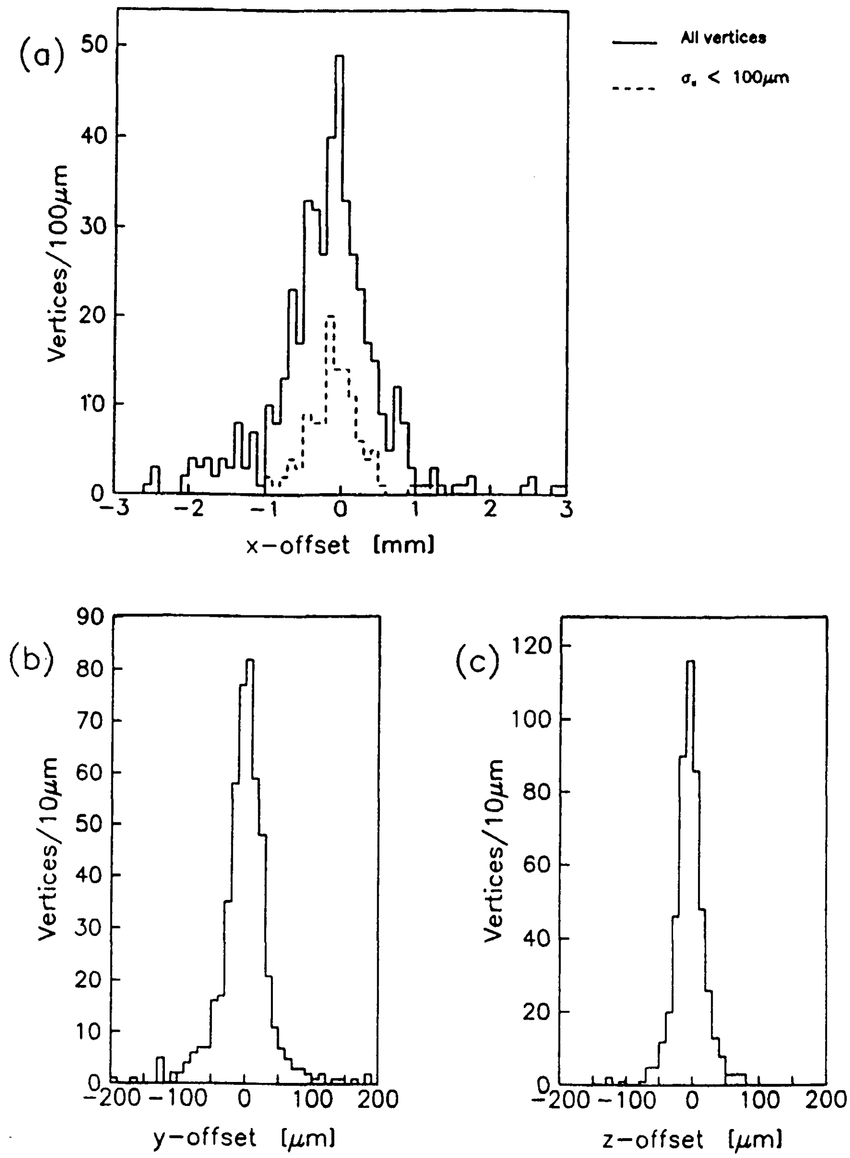

Figure 7.28 *Offset of reconstructed Intersection vertex from true vertex (Monte Carlo)*

check the performance of the vertex finding package: the offset of the reconstructed vertex from the true vertex is shown in Figure 7.28, for non-charm events. The *rms* width of the x-difference distribution gives a good measure of the performance of the single-vertex finding capability of the package. For this scheme, the *rms* width is ~ 330 μm.

Use of the active target

The active target is designed to provide information about the vertex. This can be analysed in a stand-alone manner, as is the case in ACTANL, the active target analysis patch of NEPTUN. However, we wish to utilise the information from the target to improve the vertex finding schemes that are based on the microstrip tracks, especially for the primary vertex recognition. A simple arrangement would be to check whether the vertex position found with the microstrip tracks was consistent with the active target data. In particular, if the candidate vertex was found to lie in an area of the target with no activity, then the vertex would be rejected. This approach was found to be too brutal, as any event that fails the target condition is simply rejected: it would be more useful if, instead, the vertex position was *improved* through the use of the target.

This philosophy was followed for the Intersection vertex by checking each *intersection*—rather than simply the final vertex—with the target. Furthermore, since nuclear recoil often gives a high pulse height in the strip of the target that contains the primary vertex, this feature was included in the target requirement. The cuts were chosen from scanning charm candidates; a target strip with a pulse height of at least 15 I_{min} within ± 1 mm of the intersection was required. The rejection of any intersections that fail this requirement takes place before the consistency check described earlier, and otherwise the vertex finding procedure is unchanged.

This use of the target was found to be particularly suited to events that had passed the microstrip filter, since the simple target algorithm used in the filter selects events with the required target configuration.

7.6 Constraint vertex

The Constraint vertex finding procedure was devised as a fully consistent approach to the treatment of the errors on the track parameters. It was used to investigate improvements in the mass resolution for reconstructed charmed particles. The idea was that by taking the tracks that had been identified as coming from a charm decay vertex, and constraining them to pass through that vertex, the track parameters would be closer to their true values, and so the mass resolution would be improved. This is indeed found to be the case, although the effect is small (see Section 8.4). However, the technique was then extended to form a general vertex finding procedure.

(a) (b)

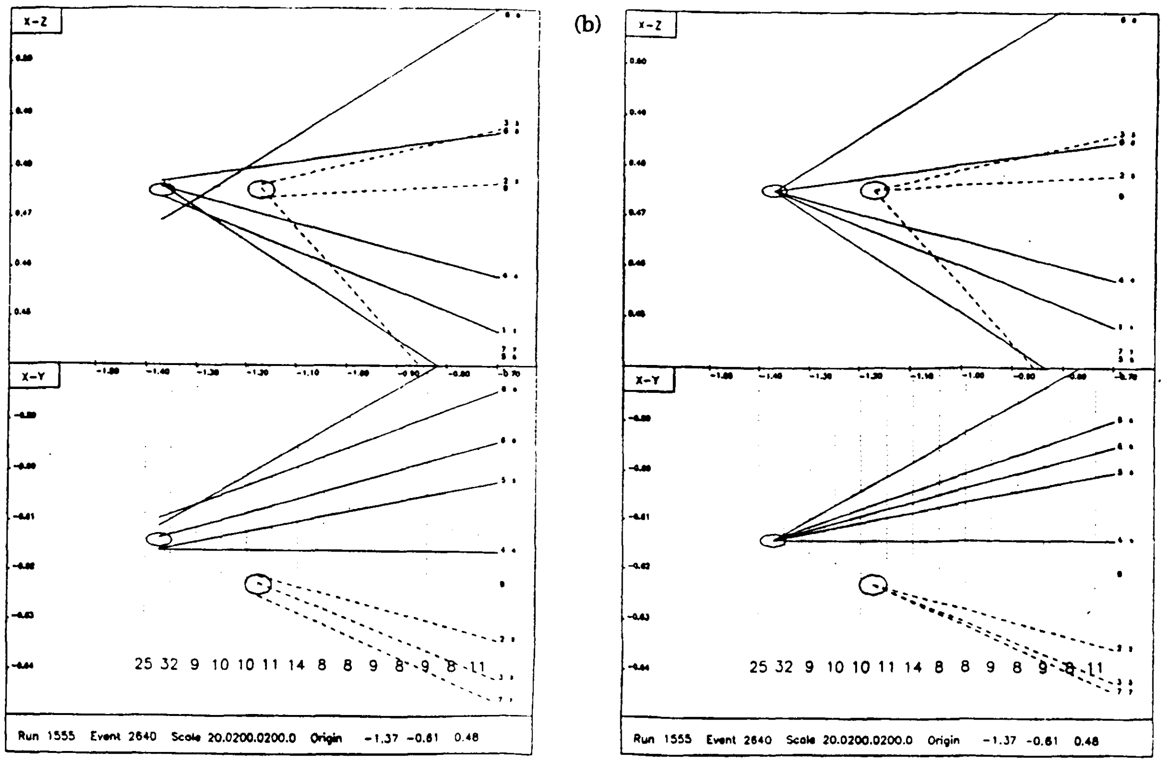

Figure 7.29 *Effect of constraining tracks to their vertices*

The basic principle is that the tracks that have been selected as belonging to a vertex are constrained to pass through a common point in space. The coordinates of that point are kept as free parameters, and provide the coordinates of the vertex. The extent to which the parameters of a track are changed to ensure that it passes through the common point is determined by the errors on the track parameters, and the movement of the track relative to its errors gives a chi-square variable.

The advantages of this approach are the following:

(i) A chi-square variable is available, which may be used as a measure of the vertex quality.

(ii) The track parameters will be adjusted by the constraints, and their precision should be improved.

(iii) Consistent use may be made of tracks from different sources; in particular, the additional tracks described in Section 7.4 may be used along with the refit tracks.

(iv) The event can be displayed with the tracks forced to their assigned vertices. See for example Figure 7.29. In (a) the vertex region of an event is displayed, showing the original (unconstrained) tracks; in (b) the constrained tracks are shown, indicating how the vertices were found.

A full treatment would include all of the track variables, including the momentum. For simplicity, however, the track parameterisation close to the vertex is taken as a starting value. A straight line parameterisation is used, in a similar manner to that described in the previous section; for the refit tracks, this involves taking the tangents to the parabolæ that were fitted in the target. The errors on the track parameters are propagated from the full track reconstruction, and so for the refit tracks they include the error due to the momentum. To further simplify the calculation, it is assumed that the errors are independent of x. This is obviously inaccurate if the variation in x is large, so an iterative technique is used: as a starting value, the TRIDENT vertex is taken. The vertex calculation is made, and if the new vertex position has moved further than a given tolerance in x, then the values of the errors are recalculated at that x-coordinate, the new tangents to the tracks are taken, and the vertex calculation is repeated. This procedure is iterated until the change in x is less than the given tolerance.

Constraint method

The linear parameterisation of the tracks close to the vertex may be expressed as follows:

$$y = a_i x + b_i$$
$$z = c_i x + d_i$$

where $(i = 1, n)$ for n tracks. The track errors are propagated to the x-coordinate of the current vertex approximation, and are transferred from the TRIDENT parameterisation to the (a, b, c, d) parameterisation, giving a (4×4) covariance matrix $\mathbf{C}_i$ for each track.

The measured parameters of the tracks may be written as a $(4n \times 1)$ vector:

$$\boldsymbol{m} = (a_1, b_1, c_1, d_1, a_2, b_2, ..., d_n)$$

The parameters that are found by the constrained fit are denoted as follows:

$$\overline{\boldsymbol{m}} = (\bar{a}_1, \bar{b}_1, ..., \bar{d}_n)$$

and we may put:

$$\overline{m_i} = m_i + \Delta m_i \qquad (i = 1, 4n)$$

The covariance matrices of the tracks are combined to give a covariance matrix $\mathbf{V}$ of $\boldsymbol{m}$:

$$\mathbf{V} = \begin{bmatrix} \mathbf{C}_1 & 0 & . & . & 0 \\ 0 & \mathbf{C}_2 & . & . & 0 \\ . & . & . & & \\ . & . & & . & \\ 0 & 0 & & & \mathbf{C}_n \end{bmatrix}$$

where there are no track-track correlations. The vertex coordinates from any approximation are represented as:

$$M = (X, Y, Z)$$

and the best fit values:

$$\overline{M}_i = M_i + \Delta M_i \qquad (i = 1, 3)$$

The constraint equations arise from the requirement that the fit vertex coordinates satisfy the fit tracks:

$$\overline{Y} = \overline{a}_i \overline{X} + \overline{b}_i$$

$$\overline{Z} = \overline{c}_i \overline{X} + \overline{d}_i$$

where ($i = 1,n$), giving $2n$ constraints. A ($2n \times 1$) vector $\boldsymbol{f}$ of residuals may then be defined:

$$f_{2i-1} = \overline{Y} - \overline{a}_i \overline{X} - \overline{b}_i$$

$$f_{2i} = \overline{Z} - \overline{c}_i \overline{X} - \overline{d}_i$$

Two matrices of derivatives are calculated:

$$\mathbf{A} = \frac{\partial f}{\partial M} = \begin{bmatrix} -a_1 & 1 & 0 \\ -c_1 & 0 & 1 \\ -a_2 & 1 & 0 \\ -c_2 & 0 & 1 \\ . & . & . \\ . & . & . \end{bmatrix}$$

is a ($2n \times 3$) matrix, and:

$$\mathbf{B} = \frac{\partial f}{\partial m} = \begin{bmatrix} -X & -1 & 0 & 0 & 0 & 0 & . & . \\ 0 & 0 & -X & -1 & 0 & 0 & . & . \\ 0 & 0 & 0 & 0 & -X & -1 & . & . \\ . & . & . & . & . & . & & \\ . & . & . & . & . & . & & \end{bmatrix}$$

is a $(2n \times 4n)$ matrix.

To perform the constrained fit, we wish to minimise:

$$S^2 = \Delta m^{\mathrm{T}}\, \mathbf{V}^{-1}\, \Delta m + 2\,\lambda^{\mathrm{T}} f$$

where λ is a $(2n \times 1)$ vector of Lagrange multipliers. The solution is found using standard matrix manipulation [101]:

$$\Delta m = -\mathbf{V}\, \mathbf{B}^{\mathrm{T}}\, \mathbf{W}_B\, (\mathbf{I} - \mathbf{A}\, \mathbf{W}_{AB}{}^{-1}\, \mathbf{A}^{\mathrm{T}}\, \mathbf{W}_B)\, f$$
$$\Delta M = -\mathbf{W}_{AB}{}^{-1}\, \mathbf{A}^{\mathrm{T}}\, \mathbf{W}_B\, f$$

where:

$$\mathbf{W}_B = (\mathbf{B}\, \mathbf{V}\, \mathbf{B}^{\mathrm{T}})^{-1}$$
$$\mathbf{W}_{AB} = \mathbf{A}^{\mathrm{T}}\, \mathbf{W}_B\, \mathbf{A}$$

and $\mathbf{I}$ is the $(2n \times 2n)$ unit matrix. The chi-square variable for the vertex is given by:

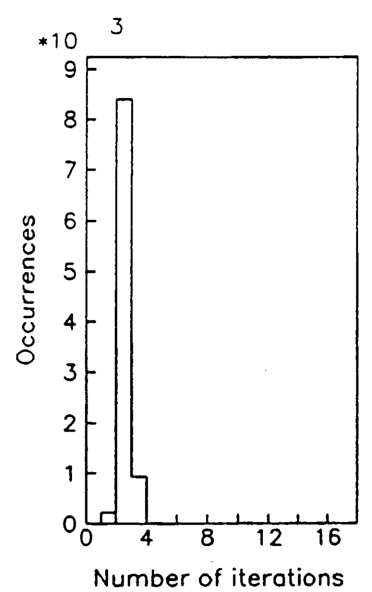

Figure 7.30 *Number of iterations for Constraint vertex calculation*

$$\chi^2 = \Delta m^{\mathrm{T}} \mathbf{V}^{-1} \Delta m$$

The number of degrees of freedom can be determined using Equation 7.11. There are $2n$ constraint equations, and 3 unmeasured variables, so the probability of chi-square is calculated with $(2n - 3)$ degrees of freedom. For the calculation of the pulls of the fit (Equation 5.1), it is necessary to know the covariance matrix for the fit vertex coordinates; this is given by $\mathbf{W}_{AB}{}^{-1}$.

The coordinates of a new candidate vertex are found in this manner, and as mentioned above, the procedure is iterated until the change in the x-coordinate of the vertex is less than a tolerance, taken as 1 mm. The iteration converges rapidly, as shown in Figure 7.30.

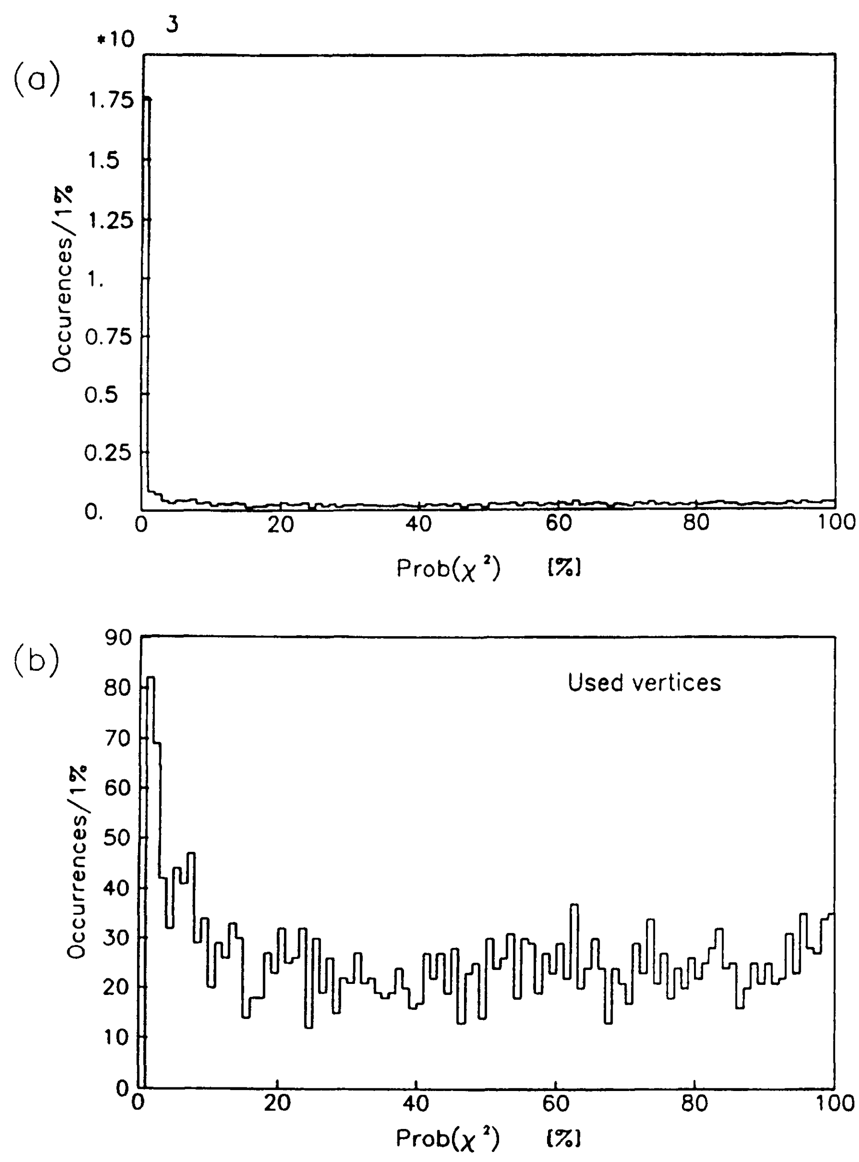

Figure 7.31 Probability of chisquare for vertex fit

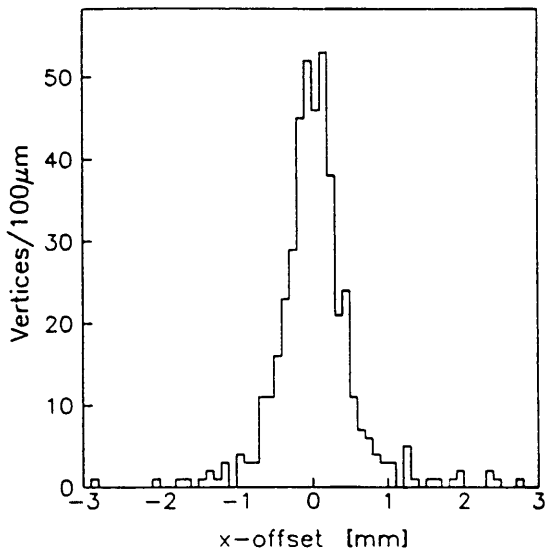

Figure 7.32 *Offset of reconstructed Constraint vertex from true vertex (Monte Carlo)*

The probability of chi-square is then checked to see whether the vertex is acceptable: the probability is required to be greater than a cut, of typically 1 %. If this criterion is not satisfied, then the track with the greatest contribution to the chi-square may be rejected from the fit, and the vertex recalculated. The chi-square of the vertex is composed of the partial chi-squares of the tracks:

$$\chi^2 = \sum_i \chi_i^2$$

and the partial chi-squares are compared to find the least acceptable track in the fit. See Figure 7.31. The vertex finding method was tested in the same manner as the Interaction vertex, by comparing the reconstructed vertex coordinates with those of the true vertex, using non-charmed Monte Carlo events—see Figure 7.32. The *rms* width of the distribution is now ~ 300 μm, representing an improvement over the earlier vertex reconstruction techniques. The errors on the vertex coordinates are shown in Figure 7.33, for the primary vertex, and in Figure 7.34, for the secondary vertex. These distributions are taken from the D_s analysis (Section 8.4), so the secondary vertex involves three particles. Note that the primary vertex errors are smaller than those of the secondary vertex, due to the larger number of tracks involved on average.

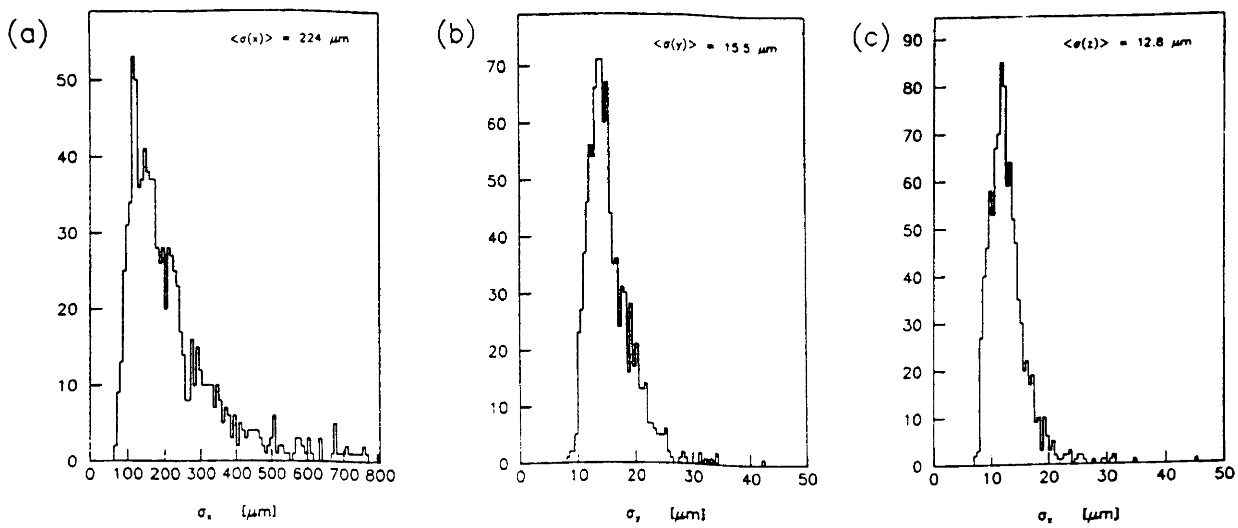

Figure 7.33 *Errors on primary vertex coordinates*

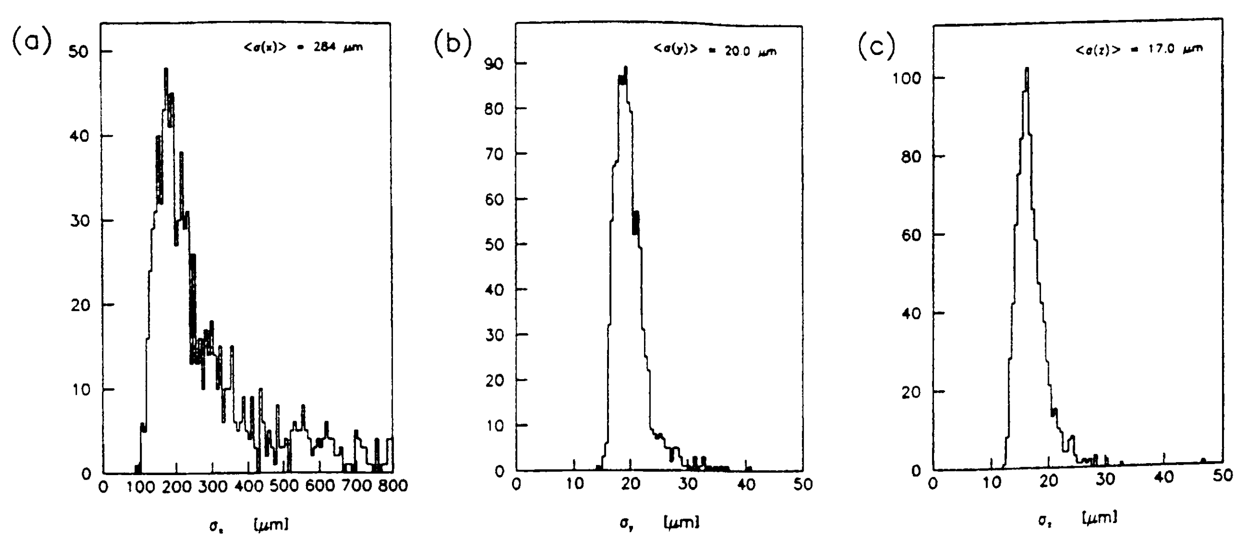

Figure 7.34 *Error on secondary vertex coordinates*

The vertex finding algorithms described in this chapter must now be used in the search for charmed particle decays. This is the subject of the next chapter.

Chapter 8

CHARM SIGNALS

In this chapter, the techniques used for the isolation of charm signals are described. The general principles of the analysis chain are discussed first, then the isolation of a charm signal in specific channels. The charm analysis depends on the vertex reconstruction methods that were described in the previous chapter; the general principles of the analysis are independent of the vertex scheme employed, so the results obtained using the different schemes will be discussed with the specific decay channels.

I Analysis Techniques

8.1 Overview

The procedure followed for isolating charm signals may be summarised as follows:

(i) *Read event*. At this stage, the charged track reconstruction (using TRIDENT—Section 6.9) has been performed, and the track information is read in along with the raw data. The Cerenkov analysis (using INDANL—Section 6.11) may or may not have been performed; if not, then this is now done.

(ii) *Find tracks*. The track refit in the microstrips is performed (Section 7.2). If the additional tracks (Section 7.4) are to be used, then that search is made. The parameters of tracks that have been found are stored in arrays, for use in the subsequent analysis.

(iii) *Select combination.* A *combination* of tracks from the refit is selected that has one of each of the particle types (determined by the Cerenkov analysis) that are required in the charm decay channel under investigation. Only combinations with the correct charges are retained. For example, for the channel $D_s^+ \to K^+K^-\pi^+$, a pair of oppositely signed kaons, and a pion are selected. Note that if the extended kaon definition is used (Section 6.11), the particle identification may be ambiguous. There are generally a number of different suitable combinations within each event, and it is the purpose of the following requirements to select the ones of interest—i.e. those that come from charm.

(iv) *Calculate effective mass.* The *effective mass* of the combination is the mass that the parent particle would possess, if the combination particles were indeed the products of a decay. Combinations with effective mass outside a selected range (centred on the expected charm mass) are rejected, to economise on computer processing time. The selection is not made too tight, however, as the *mass plot* (the histogram of effective masses) is the chief tool for demonstrating the existence of a signal.

(v) *Secondary vertex.* The tracks of the combination are used in the search for a secondary vertex, using one of the vertex finding algorithms. If the quality of the vertex fit is insufficient, the combination is rejected.

(vi) *Charm track reconstruction.* The tracks of the combination are used to reconstruct the trajectory of the candidate charmed particle. This involves the summation of the momentum components of the decay products, and some error propagation to calculate the errors on the 'charm' track.

(vii) *Primary vertex.* All the tracks of the event apart from those of the combination are used to search for a primary vertex; the reconstructed charm track is also used. There must therefore be at least one other track (as well as the charm track), so that a vertex may be formed. The vertex algorithm rejects tracks one by one from the calculation until a vertex of sufficient quality is found (or no tracks remain).

(viii) *Other cuts.* Further requirements may be made; for example, that the charm track must be included in the final primary vertex calculation.

(ix) *Vertex separation.* The separation of the secondary vertex from the primary vertex is calculated. Cuts are made on this separation to enrich the charm signal.

Some of the features of this scheme have already been discussed; further details will now be given about the others.

8.2 Further details

Mass combinations

The effective mass of a combination is simply calculated using the relationship connecting the mass m, momentum p, and energy E of a particle:

$$E^2 = p^2 + m^2 \tag{8.1}$$

The momentum components of the candidate parent particle are found from the components of the combination particles (by momentum conservation):

$$\left(p_c\right)_i = \sum_s \left(p_s\right)_i \tag{8.2}$$

where the subscripts c and s refer to the *charm* and *secondary* tracks respectively, and i runs over the spatial coordinates (x, y, z). Hence the square of the charm momentum may be calculated:

$$p_c^2 = \sum_i \left(p_c\right)_i^2$$

From the conservation of energy, and using Equation 8.1:

$$E_c = \sum_s E_s = \sum_s \left(p_s^2 + m_s^2\right)^{1/2}$$

so finally:

$$m_c = \sqrt{E_c^2 - p_c^2}$$

where m_c, the mass of the candidate charmed particle, is the effective mass of the combination.

The momenta p_s of the combination tracks are taken from TRIDENT. The components of the momentum for each track are calculated using Equations 7.2–4. These equations require the specification of the track angles λ and ϕ, which depend on the x-coordinate at which the components are calculated. Until the secondary vertex has been found, the correct x-coordinate is not known, so as a first approximation the TRIDENT vertex position is taken. Then when the secondary vertex is calculated, the effective mass is corrected. The change in mass calculated is generally not large; see Figure 8.1. The values of λ and ϕ are determined using Equations 7.5–6.

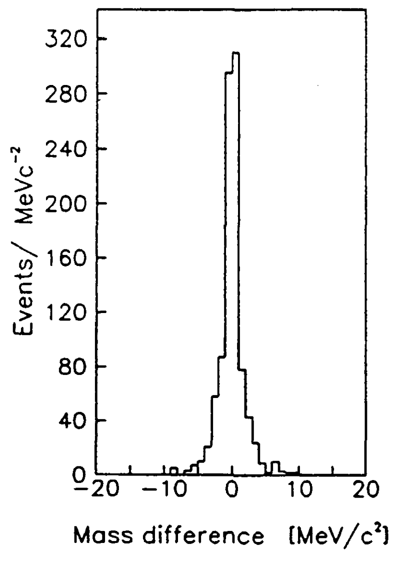

Figure 8.1 *Change in mass using correct vertex coordinates*

Secondary vertex finding

The tracks from the combination are used by the vertex finding algorithm (either the Intersection or Constraint scheme). In both cases *all* of the tracks must be accepted as belonging to the secondary vertex—contrasting with the primary vertex calculation where tracks may be dropped. Further, more specific (and channel dependent) requirements may be made. These will be discussed below.

The vertex finding routine returns the secondary vertex coordinates (x_s, y_s, z_s) and an associated error matrix $\mathbf{C}_s$. The position of the secondary vertex is required to be sensible—it must lie within the transverse extremes of the active target. In x, the limits are taken as the upstream surface of the first silicon plane of the target, and the x-coordinate of the third plane of the microstrip detector. The latter, downstream, limit is determined by the requirement of at least three hits in each projection of the microstrips for the refit tracks (which are used for the combination). It is therefore possible for the secondary vertex to lie downstream of the first microstrip plane in each projection, and the associated track still to be found. If this is the case, then a check is made that there is not a hit that has been associated with the track on the first plane. For both the upstream and downstream limits, the vertex coordinate is allowed to lie up to 3 σ_x outside the limit, where σ_x is the error on the x-coordinate measurement, calculated from:

$$\sigma_x = \sqrt{(\mathrm{C}_s)_{xx}}$$

Charmed particle trajectory reconstruction

The momentum components of the charmed particle are calculated as described in the discussion of mass combinations above (Equation 8.2). These may be used to calculate the track angles λ and ϕ, by making a linear parameterisation:

$$y = a_y{}' x + b_y{}'$$
$$z = a_z{}' x + b_z{}'$$

where:

$$a_y{}' = p_y / p_x$$
$$a_z{}' = p_z / p_x$$

The angles are given by:

$$\lambda = \tan^{-1}\left(\frac{a_z'}{\sqrt{1 + a_y'^2}} \right)$$

$$\phi = \tan^{-1}\left(a_y' \right)$$

The values calculated are valid at the x-coordinate of the secondary vertex, x_s. Equations 7.7–8 are then used to determine the coordinates of the trajectory at the front, middle and back of the active target, and a parabola is calculated that passes through all three points. This gives the parameterisation used for the charm track (in a similar fashion to the refit tracks—Section 7.2).

The error on the charm track parameters must also be calculated. This is achieved by propagating the errors on each of the secondary tracks (in the TRIDENT parameterisation), to the x-coordinate of the secondary vertex, x_s. The error from multiple scattering is added (Section 7.3), and then the errors are transferred to (p_x, p_y, p_z) at x_s, to give a (3×3) covariance matrix $\mathbf{V}_s$ for each track. These are added:

$$\mathrm{V}_{ij} = \sum_s \left(\mathrm{V}_s \right)_{ij}$$

The errors are then transferred to $(1/p, \lambda, \phi)$ using the relationships in Equations 7.2–4, to give a (3×3) matrix $\mathbf{C}_2$. The errors on the transverse coordinates of the charmed track are taken from the errors of the secondary vertex (returned by the vertex finding algorithm):

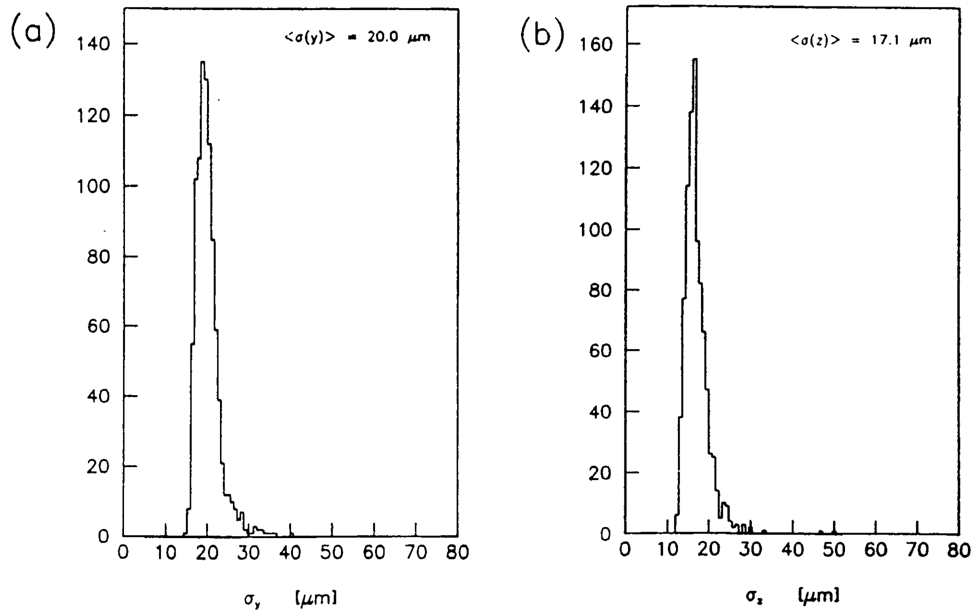

Figure 8.2 *Error on transverse coordinates of the charm track at the vertex*

$$C_1 = \begin{bmatrix} \sigma_{yy} & \sigma_{yz} \\ \sigma_{zy} & \sigma_{zz} \end{bmatrix}$$

Finally, the covariance matrix for the charmed track, in the $(y, z, 1/p, \lambda, \phi)$ parameterisation, is taken as:

$$\begin{bmatrix} C_1 & 0 \\ 0 & C_2 \end{bmatrix}$$

This is then used to propagate the errors to the parabolic parameterisation, in the same manner as for the refit tracks.

The use of the reconstructed charm track is important, because:

(i) it is calculated using a number of other tracks from the combination (typically two or three), and therefore is generally more accurately measured than standard tracks, as its transverse errors tend to be lower. The transverse errors of the charm track from the D_s analysis are shown in Figure 8.2—they should be compared with those of standard tracks in Figure 7.7;

(ii) if the combination is valid, then the charm track reconstructed should originate from the primary vertex. This is a powerful requirement for rejecting background;

(iii) it enables a primary vertex to be reconstructed for events where there is only a single track remaining once the combination tracks have been eliminated.

Primary vertex finding

The primary vertex is reconstructed by the vertex finding algorithm, using all the tracks in the event apart from those used in the secondary vertex, and including the charm track. As mentioned above, if the vertex quality is insufficient, then the track that is least well associated to the vertex is dropped, and the vertex position recalculated. This process is repeated until the vertex is acceptable, or there are less than two tracks left (in which case the combination is rejected). Due to this feature, the condition for an acceptable primary vertex may be made more strict than that for the secondary vertex, since if any track fails to be accepted for the secondary vertex the combination is immediately rejected; for the primary vertex, the stricter condition ensures that tracks that do not belong to the vertex (coming from the second charm decay, or due to track finding errors) are not used.

The position of the primary vertex is required to be sensible, in a similar manner to the secondary vertex. In this case, however, the vertex must lie within the target in x, as well as in the transverse coordinates.

Separation of vertices

The separation of the primary and secondary vertices is the most important characteristic used for the enrichment of the charm signal. A cut can be made on their separation in x (see Figure 8.3):

$$\Delta x = x_s - x_p$$

In particular, we expect at least that the secondary vertex should be downstream of the primary vertex:

$$\Delta x > 0$$

Alternatively, the 'normalised' separation N_σ may be used:

$$N_\sigma = \frac{\Delta x}{\sigma_x}$$

where σ_x is the error on Δx. This is given by:

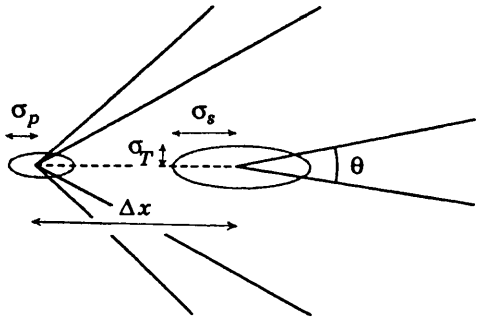

Figure 8.3 *Vertex separation parameters*

$$\sigma_x = \sqrt{\sigma_p^2 + \sigma_s^2}$$

where σ_p and σ_s are the errors on x_p and x_s respectively. The N_σ parameter has the property that it is independent of the Lorentz boost γ of the decaying particle, since:

$$\Delta x = \gamma \beta c t$$

where t is the proper time of the decay. Referring to Figure 8.3, the error on the x-coordinate of the secondary vertex is given approximately by:

$$\sigma_s \sim \frac{\sigma_T}{\theta}$$

where σ_T is the transverse error on the measurement of the secondary vertex position. But if the decaying particle has mass m and energy E, then:

$$\theta \sim \frac{m}{E} = \frac{1}{\gamma}$$

Since the error on the secondary vertex position generally dominates the error on the vertex separation, we have:

$$N_\sigma \sim \frac{\Delta x}{\sigma_s} \sim \frac{\beta c t}{\sigma_T}$$

and since σ_T is independent of γ, so too is N_σ. (Note also that the impact parameter of tracks from the charm decay: $\delta \sim \Delta x\, \theta$, is independent of γ, as stated in Chapter 1). For our experiment, $\sigma_T \sim 20\ \mu\text{m}$, and $\beta \sim 1$, so:

$$N_\sigma \sim 15 t$$

where t is measured in ps.

II Charmed Channels Investigated

The charmed channels investigated in this thesis are the following:

(i) $D^0 \to K^-\pi^+$

(ii) $D^+, D_s^+ \to \phi\,\pi^+ \to K^+K^-\pi^+$

The first of these was used in the development of the analysis techniques. It was suitable for this purpose as the signal was expected to be comparatively simple to isolate, for the following reasons:

(i) the branching ratio is relatively high (~ 5 %);

(ii) the combinatorial background is small (since there are only two decay products);

(iii) the decay products are charged, and so should be seen in the microstrip detector.

Some early results from the analysis of this channel have already been presented [84], and the analysis will therefore only be outlined here. The techniques that were developed using this channel were then applied to the analysis of the $\phi\pi$ channel, where signals are found for both the D_s and the D^+ decays. The next chapter is concerned with the extraction of physics results from these signals.

8.3 $D^0 \to K^+\,\pi^-$

Event selection

The data used for the study of this channel came from the microstrip filter run at Imperial College. This filter was run on the data taken in 1985, amounting to 5·2 million triggers. As explained in Section 6.7, one criterion of the filter was an active target algorithm, that selected events without complicated target activity near the production vertex. This was included to simplify the vertex finding of the filter, and as it only passed about 23 % of the data, it served to reduce the number of events passed by the full filter to a level at which the production could be rapidly completed. The target algorithm was not expected to modify the charm content of the data, and this was confirmed using a Monte Carlo simulation [84]. Thus the effective raw data sample passed through the microstrip filter was about 1·2 million events. The data that passed the microstrip filter were then further reduced using an additional kaon-selecting filter (described in Section 6.7), which ensured that there was at least one kaon identified in each event.

Charm analysis

For particle identification in the analysis of the filtered data, the INDRA Cerenkov was used, with the extended kaon identification scheme described in Section 6.11. Combinations were then found of a kaon and a pion with opposite charge. Events containing an effective mass combination greater than 1·5 GeV/c^2 were filtered off for further study.

The Intersection vertex finding technique (described in Section 7.5) was used to find the $K\pi$ secondary vertex and, if this was successful, the candidate D^0 trajectory was calculated, for use in the primary vertex search (again using the Intersection technique). The mass plot that is produced when both of the vertices have been found is shown in Figure 8.4, for masses lying between 1·6 and 2·1 GeV/c^2. The fit is exponential, and the plot is displayed both (a) using the errors calculated from the bin contents, and (b) as a

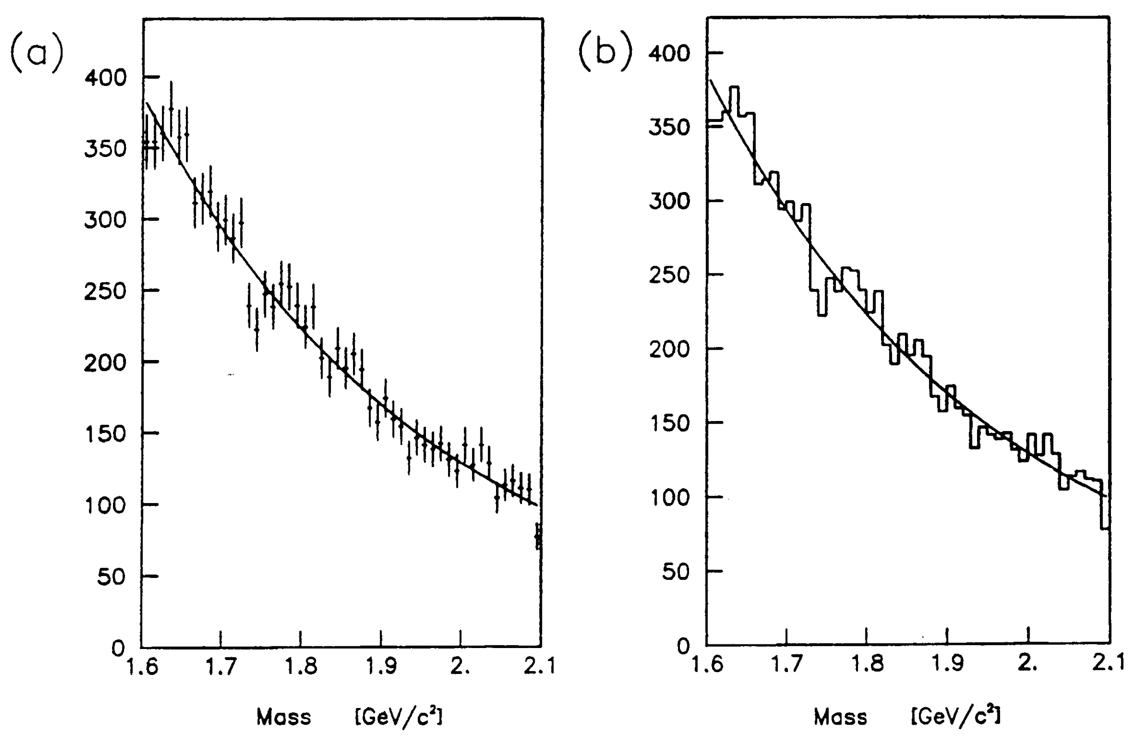

Figure 8.4 *$K\pi$ mass plot, after vertices found*

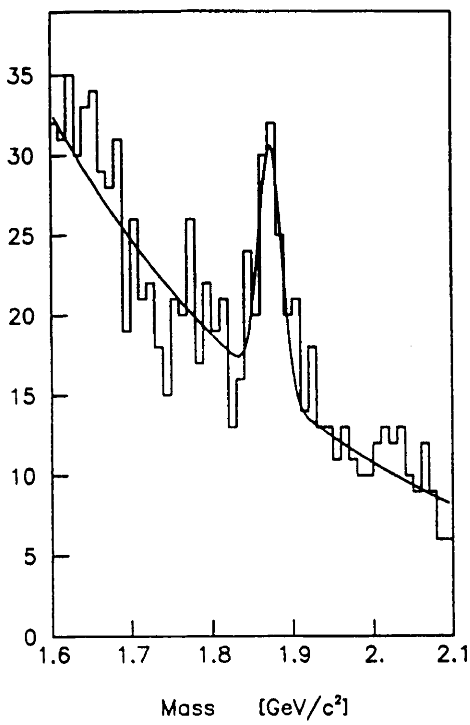

Figure 8.5 *$K\pi$ mass plot, $N_\sigma > 3$, Intersection vertex*

histogram. No signal is evident at this stage. A separation of the vertices was then required, and at $N_\sigma > 3$ a clear enhancement is seen at a mass of ~ 1·86 GeV/c^2, above a decreasing background (see Figure 8.5). This is at the mass expected for the D^0.

The information of the active target was next incorporated into the primary vertex finding, using the active target condition described in Section 7.5. The requirement imposed was that there must be a target strip with a pulse height of at least 15 I_{min} within 1 mm of each pairwise intersection of tracks used in the vertex calculation. The resulting mass plot is shown in Figure 8.6; as can be seen, the imposition of this condition leads to a reduction in the background without substantial loss of signal. The condition was found to be particularly effective for data from the microstrip filter, since the target algorithm used with this filter selected events which had a large pulse height at the start of the 'main road' in the target. These events are therefore well matched to the Intersection target condition, improving the chance that the primary vertex is correctly found.

The fit to the histogram in Figure 8.6 is the sum of an exponential fit to the background and a Gaussian fit to the signal. The fitting technique will be described in detail in Section 9.1. From the fit, the number of entries in the signal is 62 ± 9, and the

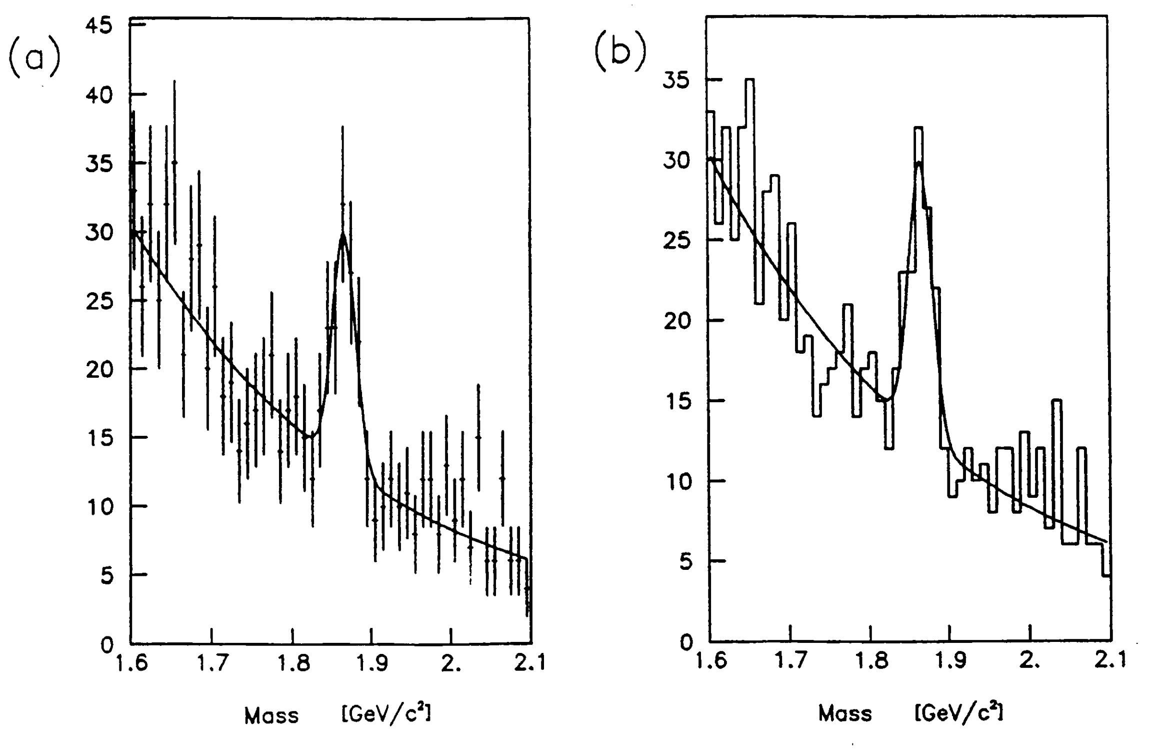

Figure 8.6 *$K\pi$ mass plot, imposing target condition*

signal-to-background ratio is ~ 1·0. The events containing an entry in this mass plot were filtered off for further analysis.

Analysis development

Unfortunately it was found that as the vertex separation cut was increased in severity, the signal-to-background ratio did not substantially improve, with background persisting even to large N_σ cuts. See for example the mass plot at $N_\sigma > 10$, shown in Figure 8.7. To improve this situation, the Constraint vertex finding technique (described in Section 7.6) was used on the events selected at $N_\sigma > 3$. The same analysis scheme was used, but now the search for the primary and secondary vertices used the Constraint method. This led to a considerable cleaning up of the signal at large N_σ cuts, as seen for example in Figure 8.8, at $N_\sigma > 10$.

When the Constraint vertex method was used on the full data set (rather than the $N_\sigma > 3$ selected events from the previous analysis), however, a signal as strong as that in Figure 8.6 was not achieved. The signal at $N_\sigma > 3$ for the Constraint vertex analysis is

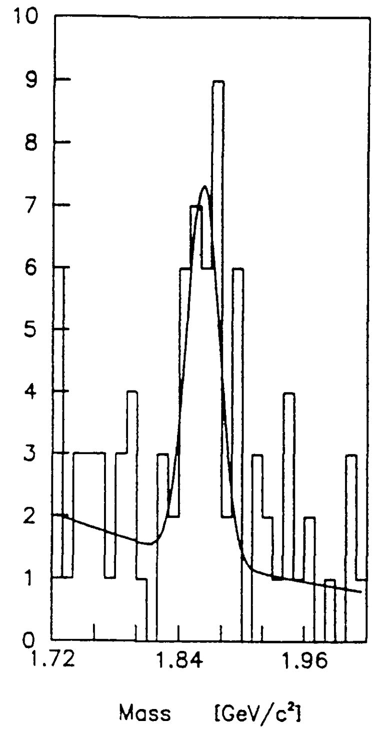

Figure 8.7 *$K\pi$ mass plot, $N_\sigma > 10$, Intersection vertex*

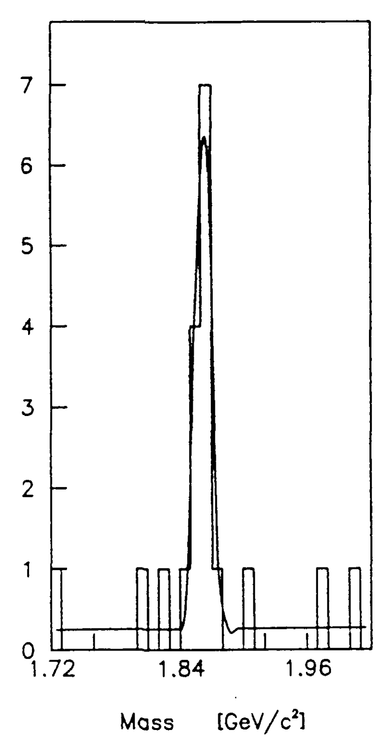

Figure 8.8 *$K\pi$ mass plot, $N_\sigma > 10$, both Intersection and Constraint vertex*

shown in Figure 8.9. Note that due to the different calculation of errors, this cut is rather more severe than the corresponding cut in the Intersection vertex scheme: the vertex errors from the Constraint vertex are slightly smaller than those from the Intersection vertex, as was seen in Section 7.6. The strong signal of Figure 8.6 was due in part to the active target condition used. Since it relied on the pairwise intersections, this condition could not be directly imposed in the Constraint vertex scheme. For the Constraint method, the active target information was incorporated in other ways, as will be seen in the analysis of the $\phi\pi$ channel.

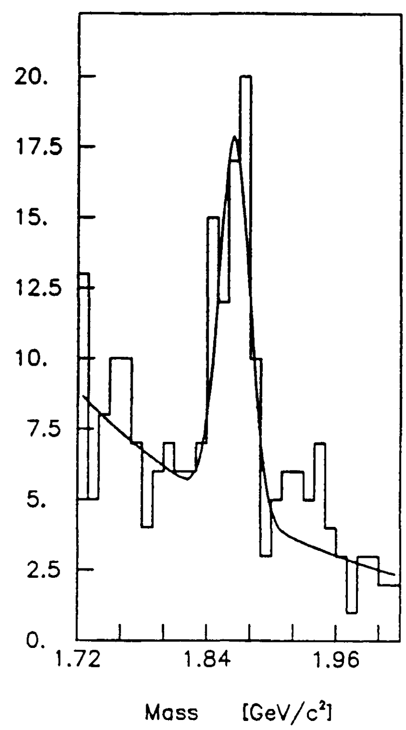

Figure 8.9 *$K\pi$ mass plot, $N_\sigma > 3$, Constraint vertex*

When the $N_\sigma > 3$ selected events from the Intersection vertex analysis are passed through the Constraint scheme, they give the mass plot at $N_\sigma > 3$ (using the Constraint scheme errors) shown in Figure 8.10. The usefulness of the additional tracks discussed in Section 7.4 was tested by running the same analysis, but including additional tracks found in the Z-projection. The additional tracks are found by pattern recognition in the microstrips, using any hits that are not associated to a TRIDENT track (and also excluding the OR-images of associated hits). See Figure 8.11—the increase in signal is

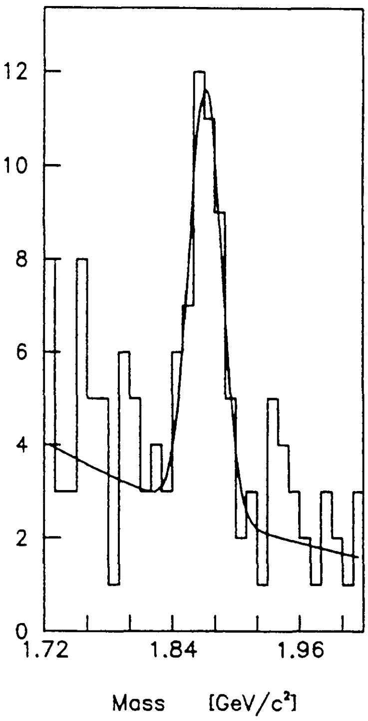

Figure 8.10 *Kπ mass plot, $N_\sigma > 3$, both Intersection and Constraint vertex*

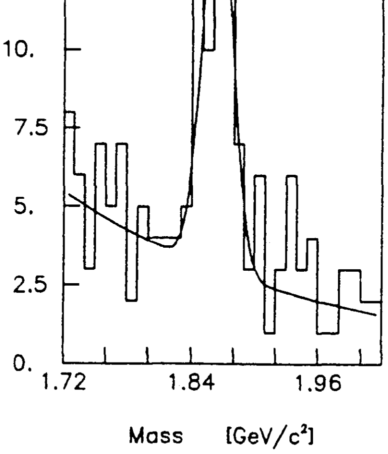

Figure 8.11 *Kπ mass plot, incorporating additional tracks*

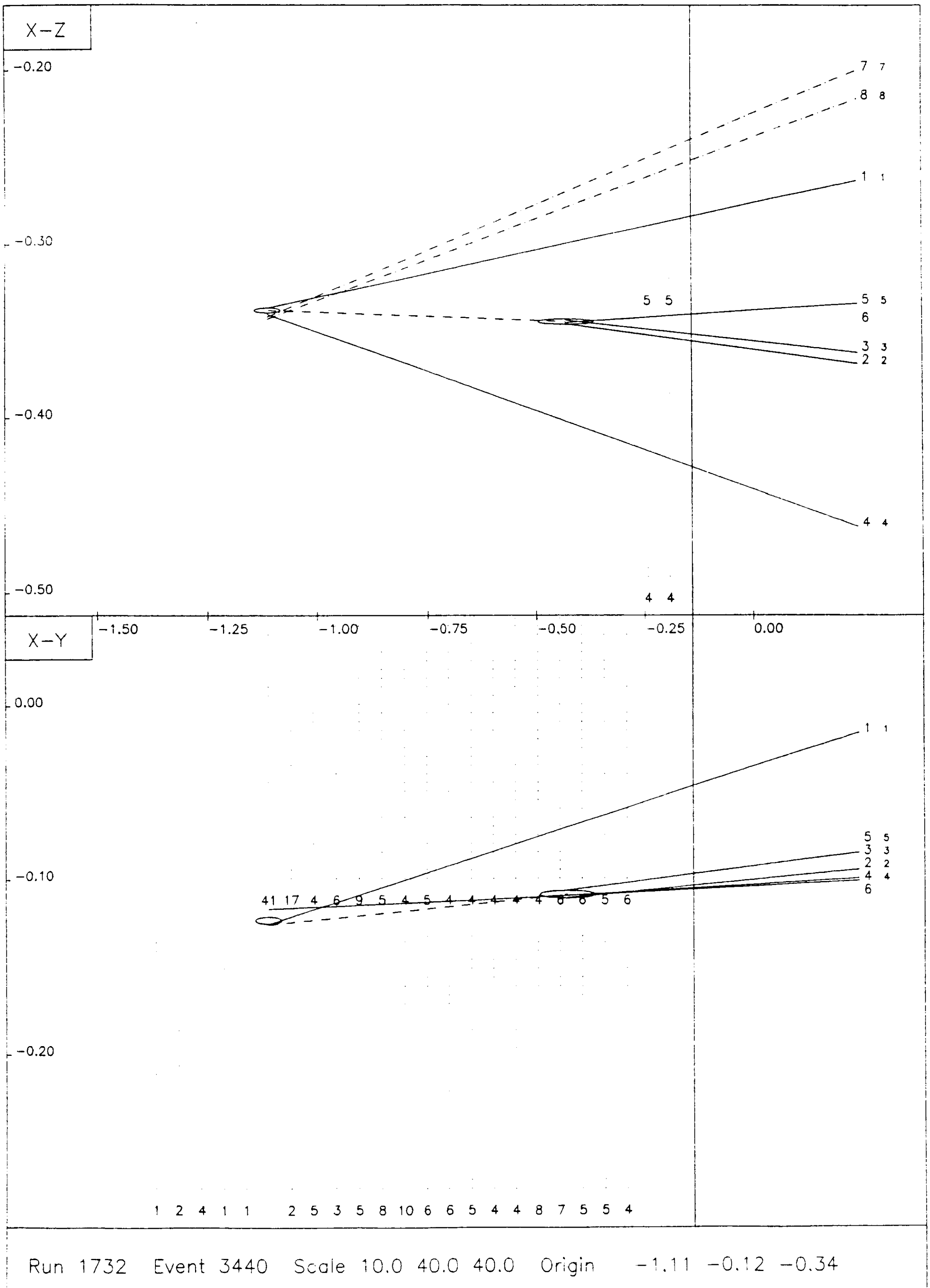

Figure 8.12 Vertex region of event using Z-projection additional tracks

clear. The Z-projection additional tracks improve the charm signal by helping to ensure that the primary vertex position is correctly found. They can also help in the rejection of background events caused by secondary interactions in the target. The vertex region of an event in which Z-projection additional tracks have been used for the primary vertex calculation is displayed in Figure 8.12, with the additional tracks shown dot-dashed. The Y-projection additional tracks, on the other hand, did not give any significant improvement to the charm signal. This was thought to be due to the increased uncertainty in the track finding for the Y-projection additional tracks, resulting from their unknown curvature (since their momentum is unknown).

The preceding analysis was all performed on data that had been passed through a kaon-selecting filter (in addition to the microstrip filter). As mentioned above, this filter was used to reduce the computing time taken by the production, as it was assumed that an identified kaon would be required in the charm channels that were first analysed. However, as explained in Section 6.11, an extended kaon definition was later introduced to increase the efficiency of kaon identification, by accepting high momentum kaons that gave light in INDRA (since they are above the appropriate Cerenkov threshold). The kaon-selecting filter had been run with the standard, unambiguous, particle

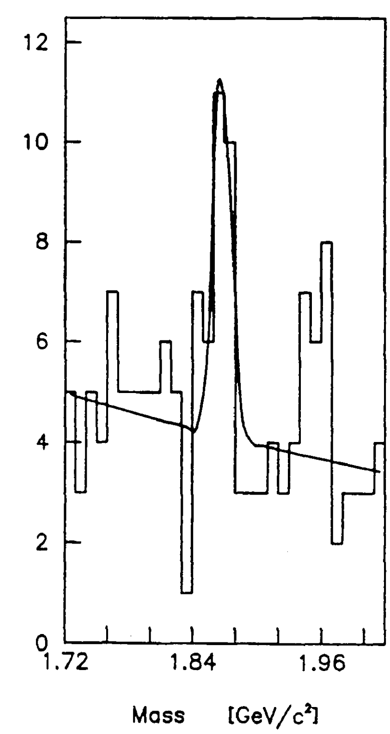

Figure 8.13 *$K\pi$ mass plot, using only events that failed the kaon filter*

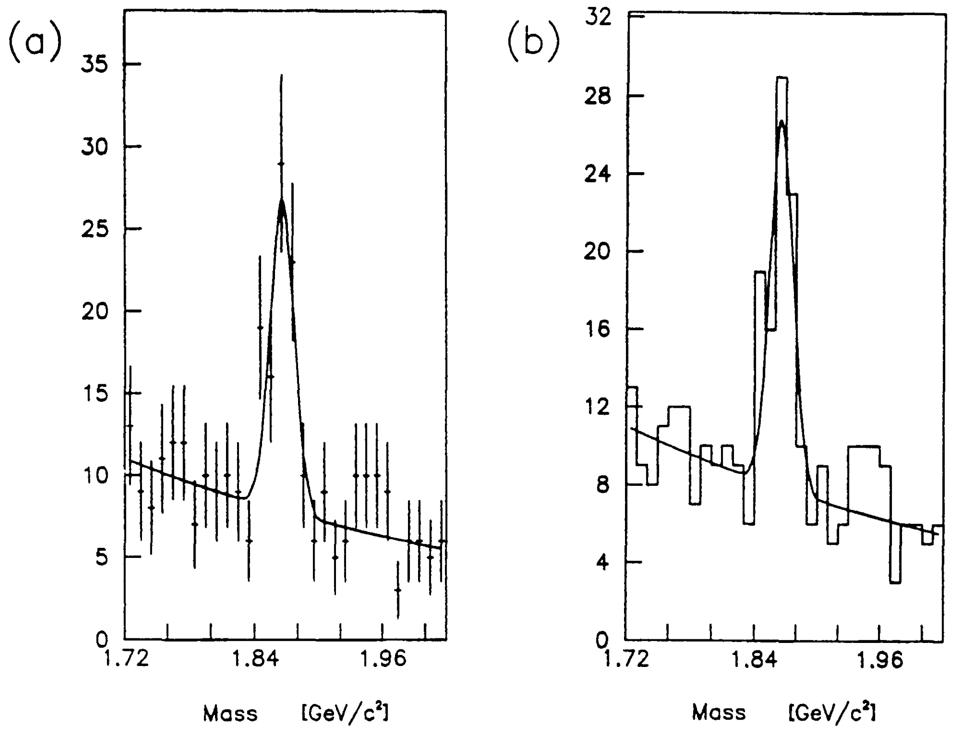

Figure 8.14 *Kπ mass plot, including events that failed the kaon filter*

assignments, and so would have excluded events that contained one of these higher momentum kaons (if they did not contain an unambiguously identified kaon as well). As more processing time was available, it was therefore decided to run the production on those events which had failed the original kaon-selecting filter, so that they could also be passed through the charm analysis. The mass plot obtained with these events (using the same analysis as that which produced Figure 8.11 for the original sample), is shown in Figure 8.13. A charm signal is evident, although at a reduced signal-to-background ratio compared with that of the original events. The total mass plot (the sum of Figures 8.11 and 8.13) is shown in Figure 8.14. The fit gives a signal of 52 ± 7 events, with a signal-to-background ratio of about 1·5.

This charm signal was used to check various analysis strategies. One example was an attempt to reject secondary interactions, and events for which the decay involves extra (charged) particles that have not been included in the combination. See Figure 8.15. Tracks were used that had been dropped from the primary vertex fit—the distance of closest approach of these tracks to the secondary vertex (*d* in the figure) was investigated, for signal events, and for background events taken from the *wings* of the mass plot (i.e.

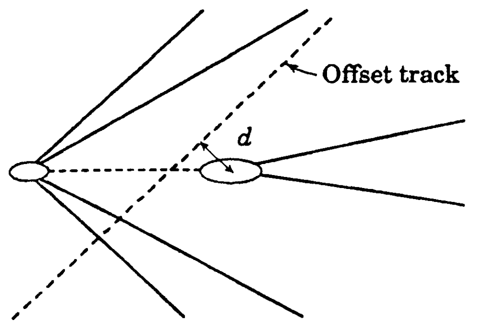

Figure 8.15 Association of tracks with secondary vertex

events for which the mass lies outside the signal region). No significant difference was found between the signal and background distributions, however, so this approach was not pursued.

Another feature investigated was the use of the reconstructed charm track. Various strategies were possible for the use of this track:

(i) Force its inclusion in the primary vertex—i.e. if the vertex algorithm indicates that the charm track should be dropped, then drop the track with the next greatest partial chi-square instead;
(ii) Use it in the same manner as other tracks in the primary vertex search, and reject events in which it has not been accepted;
(iii) Use it in the same manner as other tracks in the primary vertex search, and allow it to be dropped;
(iv) Do not use it in the search for the primary vertex, and then cut on the offset of the charm track from the found vertex.

The first strategy was found to give the best results, and so was adopted for later work.

Signals from the full data-set

The decision was made in 1986 to run the preproduction (TYPHON) on *all* of the events recorded by the experiment, rather than just a subset as had been the case for the 1985 data. With information available from the spectrometer, a more comprehensive analysis of the microstrip data than that used in the Imperial College microstrip filter was now possible. A new microstrip filter was therefore developed by our Orsay collaborators, utilising the preproduction information (as described in Section 6.8). This was run on the data from

(a) $D^0 \to K\pi$, 4σ cut

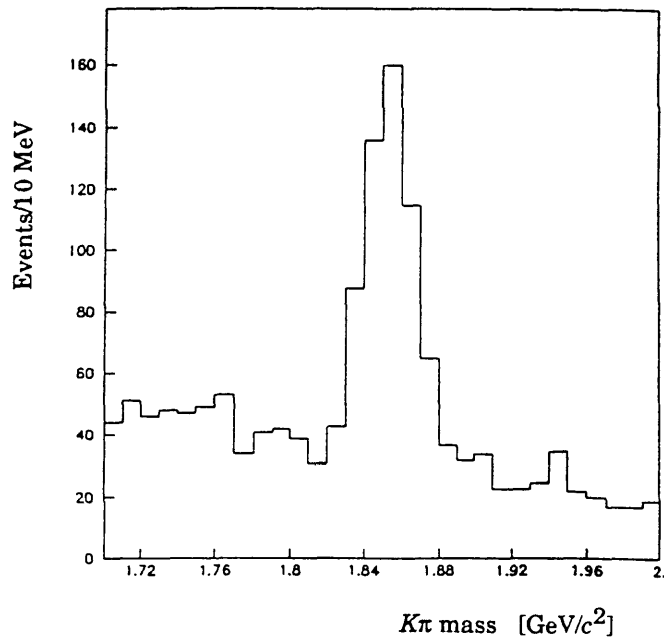

(b) $D^+ \to K\pi\pi$, 4σ cut

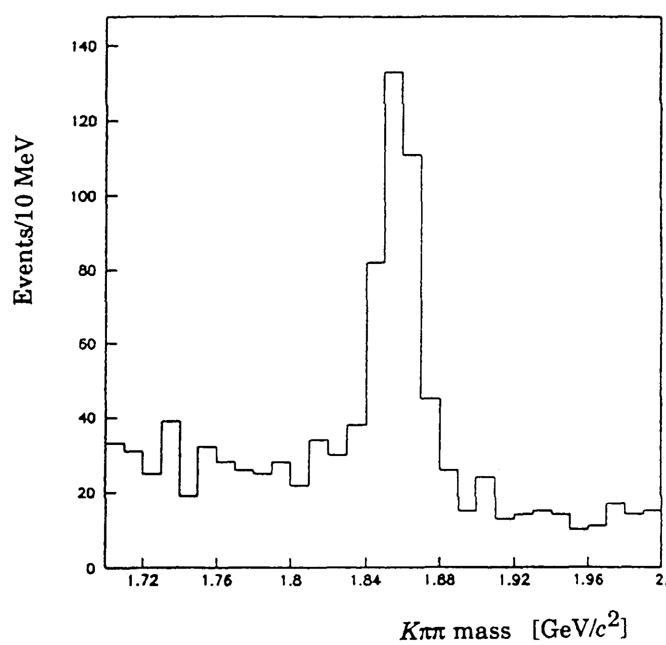

Figure 8.16 *Signals from the full data-set*

1986, and (later) on the 1985 data too. The full data-set has therefore been passed through this filter, and charm signals can be extracted in a similar manner to that described above. Examples of signals obtained [102] are shown in Figure 8.16 (a) for the $D^0 \to K^+\pi^-$ channel, and (b) for the $D^+ \to K^-\pi^+\pi^+$ channel, both at a 4 σ vertex separation cut. The signals seen are ~ 400 $D^0 \to K\pi$ and ~ 300 $D^+ \to K\pi\pi$, with a signal-to-background ratio of ~ 3. Reducing the severity of the vertex separation cuts to give a signal-to-background ratio of ~ 1, leads to signals of ~ 550 $D^0 \to K\pi$ and ~ 400 $D^+ \to K\pi\pi$. The analysis of these signals is presented elsewhere [103]. Due to the large statistics, the errors on lifetimes and other properties are dominated by systematic errors. The emulator work (Section 6.2) will be important in the precise determination of these systematic errors.

One study that has been undertaken is the search for associated production—attempting to reconstruct the second charmed particle in each event. The vertex region of an event for which this has been successful is displayed in Figure 8.17 [104], with the two secondary vertices shown, corresponding to the decays $D^+ \to K^-\pi^+\pi^+$ and $D^- \to K^+\pi^-\pi^-$. Note that the active target information of this event shows evidence for the expected multiplicity step at the decay vertex that lies within the target.

8.4 $D^+, D_s^+ \to \phi\pi^+$

Event selection

The measurement of absolute branching ratios for the D_s-meson is difficult. The branching ratio in the channel $D_s \to \phi\pi$ has been estimated by e^+e^- experiments [16] as:

$$B(D_s \to \phi\pi) = 4 \pm 1\ \% \tag{8.3}$$

This, however, involves some questionable assumptions:

(i) The charm cross-section in high energy e^+e^- annihilations is 4/10 of the total hadronic cross-section (or 4/11 if above the beauty threshold), since the strength of coupling is proportional to the square of the quark charge;

(ii) The fraction of the charm cross-section involved in the production of D_s-mesons is 15 % (as discussed in Section 2.9);

(iii) The cross-section measurements must be extrapolated to include kinematic regions for which the experiments have low acceptance—in particular to low x.

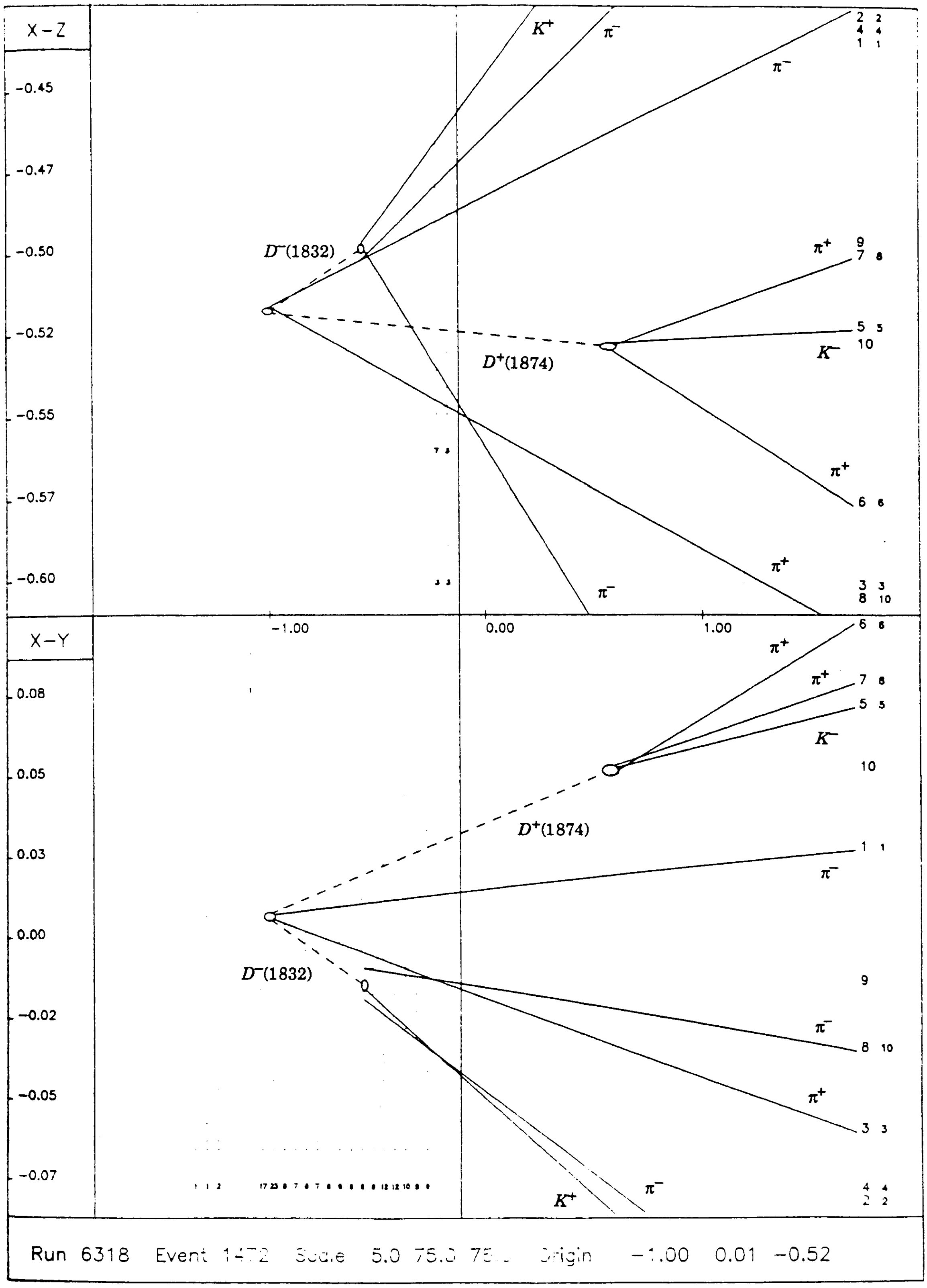

Figure 8.17 An event with both charmed particles reconstructed

Channel	ARGUS	MarkIII	E691
$K^{*0}K^{+}$	$1{\cdot}44 \pm 0{\cdot}37$ *	$0{\cdot}85 \pm 0{\cdot}23$	$0{\cdot}74 \pm 0{\cdot}13$
$K^{0}K^{+}$		$0{\cdot}90 \pm 0{\cdot}25$	
$K^{+}K^{-}\pi^{-}$ ($NR^{\dagger}$)			$0{\cdot}23 \pm 0{\cdot}10$
$\phi\pi^{+}\pi^{+}\pi^{-}$	$1{\cdot}11 \pm 0{\cdot}46$		$0{\cdot}77 \pm 0{\cdot}34$
$\rho^{0}\pi^{+}$	$< 0{\cdot}22$ [90 % CL]		$< 0{\cdot}08$ [90 % CL]
$\pi^{+}\pi^{+}\pi^{-}$ (NR)			$0{\cdot}29 \pm 0{\cdot}09$

* Branching ratios given as the ratio to $B(D_s \to \phi\pi) \sim (4 \pm 1)$ % from $e^{+}e^{-}$

† Non Resonant

Table 8.1 *D_s branching ratios*

Other branching ratios have been measured relative to this, as shown in Table 8.1 [105]. These indicate that the decay to $\phi\pi$ is a suitable channel in which to search for the D_s. This is a spectator decay (Section 2.11), as shown in Figure 8.18 (a). The D^{+}-meson may also decay to $\phi\pi$, as shown in Figure 8.18 (b). Since this involves the coupling of a u- to an $\bar{s}$-quark, it will be Cabibbo suppressed. The ϕ-meson decays to kaons:

$$\phi \to K^{+}K^{-}$$

with a high branching ratio of ~ 50 %.

(a)

(b)

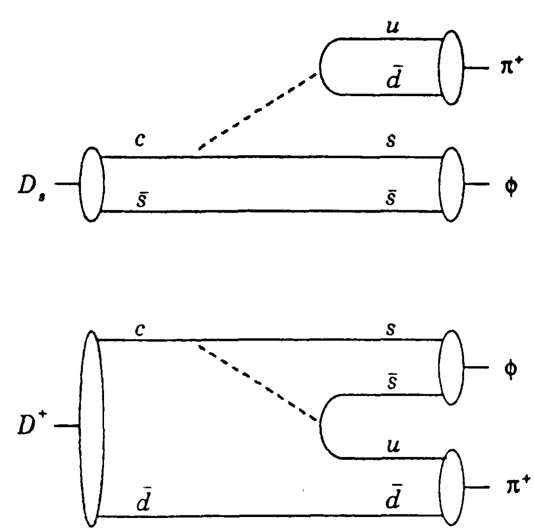

Figure 8.18 *Charm decays in the $\phi\pi$ channel*

The data for the analysis of the $\phi\pi$ channel are taken from the kaon filter. This filter selected events in which one of the tracks found by the preproduction analysis was identified as a kaon, as was noted in Section 6.6. The criteria for identification were that the track passed through the INDRA Cerenkov, with momentum in the range 6–50 GeV/c, and no light was seen in the corresponding Cerenkov mirror. The filter was run on the full data-set (~ 17 million events) and the events that passed it were run through the TRIDENT reconstruction program.

A post-TRIDENT filter was then used, to select events with a pair of oppositely charged kaons. As the momentum measurement from TRIDENT is more precise than that of the preproduction, the momentum range for the kaon identification could be tightened, to 6·5–20 GeV/c. It was also required that the kaon tracks should be matched with the microstrips (i.e. TRIDENT track flag greater than 20, see Section 6.9). This reduced the data-set to ~ 250 thousand events. The effective mass of the K^+K^- pair was calculated and a clear peak was found at the ϕ-meson mass (see Figure 8.19). The fit shown in the figure is the sum of a polynomial for the background, and a Breit-Wigner for the phi peak [93]:

$$N = \frac{\sigma}{\pi\left((m-\mu)^2 + \sigma^2\right)}$$

where m is the mass, and μ and σ are the mean and width of the distribution. The fit gives:

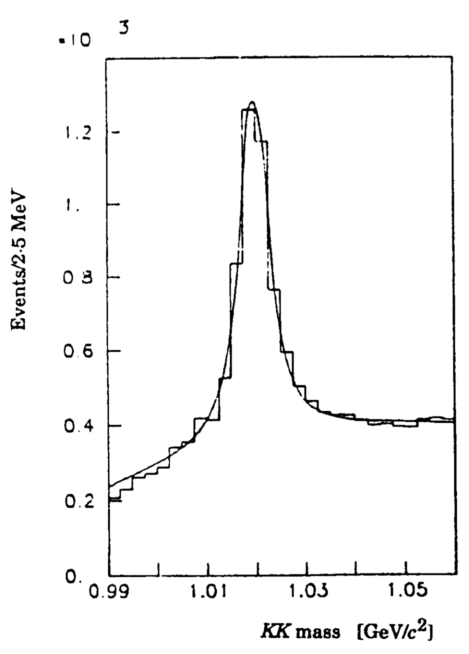

Figure 8.19 K^+K^- mass plot

$$\mu = 1019{\cdot}7 \pm 0{\cdot}1 \text{ MeV}/c^2$$
$$\sigma = 3{\cdot}28 \pm 0{\cdot}13 \text{ MeV}/c^2$$

The mean agrees well with the accepted value of 1019·6 MeV/c^2 [1] for the mass of the phi. A selection of events containing the phi was made at $\pm$ 10 MeV/c^2 of this value, giving ~ 11600 events, with a signal-to-background ratio of about 1·2. These events were written to tape for further analysis.

Charm analysis

The charm analysis of the phi-selected events proceeded as follows. First, the track finding discussed in Chapter 7 is performed. Tracks that have been refitted in the microstrips are required for the secondary vertex. On the basis of the D^0 work, additional tracks in the Z-projection are permitted for the primary vertex calculation.

The K^+K^- pair that was selected as originating from a phi is found again, by calculating the effective mass of all oppositely signed kaon pairs in each event, and selecting those with mass within 10 MeV/c^2 of the ϕ-meson mass. Each pion in the event is then taken in turn with the kaon pair, to form a $KK\pi$ combination. The pion 'identification' involves taking as a candidate pion any particle not identified as a kaon or a proton using the standard INDANL criteria, including tracks outside the INDRA Cerenkov acceptance. The justification for this is that pions are the most copiously produced particles, so that any unidentified particle is most likely to be a pion.

The mass of the combination is next calculated, imposing the ϕ-meson mass on the K^+K^- pair. The raw mass plot achieved in this manner is shown in Figure 8.20—no signal is evident at this stage. The vertex analysis is then performed. The Intersection vertex scheme was found to give inferior results to the Constraint scheme, due (it is thought) to the fact that the data for this channel has not passed through the microstrip filter, so that the benefits of the active target requirement of the Intersection vertex are not present. The Constraint vertex was therefore used.

For the secondary vertex, *Prob*(χ^2) is required to exceed 0·001. If this is satisfied, then the charm meson trajectory is reconstructed from the parameters of the decay tracks, and is used in the primary vertex calculation, along with all remaining tracks in the event. If *Prob*(χ^2) of the candidate primary vertex is less than 0·01, then the track with the largest contribution to the chi-square is rejected, and the vertex recalculated (as discussed in

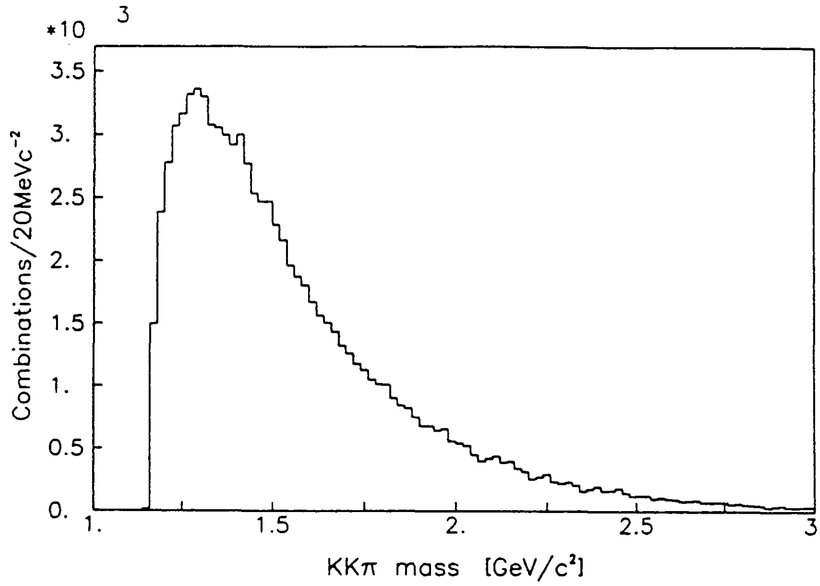

Figure 8.20 Raw KKπ mass plot

Section 8.1). The mass plot achieved when both vertices have been found is shown in Figure 8.21, and still shows no signal.

A cut is now made on the separation of the primary and secondary vertices, and the resulting mass plots are shown in Figure 8.22, for various values of the Δx cut (marked in mm). The mass calculation here uses the constrained parameters of the tracks. Signals are now evident at the mass of the D^+ (~ 1·86 GeV/c^2), and at the mass of the D_s

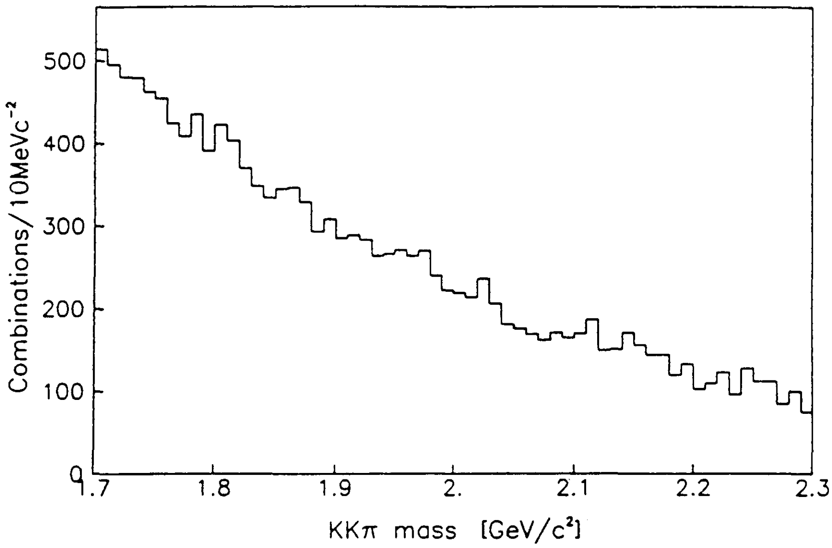

Figure 8.21 KKπ mass plot, vertices found

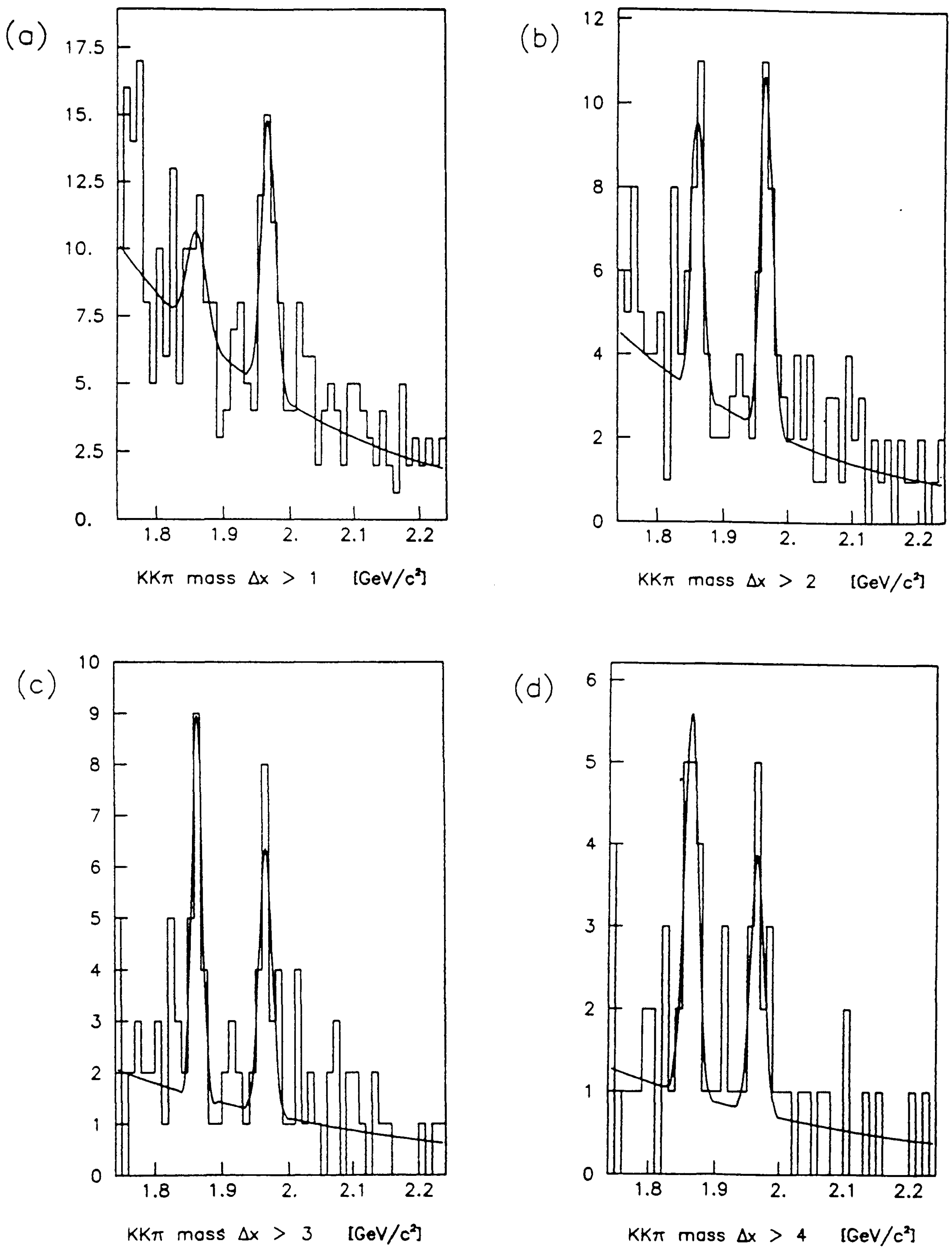

Figure 8.22 *$KK\pi$ mass plot, cutting on vertex separation*

($\sim 1{\cdot}97$ GeV/c^2). Note that the significance of the signals increases as the vertex separation cut is increased. The mass plot fits are (as for the D^0) the sum of an exponential fit to the background and a Gaussian fit to each of the signals.

Further cuts

To increase the signal-to-background ratio, further cuts are imposed.

(i) A significant background to the hadronic interaction of the photon beam is e^+e^- pairs, produced by photon electromagnetic conversions, as explained in Section 3.5. The pairs are produced collinear with the beam (i.e. with dip and azimuthal angles $\lambda = \phi = 0$), and with a small opening angle. The opening angle is then increased by their deflection in the magnetic field, and since the field is vertical they retain a small dip angle, λ. As these pairs can mimic a secondary vertex, a cut was introduced to exclude them, requiring that:

$$|\lambda| > 2 \text{ mrad}$$

for tracks from the secondary vertex.

(ii) Tracks with very low momentum have large associated errors due to multiple scattering (Section 7.3). For tracks with very large momentum, on the other hand, the momentum measurement tends to be inaccurate, as the track does not deviate much under the influence of the magnetic field. Limits were therefore placed on the momentum of the pion from the secondary vertex:

$$1{\cdot}0 < p_\pi < 50 \text{ GeV}/c$$

(The kaons from the secondary vertex necessarily satisfy these limits due to their identification criteria.)

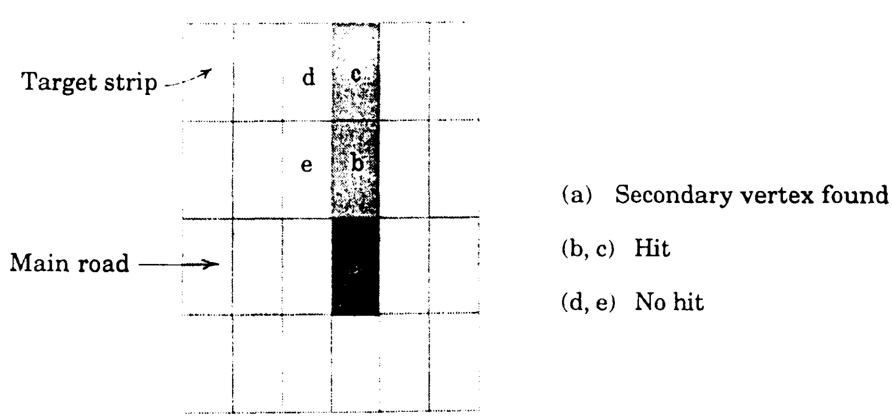

Figure 8.23 *Secondary interaction recognition in the active target*

(iii) At least one of the secondary tracks was required to have a transverse offset from the primary vertex greater than 30 μm.

(iv) The partial chi-square of the reconstructed charm track in the calculation of the primary vertex was required to satisfy:

$$\chi_c^2 < 8{\cdot}0$$

(v) The active target information was checked. The vertex information from the target may be used to recognise events in which the secondary vertex is in reality a secondary interaction. The algorithm used [93] was one which rejects secondary vertices that are surrounded by target activity of the form shown in Figure 8.23. An example of an event that was rejected by this algorithm is shown in Figure 8.24. The active target information was also used to check whether the primary vertex position was sensible. If it lay in a strip of the target with less than 2·0 I_{min} (see for example Figure 8.25) then the most upstream track used in the calculation of the vertex was rejected, and the position recalculated (as shown in Figure 8.26).

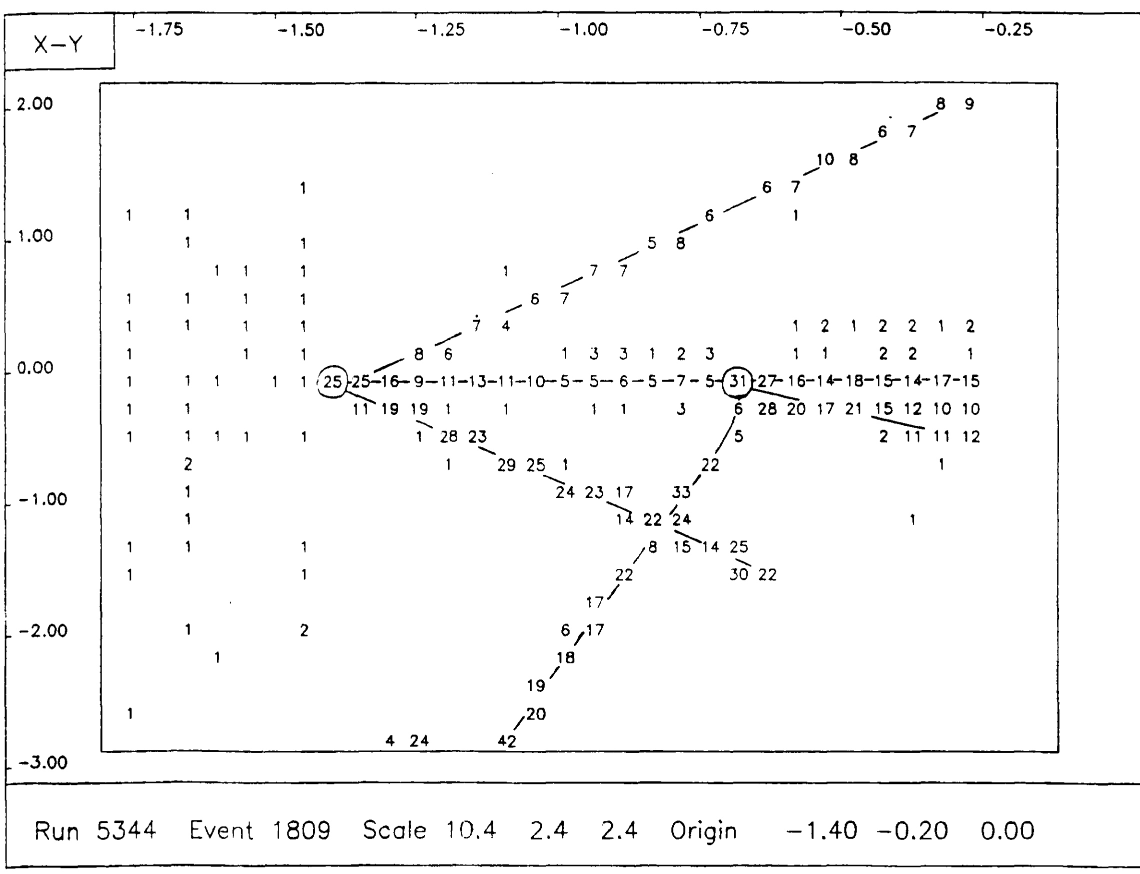

***Figure 8.24** Event rejected by secondary interaction recognising algorithm*

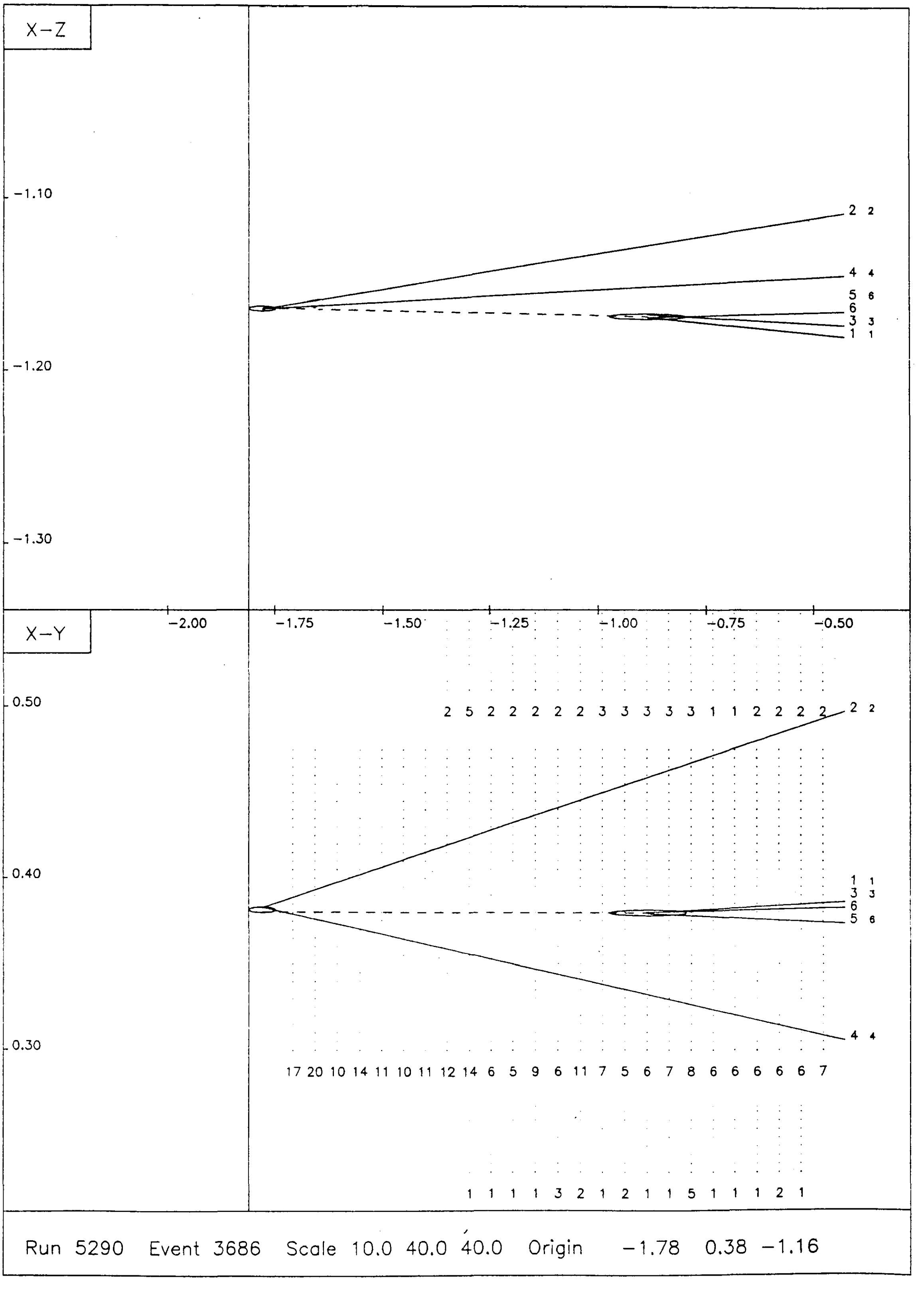

***Figure 8.25** Event with primary vertex in an empty target strip*

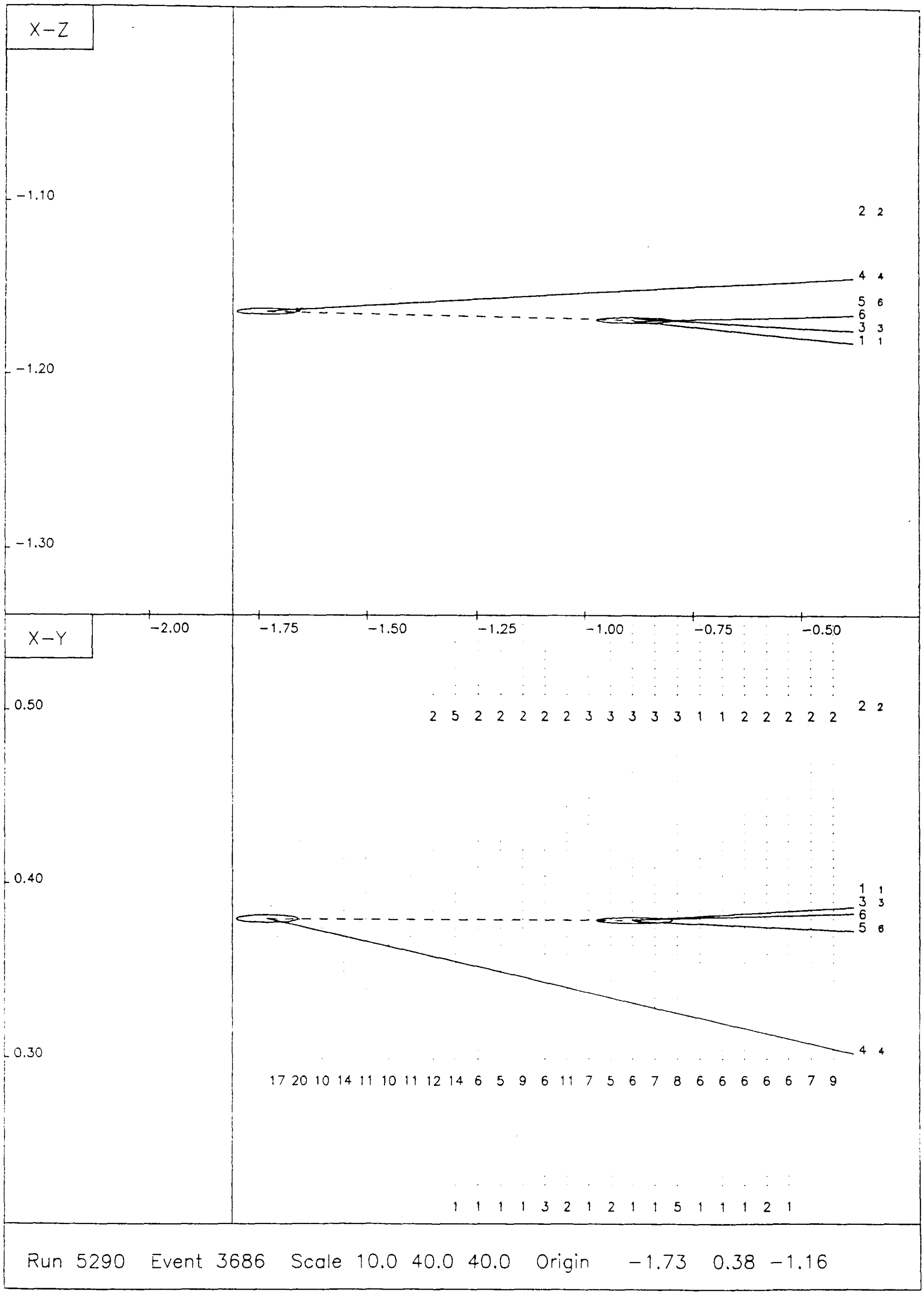

Figure 8.26 *Event after most upstream track rejected*

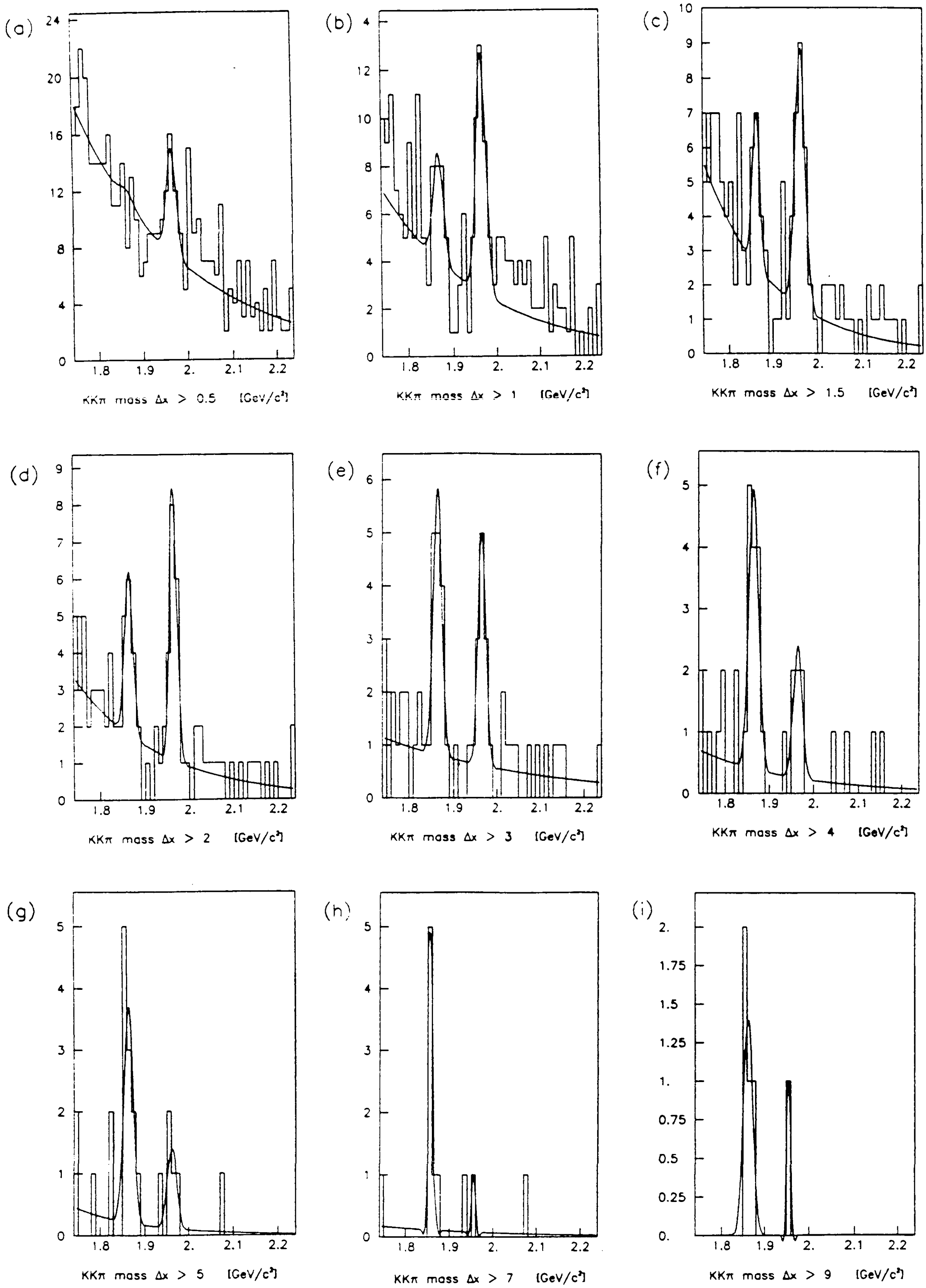

Figure 8.27 *KKπ mass plots after cuts, evolution with Δx*

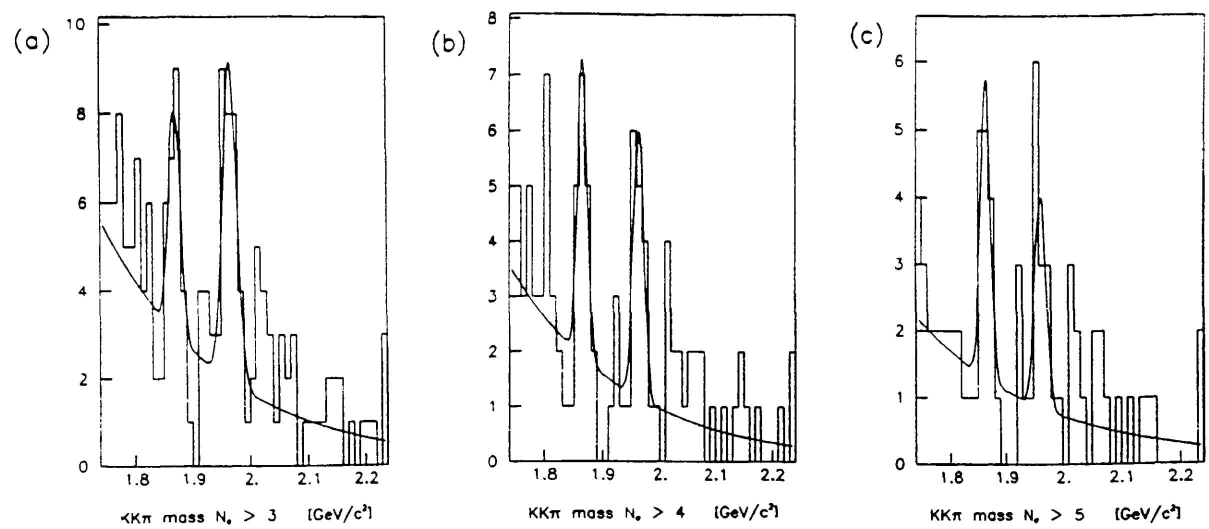

Figure 8.28 *KKπ mass plots after cuts, evolution with N_σ*

When these cuts are imposed the resulting mass plots are shown in Figure 8.27, for various cuts on the vertex separation distance, and in Figure 8.28 for cuts on N_σ. As can be seen, the signals found using a cut on the vertex separation *distance* tend to be slightly

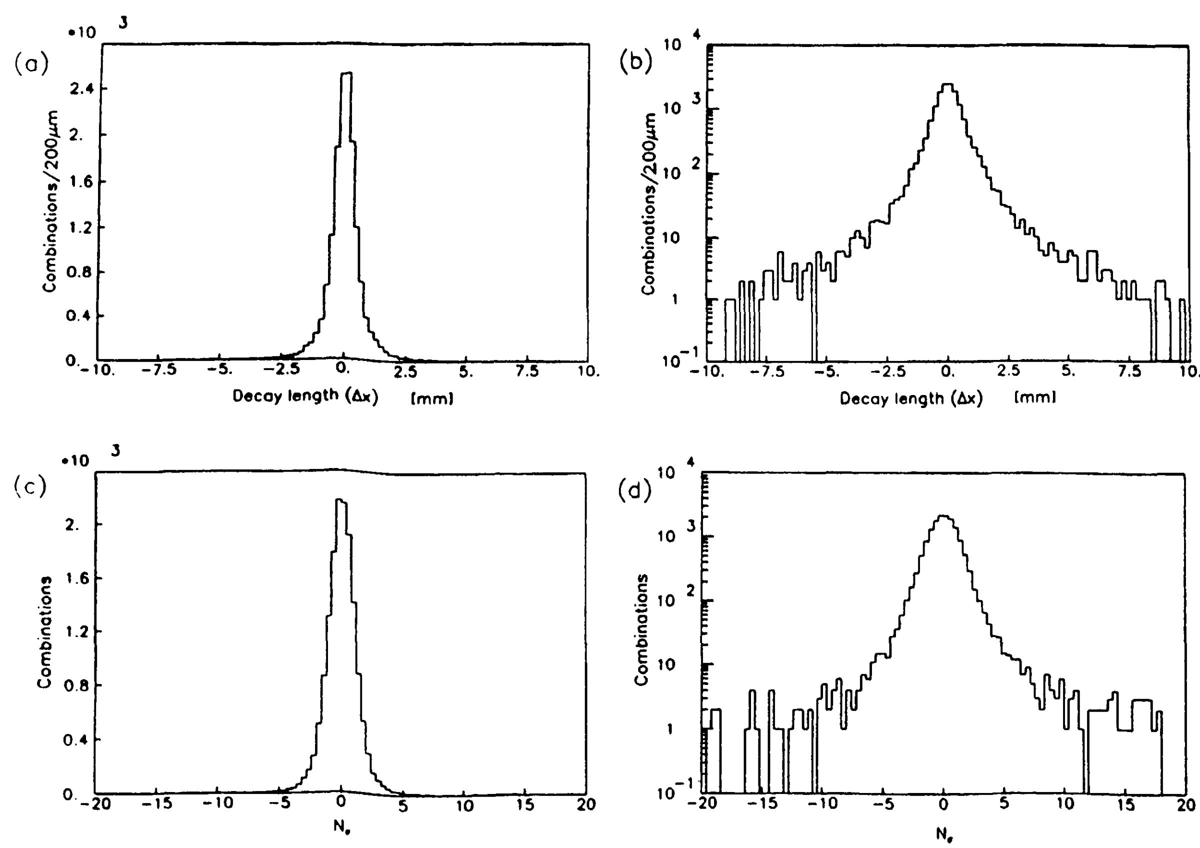

Figure 8.29 *Vertex separation variable distributions*

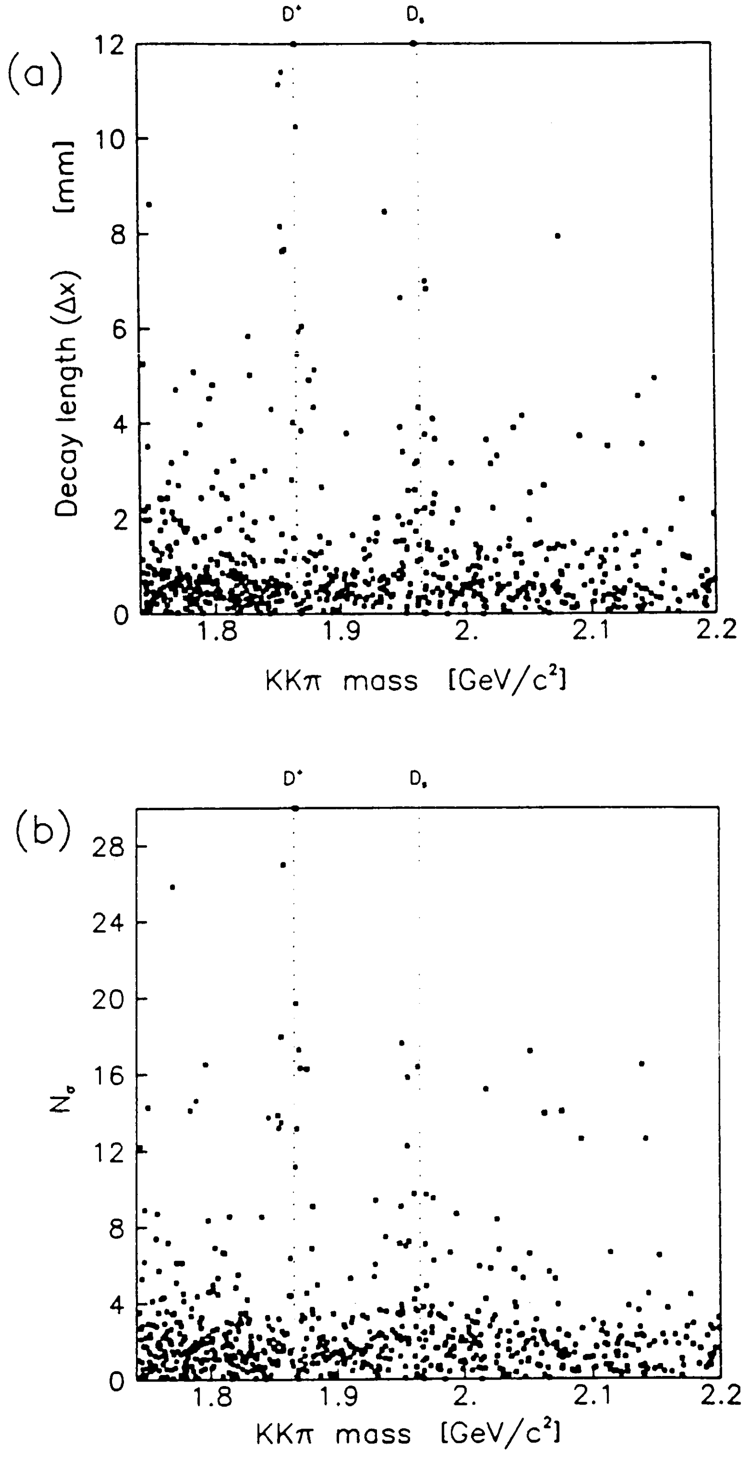

Figure 8.30 *Variation of vertex separation variables with mass*

cleaner than those found using a cut on N_σ. This is rather surprising, as the N_σ cut is expected to involve the optimal use of available information. As a result, the signals used for the physics analysis were often defined with a cut on Δx rather than N_σ, although the differences measured were not statistically significant. The distributions of the separation variables are given in Figure 8.29, for both logarithmic and linear scales; they show a roughly Gaussian distribution of background events about zero separation, and charm events should be seen as an enhancement of positive values. The behaviour of the separation variables with mass is shown in Figure 8.30.

The effect of using the constrained track parameters on the mass calculation was tested by running the same analysis as above, but without using the constrained parameters in the mass calculation. The resulting mass plots at $\Delta x > 2$ mm are compared in Figure 8.31. The width measured for the signal in the unconstrained case, of 12 ± 2 MeV/c^2, is slightly greater than the value measured in the constrained case, 10 ± 2 MeV/c^2, indicating the the track constraint does improve the mass resolution.

The events that passed a 1 mm cut on the vertex separation were individually scanned. From the target information, it was found that there remained some events for

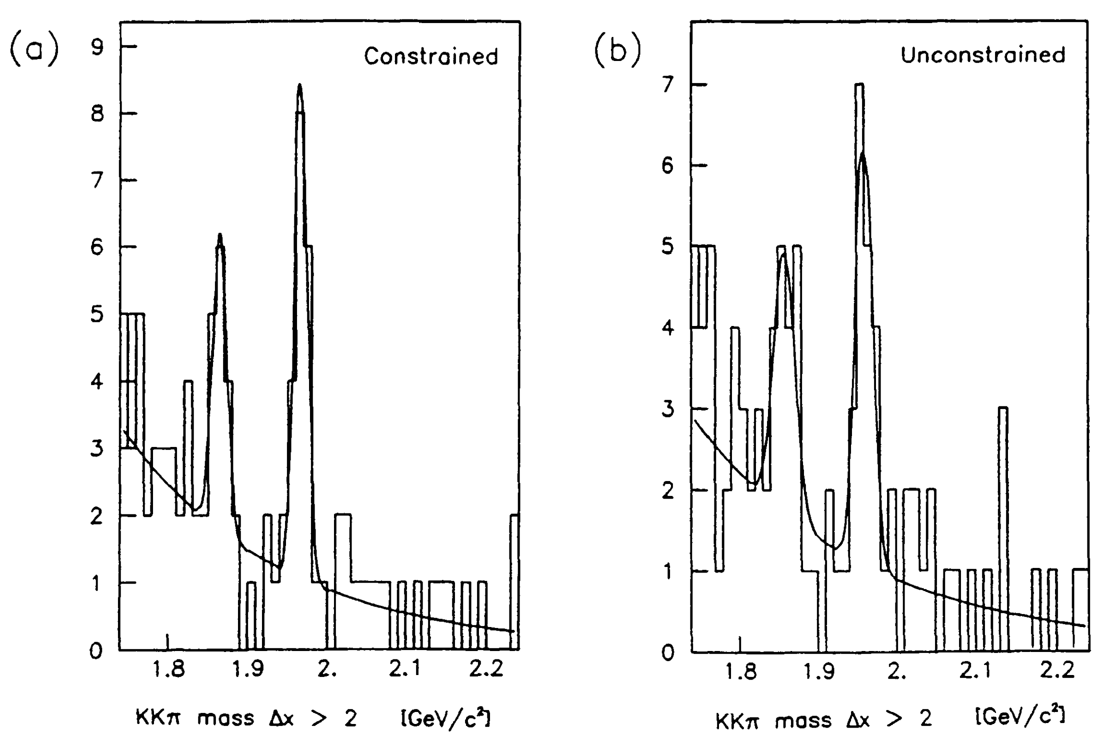

Figure 8.31 *Effect of track constraint on mass calculation*

(a)

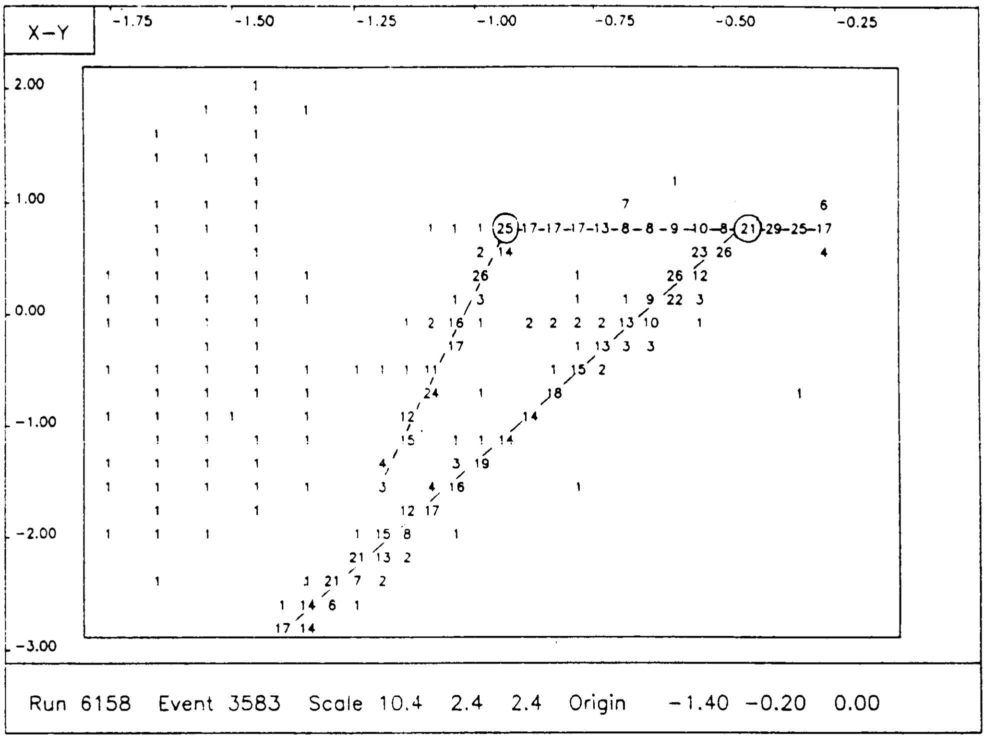

(b)

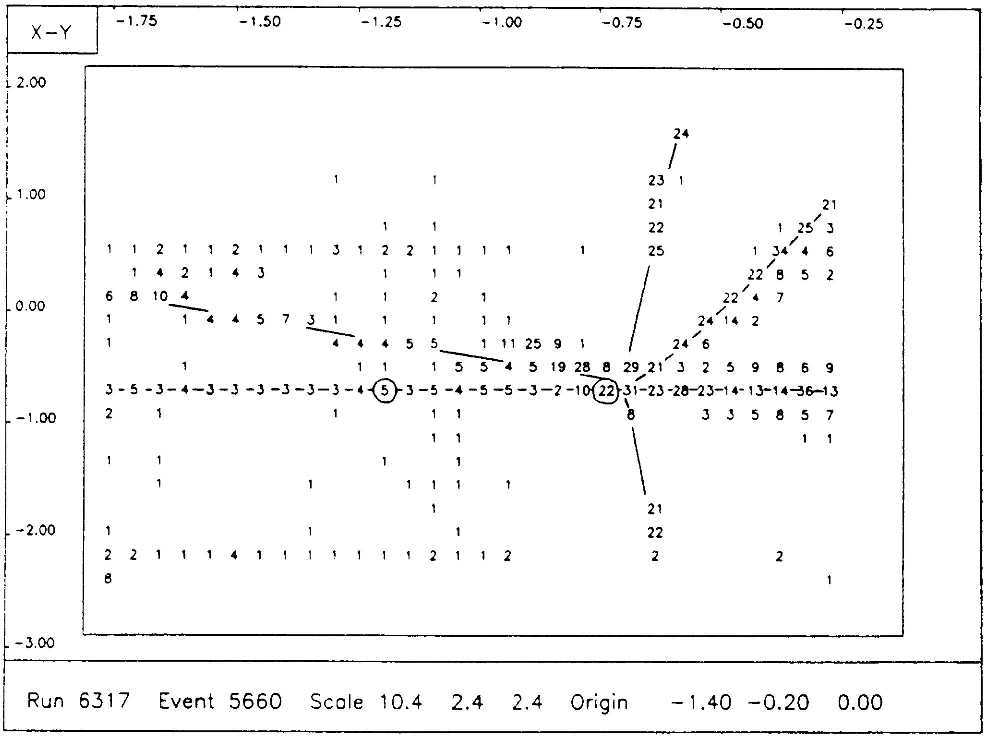

Figure 8.32 *Events rejected by scanning*

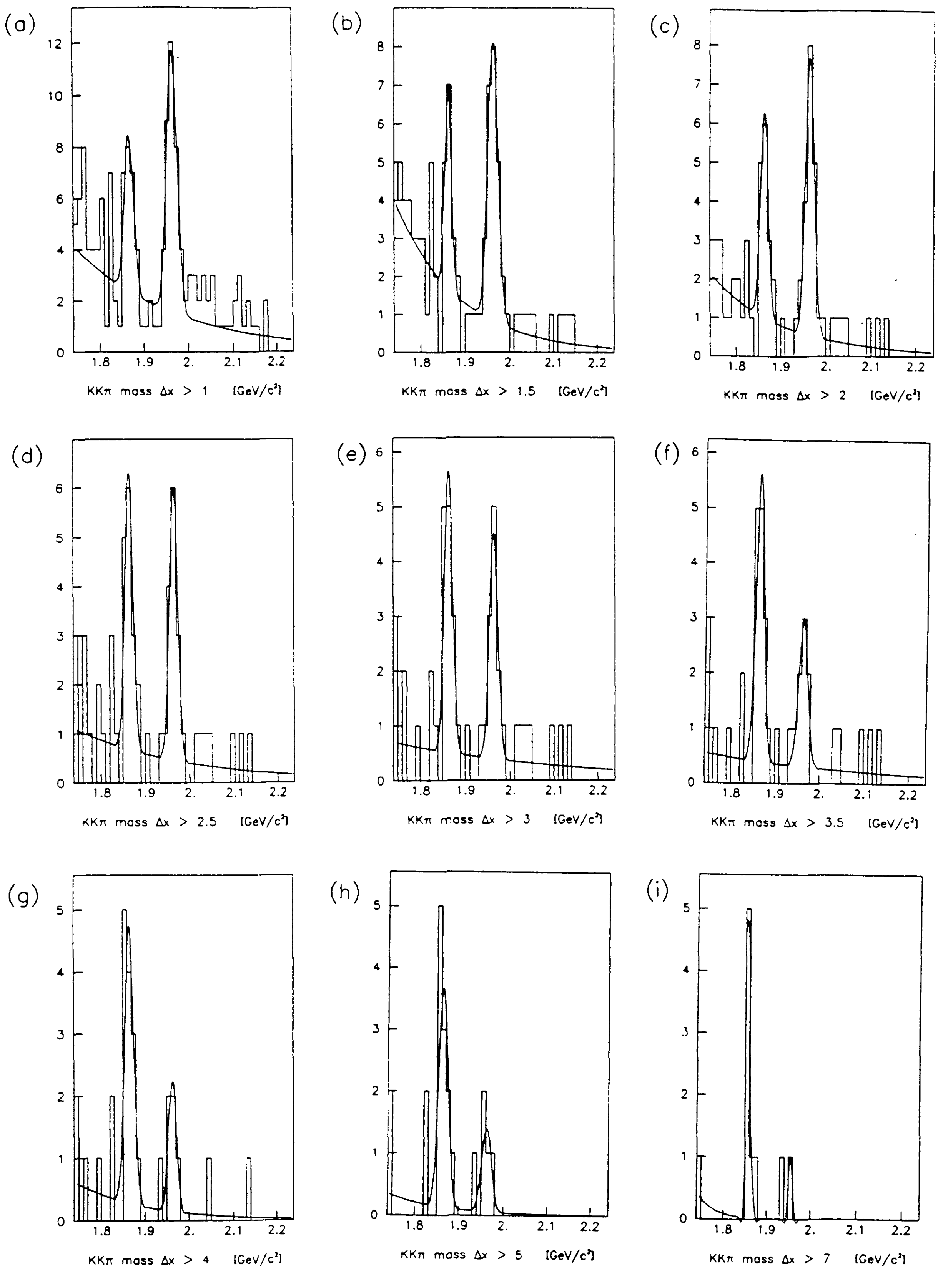

Figure 8.33 *KKπ mass plots after scanning, evolution with Δx*

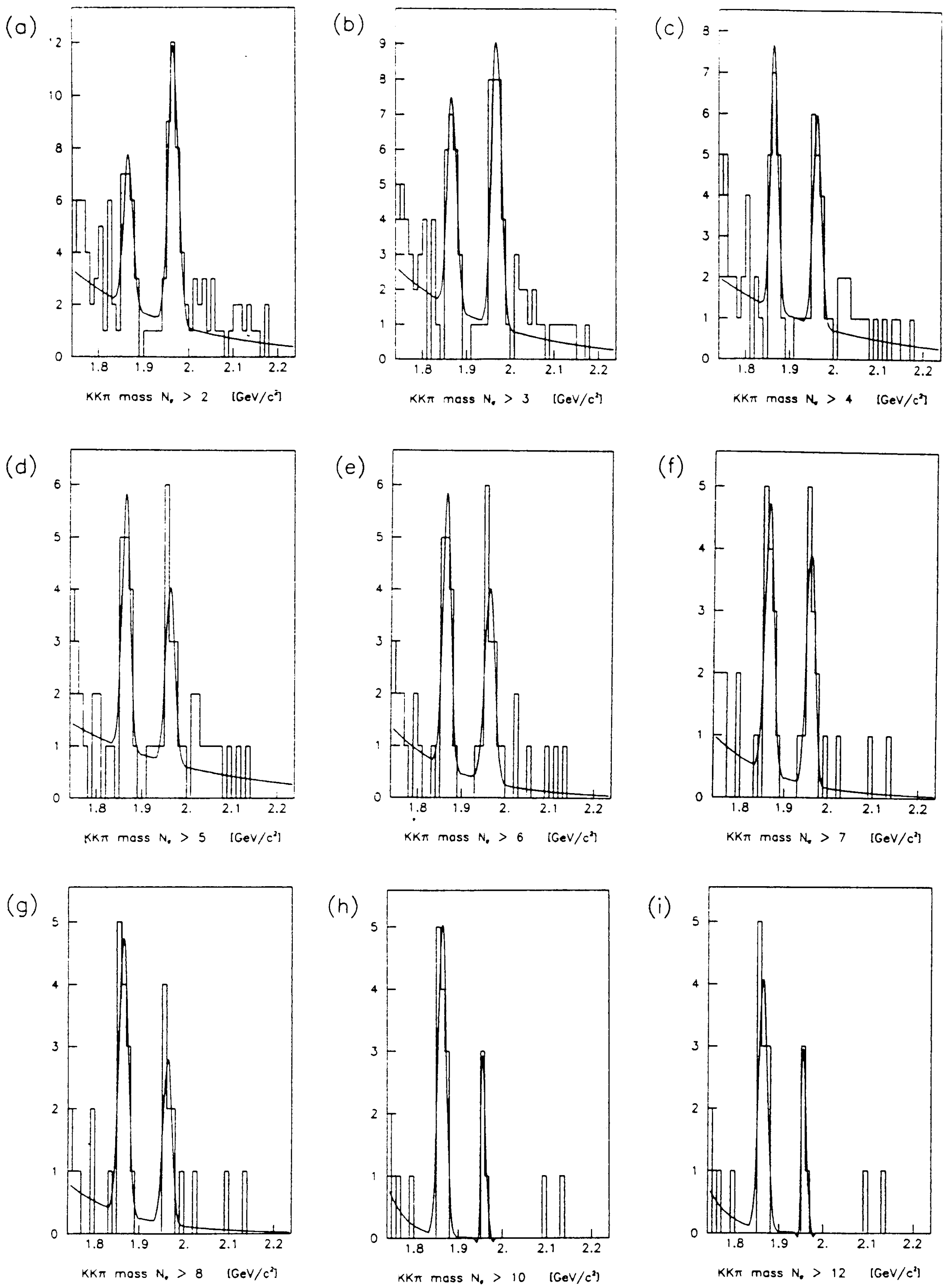

***Figure 8.34** KKπ mass plots after scanning, evolution with N_σ*

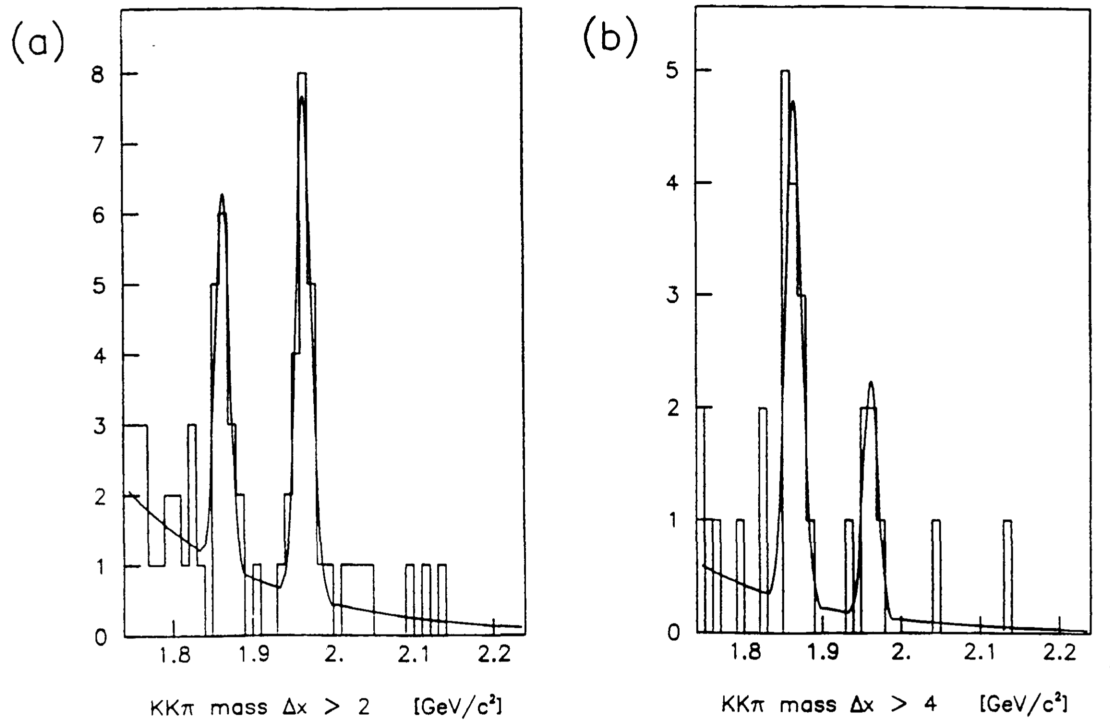

Figure 8.35 *Demonstration that $\tau(D^+) > \tau(D_s)$*

which the candidate secondary vertex was in fact a secondary interaction (for example see Figure 8.32 (a)), and others where the primary vertex was misplaced (see Figure 8.32 (b)). An algorithm capable of rejecting events of these sorts would require extensive pattern recognition using the target information. It has been found that due to the great complexity of the target activity in some events, an algorithm that is sufficiently specific for the rejection of background events will also reject an unacceptable fraction of the signal. Visual scanning was therefore used to reject events of the sorts shown in Figure 8.32.

The vertex region of a typical signal event that was accepted by this analysis was displayed in Figure 6.2. The final mass plots are shown in Figures 8.33 and 8.34, again for a selection of cuts on the vertex separation. It is clear from these plots that as the cut on the vertex separation is increased, the D^+ signal persists more strongly than that of the D_s. See for example the mass plots redisplayed in Figure 8.35, at (a) $\Delta x > 2$ mm, and (b) $\Delta x > 4$ mm. This is a result of the longer lifetime of the D^+, as will be seen in the next chapter.

Chapter 9

PHYSICS RESULTS

In this chapter, the physics results that have been obtained using the charm signals from the $\phi\pi$ channel analysis are presented.

9.1 Masses and widths

Mass plot fitting

The procedure used to fit the histograms of effective mass for the charm channels is as follows. A 'window' in effective mass is opened around each signal peak, of width $\pm$ 25 MeV/c^2. The histogram entries within these windows are ignored, and the 'wings' that remain are used for the background fit. The procedure used is illustrated in Figure 9.1 for the $\phi\pi$ channel mass plot shown in (a). The error on the contents of each histogram bin (b) is taken as the square root of the contents (assuming Poisson statistics). If the population of the bins is low, however, the contents of each bin becomes a less good estimate of the distribution mean—for bins that are empty, an error of $\pm$ 1 is used. An exponential fit is then made to the background (c).

Within each signal window, the calculated background at each bin is subtracted from the bin contents (d), and a Gaussian fit is made to the signal (e, f):

$$N = \left(\frac{1}{\sqrt{2\pi}\,\sigma}\right) e^{-\left[\frac{(m-\mu)^2}{2\sigma^2}\right]}$$

where μ is the mean and σ is the width of the distribution. The natural widths of the

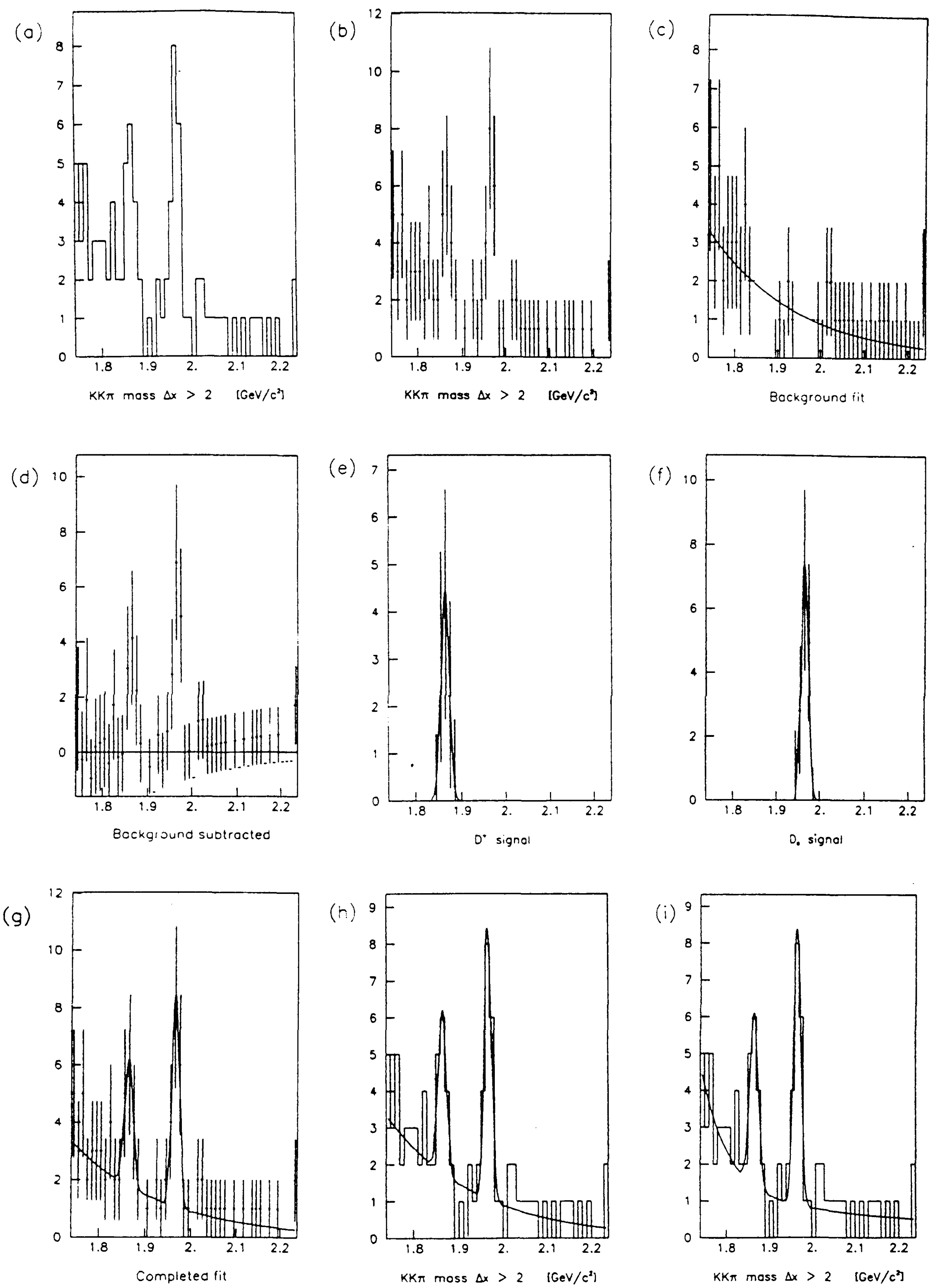

***Figure 9.1** Mass plot fitting procedure*

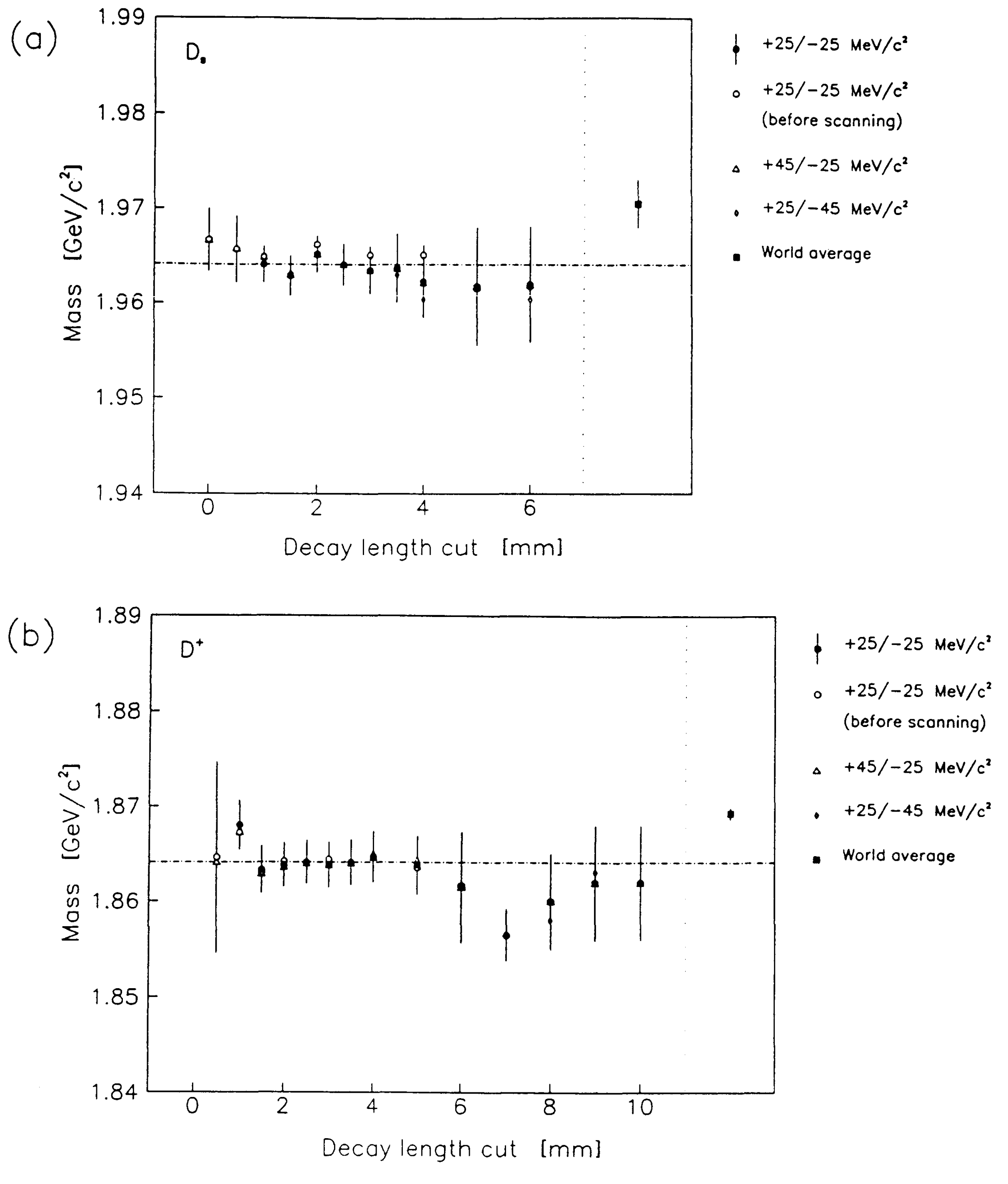

Figure 9.2 *Charm signal mass measurements*

signals are much less than the mass resolution of the apparatus, hence the use of a Gaussian rather than a Breit-Wigner fit. The separate contributions are summed to give the final fit (g, h).

For the fit to the background, the form:

$$N = e^{(am + b)}$$

was initially used (as in (c) above), where a and b are free parameters. It was noticed that for the $\phi\pi$ channel, this parameterisation appeared to overestimate the background in the centre of the plot, under the peaks. A second exponential term was introduced to improve the fit:

$$N = e^{(am + b)} + e^{(a'm + b')}$$

The influence of this extra term may be seen in (i), where it has been used in the background fit.

Measurement of masses and widths

The fitting procedure described above was used to measure the masses and widths of the charm signals. The values of the masses measured for the D^+ and the D_s are shown in Figure 9.2, where the evolution of the measurement with the cut on the vertex separation is shown.

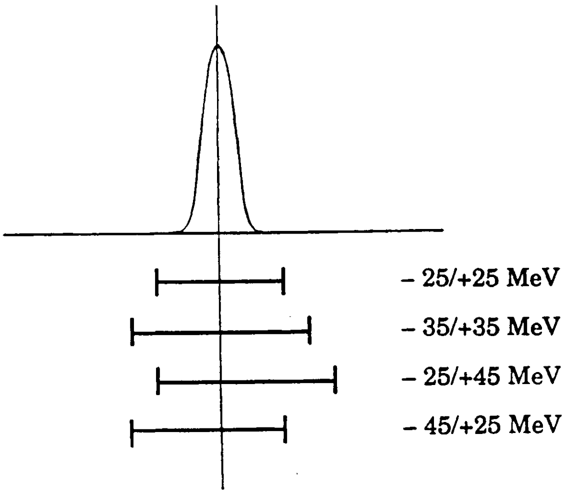

Figure 9.3 *Use of different windows in mass for the signal definition*

There is a danger that the use of a window around the signal for its fit might bias the values measured. To test whether this is the case, windows of different sizes and centred on different masses were used, as illustrated in Figure 9.3, and the results compared. Some of the values measured are plotted in Figure 9.2—no significant changes were found, giving confidence in the procedure. The evolution of the measured widths with the vertex separation cut is shown in Figure 9.4. These plots show the general features of such measurements: at low cut, the results may be systematically shifted due to the

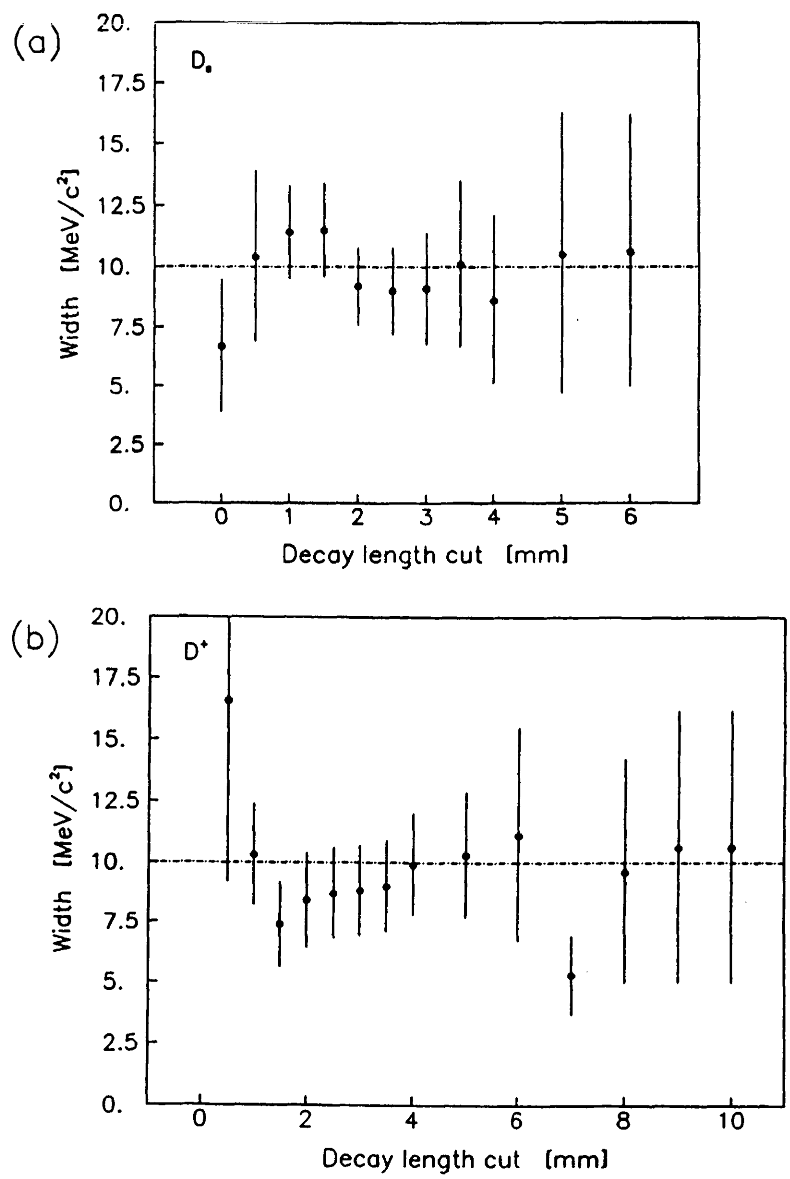

Figure 9.4 *Charm signal width measurement*

considerable background, whilst at large cuts the signal remaining is small, and the statistical errors are therefore large. The most precise measurements are found in the region of most significant signal, at about 1–2 mm cut on the vertex separation.

Taking the values with the lowest errors, it can be seen that for the D^+, the best measurement is at $\Delta x > 2{\cdot}5$ mm. The fit gives a mass of $1864{\cdot}1 \pm 2{\cdot}3$ MeV/c^2 and a width of $8{\cdot}7 \pm 1{\cdot}9$ MeV/c^2. There are 12 ± 3 entries in the signal peak, with a signal-to-background ratio of 3·7. For the D_s, the best measurement is at $\Delta x > 1$ mm; the fit gives a mass of $1964{\cdot}1 \pm 1{\cdot}9$ MeV/c^2 and a width of $11{\cdot}4 \pm 2{\cdot}0$ MeV/c^2. There are 31 ± 5 entries in the signal peak, with a signal-to-background ratio of 4·6.

The mass of the D^+-meson is relatively well known. The current world average for its value [1] is $1869{\cdot}3 \pm 0{\cdot}6$ MeV/c^2. This differs significantly from the value measured above, by 5·2 MeV/c^2. One potential source of error in the measurement of the mass is the use of a slightly incorrect value for the magnetic field of the spectrometer, as the mass is calculated using the particle momenta, which are measured using the magnetic field. An error δB in the field measurement will cause an error δm in the mass, given approximately by:

$$\frac{\delta m}{m} \sim \frac{\delta B}{B}$$

The magnetic field was measured using a Hall probe, and the error was estimated as 0·1 %, checked by a later remeasurement of the field. Another effect leading to uncertainty in the field was the accuracy of positioning the vertex detector within the AEG magnet, of about ± 1 mm; the change in magnetic bending power over this distance is about 0·1%. The mass shift found (~ 0·2 %) is therefore compatible with the known sources of error.

The mass shift that has been determined with the D^+ can now be used to correct the mass scale, and obtain a corrected measurement for the mass of the D_s. To calculate the correction, it must be noted that the mass of the charmed particle does not all appear as momentum of the decay products, but also in their mass. The mass of a particle M is given (in terms of the kinematics of its decay products) by:

$$M^2 = m_1{}^2 + m_2{}^2 + 2\,(E_1\,E_2 - p_1\,p_2 \cos\theta)$$

where θ is the angle between the decay products. At the energies we are concerned with, the last term is approximately proportional to the momentum scale, i.e:

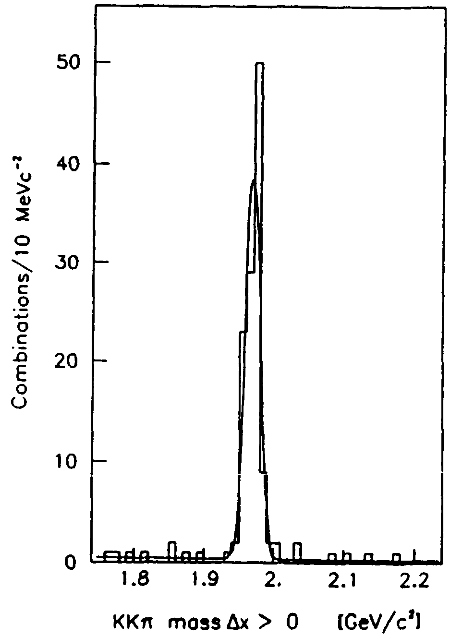

Figure 9.5 *KKπ mass plot, Monte Carlo*

$$m_D{}^2 = m_\phi{}^2 + m_\pi{}^2 + f(p)$$

The mass correction is then determined by calculating the fractional change in $f(p)$ required to give the correct D^+ mass. The fractional correction is applied to the D_s mass measurement, giving:

$$m(D_s) = 1969{\cdot}8 \pm 1{\cdot}9 \pm 2{\cdot}4 \text{ MeV}/c^2$$

The statistical error comes from the fit, and the systematic error is a combination of the error on the world average value for the mass of the D^+, and the statistical error on its measurement here. The value found compares well with the world average [1], $1970{\cdot}5 \pm 2{\cdot}5$ MeV/c^2, and a more recent result [106], $1968{\cdot}3 \pm 0{\cdot}7 \pm 0{\cdot}7$ MeV/c^2.

As a check, the analysis was run on Monte Carlo events generated to give $D_s \rightarrow \phi\pi$. See Figure 9.5. The reconstructed mass of $1969{\cdot}7 \pm 0{\cdot}9$ MeV/c^2 was consistent with the generated mass, $1970{\cdot}5$ MeV/c^2. The reconstructed width was $10{\cdot}0 \pm 0{\cdot}6$ MeV/c^2, compatible with the values measured for the data. Note that (as pointed out above) this width is purely instrumental.

9.2 Lifetimes

Lifetime resolution

The ability of the detector to measure proper time is determined by the spatial precision along the beam direction, σ_x:

$$\sigma_t \sim \frac{\sigma_x}{\gamma c}$$

For a typical charmed particle with momentum ~ 40 GeV/c, $\gamma \sim 20$; $\sigma_x \sim 300\ \mu\text{m}$, so:

$$\sigma_t \sim 0{\cdot}05 \text{ ps}$$

To estimate the lifetime resolution of the experiment, we may use the property of the exponential lifetime distribution, that a single measurement from the distribution gives an estimate of the mean lifetime τ with error τ. Thus:

$$\sigma_\tau \sim \frac{\sqrt{\tau^2 + \sigma_t^2}}{\sqrt{N}}$$

where N is the total number of signal events (assumed background free). Since for the lifetimes we are measuring (~ 0·5 ps) $\tau \gg \sigma_t$, we have:

$$\frac{\sigma_\tau}{\tau} \sim \frac{1}{\sqrt{N}}$$

and for a signal of 20 events we may expect a statistical error of about 20 % on the lifetime measurement.

Lifetime measurement

For a collection of particles with mean lifetime τ, the number of decays per unit time is given by:

$$\frac{\mathrm{d}N}{\mathrm{d}t} = -\frac{N(t)}{\tau}$$

where $N(t)$ is the number of particles remaining at time t. Hence if there are initially N_0 particles:

$$N(t) = N_0\, \mathrm{e}^{-t/\tau} \tag{9.1}$$

The associated probability density function is therefore given by:

$$f(t) = \frac{1}{\tau} e^{-t/\tau}$$

where the factor $(1/\tau)$ has been introduced to ensure that the function is normalised:

$$\int_0^\infty f(t)\, dt = 1$$

When the measurement of the particle proper lifetimes t by the experimental apparatus is considered, this exponential distribution must be convoluted with a Gaussian, representing the error on the measurement of t:

$$f(t) = \int_0^\infty \frac{1}{\tau} e^{-t'/\tau} \frac{1}{\sqrt{2\pi}\,\sigma} e^{-\left[\frac{(t-t')^2}{2\sigma^2}\right]} dt'$$

where σ is the error on the measurement of t. Hence:

$$f(t) = \frac{1}{2\tau} e^{\left(\frac{\sigma^2}{2\tau^2} - \frac{t}{\tau}\right)} \left[1 - \mathrm{erf}\left(\frac{\sigma}{\sqrt{2}\,\tau} - \frac{t}{\sqrt{2}\,\sigma}\right)\right] \tag{9.2}$$

where the 'error function' is given by:

$$\mathrm{erf}(x) = \frac{2}{\sqrt{\pi}} \int_0^x e^{-u^2}\, du$$

If there is background under the signal, then the different lifetime behaviour of the background events must be allowed for. A corrected probability density function, $F(t)$, is introduced:

$$F(t) = \varepsilon\, f_B(t) + (1 - \varepsilon)\, f_S(t)$$

where ε is the background fraction, and f_B and f_S are the probability density functions for the background and signal events respectively.

Finally, an acceptance correction $A(t)$ must be introduced, to allow for the acceptance of the apparatus, the trigger, and the analysis chain. A *maximum likelihood* method [98] is then used to determine the best estimate of the lifetime for a collection of N events. The *likelihood function* L is defined as the joint probability density for the N measurements t_i:

$$L = \prod_{i=1}^{N} A(t_i)\, F(t_i)$$

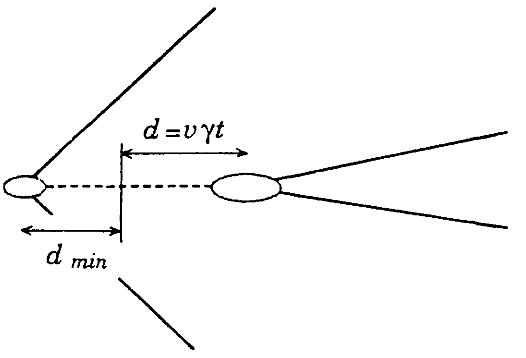

Figure 9.6 *Variables for lifetime measurement*

and the estimate of τ is made by maximising L. This is equivalent to minimising the negative log-likelihood function:

$$-\log L = -\sum_{i=1}^{N} \log\left(A(t_i)\,F(t_i)\right)$$

The procedure used

For each channel that is studied, a cut on the separation of production and decay vertices is chosen, to give the most significant signal possible. The cut may be on the vertex separation distance Δx, or N_σ, as discussed in Section 8.1. In each case, the cut corresponds to a minimum flight distance for each event, d_{min} (see Figure 9.6). The distance d from this cut to the decay vertex is determined, and the corresponding proper time t calculated:

$$t = \frac{d - d_{min}}{\gamma\beta c}$$

This time is then used in the calculation of the likelihood function, utilising the property of the exponential distribution that the mean of the distribution is unaffected by the lower limit of its argument. The error σ_i on each measurement t_i (for use in Equation 9.2) is determined by propagating the errors from the coordinates of the primary and secondary vertices.

The signal is defined using the relevant mass plot. For the $\phi\pi$ channel, we take:

$$D^+: 1840 < m < 1890 \text{ MeV}/c^2 \qquad (9.3)$$
$$D_s: 1940 < m < 1990 \text{ MeV}/c^2$$

The low statistics in this channel make a global fit for all the parameters of the likelihood function impracticable. Instead, the lifetime distribution of the background is assumed to have the same form as that of the signal, but with an effective lifetime τ_B which is determined from the wings of the mass plot. For the $\phi\pi$ analysis, both the 'low wing' and the 'high wing' were used, defined as:

$$\textit{Low wing}: m < 1820 \text{ MeV}/c^2 \qquad (9.4)$$
$$\textit{High wing}: m > 2010 \text{ MeV}/c^2$$

The background fraction ε is measured using the fit to the mass plot. Since the background is found to have a shorter effective lifetime than the signals, the background correction leads to a small increase in the measured lifetimes.

The acceptance correction was determined using Monte Carlo data, as described below. The contribution of each event to the likelihood function could then be calculated. The negative log-likelihood was minimised using the MINUIT minimisation library programs [107]. The statistical errors (1 σ) on the fit parameters returned by the minimisation routines correspond to a change in the negative log-likelihood function of 0·5.

Acceptance calculation

The acceptance for proper lifetimes was measured using Monte Carlo data. Data were generated for the channel $D^+, D_s \to \phi\pi$, with a selection of lifetimes for the charmed mesons. The charmed particles were generated using a simulation of the process of γg-fusion, as described in Section 6.3. Only events in which the required particle was produced were kept, and their decay was forced into the channel required (here $D^+, D_s \to \phi\pi \to KK\pi$). Hadronisation was achieved using the Lund scheme, and the detector simulation carried out using GEANT. The trigger condition was simulated, and the events accepted by it were passed through the production analysis (in the same manner as real data). Finally, the full analysis chain was run on the events, including the vertex separation cut.

The proper lifetimes measured for the events that passed the analysis chain were then compared with the exponential distribution with which the events were generated. The

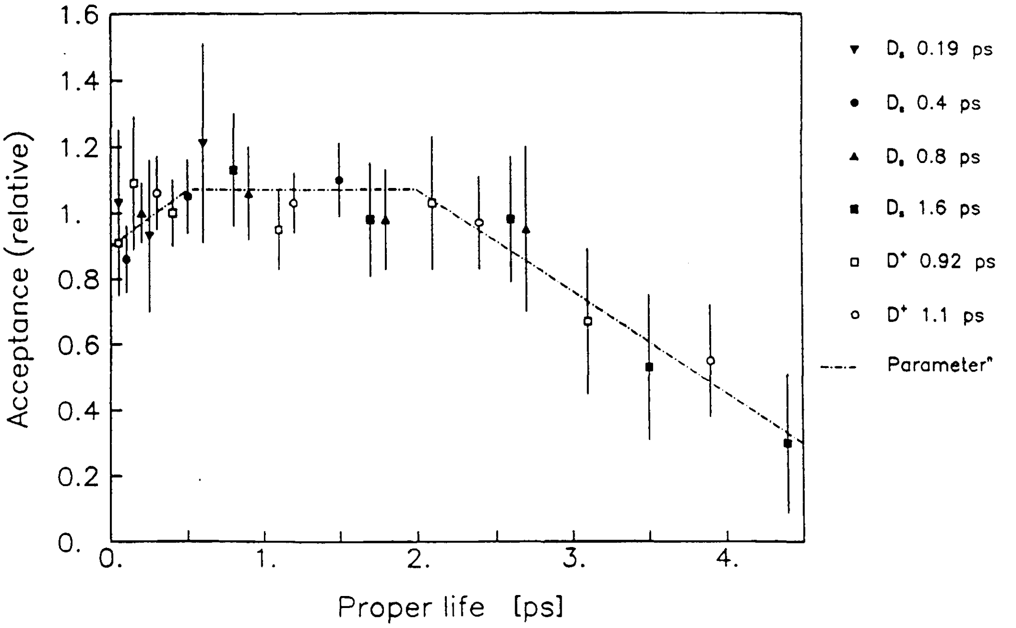

Figure 9.7 *Proper lifetime acceptance (Monte Carlo)*

ratio of the measured distribution to the input distribution (normalised to contain the same number of events) is shown in Figure 9.7, for the various data-sets.

The acceptance was parameterised as shown in Figure 9.8. The lifetime results were found to be insensitive to the exact parameterisation; the parameters chosen were adjusted to ensure that the lifetimes measured for the Monte Carlo data-sets were all consistent with the input lifetimes.

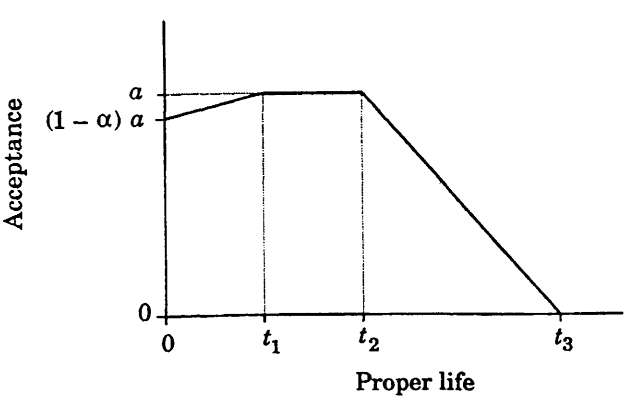

Figure 9.8 *Acceptance parameterisation*

Two features are evident in the acceptance correction:

(i) A small depletion at short times. This is caused by the offset track requirement of the analysis (Section 8.4), and by occasional primary vertex misidentification causing the value of d_{min} to be upstream of the true position. Also the vertex resolution terms in the likelihood function cause a smearing of the exponential.

(ii) A depletion at long times (greater than about 3 ps). This is a result of the fiducial cut imposed at the third plane of the microstrip detector. Its effect is insignificant for the D_s lifetime.

The acceptance must be normalised, and the normalisation factor depends on the lifetime measured. The parameters of the acceptance correction are defined in Figure 9.8:

$$A(t) = \begin{cases} (1-\alpha)\,a + \alpha\, a \dfrac{t}{t_1} & (t < t_1) \\ a & (t_1 < t < t_2) \\ a \dfrac{t_3 - t}{t_3 - t_2} & (t_2 < t < t_3) \\ 0 & (t_3 < t) \end{cases}$$

The normalisation condition is:

$$\int_0^\infty A(t)\, f(t)\, \mathrm{d}t = 1$$

from which the overall normalisation factor a may be calculated. The values of the parameters used in the acceptance parameterisation are shown in Table 9.1, and the resulting curve superimposed on Figure 9.7.

Parameter	Value
α	0·15
t_1	0·5 ps
t_2	2·0 ps
t_3	5·5 ps

Table 9.1 *Lifetime acceptance parameterisation*

Particle	Input lifetime [ps]	No. of events generated	No. of events $\Delta x > 2$ mm	Reconstructed lifetime [ps]
D^+	0·92	3954	277	$0{\cdot}85\,^{+0{\cdot}09}_{-0{\cdot}08}$
D^+	1·1	4332	285	$1{\cdot}10\,^{+0{\cdot}13}_{-0{\cdot}11}$
D_s	0·19	3322	48	$0{\cdot}20\,^{+0{\cdot}05}_{-0{\cdot}04}$
D_s	0·3	2265	79	$0{\cdot}30\,^{+0{\cdot}05}_{-0{\cdot}04}$
D_s	0·4	10470	298	$0{\cdot}43\,^{+0{\cdot}04}_{-0{\cdot}03}$
D_s	0·8	3679	212	$0{\cdot}78\,^{+0{\cdot}09}_{-0{\cdot}08}$
D_s	1·6	2609	165	$1{\cdot}45\,^{+0{\cdot}22}_{-0{\cdot}17}$

Table 9.2 *Monte Carlo lifetime measurement*

Using this acceptance parameterisation, the lifetimes of the Monte Carlo data-sets were determined, measured after passing through the full analysis chain. A comparison of the reconstructed lifetimes with the input lifetimes is given in Table 9.2. As can be seen, the reconstructed values are all consistent with those input.

D_s lifetime

The effective lifetime of the background was measured using the wings of the mass plots, as defined in Equation 9.4. The high and low wings were used separately, and together, and the values measured (with acceptance correction) are given in Table 9.3 for a selection of vertex separation cuts. The measurements all give consistent values. Taking the value measured at $\Delta x > 1$ mm with both wings, for least fractional error, the effective lifetime of the background is thus:

$$\tau_B = 0{\cdot}18 \pm 0{\cdot}03 \text{ ps}$$

(where the error is statistical), measured over 72 events. The proper lifetime distribution for these events is shown in Figure 9.9, with the curve corresponding to the measured effective lifetime superimposed. If the measurement is made without acceptance correction, it gives:

$$\tau_B\,(\textit{uncorrected}) = 0{\cdot}19\,^{+0{\cdot}04}_{-0{\cdot}03} \text{ ps}$$

Wing	Vertex separation cut	No. of events	Lifetime [ps]
Both	1 mm	72	$0{\cdot}18^{+0{\cdot}03}_{-0{\cdot}03}$
Both	2 mm	23	$0{\cdot}23^{+0{\cdot}08}_{-0{\cdot}06}$
Both	3 mm	12	$0{\cdot}19^{+0{\cdot}10}_{-0{\cdot}06}$
Both	2 σ	60	$0{\cdot}23^{+0{\cdot}05}_{-0{\cdot}04}$
Low	1 mm	40	$0{\cdot}20^{+0{\cdot}05}_{-0{\cdot}04}$
Low	2 mm	16	$0{\cdot}21^{+0{\cdot}09}_{-0{\cdot}06}$
High	1 mm	32	$0{\cdot}16^{+0{\cdot}05}_{-0{\cdot}03}$
High	2 mm	7	$0{\cdot}28^{+0{\cdot}17}_{-0{\cdot}09}$

Table 9.3 *Background lifetime measurement*

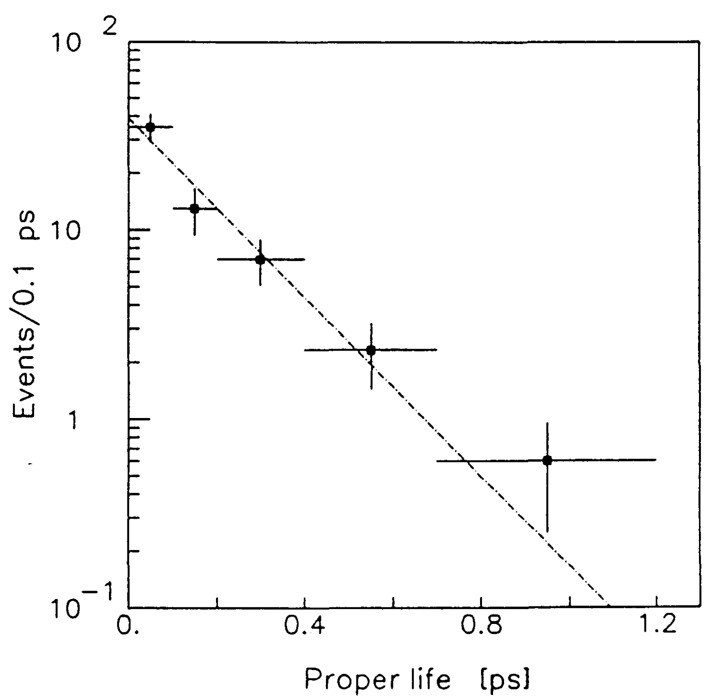

Figure 9.9 *Background proper lifetime distribution*

The measured lifetimes of the D_s signal, with background and acceptance correction, are given in Table 9.4 for a selection of vertex separation cuts. They are all consistent within errors, indicating that the systematic errors in the lifetime measurement are not large compared to the statistical errors. Taking the measurement at $\Delta x > 1{\cdot}5$ mm for least fractional errors:

$$\tau_{D_s} = 0{\cdot}33\ {}^{+0{\cdot}12}_{-0{\cdot}08}\ \text{ps}$$

(where the error is statistical), measured over 25 events, with a background fraction determined from the mass plot fit:

$$\varepsilon = 0{\cdot}15\ \pm 0{\cdot}07$$

The proper lifetime distribution for these events is shown in Figure 9.10, with the curve corresponding to the measured lifetime superimposed. If the measurement is made without acceptance or background corrections, the value achieved is:

$$\tau_{D_s}\ (uncorrected) = 0{\cdot}31\ {}^{+0{\cdot}11}_{-0{\cdot}07}\ \text{ps}$$

demonstrating that the corrections are small (~ 6 %).

Systematic errors

One potential source of systematic errors is *reflections* from other channels, i.e. the contamination of the signal with particles of a different type, which have been reconstructed with the D_s mass due to misidentification of their decay products. The two most likely candidates are:

(i) $\Lambda_c^+ \to p K^- \pi^+$

The proton of the decay is misidentified as a kaon. This is possible since the criteria for kaon identification (no light in the INDRA Cerenkov, momentum 6–20 GeV/c) are satisfied by protons too.

(ii) $D^+ \to K^- \pi^+ \pi^+$

One of the pions must be misidentified as a kaon. This can only occur through an inefficiency of the Cerenkov, i.e. the Cerenkov must fail to give light, even though the pion is expected to produce light in the required momentum range; this may occur if the pion passes through an inefficient region of the Cerenkov, such as at the mirror edges.

Vertex separation cut	No. of events	Background fraction	Lifetime [ps]
1 mm	37	0·18	$0{\cdot}30^{+0{\cdot}12}_{-0{\cdot}07}$
1·5 mm	25	0·15	$0{\cdot}33^{+0{\cdot}12}_{-0{\cdot}08}$
2 mm	20	0·14	$0{\cdot}30^{+0{\cdot}14}_{-0{\cdot}09}$
2·5 mm	15	0·17	$0{\cdot}30^{+0{\cdot}17}_{-0{\cdot}10}$
3 mm	12	0·18	$0{\cdot}29^{+0{\cdot}20}_{-0{\cdot}11}$
2σ	36	0·18	$0{\cdot}32^{+0{\cdot}12}_{-0{\cdot}08}$
3σ	29	0·17	$0{\cdot}30^{+0{\cdot}12}_{-0{\cdot}08}$
4σ	17	0·26	$0{\cdot}41^{+0{\cdot}23}_{-0{\cdot}13}$
5σ	14	0·27	$0{\cdot}40^{+0{\cdot}26}_{-0{\cdot}14}$
6σ	14	0·12	$0{\cdot}30^{+0{\cdot}17}_{-0{\cdot}10}$

Table 9.4 *D_s lifetime measurement*

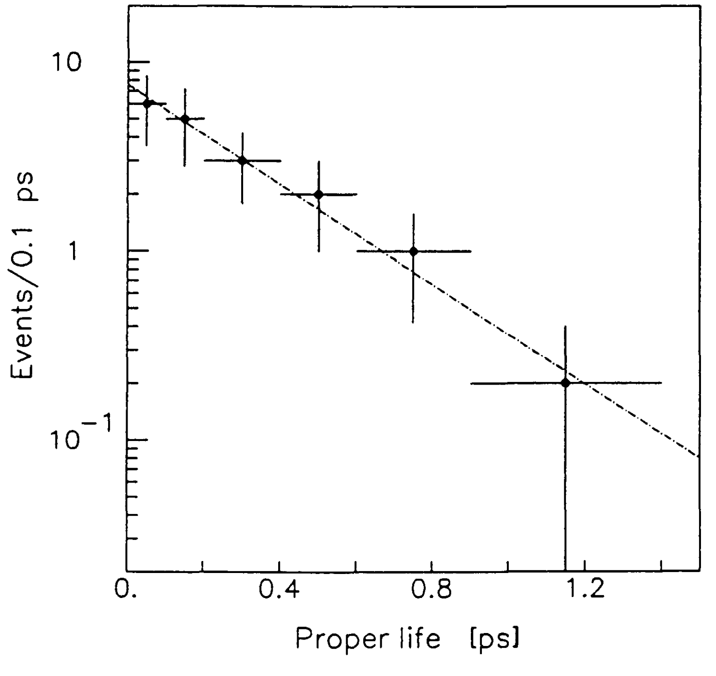

Figure 9.10 *D_s proper lifetime distribution*

The masses of the events in the $\Delta x > 1{\cdot}5$ mm mass plot were recalculated assuming both of the above reflection hypotheses in turn. Those events that were then found to lie in the Λ_c or D^+ mass ranges respectively (taken as 2255–2305 MeV/c^2 and 1840–1890 MeV/c^2) are shown in Figure 9.11. To test whether these reflections could be the source of a significant systematic error on the lifetime measurement, the lifetime was recalculated excluding the candidate reflection events for each channel in turn. The resulting values were:

$$\tau_{D_s}\ (\textit{excluding candidate } \Lambda_c \textit{ reflections}) = 0{\cdot}33\ ^{+0{\cdot}14}_{-0{\cdot}09}\ \text{ps}$$

$$\tau_{D_s}\ (\textit{excluding candidate } D^+ \textit{ reflections}) = 0{\cdot}32\ ^{+0{\cdot}15}_{-0{\cdot}10}\ \text{ps}$$

indicating that the effect is not significant. Note also that since the kaons of the D_s signal events have come through the ϕ, the probability that the reflections are real is further reduced.

Uncertainty in the acceptance correction gives a contribution to the systematic error. The acceptance parameterisation was determined using Monte Carlo data as described above, and was adjusted so that the reconstructed lifetime of the Monte Carlo data (after passing the full analysis chain) was consistent with the input value. The accuracy of the acceptance correction is thus only tested to the level of the statistical errors on the

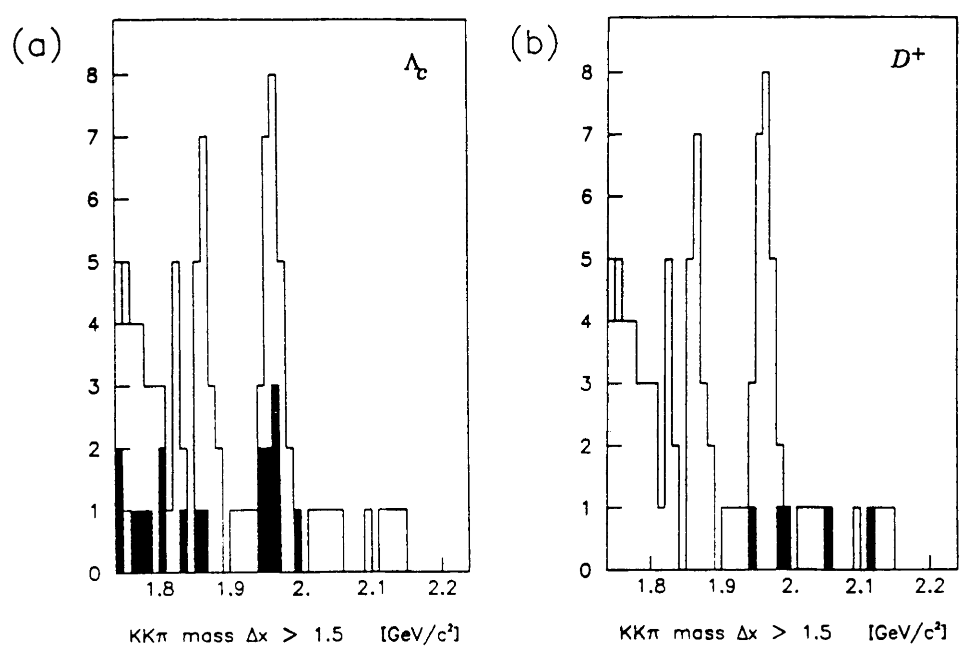

Figure 9.11 *Candidate reflections*

reconstructed lifetime of the Monte Carlo data. A large sample of events was therefore generated giving $D_s \rightarrow \phi\pi$, with an input lifetime of 0·4 ps. They were run through the analysis: out of the total 10470 events, 298 survived the analysis cuts, and the reconstructed lifetime (after acceptance correction, see Table 9.2) was:

$$\tau_{D_s}(MC) = 0{\cdot}430\,^{+0{\cdot}037}_{-0{\cdot}033}\ \mathrm{ps}$$

The fractional statistical error is taken as a contribution to the systematic error on the measurement of the D_s lifetime with real data, giving a contribution:

$$\sigma_{sys}\,(acceptance) = \,^{+0{\cdot}028}_{-0{\cdot}025}\ \mathrm{ps}$$

Another source of systematic error is the uncertainty on the background correction. The background fraction and effective lifetime both have associated errors; to determine the resulting systematic error, the D_s lifetime was recalculated using each of the values adjusted by $\pm 1\ \sigma$ error. The contribution to the systematic error from each effect was:

$$\sigma_{sys}\,(background\ fraction) = \,^{+0{\cdot}010}_{-0{\cdot}009}\ \mathrm{ps}$$

$$\sigma_{sys}\,(background\ lifetime) = \,^{+0{\cdot}004}_{-0{\cdot}005}\ \mathrm{ps}$$

The various contributions to the systematic error are assumed to be independent, and are added in quadrature to give:

$$\sigma_{sys}\,(total) = \,^{+0{\cdot}030}_{-0{\cdot}027}\ \mathrm{ps}$$

and thus the final value for the lifetime is:

$$\tau_{D_s} = 0{\cdot}33\,^{+0{\cdot}12}_{-0{\cdot}08} \pm 0{\cdot}03\ \mathrm{ps}$$

This measurement is compared with those of other experiments in Table 9.5. As can be seen, it is consistent with the world average, although it is rather lower than (but still compatible with) recent measurements.

D^+ lifetime

The procedure described above was used to measure the lifetime of the D^+ in the $\phi\pi$ channel. This Cabibbo suppressed channel is not, of course, the most favourable channel for the measurement of the D^+ lifetime, as the statistics are low and the errors are therefore considerable. As noted earlier, there is a much higher statistics sample available to the experiment, from the channel $D^+ \rightarrow K\pi\pi$ (as shown in Figure 8.16 (b)). It is, however, interesting as a check of consistency to determine the lifetime in the $\phi\pi$ channel.

Experiment	$\tau(D_s)$ [ps]
World average (1986) [1]	$0{\cdot}28\ ^{+0{\cdot}16}_{-0{\cdot}07}$
HRS [108]	$0{\cdot}35\ ^{+0{\cdot}24}_{-0{\cdot}18}\ \pm0{\cdot}09$
E531 [109]	$0{\cdot}26\ ^{+0{\cdot}16}_{-0{\cdot}09}$
ACCMOR, NA11+32 [110]	$0{\cdot}33\ ^{+0{\cdot}10}_{-0{\cdot}06}$
TASSO [111]	$0{\cdot}57\ ^{+0{\cdot}36}_{-0{\cdot}26}\ \pm0{\cdot}09$
E691 [112]	$0{\cdot}48\ ^{+0{\cdot}06}_{-0{\cdot}05}\ \pm0{\cdot}02$
CLEO [113]	$0{\cdot}47 \pm0{\cdot}22 \pm0{\cdot}05$
ARGUS [105]	$0{\cdot}56\ ^{+0{\cdot}13}_{-0{\cdot}12}\ \pm0{\cdot}08$
ACCMOR, NA32 [114]	$0{\cdot}45\ ^{+0{\cdot}19}_{-0{\cdot}11}$
This measurement	$0{\cdot}33\ ^{+0{\cdot}12}_{-0{\cdot}08}\ \pm0{\cdot}03$

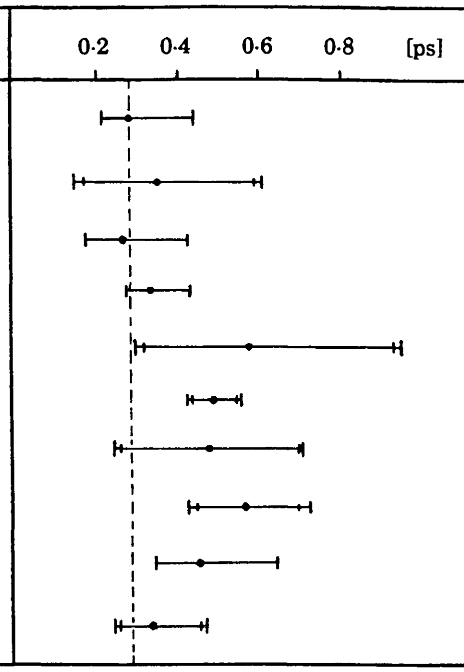

Table 9.5 *D_s lifetime comparison*

Measurements made using different vertex separation cuts are shown in Table 9.6, with background and acceptance correction. Once again, the values are all consistent, within errors. Taking the value at $\Delta x > 2$ mm for least fractional error:

$$\tau_{D^+} = 0{\cdot}98\ ^{+0{\cdot}51}_{-0{\cdot}32}\ \text{ps}$$

measured over 16 events, with a background fraction 0·28. This agrees well with the world average value [1]:

$$\tau_{D^+}\ (\textit{world average}) = 0{\cdot}92\ ^{+0{\cdot}13}_{-0{\cdot}10}\ \text{ps}$$

The distribution of proper lifetimes of these events is shown in Figure 9.12, with the curve corresponding to the measured lifetime superimposed. If the background and acceptance corrections are not made, the value becomes:

$$\tau_{D^+}\ (\textit{uncorrected}) = 0{\cdot}87\ ^{+0{\cdot}39}_{-0{\cdot}25}\ \text{ps}$$

Vertex separation cut	No. of events	Background fraction	Lifetime [ps]
1 mm	27	0·35	$0{\cdot}90\,^{+0{\cdot}43}_{-0{\cdot}26}$
1·5 mm	17	0·35	$1{\cdot}04\,^{+0{\cdot}55}_{-0{\cdot}32}$
2 mm	16	0·28	$0{\cdot}98\,^{+0{\cdot}51}_{-0{\cdot}30}$
2·5 mm	16	0·21	$0{\cdot}89\,^{+0{\cdot}48}_{-0{\cdot}28}$
3 mm	14	0·18	$0{\cdot}88\,^{+0{\cdot}48}_{-0{\cdot}28}$
$2\,\sigma$	24	0·40	$1{\cdot}01\,^{+0{\cdot}52}_{-0{\cdot}31}$
$3\,\sigma$	22	0·33	$0{\cdot}94\,^{+0{\cdot}49}_{-0{\cdot}29}$
$4\,\sigma$	18	0·32	$0{\cdot}97\,^{+0{\cdot}52}_{-0{\cdot}30}$
$5\,\sigma$	15	0·30	$0{\cdot}98\,^{+0{\cdot}54}_{-0{\cdot}31}$
$6\,\sigma$	15	0·20	$0{\cdot}88\,^{+0{\cdot}48}_{-0{\cdot}28}$

Table 9.6 *D^+ lifetime measurement*

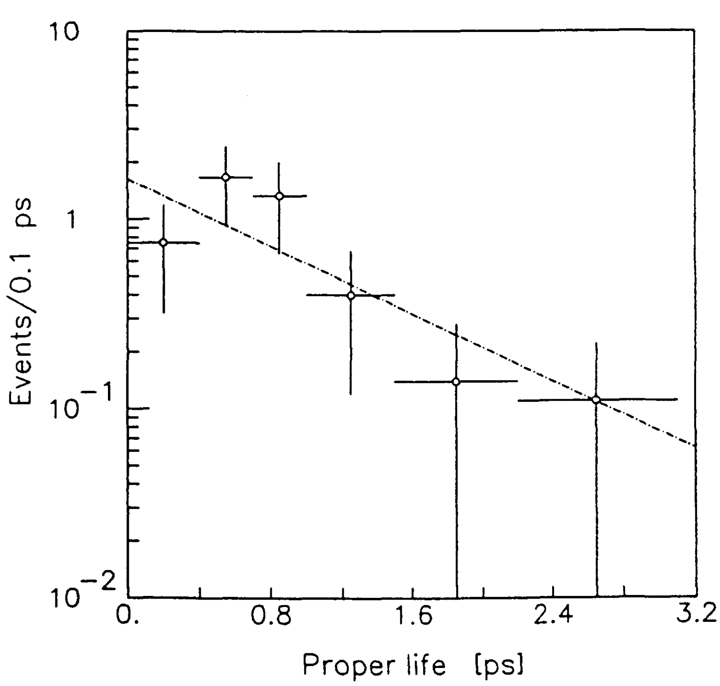

Figure 9.12 *D^+ proper lifetime distribution*

9.3 Angular distributions

There are two independent angles of interest for the decay in the $\phi\pi$ channel (they will be discussed here for the $D_s \to \phi\pi$ decay, although the situation is the same for the $D^+ \to \phi\pi$ decay):

(i) θ_ϕ^*: the angle of the ϕ (or π) relative to the direction of the D_s, in the rest-frame of the D_s. See Figure 9.13. The decay $D_s \to \phi\pi$ involves the spin-parity assignments (J^P):

$$0^- \to 1^- 0^-$$

i.e. the decay of a pseudoscalar particle to a vector and a pseudoscalar. Since the D_s has spin 0, however, there is no preferred direction for this system, and the decay must be isotropic—the distribution of decays should be flat with respect to $\cos(\theta_\phi^*)$.

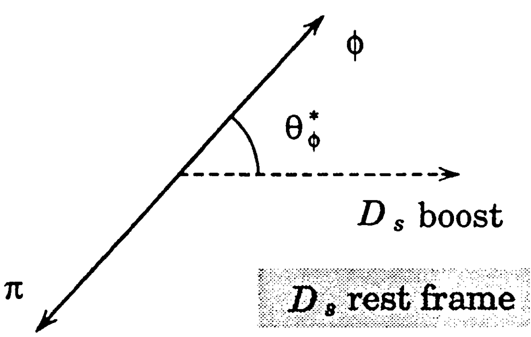

Figure 9.13 Definition of θ_ϕ^*

A further consequence of the D_s having spin 0 is that in the rest-frame of the D_s, the orbital angular momentum $\boldsymbol{l}$ of the $\phi\pi$ system must be normal to the direction defined by the ϕ (or π) momentum:

$$\boldsymbol{p}_\phi \cdot \boldsymbol{l}_\phi = 0$$

i.e. the ϕ has helicity 0.

(ii) θ_K^*: the angle of either kaon from the ϕ decay relative to the direction of the π in the rest-frame of the ϕ. See Figure 9.14. The decay $\phi \to KK$ involves the spin-parity assignments (J^P):

$$1^- \to 0^- 0^-$$

i.e. the decay of a vector particle to two pseudoscalars. The decay therefore involves

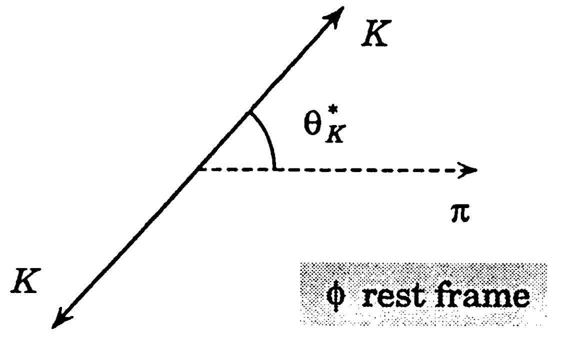

Figure 9.14 Definition of θ_K^*

one unit of orbital angular momentum: $l = 1$. Choosing the quantization axis along the pion direction, the component of angular momentum $m = 0$, since the ϕ-meson has helicity 0. From angular momentum theory, the decay amplitude will behave under spatial rotations like the Legendre polynomial $P_l^m(\cos\theta)$, from the corresponding spherical harmonic $Y_{lm}(\theta,\phi)$. In this case we have:

$$P_1^0 \propto \cos\theta_K^*$$

and therefore the distribution of decays should vary as $\cos^2(\theta_K^*)$.

The Monte Carlo was used to check the angular acceptance for both angles. See Figure 9.15; the acceptance was taken as uniform in both cases. The angular

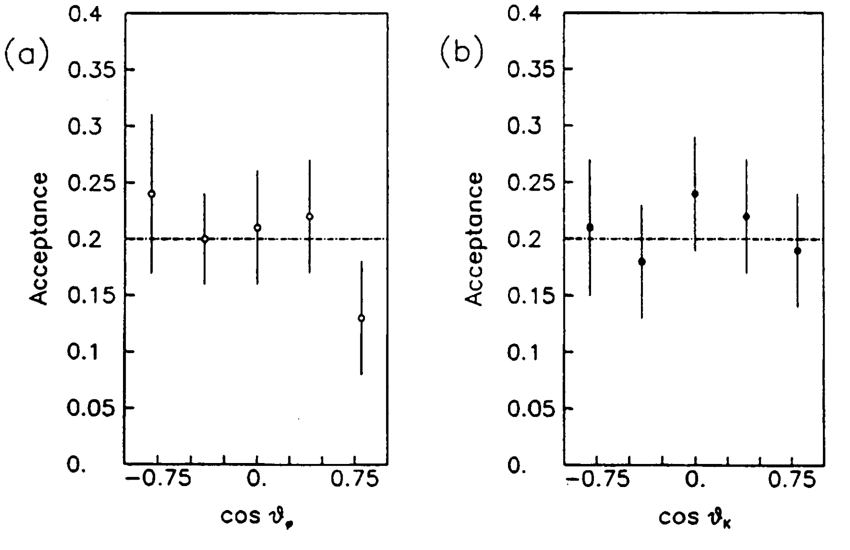

Figure 9.15 Angular acceptance (Monte Carlo)

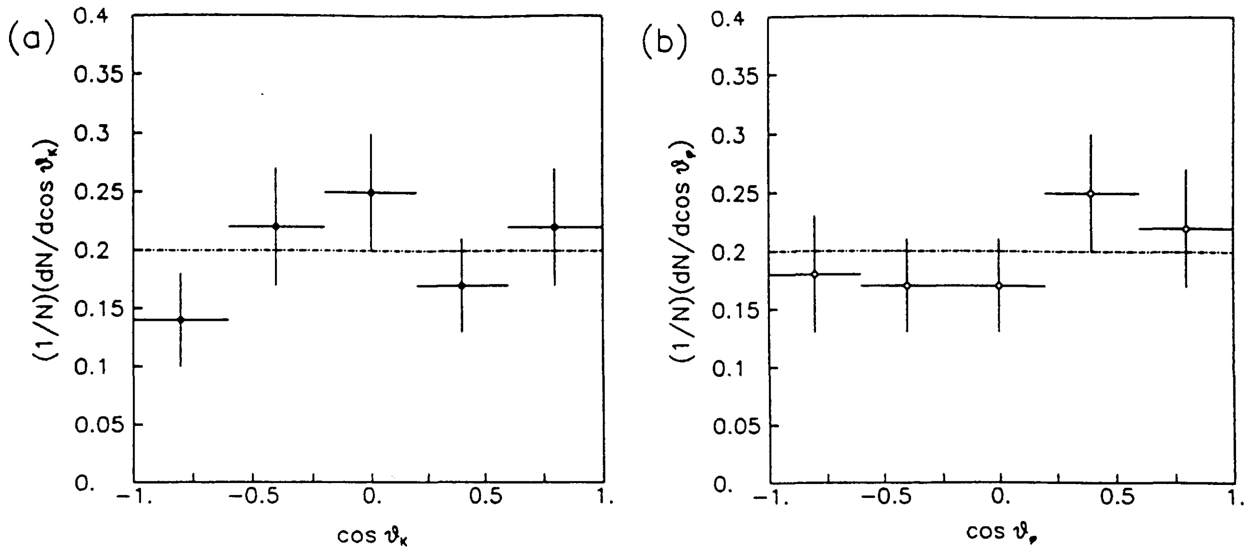

Figure 9.16 *Background angular distributions*

distributions were then investigated for both the D_s and the D^+ decays, and for background events. Mass plots at different cuts on the vertex separation distance were used to define the signals: for the D_s, the $\Delta x > 1$ mm plot was used, and for the D^+, the $\Delta x > 2$ mm plot. The background events were taken from the wings of the $\Delta x > 1$ mm plot.

The two angular distributions for the background events are shown in Figure 9.16. As can be seen, they are both consistent with a flat distribution. The distributions for the

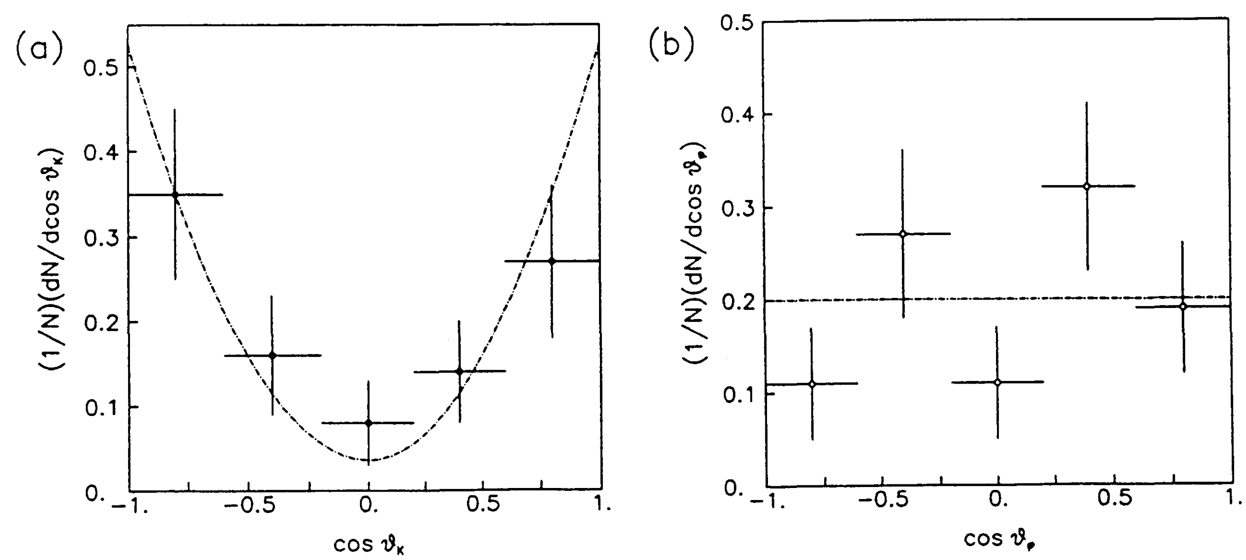

Figure 9.17 *D_s angular distributions*

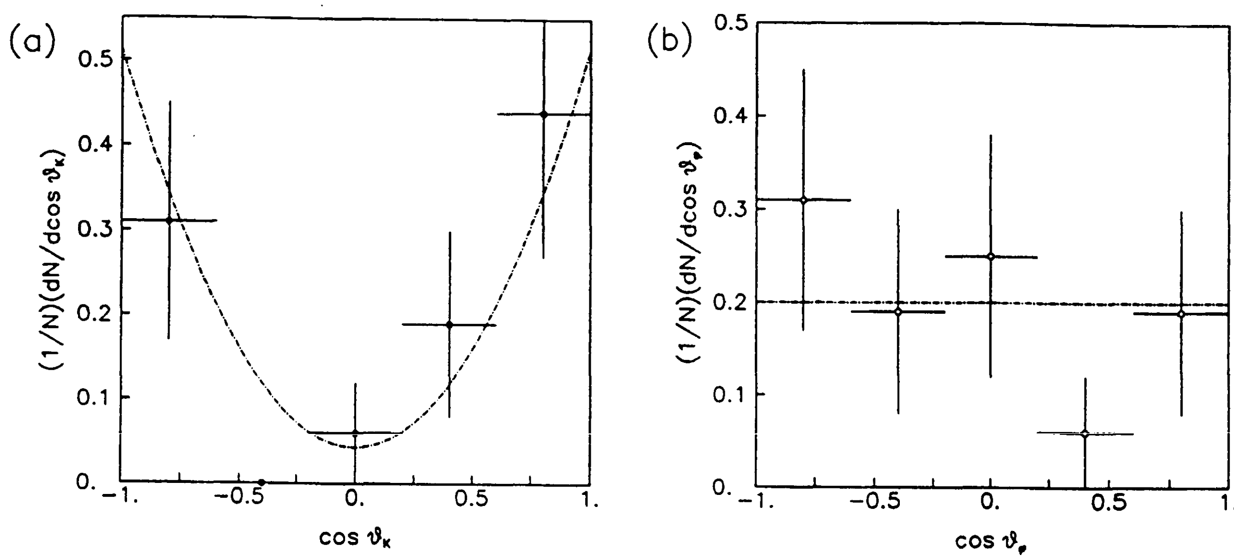

Figure 9.18 *D^+ angular distributions*

D_s are given in Figure 9.17, and for the D^+ in Figure 9.18. For both particles, the distributions with respect to $\cos(\theta_\phi{}^*)$ are consistent with being flat, as expected. The distributions with respect to $\cos(\theta_K{}^*)$, on the other hand, show clear evidence of the expected $\cos^2(\theta_K{}^*)$ dependence. The superimposed curves for these plots are calculated using a constant term for the background, and a $\cos^2(\theta_K{}^*)$ term for the signal, normalised to the number of events in the distribution. The background fraction is determined from the appropriate mass plot.

9.4 Target activity

The active target activity was classified into three categories, for the events from the $\Delta x > 2$ mm mass plot. The classifications were:

(i) Events in which there was clear evidence of nuclear breakup. An example is shown in Figure 9.19 (a);

(ii) Events for which the target was 'clean', i.e. consistent with coherent production. See Figure 9.19 (b);

(iii) Events that did not clearly fall into either of the preceding categories. See Figure 9.19 (c).

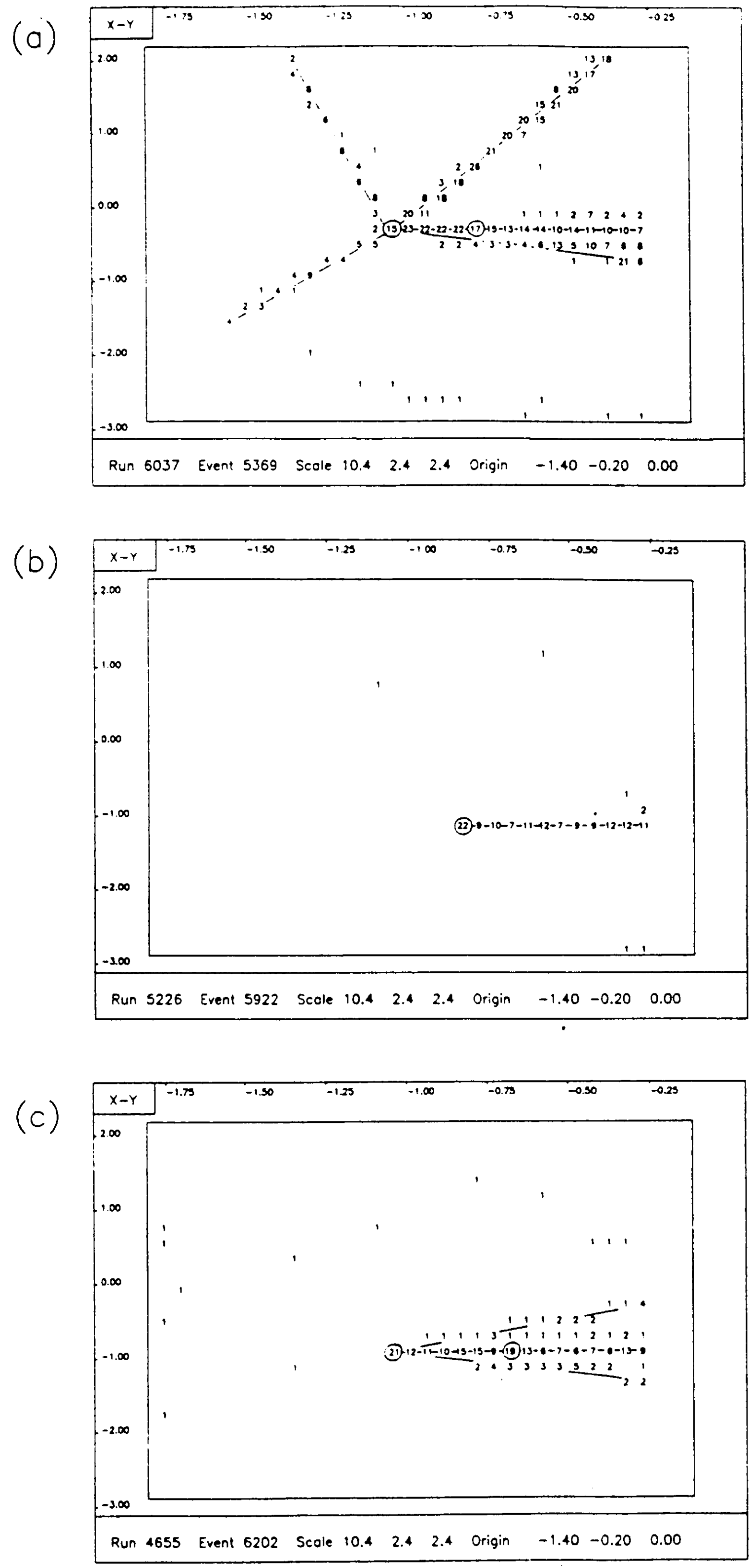

***Figure 9.19** Target activity categories*

	D^+	D_s	Background
Breakup	10 (62 %)	7 (39 %)	17 (55 %)
Clean	3 (19 %)	3 (17 %)	0 (0 %)
Ambiguous	3 (19 %)	8 (44 %)	14 (45 %)

Table 9.7 *Target activity*

The number of events falling into each category is given in Table 9.7, for the D^+ and D_s signals, and for the background events from the wings. Although the statistics are low, the charm signals appear to have a larger fraction of clean events. The mean ionisation in the last two strips of the 'main road' in the target was compared with the track multiplicity in the microstrips, to obtain an estimate of the charged multiplicity of these clean events. See Table 9.8. The charged multiplicity was found to be typically ~ 8, indicating that the charm production rarely occurs via the production of a charmed meson and antimeson pair alone.

Signal	Target pulse height		Microstrip multiplicity
	plane 29	*plane* 30	
D_s	6	9	8
D_s	16	13	11
D_s	7	7	8
D^+	12	9	8
D^+	11	12	9
D^+	12	11	8

Table 9.8 *Clean event multiplicity*

9.5 Energy spectra

The energy spectrum of the candidate charmed particles was studied, for events from the D^+ and D_s signal peaks, and for background, taken from the wings of the mass plot. The signals were taken from the $\Delta x > 2$ mm mass plot, with the usual mass ranges (Equation 9.3). The energy spectra found are shown in Figure 9.20 (a) and (b). For the background study, the vertex separation cut was reduced to $\Delta x > 0$, to increase the statistics. The energy spectrum obtained is shown in Figure 9.20 (c). Finally the distribution for Monte Carlo D_s events (obtained after the same analysis) is shown in

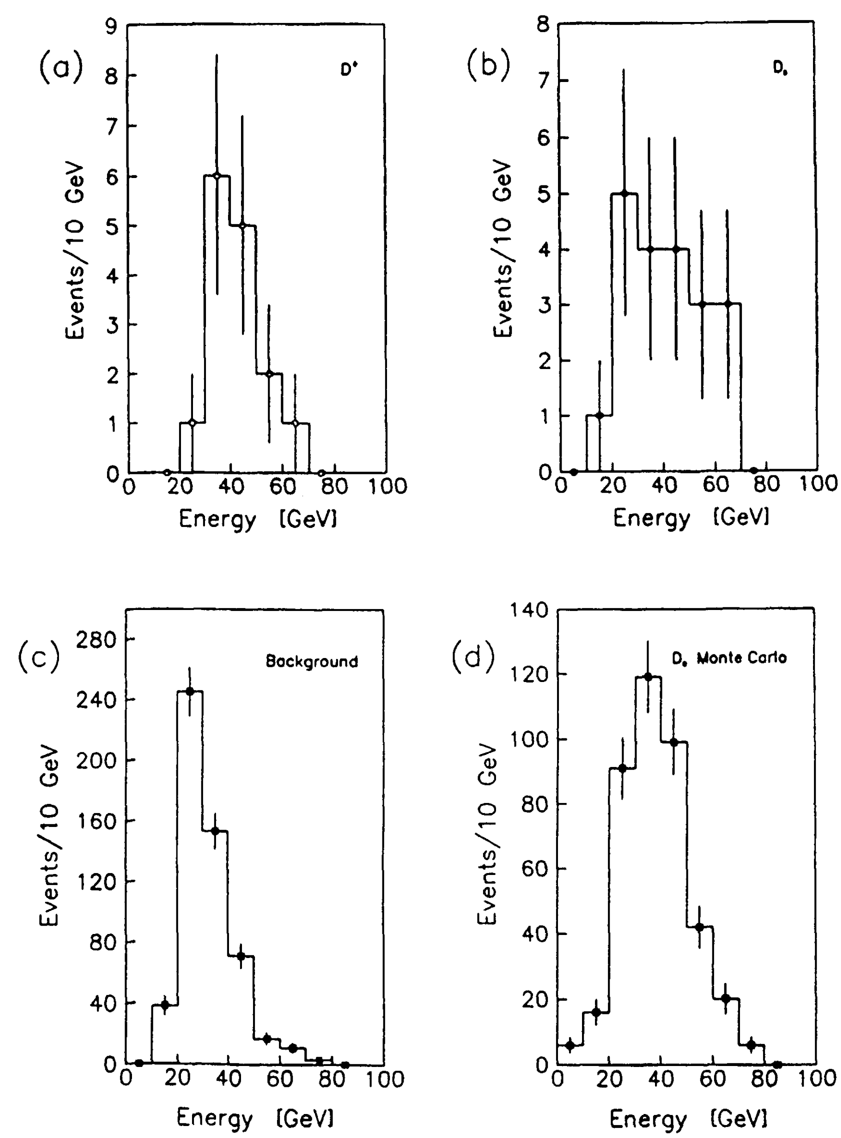

Figure 9.20 Energy spectra

Data-set	Mean E (raw) [GeV]	Mean E (corrected) [GeV]	Mean p_T^2 (raw) [GeV^2/c^2]	Mean p_T^2 (corrected) [GeV^2/c^2]
Background	31·7	27·7 ± 1·2	0·76	0·65 ± 0·03
D_s	41·4	37·6 ± 8·4	1·55	1·43 ± 0·32
$D_s(MC)$	43·8	34·5 ± 1·0	1·23	1·16 ± 0·04
D^+	40·8	37·8 ± 9·5	1·58	1·53 ± 0·38
$D^+(MC)$	39·9	35·0 ± 1·0	1·33	1·26 ± 0·04

Table 9.9 Signal properties

Figure 9.20 (d). The background and acceptance corrected mean values are compared in Table 9.9, where the errors are statistical.

9.6 p_T^2 distribution

The acceptance in p_T was determined using the Monte Carlo and is shown in Figure 9.21. The p_T^2 distribution of the background events was investigated, using the wings of the

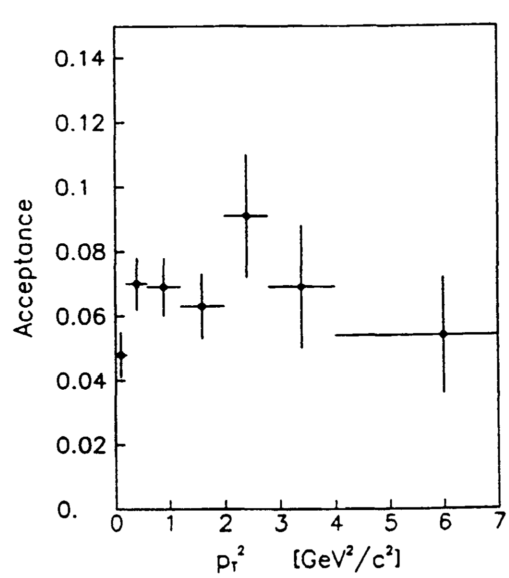

Figure 9.21 p_T^2 acceptance (Monte Carlo)

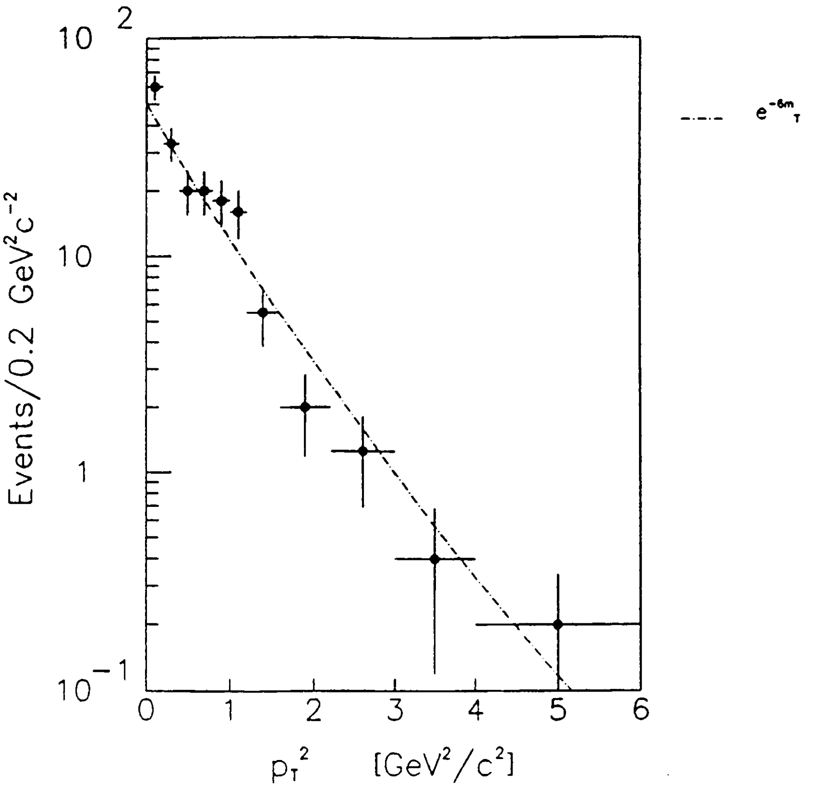

Figure 9.22 *p_T^2 distribution of background*

$\Delta x > 0$ mass plot. See Figure 9.22. The superimposed curve is the standard parameterisation [39]:

$$\frac{d\sigma}{dp_T^2} = e^{-6m_T}$$

where the transverse mass, m_T, is given by:

$$m_T = \sqrt{m_D^2 + p_T^2}$$

where m_D is the candidate charmed meson mass. As can be seen, the background p_T^2 distribution is well fitted by this parameterisation.

The p_T^2 distributions of the D_s and D^+ signals were calculated using the events from the $\Delta x > 2$ mm mass plot. See Figure 9.23. The signals show a clear excess over the background at high values of p_T^2, as expected if γg-fusion (Section 2.7) contributes to the production mechanism. The distribution from the Monte Carlo simulation of the D_s signal is also shown on the plots, and agrees well with the real data. The comparison of the background and acceptance corrected mean values for p_T^2 from the data and the Monte Carlo is made in Table 9.9.

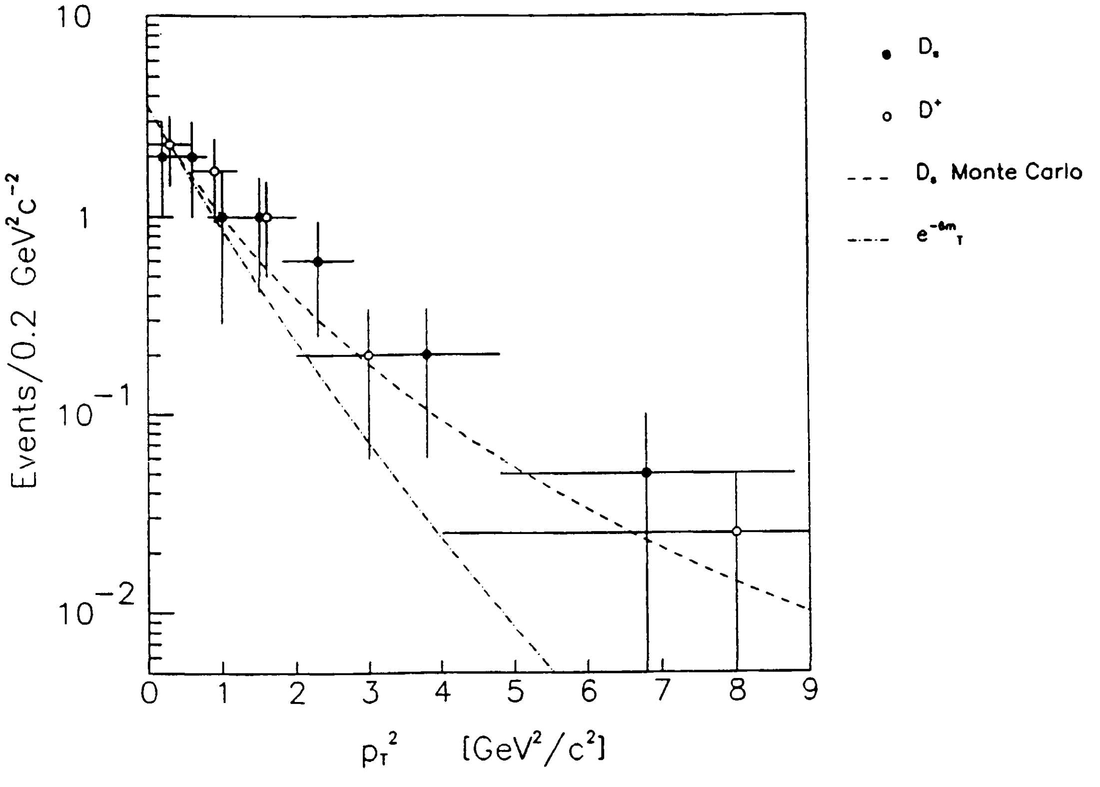

Figure 9.23 *p_T^2 distribution of signals*

9.7 x_F distributions

The Feynman-x variable provides useful information about the production dynamics. It is defined as:

$$x_F = \frac{p_L(D)}{p_L(max)}$$

where $p_L(D)$ is the longitudinal momentum of the candidate charmed meson (in the centre-of-mass frame), and $p_L(max)$ is the maximum available longitudinal momentum, given by:

$$p_L(max) = \sqrt{E_\gamma^2 - m_D^2}$$

The beam photon energy E_γ is determined using the *tagging* described in Section 3.3. This is problematic because:

(i) The tagging efficiency is quite low, ~ 45 %, and therefore the statistics (which are already low for the $\phi\pi$ channel) are reduced still further.

(ii) The tagging does not correct for double bremsstrahlung (see Section 3.3), and as a result the photon energy is overestimated for the fraction of events (about 17 %) in which it is significant. The correction can only be made for distributions, rather than individual events, and—due to the low statistics observed in this channel—was not pursued further.

The acceptance in x_F was determined using the Monte Carlo, for the analysis with $\Delta x > 1$ mm. See Figure 9.24. The following features are apparent:

(i) The acceptance decreases for x_F greater than about 0·7. This is caused by the condition that the kaons are identified, which limits their momentum to less than 20 GeV/*c*. The reconstructed charm meson is therefore prevented from having very high momentum, and the acceptance in x_F is reduced.

(ii) The acceptance also decreases for values of x_F less than about 0·3, and is zero for $x_F < 0$. This is a result both of the geometrical acceptance of the spectrometer, and the lower limit to the kaon momentum.

The x_F distributions for the D_s and D^+ signals (from the $\Delta x > 1$ mm mass plot) were corrected for the acceptance, and are shown in Figure 9.30. The superimposed fits are of the standard form [44]:

$$\frac{d\sigma}{dx_F} = (1 - x_F)^n$$

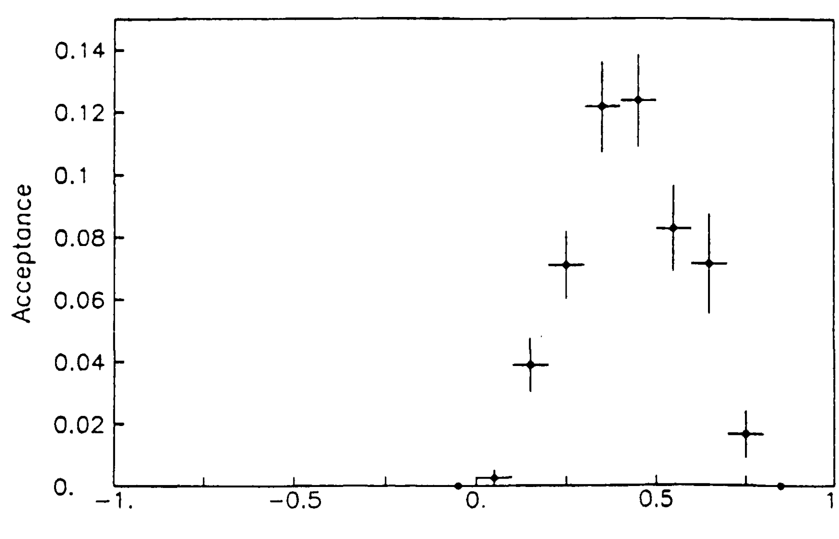

Figure 9.24 *x_F acceptance (Monte Carlo)*

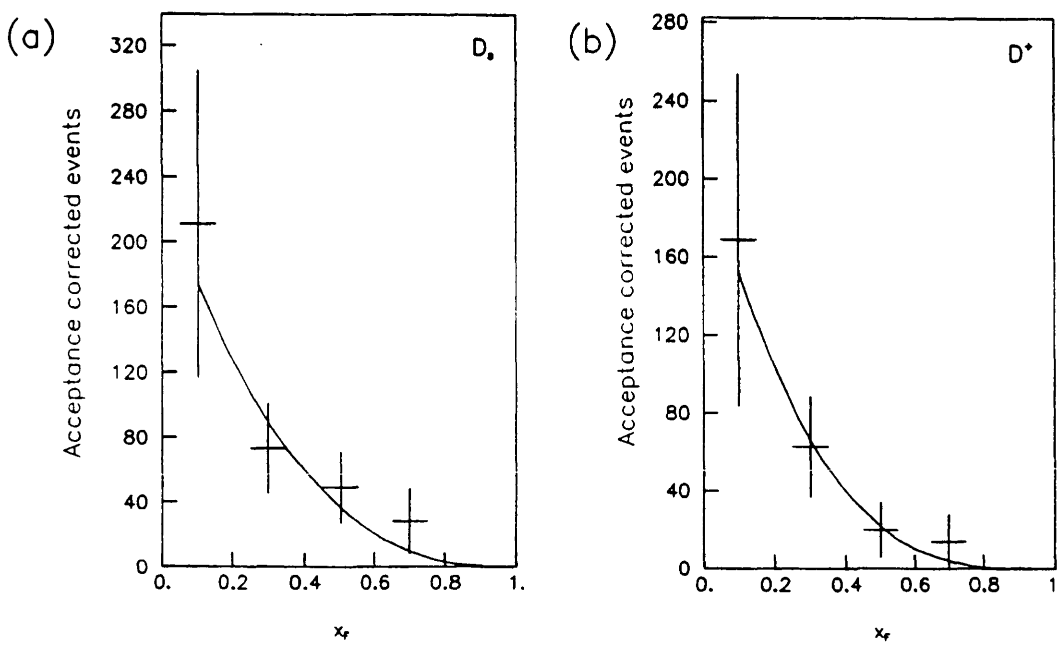

Figure 9.25 *x_F distribution of signals*

The exponent n is kept as a free parameter in the fits, which give the values:

$$n(D_s) = 2{\cdot}7 \pm 0{\cdot}6$$
$$n(D^+) = 3{\cdot}3 \pm 0{\cdot}9$$

These values are compatible with a corresponding recent measurement by E691 [115], using D^0s, of $2{\cdot}7 \pm 0{\cdot}1 \pm 0{\cdot}6$. The Monte Carlo simulation of the D_s signal gives the distribution shown in Figure 9.26. This gives a value:

$$n(MC) = 2{\cdot}37 \pm 0{\cdot}08$$

consistent with the data.

9.8 Particle-antiparticle asymmetry

The particle-antiparticle asymmetry was measured for the D^+ and D_s signals. It was calculated by counting the number of entries into the signal peak with positive or negative charge, n_+ and n_- respectively, and then calculating:

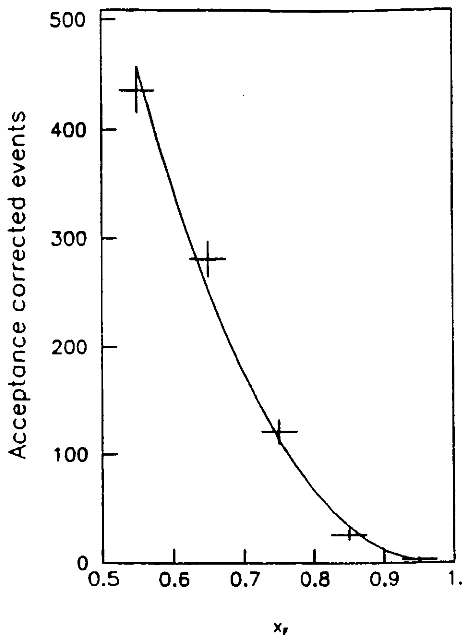

Figure 9.26 *x_F distribution, Monte Carlo*

$$a = \frac{n_+ - n_-}{n_+ + n_-}$$

The number of positive or negative entries is subject to Binomial errors, since an entry must be one or the other. Putting:

$$n_+ = Np$$

where:

$$N = n_+ + n_-$$

and p is the probability of finding a positive entry, then the error on n_+ is given by:

$$\sigma_+ = \sqrt{Np(1-p)}$$

Taking as our best estimate:

$$p = \frac{n_+}{N}$$

we have:

$$\sigma_+ = \sqrt{n_+\left(1 - \frac{n_+}{N}\right)} = \sqrt{\frac{n_+ n_-}{N}}$$

and finally the error on the asymmetry measured is:

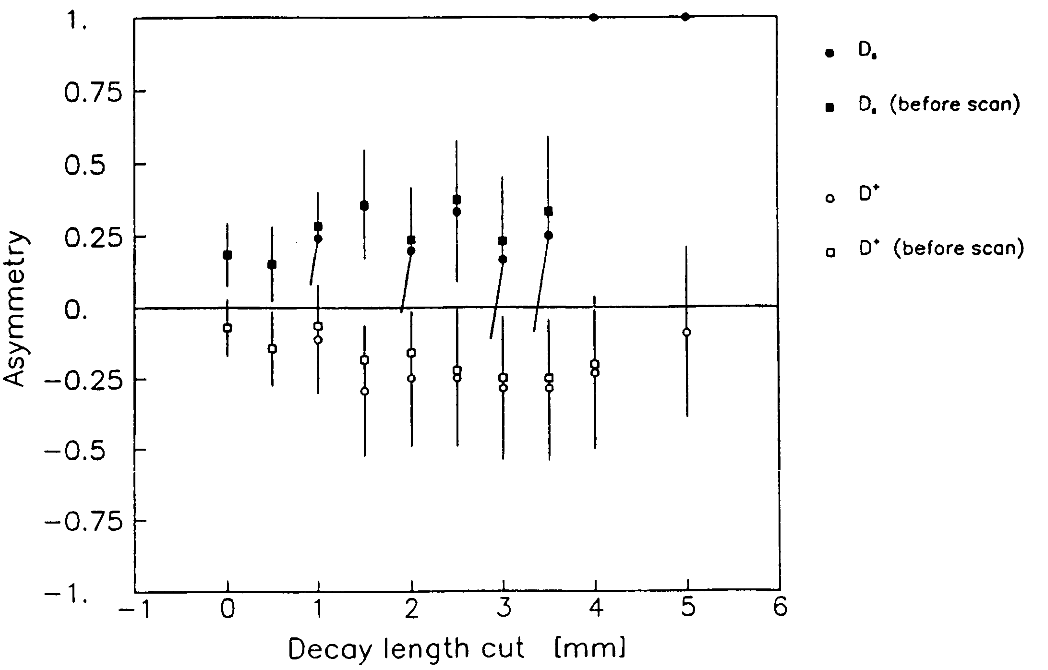

***Figure 9.27** Particle-antiparticle asymmetries*

$$\sigma_a = \frac{2\sigma_+}{N}$$

The asymmetry values found for the D^+ and D_s are shown in Figure 9.27, which shows their evolution with the cut on vertex separation. The asymmetry of the background was measured using events from the wings of the mass plot at $\Delta x > 0$ as:

$$a(background) = 0{\cdot}03 \;\pm 0{\cdot}04$$

Taking the values measured for the signals at a vertex separation cut that gives the most significant signal, and correcting for background, gives:

$$a(D^+) = -0{\cdot}31 \;\pm 0{\cdot}30$$
$$a(D_s) = 0{\cdot}29 \;\pm 0{\cdot}19$$

The value for the D_s may be compared with a recent result from E400 [116] of 0·31 ± 0·36. The measurements have the senses predicted by the Monte Carlo simulation (Section 2.9), with D^- being more copiously produced than D^+, and D_s^+ being more copiously produced than D_s^-; the asymmetries are, however, rather greater in magnitude than those expected (~ -0·09 and ~ 0·05, shown in Figure 2.21).

9.9 Production ratio of D_s and D^+

Measurement of cross-sections

The measurement of production cross-sections provides useful information about the mechanisms involved in particle production. The accurate measurement of absolute cross-sections is complex, however, whilst the determination of cross-section ratios is relatively straightforward.

The calculation of a cross-section σ for the production of a particle, given a number of signal events N, requires knowledge of the acceptance A of the analysis procedures, the branching ratio B of the particle to the channel detected, and the sensitivity s of the experiment. Then:

$$\sigma = \frac{N}{ABs} \tag{9.5}$$

The acceptance gives the fraction of events which satisfy the trigger and are detected as signal. This is measured using the Monte Carlo simulation. The *sensitivity* is the total number of events that are acquired by the experiment in a given process, per unit cross-section for that process. The sensitivity for this experiment may be calculated as follows:

$$s = \frac{N_{trig}\, h}{\sigma_{TOT}\, A_{trig}} \tag{9.6}$$

where N_{trig} is the number of triggers taken, h is the hadronic fraction of the events, σ_{TOT} is the total hadronic photoproduction cross-section (on the particular target material used), and A_{trig} is the acceptance of the trigger to hadronic events. An accurate measurement of these quantities (apart from the number of triggers) is difficult, and the value found for the sensitivity is correspondingly uncertain.

In the $\phi\pi$ channel, however, we have signals for both the D^+ and the D_s. It is therefore possible to make a measurement of the production ratio of these two particles, avoiding the need for a measurement of the sensitivity:

$$\frac{\sigma(D_s)}{\sigma(D^+)} = \frac{N(D_s)\, A(D^+)\, B(D^+ \to \phi\pi)}{N(D^+)\, A(D_s)\, B(D_s \to \phi\pi)}$$

Vertex separation cut [mm]	No. of D_s	No. of D^+	Signal ratio (D_s/D^+)
1	30·9 ± 4·6	17·6 ± 3·8	1·76 ± 0·46
1·5	21·6 ± 3·8	10·9 ± 2·9	1·98 ± 0·63
2	16·7 ± 3·1	11·6 ± 2·8	1·44 ± 0·44
2·5	12·6 ± 2·8	12·4 ± 2·9	1·02 ± 0·33
3	9·7 ± 2·4	11·5 ± 2·7	0·84 ± 0·29
3·5	6·9 ± 2·2	12·0 ± 2·7	0·58 ± 0·23
4	4·7 ± 1·8	11·1 ± 2·7	0·42 ± 0·19

Table 9.10 *Signal ratio (D_s/D^+)*

Instead of the absolute acceptance, it is also now only the relative acceptance that is required, reducing the associated systematic errors.

Production ratio measurement

The number of entries in the signal peaks for the D^+ and D_s was determined using the fitting procedure described in Section 9.1, at different cuts on the vertex separation distance. See Table 9.10. The double exponential fit was used for the background, and the

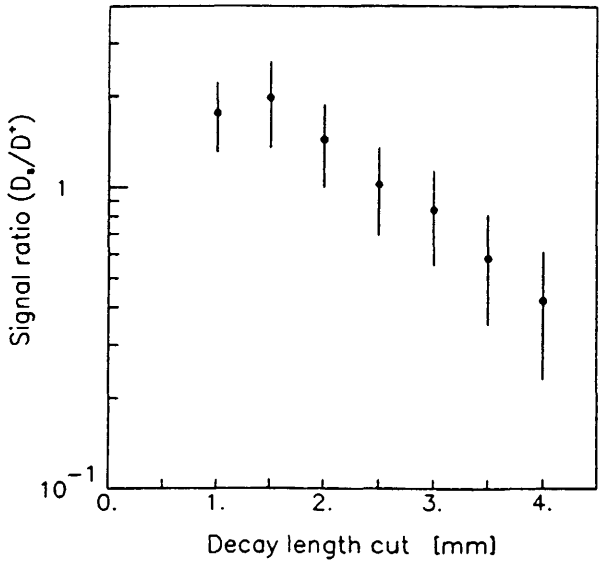

Figure 9.28 *Raw signal ratio (D_s/D^+)*

error on the signal is taken from the fit. The evolution of the raw ratio of the signals with the vertex separation cut is shown in Figure 9.28. A clear exponential dependence is evident, resulting from the lifetime behaviour of the two signals. Note that the vertex separation requirement accepts all events greater than the cut, so the events at any particular cut include those at greater cuts, and hence the entries in Figure 9.28 are strongly correlated, making a fit to the points as shown inappropriate.

To understand the behaviour of the signal ratio, Monte Carlo data was used. The data were passed through a simulation of the trigger, reconstructed using TRIDENT, and were then passed through the same analysis as the real data. Monte Carlo data-sets with different input lifetimes for the D^+ and D_s were used. The number of events in the signal peak was counted at different cuts on the vertex separation, for the various data-sets. These numbers were then divided by the number of events in the data-set, to give the acceptances shown in Figure 9.29. The values for two of the data-sets, the 0·3 ps D_s and the 1·1 ps D^+, are given in Table 9.11. Note that the fraction of these charm Monte Carlo data-sets passing the trigger are 54 % and 51 % respectively. This may be compared with the fraction measured with non-charm Monte Carlo events, 23 %, indicating that the trigger leads to a charm enrichment of ~ 2.

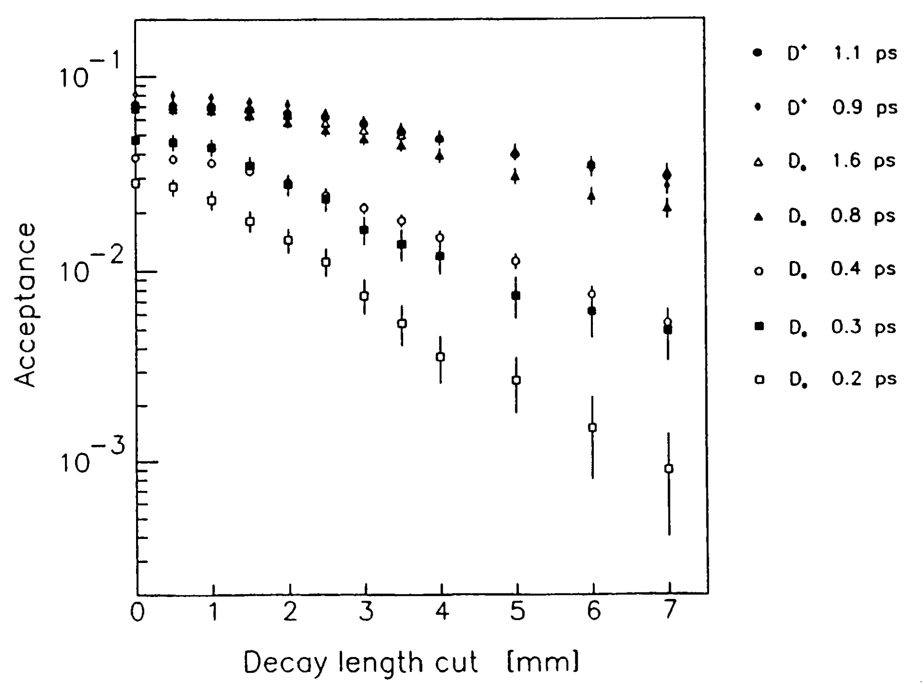

Figure 9.29 *Acceptance (Monte Carlo)*

Signal	D^+ (1·1 ps)				D_s (0·3 ps)			
Generated Pass trig.	4332 2214				2265 1215			
Vertex sep. cut [mm]	Signal (raw)	Accept. (raw) [%]	Signal (corr.)	Accept. (corr.) [%]	Signal (raw)	Accept. (raw) [%]	Signal (corr.)	Accept. (corr.) [%]
0	317	7·3 ± 0·4	330	7·6 ± 0·4	107	4·7 ± 0·5	111	4·9 ± 0·5
1	311	7·2 ± 0·4	377	8·7 ± 0·5	98	4·3 ± 0·4	174	7·7 ± 0·8
2	285	6·6 ± 0·4	406	9·4 ± 0·6	63	2·8 ± 0·4	183	8·1 ± 1·0
3	253	5·8 ± 0·4	424	9·8 ± 0·6	37	1·6 ± 0·3	171	7·5 ± 1·2
4	208	4·8 ± 0·3	407	9·4 ± 0·7	27	1·2 ± 0·2	211	9·3 ± 1·8
5	170	3·9 ± 0·3	389	9·0 ± 0·7	17	0·8 ± 0·2	124	5·5 ± 1·3
6	148	3·4 ± 0·3	399	9·2 ± 0·8	14	0·6 ± 0·2	157	7·0 ± 1·9
7	129	3·0 ± 0·3	417	9·6 ± 0·9	11	0·5 ± 0·2	146	6·4 ± 1·9

Table 9.11 *Acceptance measurement (Monte Carlo)*

As can be seen, the exponential behaviour is reproduced for vertex separations greater than about 2 mm. For a collection of particles with mean lifetime τ, the number remaining at time t is given by (Equation 9.1):

$$N(t) = N_0\, e^{-t/\tau}$$

The decay distance d is given approximately by:

$$d \sim \gamma c t$$

and so the exponential behaviour of the acceptance is not surprising.

For small values of the vertex separation cut (less than about 2 mm), the acceptance curves flatten off to a constant value. This can be caused by the criterion in the analysis that there is a secondary track offset by at least 30 μm from the primary vertex. Also, as was seen earlier, the exponential lifetime distribution is smeared by the detector resolution. The effect of the detector resolution is to cause a loss of events that are reconstructed with a negative vertex separation. This effect will be more important for decays with a shorter lifetime, and is the source of the decrease in acceptance at $\Delta x > 0$ as the input D_s lifetime is reduced. In the limit of vanishing lifetime, the fraction of events reconstructed with positive vertex separation would be 0·5.

The effect of the detector resolution is incorporated by convoluting the exponential lifetime distribution with a Gaussian distribution, as discussed in Section 9.2. The resulting probability density is plotted in Figure 9.30, taking a typical value of 0·05 ps for

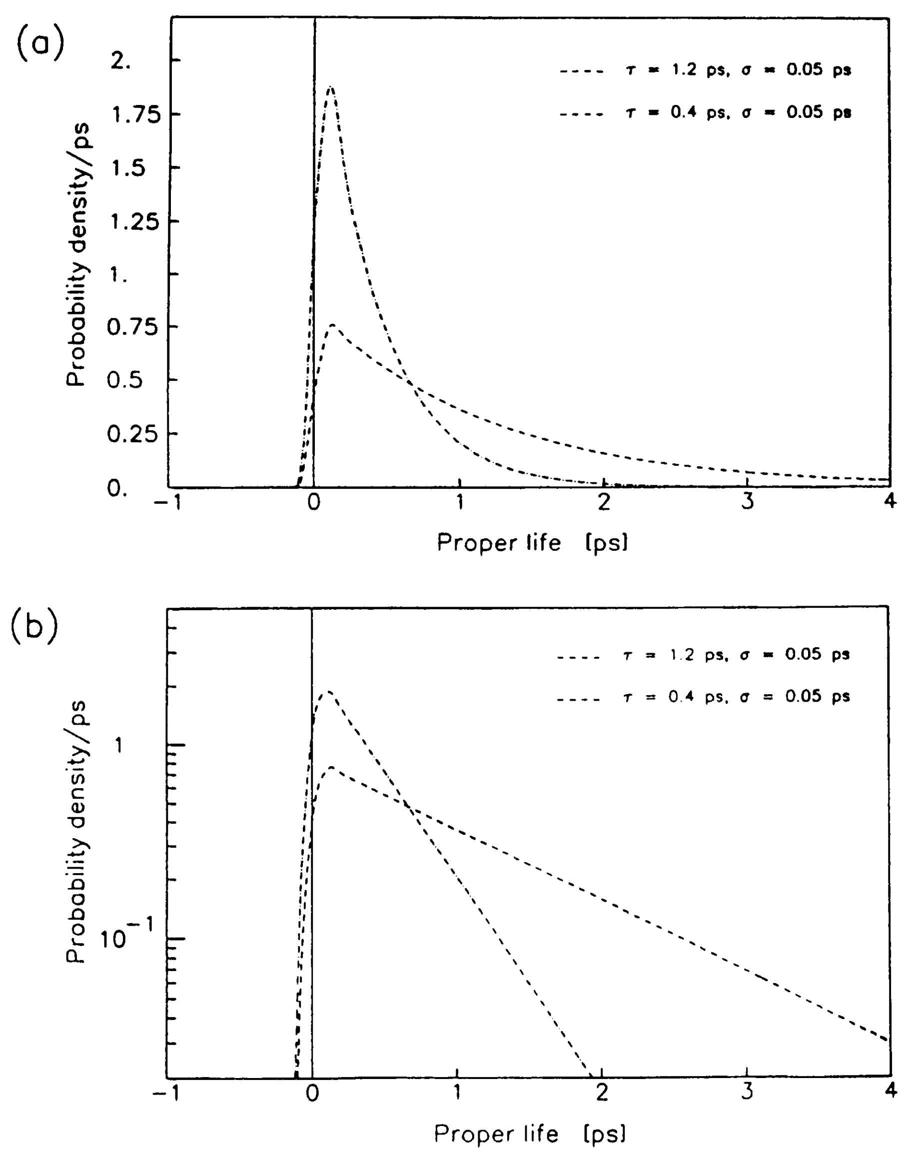

Figure 9.30 *Proper life probability density distributions*

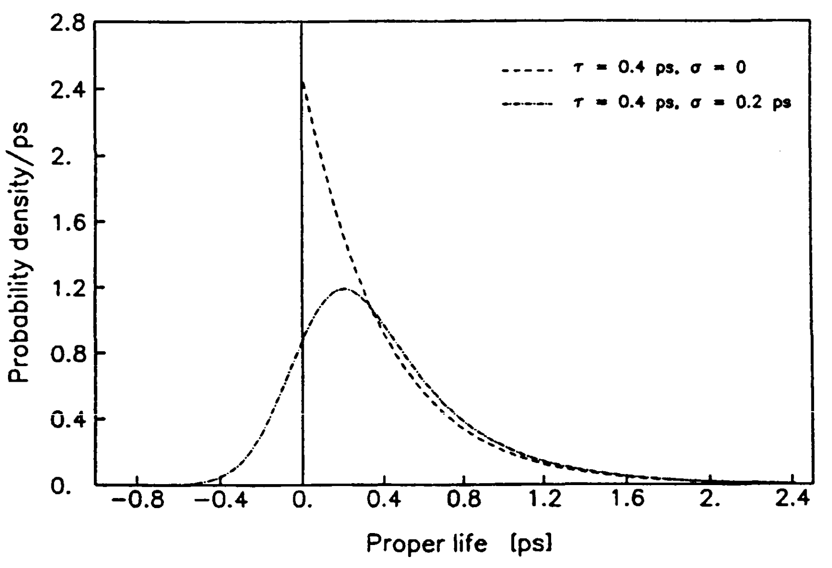

Figure 9.31 *Effect of lifetime measurement error*

the resolution σ, using approximately the D_s and D^+ lifetimes, and with a linear scale (a) or logarithmic scale (b). The effect of the detector resolution is illustrated in Figure 9.31, where the probability density function is shown for a lifetime of 0·4 ps, with values of the resolution of both $\sigma = 0$, and an exaggerated value of $\sigma = 0{\cdot}2$ ps. In the latter case, the loss of events for low cuts on the proper life (or on the decay distance) is clear. Note, however, that for higher cuts, this effect does not cause any substantial change in the probability density, and in fact the probability density is slightly *greater* for the curve with larger σ.

The effect of the lifetime behaviour of the signals on the acceptance was corrected for by weighting each event in the signal with a suitable normalisation from the probability density function. For each event there is a minimum time t_{min} determined by the vertex separation cut, and a maximum time t_{max} resulting from the fiducial cut (at the microstrip planes). The weight is therefore taken as:

$$w = \left[\int_{t_{min}}^{t_{max}} f(t)\,\mathrm{d}t \right]^{-1}$$

From Equation 9.2 we have:

$$\int_{t_{min}}^{t_{max}} f(t)\,\mathrm{d}t = \int_{t_{min}}^{t_{max}} \frac{1}{2\tau}\,\mathrm{e}^{\left(\frac{\sigma^2}{2\tau^2}-\frac{t}{\tau}\right)}\left[1-\mathrm{erf}\left(\frac{\sigma}{\sqrt{2}\,\tau}-\frac{t}{\sqrt{2}\,\sigma}\right)\right]\mathrm{d}t$$

Putting:

$$\alpha = \frac{\sigma}{\sqrt{2}\,\tau}, \quad x = \frac{1}{\sqrt{2}}\left(\frac{\sigma}{\tau}-\frac{t}{\sigma}\right)$$

and with $\mathrm{erfc}(x) = 1 - \mathrm{erf}(x)$, this becomes:

$$\int_{x_{min}}^{x_{max}} -\alpha\,\mathrm{e}^{(2\,\alpha\,x-\alpha^2)}\,\mathrm{erfc}(x)\;\mathrm{d}x = -\frac{1}{2}\left[\mathrm{e}^{(2\,\alpha\,x-\alpha^2)}\,\mathrm{erfc}(x) - \mathrm{erfc}(x-\alpha)\right]_{x_{min}}^{x_{max}}$$

from which the weight may be calculated. Note that if the detector resolution effect is ignored, the weight becomes simply:

$$w = \frac{1}{\mathrm{e}^{-t_{min}/\tau} - \mathrm{e}^{-t_{max}/\tau}}$$

The sum of the weighted events are given for the Monte Carlo samples in Table 9.11. They are used to calculate a corrected acceptance, shown in Figure 9.32, with (a) the same scale as Figure 9.29, and (b) a linear scale. The acceptances are clearly now less dependent either on decay length cut or on the data-set used. It appears, however, in Figure 9.32 (b) that the spread in the corrected acceptance values is greater than the marked statistical errors, but since there is no systematic variation of acceptance with lifetime or with particle type the acceptances were taken as equal.

This correction procedure was next applied to the data, using the lifetimes measured in Section 9.2. The corrected signals were adjusted for background, measured from the relevant mass plots, and gave the values shown in Table 9.12 for a selection of vertex separation cuts. The measurements are all consistent, and taking the value at $N_\sigma > 2$, for least fractional errors, we have:

$$\frac{\sigma(D_s)\,B(D_s \rightarrow \phi\,\pi)}{\sigma(D^+)\,B(D^+ \rightarrow \phi\,\pi)} = 3{\cdot}18 \pm 1{\cdot}02$$

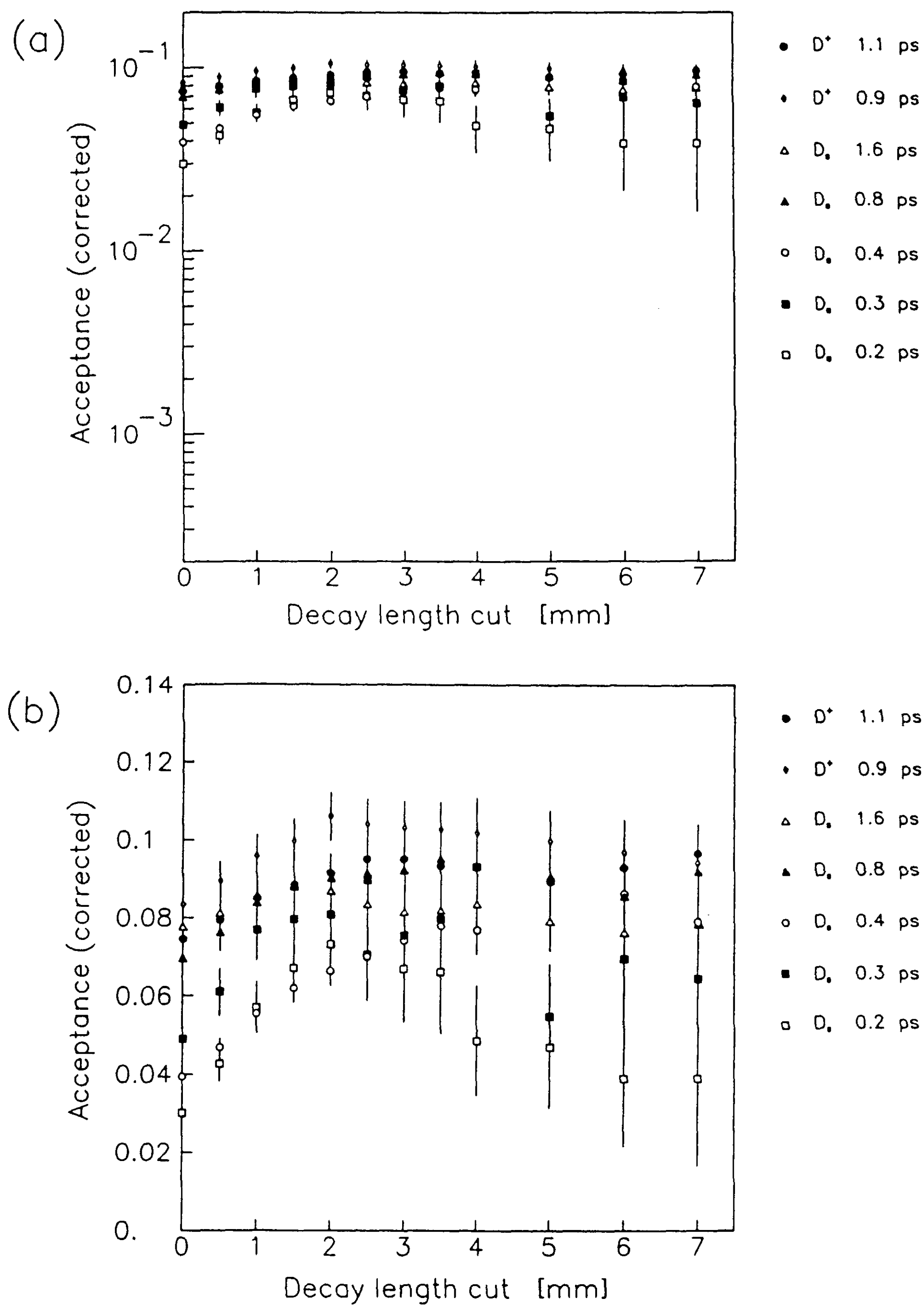

Figure 9.32 *Lifetime corrected acceptance (Monte Carlo)*

Vertex separation cut	D_s			D^+			$\frac{\sigma \cdot B(D_s \to \phi\pi)}{\sigma \cdot B(D^+ \to \phi\pi)}$
	No. of events		Background fraction	No. of events		Background fraction	
	(raw)	(corr.)		(raw)	(corr.)		
1 mm	37	66·4	0·18	27	33·2	0·35	2·52 ± 0·83
1·5 mm	25	57·6	0·15	17	22·3	0·35	3·38 ± 1·25
2 mm	20	63·6	0·14	16	22·9	0·28	3·32 ± 1·26
2·5 mm	15	66·6	0·15	16	24·9	0·21	2·87 ± 1·14
3 mm	12	67·4	0·17	14	24·2	0·18	2·82 ± 1·22
2σ	36	66·7	0·18	24	28·7	0·40	3·18 ± 1·02
3σ	29	61·4	0·17	22	28·2	0·33	2·70 ± 0·87
4σ	17	42·5	0·26	18	25·2	0·32	1·84 ± 0·74
5σ	14	43·4	0·27	15	22·9	0·39	1·98 ± 0·87
6σ	14	54·8	0·12	15	24·9	0·20	2·42 ± 0·98

Table 9.12 *Production ratio measurement*

Systematic errors

One source of systematic error on this measurement is the error on the acceptance correction, which is determined by the statistical error on the Monte Carlo calculations. For $N_\sigma > 2$ the corrected acceptance ratio measured with the 0·3 ps D_s and 1·1 ps D^+ Monte Carlo data-sets was:

$$\frac{A(D_s)}{A(D^+)} = 0{\cdot}89 \pm 0{\cdot}11$$

(taken as 1·0). Taking the fractional error on this value leads to:

$$\sigma_{sys}\,(acceptance) = \pm\, 0{\cdot}40$$

Another source of systematic error comes from the error on the measurement of the particle lifetimes. Adjusting the values used by ± 1 σ leads to a contribution:

$$\sigma_{sys}\,(lifetime) = {}^{+0{\cdot}82}_{-0{\cdot}54}$$

Finally the background fractions used in the measurement have associated errors:

$$\varepsilon(D_s) = 18 \pm 2\,\%$$
$$\varepsilon(D^+) = 40 \pm 5\,\%$$

at $N_\sigma > 2$, giving:

$$\sigma_{sys}\,(background) = \pm\,0{\cdot}25$$

These contributions to the systematic error are assumed to be independent, and are added in quadrature to give:

$$\sigma_{sys}\,(total) = {}^{+0{\cdot}94}_{-0{\cdot}72}$$

The final value for this measurement is therefore:

$$\frac{\sigma(D_s)\,B(D_s \rightarrow \phi\,\pi)}{\sigma(D^+)\,B(D^+ \rightarrow \phi\,\pi)} = 3{\cdot}2\ \pm 1{\cdot}0\ {}^{+0{\cdot}9}_{-0{\cdot}7}$$

Taking the most accurate values available for the branching ratios:

$$B(D_s \rightarrow \phi\pi) = 4\ \pm 1\ \%$$

from Equation 8.3, and [106]:

$$B(D^+ \rightarrow \phi\pi) = 0{\cdot}68\ \pm 0{\cdot}07\ \pm 0{\cdot}12\ \%$$

we obtain:

$$\frac{\sigma(D_s)}{\sigma(D^+)} = 0{\cdot}54\ \pm 0{\cdot}17\ \pm 0{\cdot}23$$

The main contribution to the systematic error now comes from the errors on the branching ratios. This measurement is in good agreement with the prediction from the Monte Carlo simulation (Section 2.9) of ~ 0·5.

Comparison of result

The result has been given above in the form of a ratio of $\sigma{\cdot}B$ as well as a ratio of σ, since the branching ratios are not very accurately known, especially for the decay $D_s \rightarrow \phi\pi$ (as discussed in Section 8.4). This uncertainty is common to all measurements of the production ratio, so the value in the form of a ratio of $\sigma{\cdot}B$ can therefore be compared more directly with the measurements of other experiments. The comparison is difficult, however, due to the lack of published results. See Table 9.13. The E400 result was quoted [116] in a directly comparable form to this measurement. E691 have not published cross-section information for their $\phi\pi$ analysis, although at a 6 σ cut (~ 2 mm) they find [106] $122 \pm 12\ D_s$ and $84 \pm 10\ D^+$—a raw ratio of $1{\cdot}45 \pm 0{\cdot}22$, which may be compared with the value from this analysis at 2 mm of $1{\cdot}44 \pm 0{\cdot}44$. A preliminary result on 15 % of their data sample [117] is given in the table.

Experiment	$\frac{\sigma \cdot B(D_s \to \phi\pi)}{\sigma \cdot B(D^+ \to \phi\pi)}$
E400	1.6 ± 1.2
E691 (15 %)*	2.2 ± 1.2
CLEO †	4.0 ± 1.1
CLEO*	4.2 ± 1.5
HRS*	4.9 ± 1.7
This measurement	$3.2 \pm 1.0 ^{+0.9}_{-0.7}$

* See text.

† Based on [16], see text.

Table 9.13 *Production ratio comparison*

For the comparison with e^+e^- results, the original CLEO observation of the D_s [16] included an estimation of $B(D_s \to \phi\pi)$ outlined in Section 8.4, that *assumed*:

$$\frac{\sigma(D_s)}{\sigma(D^0 + D^+ + D_s)} = 0.15$$

Reversing this argument, using the branching ratios given above, and taking [118]:

$$\frac{\sigma(D^0)}{\sigma(D^+)} = 2.4 \pm 0.4$$

leads to the value quoted in the table. More recent CLEO results [118], taken at 10·55 GeV (in the continuum), give:

$$\sigma \cdot B(D_s \to \phi\pi) = 14.7 \pm 3.9 \pm 2.0 \text{ pb}$$
$$\sigma(D^+) = 0.52 \pm 0.08 \pm 0.08 \text{ nb}$$

Combining these values with the D^+ branching ratio above leads to the second CLEO result in the table. Finally a similar procedure is followed using results from HRS [119], taken at 29 GeV.

To obtain an estimate of the absolute cross-section for D_s production, an earlier measurement of the experimental sensitivity may be adapted [78]. In this reference the trigger acceptance was determined using a Monte Carlo simulation, and found to be ~ 0·4. The hadronicity of the triggered events is ~ 0·9, and the total inelastic photoproduction cross-section (on silicon) $\sigma_{eff}(Si) \sim 80\ \mu b$ (corrected for shadowing). The current analysis uses a total of ~ 17·2 million triggers, so the sensitivity (from Equation 9.6) is:

$$s \sim 400 \text{ events/nb}$$

Taking the D_s signal found at $\Delta x > 1$ mm, there are ~ 31 events. The acceptance is measured using Monte Carlo to be ~ 0·04 (see Figure 9.29), and the branching ratio is given by:

$$B = B(D_s \to \phi\pi)\, B(\phi \to KK) \sim 0{\cdot}02$$

Therefore, using Equation 9.5, we obtain:

$$\sigma(D_s) \sim 100 \text{ nb}$$

To obtain a more accurate determination of this cross-section, further study would need to be made of the associated systematic errors.

CONCLUSIONS

The photoproduction experiment NA14 ran successfully over the period 1985–86, taking a total of just over 17 million triggers, at a mean photon energy of about 100 GeV. These data have been processed through a variety of filters, selecting different features of charmed events.

Central to the enrichment of charm in the data was the use of a silicon vertex detector, comprising an active target and a microstrip tracking detector, which worked reliably throughout the data taking. The microstrip detector, with 10 planes containing a total of 10,000 strips at a 50 μm pitch, achieved a spatial resolution of 16 μm, and 97 % per-plane efficiency.

A strong D^0 signal was found in the $K\pi$ channel, using data from a filter based on the microstrip detector information which selected events with a complex vertex topology. From an equivalent of ~ 1·2 million raw-data events, a signal of 52 ± 7 events with a signal-to-background ratio of ~ 1·5 was achieved, at a 3 σ cut on the separation of the reconstructed production and decay vertices. This signal was used in the development of the charm analysis techniques.

A kaon selecting filter was run on the full data-set, and a ϕ signal was isolated in the KK channel, with a signal of ~ 6330 events and a signal-to-background ratio of ~ 1·2. The ϕ events were used to investigate the $\phi\pi$ channel, and signals were found for the D_s and the Cabibbo-suppressed D^+. For the D_s, a signal of 31 ± 5 events with a signal-to-background ratio of ~ 4·6 was achieved, at a 1 mm cut on the separation of the reconstructed production and decay vertices. This number of events is comparable to the 1986 total world statistics. A signal of 12 ± 3 events was found for the D^+ at a 2·5 mm vertex cut, with a signal-to-background ratio of ~ 3·7.

The mass measured for the D^+ was used to adjust the mass scale, and a value of $1969{\cdot}8 \pm 1{\cdot}9 \pm 2{\cdot}4$ MeV/c^2 was calculated for the D_s. This value is consistent with the world average value, with comparable errors, and is also consistent with more recent measurements. The measured width of 10 ± 2 MeV/c^2 is compatible with the expected instrumental width determined by Monte Carlo simulation.

The lifetimes of the D_s and D^+ signals were measured using a maximum likelihood method. The acceptance and background corrections were found to be small, approximately 6 %. The lifetime measured for the D_s was:

$$\tau(D_s) = 0{\cdot}33\,^{+0{\cdot}12}_{-0{\cdot}08} \pm 0{\cdot}03 \text{ ps}$$

and with that of the D^+ gave a ratio:

$$\frac{\tau(D_s)}{\tau(D^+)} = 0{\cdot}34\,^{+0{\cdot}22}_{-0{\cdot}15}$$

These measurements are consistent with those of other experiments. The ratio demonstrates the importance of non-spectator processes in the weak decays of charmed mesons.

The angular distributions of the D_s and D^+ decays were checked, and found to be consistent with the expected pseudoscalar spin-parity assignment of the particles.

The distributions of production variables, including energy, x_F, and p_T, were measured, and found to be consistent with the predictions of the Monte Carlo simulation, which is based on the first order QCD γg-fusion process. The mean energy was measured as 38 ± 8 GeV for the D_s, and 38 ± 10 GeV for the D^+. The $p_T{}^2$ distribution of background events was found to be described well by an e^{-6m_T} parameterisation, and a significant excess of events was discovered at large p_T for the D_s and D^+ signals, in accordance with the QCD expectations, with a mean $p_T{}^2$ value of $1{\cdot}4 \pm 0{\cdot}3$ GeV^2/c^2 for the D_s and $1{\cdot}5 \pm 0{\cdot}4$ GeV^2/c^2 for the D^+. The x_F distributions of the signals were found to be well described by a $(1-x)^n$ parameterisation, with $n = 2{\cdot}7 \pm 0{\cdot}6$ for the D_s and $n = 3{\cdot}3 \pm 0{\cdot}9$ for the D^+.

The particle-antiparticle asymmetries were measured as $-0{\cdot}31 \pm 0{\cdot}30$ for the D^+, and $0{\cdot}29 \pm 0{\cdot}19$ for the D_s, which have the same sense as the Monte Carlo expectations, but with rather larger magnitude. The D_s and D^+ signals were used to measure the D_s/D^+

production ratio. The acceptance correction was found to be important, due to the different lifetimes of the signals. An acceptance and background corrected value of:

$$\frac{\sigma(D_s)\,B(D_s \to \phi\,\pi)}{\sigma(D^+)\,B(D^+ \to \phi\,\pi)} = 3{\cdot}2 \pm 1{\cdot}0\,^{+0{\cdot}9}_{-0{\cdot}7}$$

was measured. If the best available values are used for the relevant branching ratios this gives:

$$\frac{\sigma(D_s)}{\sigma(D^+)} = 0{\cdot}54 \pm 0{\cdot}17 \pm 0{\cdot}23$$

This is in good agreement with the prediction of ~ 0·5 from the Monte Carlo simulation, which uses the Lund scheme for hadronisation. These results suggest that the parameters of the Lund scheme, taken largely from e^+e^- results, are suitable for the description of charm photoproduction.

The NA14 experiment has provided high statistics samples of charmed particles, suitable for precise measurement of the physics of photoproduction and weak decay—fruitful areas for tests of QCD and the electroweak theory. The results are to some extent complementary to those of the other experiment with comparable statistics, as they lie in a different energy range. There remains a great deal of physics to be extracted from the data [120]—including the properties of charmed baryons, and cross-section studies—and the techniques of vertex detection and analysis used will remain central to much of the high energy physics of the foreseeable future.

Τα ξυνουμε συνεχεια

ACKNOWLEDGEMENTS

It is a pleasure to thank Dr Dave Websdale for his enthusiastic and diligent supervision of my work. I am also deeply indebted to Dr Marco Cattaneo, Mr Mike Koratzinos and Dr Mitch Wayne for their help and friendship.

The successful operation of the experiment owed a great deal to the competence of Dr Tony Duane and the inspiration of Dr Garry M^{c} Ewen, as well as the many other members of the collaboration. In particular I have gained benefit from the assistance of my colleagues in the search for the F, Mr Pascal Druet and Dr Christophe Magneville.

I am grateful to Prof David Binnie for accepting me into the high energy physics group at Imperial College, a group that I have found both congenial and encouraging to work with. My thanks go to Dr Bill Cameron for reading through this thesis.

Acknowledgement is due to the SERC for providing financial assistance, and to the staff at the San Pauli for using it.

Finally, I should like to express heartfelt thanks to my family for their support.

REFERENCES

[1] Particle Data Group, *Phys. Lett.* **170B** (1986) 1

[2] F. Halzen and A.D. Martin, *Quarks & Leptons*, John Wiley & Sons (1984)

P. Langacker, *Standard Model of the Electroweak Interaction*, DESY 87-153 (1987)

[3] E. Fermi, *Z. Phys.* **88** (1934) 161

[4] E. Ambler, R.W. Hayward, D.D. Hopper, R.P. Hudson and C.S. Wu, *Phys. Rev.* **105** (1957) 1413

[5] R.P. Feynman and M. Gell-Mann, *Phys. Rev.* **109** (1958) 193

[6] S.L. Glashow, *Nucl. Phys.* **22** (1961) 579

A. Salam and J.C. Ward, *Phys. Lett.* **13** (1964) 168

S. Weinberg, *Phys. Lett.* **19** (1967) 1264

[7] P.W. Higgs, *Phys. Rev. Lett.* **13** (1964) 508

[8] N. Cabibbo, *Phys. Rev. Lett.* **10** (1963) 531

[9] S.L. Glashow, J. Iliopoulos and L. Maiani, *Phys. Rev. D* **2** (1970) 1285

[10] M. Kobayashi and T. Maskawa, *Prog. Theor. Phys.* **49** (1973) 652

[11] S. Pakvasa and H. Sugawara, *Phys. Rev. D* **14** (1976) 240

[12] L. Wolfenstein, *Phys. Rev. Lett.* **51** (1984) 1945

[13] J.E. Augustin *et al.* (Mark I), *Phys. Rev. Lett.* **33** (1974) 1406

J.J. Aubert *et al*, *Phys. Rev. Lett.* **33** (1974) 1404

[14] J.E. Augustin *et al.* (Mark I), *Phys. Rev. Lett.* **34** (1975) 233

[15] R. Brandelik *et al.* (DASP), *Phys. Lett.* **70B** (1977) 132

[16] A. Chen *et al.* (CLEO), *Phys. Rev. Lett.* **51** (1983) 634

[17] S.F. Biagi *et al.* (WA62), *Z. Phys. C* **28** (1985) 175

[18] J. Prentice, *Proc. of the Int. Europhys. Conf. on HEP*, Uppsala (1987) 910

[19] H. Albrecht *et al.* (ARGUS), *Phys. Lett.* **134B** (1984) 137

[20] D. Bernstein *et al.* (Mark III), *Nucl. Instr. and Meth.* **226** (1984) 301

[21] R. Bailey *et al.* (NA32), *Phys. Lett.* **132B** (1983) 230

[22] J. Raab *et al.* (E691), Fermilab-Pub-87-144, submitted to *Phys. Rev. D* (1987)

[23] P. Astbury *et al.* (NA14), *Proposal to the SPSC*, CERN/SPSC/78-76, SPSC/P 109

P. Astbury *et al.* (NA14), *Addendum to proposal*, CERN/SPSC/78-139, SPSC/P 109 Add. 1

[24] P. Astbury *et al.* (NA14), *Phys. Lett.* **152B** (1985) 419

E. Auge *et al.* (NA14), CERN EP 86-176

R. Barate *et al.* (NA14), *Z. Phys. C* **33** (1987) 505

[25] *Addendum to NA14 experiment*, CERN/SPSC/82-73, SPSC/P 109 Add. 2

[26] TU Tung-Sheng, *Phys. Lett.* **89B** (1980) 232

[27] L. Stodolsky, *Phys. Rev. Lett.* **18** (1967) 135

J.J. Sakurai, *Phys. Rev. Lett.* **22** (1969) 81

[28] H. Fritsch and K.-H. Streng, *Phys. Lett.* **72B** (1978) 385

[29] J. Babcock, D. Sivers and S. Wolfram, *Phys. Rev. D* **18** (1978) 162

[30] L.M. Jones and H.W. Wyld, *Phys. Rev. D* **17** (1978) 759

[31] M. Jonker *et al.* (CHARM), *Phys. Lett.* **99B** (1981) 265

[32] S.J. Brodsky, R. Blankenbecler and D. Sivers, *Phys. Rep.* **23C** (1976) 1

[33] A.J. Buras and K.J.F. Gaemers, *Nucl. Phys. B* **132** (1978) 249

[34] M. Fontannaz, B. Pire and D. Schiff, *Z. Phys. C* **11** (1981) 211

[35] C.H. Llewellyn Smith, *Phys. Lett.* **79B** (1978) 83

D.W. Duke and J.F. Owens, *Phys. Rev. D* **22** (1980) 2280

[36] G. De Bouard, Thesis (unpublished), LAL 85-09

[37] D. Sivers, J. Townsend and G. West, *Phys. Rev. D* **13** (1976) 1234

[38] M. D. Sokoloff *et al.* (E691) *Phys. Rev. Lett.* **57** (1986) 3003

[39] P. Roudeau, presented at *2^{nd} Top. Sem. on Heavy Flav.* San Miniato (1987) LAL 87-39

[40] A. Capella and J. Tran Thanh Van, *Phys. Lett.* **93B** (1980) 146

[41] T. Sjostrand, *The Lund Monte Carlo for Jet Fragmentation and e^+e^- Physics*, LUTP 85-10

[42] X. Artu, *Z. Phys. C* **26** (1984) 83

[43] K. Abe *et al.* (SHF), *Phys. Rev. D* **33** (1986) 1

[44] M.V. Purohit, Fermilab-Conf-87/82

[45] D.G. Hitlin, presented at *Techniques and Concepts of HEP IV*, St. Croix (1986)

[46] E.D. Commins and P.H. Bucksbaum, *Weak Interactions of Leptons and Quarks*, C.U.P. (1983)

[47] S. Godfrey and N. Isgur, *Phys. Rev. D* **32** (1985) 189

[48] R.H. Schindler *et al.* (Mark III), *Proc. of the 23^{rd} Int. Conf. on HEP*, Berkeley (1986)

[49] J. Ellis, M.K. Gaillard and D.V. Nanopoulos, *Nucl. Phys B* **100** (1975) 313

[50] V. Lüth, SLAC-Pub-4222, to appear in *Proc. of the APS Division of Particle and Fields Meeting*, Salt Lake City (1987)

[51] R.M. Baltrusaitis *et al.* (Mark III), *Phys. Rev. Lett.* **54** (1985) 1976

[52] M.K. Gaillard and B.W. Lee, *Phys. Rev. Lett.* **33** (1974) 108

G. Altarelli and L. Maiani, *Phys. Lett.* **52B** (1974) 351

[53] D. Bailin, *Weak Interactions*, Adam Hilger Ltd. (1982)

[54] G. Altarelli, G. Curci, G. Martinelli and R. Petrarca, *Phys. Lett.* **99B** (1981) 141

[55] N. Cabibbo and L. Maiani, *Phys. Lett.* **73B** (1978) 418

[56] H. Fritzsch and P. Minkowski, *Nucl. Phys. B* **171** (1980) 413

[57] G. Altarelli, CERN TH-3709 (1983)

[58] I.I. Bigi and M. Fukugita, *Phys. Lett.* **91B** (1980) 121

[59] H. Albrecht *et al.* (ARGUS), *Phys. Lett.* **158B** (1985) 525

[60] J. Donoghue, *Phys. Rev. D* **33** (1986) 1516

[61] M.A. Shifman, A.I. Vainshtein and V.I. Zakharov, *Nucl. Phys. B* **120** (1977) 316

[62] R.M. Baltrusaitis *et al.* (Mark III), *Phys. Rev. Lett.* **55** (1985) 150

[63] A.J. Buras, J.-M. Gérard and R. Rückl, *Nucl. Phys. B* **268** (1986) 16

[64] R.D. Peccei and R. Rückl, *Proc. of the Ahrenhoop Symp.* (1981)

B. Guberina, R.D. Peccei and R. Rückl, *Phys. Lett.* **89B** (1979) 111

[65] M. Winter, Thesis (unpublished), Strasbourg (1981) CRN/HE 81-03

[66] M. Wayne, *The Tagging talk* (unpublished), Universidad Autónoma de Barcelona (1987)

[67] C. Seez, Thesis (unpublished), Imperial College London (1983) HEP-T-118

[68] G. Wormser, Thesis (unpublished), Orsay (1984) LAL 84-45

[69] Y. Tsai, *Rev. Mod. Phys.* **46** (1974) 815

[70] U. Fano, *Ann. Rev. Nucl. Sci.* **13** (1963) 1

[71] C.J.S. Damerell, *Developments in Solid State Vertex Detectors*, RAL 84-123 (1984)

[72] S.M. Sze, *Physics of Semiconductor Devices*, John Wiley & Sons (1981)

[73] L.G. Ixaru, contribution to *Formulæ and Methods in Experimental Data Evaluation*, Vol. 3, EPS (1983)

[74] M. Burchell, Thesis (unpublished), Imperial College London (1985) RAL-T-021

[75] E. Auge, Thesis (unpublished), Orsay (1983) LAL 83-09

D. Bloch, Thesis (unpublished), Strasbourg (1985) CRN/HE 85-06

[76] L. Landau, *J. Phys. (USSR)* **8** (1944) 201

[77] P. Vavilov, *Sov. Phys. JETP* **5** (1957) 749

G. Hall, *Nucl. Instr. and Meth.* **220** (1984) 356

[78] J. Dixon, Thesis (unpublished), Imperial College London (1986)

[79] K.H. Weber, *Nucl. Instr. and Meth.* **25** (1964) 261

[80] J.A. Ellison, Thesis (unpublished), Imperial College London (1987) RAL-T-046

[81] J. Kemmer, *Nucl. Instr. and Meth.* **226** (1984) 89

[82] R. Barate *et al*, *Nucl. Instr. and Meth. A* **235** (1985) 235

[83] G. Barber *et al*, *Nucl. Instr. and Meth. A* **253** (1987) 530

[84] M. Cattaneo, Thesis (unpublished), Imperial College London (1987) RAL-T-048

[85] P. Jarron and M. Goyot, *Nucl. Instr. and Meth.* **226** (1984) 156

[86] P. Jarron and L. Sohet, private communication.

[87] ESONE committee, *CAMAC, a Modular Instrumentation System for Data Handling*, EUR-4100-e (1968)

[88] H. Dietl *et al*, *Nucl. Instr. and Meth. A* **253** (1987) 460

[89] M. Koratzinos, private communication.

[90] R. Brun *et al*, *GEANT User Guide and Reference Manual*, CERN DD/US/86 (1983)

[91] R. Brun *et al*, *HPLOT User Guide*, CERN DD/US/87 (1982)

[92] A. Duane, private communication.

[93] C. Magneville, Thesis (unpublished), Orsay (1987)

[94] F. Bourgeois, *ASSIGN*, CERN Program Library.

[95] J.C. Lassalle *et al*, *TRIDENT Track Finding and Vertex Identification for the Omega Particle Detector System*, CERN DD/EE/79-2 (1983)

[96] *Formulæ and Methods in Experimental Data Evaluation*, Vol. 1, EPS (1983)

[97] W.T. Scott, *Rev. Mod. Phys.* **35** (1963) 231

[98] S. Brandt, contribution to *Formulæ and Methods in Experimental Data Evaluation*, Vol. 3, EPS (1983)

[99] C. Letertre, *PROB*, CERN Program Library.

[100] H. von Eicken, *DDVETA*, CERN Program Library.

[101] V. Blobel, contribution to *Formulæ and Methods in Experimental Data Evaluation*, Vol. 3, EPS (1983)

[102] P. Roudeau, private communication.

[103] C. Krafft, Thesis (unpublished), Orsay (1987) LAL 87-28

[104] R. Barate, private communication.

[105] K.R. Schubert, *Proc. of the Int. Europhys. Conf. on HEP*, Vol. II, Uppsala (1987) 791

[106] J.C. Anjos *et al.* (E691) Fermilab-Pub-87/203-E, submitted to *Phys. Rev. Lett.* (1988)

[107] F. James and M. Roos, *MINUIT*, CERN Program Library.

[108] C. Jung *et al.* (HRS), *Phys. Rev. Lett.* **56** (1986) 1775

[109] N. Ushida *et al.* (E531), *Phys. Rev. Lett.* **56** (1986) 1767

[110] H. Becker *et al.* (ACCMOR), *Phys. Lett.* **184B** (1987) 277

[111] W. Braunschweig *et al.* (TASSO), *Z. Phys. C* **35** (1987) 317

[112] J.C. Anjos *et al.* (E691), *Phys. Rev. Lett.* **58** (1987) 1818

[113] S.E. Csorna *et al.* (CLEO), *Phys. Lett.* **191B** (1987) 318

[114] D. Kelsey *et al.* (ACCMOR), *Proc. of the Int. Europhys. Conf. on HEP*, Vol. I, Uppsala (1987) 351

[115] J.C. Anjos *et al.* (E691), *Proc. of the APS Division of Particle and Fields Meeting*, Salt Lake City (1987)

[116] M. Binkley *et al.* (E400), Fermilab-Pub-87/220-E, submitted to *Phys. Rev. Lett.* (1988)

[117] B.R. Kumar, private communication.

[118] D. Bordoletto *et al.* (CLEO), CLNS-87/105, to be submitted to *Phys. Rev. D* (1988)

[119] M. Derrick *et al.* (HRS), *Phys. Rev. Lett.* **54** (1985) 2568

D.H. Miller *et al.* (HRS), PU-86-582 (1986)

[120] M. Koratzinos, Thesis in preparation, Imperial College London.